Measurement of the Disappearance of Muon Neutrino in 250 km Long Base Line Experiment

Takahiro Inagaki

Department of Physics,   Faculty of Science
Kyoto University

Abstract

This thesis presents the results of the first accelerator experiment of the neutrino oscillation with 250 km long base line. Muon neutrinos are generated by 12 GeV proton synchrotron, travel 250 km, and are detected in Super-Kamiokande, to measure reduction during the travel.

From June 1999 to June 2000, 2.29×10^{19} protons on target have been accumulated. The distribution of produced pions is measured by a gas Cherenkov detector. The measurement provides the neutrino energy spectra and the flux ratio at far/near site. The direction of the neutrino beam and the stability of the flux are monitored by a near neutrino detector. Measurements of the secondary muon and the proton profile in beam line hold the stability on spill-by-spill basis. These measurements confirm that the neutrino beam is stable enough to extrapolate the number of neutrino events from near to far detector. The absolute value of the event rate is derived from the measurements at 1kt water Cherenkov detector in the near site. The extrapolation shows the expected number of events in Super-Kamiokande is $37.8^{+3.8}_{-4.0}$.

Data of the corresponding period at Super-Kamiokande are analyzed. Super-Kamiokande observes 28 fully-contained events in 22.5 kt fiducial volume, with negligible background of $\mathcal{O}(10^{-3})$. Comparing the expectation and the observation, the probability of no change is 9.6%. The most likely explanation of this reduction is the neutrino oscillation. Assuming the hypothesis of $\nu_\mu \rightarrow \nu_x$ oscillation with large mixing angle, the best estimation of Δm^2 is around sevral of 10^{-3} eV^2. This is consistent with the recent assertion of the atmospheric neutrino observations.

Contents

Chapter 1

Introduction

1.1 Neutrino Mass

In the Standard Model of the weak interactions, neutrinos are considered as the massless leptons. In this case, three different neutrinos, ν_e, ν_μ, and ν_τ are identified by the correspondence to e, μ, and τ in the weak interaction. Then, the neutrinos are only expressed as the eigenstate of the weak interaction.

However, if the neutrinos have non-zero mass, they can be also expressed as the eigenstate of the mass. If the weak eigenstate is not equal to the mass eigenstate, the mixing causes the flavor change as that is observed in the quark sector. Furthermore, when three generations of leptons are mixed, one phase parameter may lead a CP violation. Thus, the observation of the non-zero neutrino mass and the existence of the lepton mixing make a significant extension beyond the Standard Model.

Direct mass measurement of the neutrinos has been performed by precise measurement of the decay kinematics. However, no experiment has found the finite mass over the measurement error. The most sensitive measurement of the ν_e mass was the electron spectrum measurement in the tritium beta decay (summarized in [1] and [2], and recent results are reported in [3]).

$${}^3_1\mathrm{H} \rightarrow {}^3_2\mathrm{He}^+ + e^- + \bar{\nu}_e \tag{1.1}$$

If $\bar{\nu}_e$ has a finite mass, the end-point of the electron energy spectrum shifts due to the 4-momentum conservation. Various experiments have been analyzed, and they give only the upper limit of several eV. In addition, the arrival time spread of the neutrinos from Supernova-1987A provides the upper limit of m_{ν_e} at a few 10 eV [4].

The best limit of the ν_μ mass was obtained from the muon momentum measurement of the pion decay at rest in PSI [5]. Based on this measurement and the average for the pion mass, PDG evaluated the mass limit of $m_{\nu_\mu} < 190$ keV in 90% confidence level [1].

Neutrino	Mass limit (by PDG [1])	Experiment
ν_e	3 eV	tritium β decay [3]
ν_μ	190 keV (90% C.L.)	pion decay [5]
ν_τ	18.2 MeV (95% C.L.)	tau decay [6]

Table 1.1: The present limit of the each neutrino mass, evaluated by Particle Data Group.

The present limit of the ν_τ mass was obtained from the kinematics of the tau decay in ALEPH detector [6]. Two separate limits were derived by fitting the distribution of visible energy versus invariant mass in

$$\tau^- \quad \rightarrow \quad 2\pi^-\pi^+\nu_\tau \tag{1.2}$$

$$\tau^- \quad \rightarrow \quad 3\pi^-2\pi^+(\pi^0)\nu_\tau \tag{1.3}$$

The two results are combined to obtain a 95% confidence level upper limit of $m_{\nu_\mu} <$ 18.2 MeV. Table 1.1 summarizes the mass limit referred by PDG [1].

1.2 Neutrino Oscillation

Another experimental search of the finite neutrino mass is the search of the "neutrino oscillation". This is the phenomenon that a neutrino changes its flavor, caused by the mixing between the flavor eigenstate and the mass eigenstate, when the neutrino has a non-degenerate mass. In following sections, the principle of the oscillation and the observation results are explained.

1.2.1 Oscillation formula

A flavor eigenstate $|\nu_\alpha\rangle(\alpha = e, \mu, \tau)$ is generally expressed by a mixing of mass eigenstate $|\nu_i\rangle(i = 1, 2, 3)$ as follows;

$$|\nu_\alpha\rangle \quad = \quad \sum_i U_{\alpha i}|\nu_i\rangle \tag{1.4}$$

where $U_{\alpha i}$ is the element of the unitary matrix U (Maki-Nakagawa-Sakata matrix [7]), corresponding to Cabbibo-Kobayashi-Maskawa matrix [8] in quark sector. When lepton sector consists of 3 generations, there are for free parameters, the 3×3 matrix U can be parameterized by three mixing angle θ_{12}, θ_{23} and θ_{13}, and one CPV phase δ;

$$U \quad = \quad \begin{pmatrix} 1 & 0 & 0 \\ 0 & c_{23} & s_{23} \\ 0 & -s_{23} & c_{23} \end{pmatrix} \begin{pmatrix} c_{13} & 0 & s_{13}e^{-i\delta} \\ 0 & 1 & 0 \\ -s_{13}e^{i\delta} & 0 & c_{13} \end{pmatrix} \begin{pmatrix} c_{12} & s_{12} & 0 \\ -s_{12} & c_{12} & 0 \\ 0 & 0 & 1 \end{pmatrix}$$

$$= \left(\begin{array}{ccc} c_{12}c_{13} & s_{12}c_{13} & s_{13}e^{-i\delta} \\ -s_{12}c_{23} - c_{12}s_{23}s_{13}e^{i\delta} & c_{12}c_{23} - s_{12}s_{23}s_{13}e^{i\delta} & s_{23}c_{13} \\ s_{12}s_{23} - c_{12}c_{23}s_{13}e^{i\delta} & -c_{12}s_{23} - s_{12}c_{23}s_{13}e^{i\delta} & c_{23}c_{13} \end{array} \right) \tag{1.5}$$

where $c_{ij} = \cos\theta_{ij}$ and $s_{ij} = \sin\theta_{ij}$.

When neutrinos are generated and interacted by weak interaction, they are identified as the flavor eigenstate. On the other hand, the time evolution of the state is described as the mass eigenstate in following Schrödinger equation;

$$i\frac{d}{dt}|\nu(t)\rangle = \mathcal{H}_0|\nu(t)\rangle \tag{1.6}$$

where $\mathcal{H}_0$ is Hamiltonian for the free neutrinos. When neutrinos have common momentum p, this equation can be solved as following energy eigenstate with $E_i = \sqrt{p^2 + m_i^2}$,

$$|\nu_i(t)\rangle = e^{-iE_it}|\nu_i(0)\rangle \tag{1.7}$$

Thus, ν_1, ν_2, ν_3 have different time evolution.

Assume the neutrino is generated as pure ν_α, probability for observing ν_β after finite time t (or at distance L) is expressed as follows;

$$\begin{aligned} P(\nu_\alpha \to \nu_\beta) &= |\langle\nu_\beta|U\mathcal{H}_0U^\dagger|\nu_\alpha\rangle|^2 \\ &= \delta_{\alpha\beta} - 2\sum_{i<j} Re\left[U^*_{\beta i}U_{\alpha i}U_{\beta j}U^*_{\alpha j}\left(1 - \exp\left(-i\frac{\Delta m^2_{ij}L}{2p}\right)\right)\right] \end{aligned} \tag{1.8}$$

where $\Delta m^2_{ij} \equiv m_i^2 - m_j^2$ is the difference of mass squared. If U has non-zero mixing angle θ and non-zero Δm^2, the second term of this formula changes the probability depending on the distance L. This phenomenon is called "Neutrino Oscillation".

As mentioned in following sections, the atmospheric neutrino observations indicate $\Delta m^2_{atm} \sim \mathcal{O}(10^{-2} \sim 10^{-3})$ eV^2, whereas the solar neutrino observations indicate $\Delta m^2_{sol} < \mathcal{O}(10^{-4})$ eV^2. Then, Δm^2_{ij} is approximated as follows;

$$\Delta m^2_{12} \ll \Delta m^2_{23} \simeq \Delta m^2_{13} \tag{1.9}$$

In this case, the contribution of Δm^2_{12} term becomes negligible and the oscillation probability relevant to the experiment can be expressed by following formula;

$$\begin{aligned} P(\nu_\mu \to \nu_\mu) &\simeq 1 - \cos^4\theta_{13} \cdot \sin^2 2\theta_{23} \cdot \sin^2\Phi_{23} \\ &\equiv 1 - \sin^2 2\theta_{\mu\mu} \cdot \sin^2\Phi_{23} && (1.10) \\ P(\nu_\mu \to \nu_e) &\simeq \sin^2\theta_{23} \cdot \sin^2 2\theta_{13} \cdot \sin^2\Phi_{23} \\ &\equiv \sin^2 2\theta_{\mu e} \cdot \sin^2\Phi_{23} && (1.11) \\ P(\nu_e \to \nu_e) &\simeq 1 - \sin^2 2\theta_{13} \cdot \sin^2\Phi_{23} && (1.12) \end{aligned}$$

Experiments	analysis	L	E_ν	Δm^2	results
Atmospheric neutrino observations					
	$\nu_\mu/\nu_e \to \nu_\mu/\nu_e$	$15 \sim 13000$ km	$0.1 \sim 100$ GeV	$10^{-4} \sim 10^{-2}\mathrm{eV}^2$	exist no
Solar neutrino observations					
	$\nu_e \to \nu_e$	1.5×10^8 km	$0.2 \sim 15$ keV	$< 10^{-4}\mathrm{eV}^2$	exist
Reactor neutrino experiments					
	$\bar{\nu_e} \to \bar{\nu_e}$	$0.02 \sim 1$ km	3 MeV	$> 10^{-3}\mathrm{eV}^2$	no
Accelerator neutrino experiments					
CHORUS NOMAD	$\nu_\mu \to \nu_\tau$	0.8 km	$20 \sim 30$ GeV	$> 1\mathrm{eV}^2$	no [30, 31]
CDHSW CHARM	$\nu_\mu \to \nu_\mu, \nu_e$	0.1, 0.9 km	$1 \sim 1.5$ GeV	$> 0.3\mathrm{eV}^2$	no [32, 33]
LSND	$\bar{\nu_\mu}, \nu_\mu \to \bar{\nu_e}, \nu_e$	0.03 km	< 53 MeV	$> 10^{-1}\mathrm{eV}^2$	exist [34]
KARMEN	$\bar{\nu_\mu} \to \bar{\nu_e}$	0.02 km	< 53 MeV	$> 10^{-1}\mathrm{eV}^2$	no [35]
K2K	$\nu_\mu \to \nu_\mu, \nu_e$	250 km	1.3 GeV	$> 10^{-3}\mathrm{eV}^2$	this thesis

Table 1.2: Comparison of the various neutrino oscillation experiments.

where

$$\Phi_{ij} \equiv \Delta m_{ij}^2 \cdot L/4p = 1.27 \cdot \Delta m_{ij}^2[\mathrm{eV}^2] \cdot L[\mathrm{km}]/E_\nu[\mathrm{GeV}] \tag{1.13}$$

gives the oscillation pattern depending on the baseline distance L and the neutrino energy E_ν. These expressions can be regarded as the 2 flavor oscillation with the effective mixing angle $\theta_{\mu\mu}$ and $\theta_{\mu e}$.

If the neutrino oscillation is actually observed, it proves the fact that the neutrinos have at least two different mass eigenstates, and at the same time, proves the existence of the mixing between the mass eigenstate and the flavor eigenstate. Taking a long base-line L and using the low energy E_ν neutrinos, the search of the oscillation has a good sensitivity to find non-zero Δm_{ij}^2 much less than eV^2. Various experiments have been performed to find the oscillation as summarized in Table 1.2. They are explained in following sections.

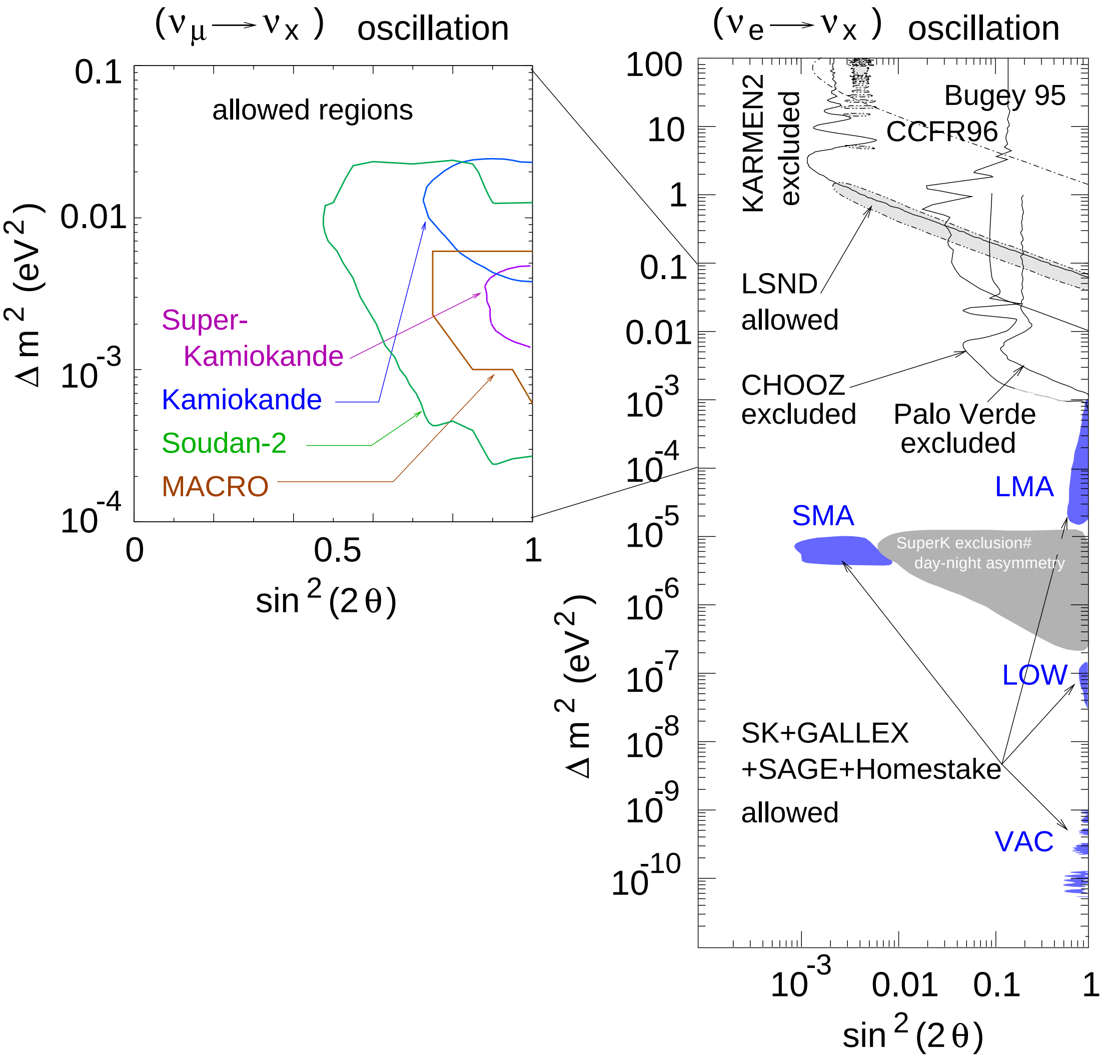

Figure 1.1: Allowed region of $\nu_\mu \to \nu_x$ oscillation (left), and $\nu_e \to \nu_x$ oscillation (right). The right figure refers to [1]

1.2.2 Atmospheric neutrino observations

Atmospheric neutrinos are produced by the decay of pions, kaons, and muons, which are produced by the collision of high energy cosmic ray protons injected to the upper atmosphere. The peak energy of these neutrinos is at about 1 GeV, and their energy spectrum extends to the order of 100 GeV. The main production process around sub-GeV range is following sequential pion decay;

$$\pi^{\pm} \quad \rightarrow \quad \mu^{\pm} \overset{(-)}{\nu}_{\mu} \tag{1.14}$$

$$\mu^{\pm} \quad \rightarrow \quad e^{\pm} \overset{(-)}{\nu}_{\mu} \overset{(-)}{\nu}_{e} \tag{1.15}$$

Therefore, the flux ratio of $(\nu_\mu + \bar{\nu_\mu})/(\nu_e + \bar{\nu}_e)$ is ideally 2. Considering the finite atmosphere geometry, the simulation predicts the ratio with 5% uncertainty, whereas the absolute flux has about 20% uncertainty.

This ratio has been measured in several underground experiments. Super-Kamiokande [9, 10], Kamiokande [11, 12], and IMB experiments [13, 14] use water-Cherenkov type neutrino detectors. Soudan-2 [15], Fréjus [16], and NUSEX [17] experiments use iron-calorimeter type detectors. In each detector, neutrino events are identified by the containment of the interaction vertex. Observed events are classify ed to the μ-type events N_μ or the e-type events N_e, by the Cherenkov ring pattern in the water-Cherenkov type detectors, or the hit distribution of the charged particles in the iron-calorimeter type detectors. The measured event ratio $(N_\mu/N_e)_{meas}$ are compared to the simulated value as follows;

$$R \equiv \frac{(N_\mu/N_e)_{meas}}{(N_\mu/N_e)_{MC}} \tag{1.16}$$

Table 1.3 summarizes the results R in these experiments. Historically, Kamiokande and IMB gave the significantly lower R value, which is called "atmospheric neutrino anomaly". On the other hand, in NUSEX and Fréjus experiment, R value was consistent to 1, while the data statistics are poor. Recently, Super-Kamiokande and Soudan-2 experiments has been performed with higher statistics. They show lower R values, which are consistent results with Kamiokande measurement.

Existence of the neutrino oscillation was clearly proved by the zenith angle dependence of the R value in Kamiokande and Super-Kamiokande experiments [10]. The upward-going neutrinos are originally produced at the atmosphere of opposite side of the globe and travel more than 10000 km distance through the earth, while the downward-going neutrinos travel only several 10 km from the upper atmosphere. Since the observed charged particles generally conserve the induced neutrinos' direction, the zenith angle of the observed Cherenkov ring distributions corresponds to the oscillation baseline L in the Formula 1.10 and 1.11. Figure 1.2 shows the distributions of μ-like and e-like events for 4 energy ranges. "sub-GeV (multi-GeV)" indicates the events that the visible energy is less (more) than

Experiment	exposure	R
Super-K (sub-GeV)	33 kt-yr	$0.63 \pm 0.03^{stat} \pm 0.05^{syst}$ [10]
Super-K (multi-GeV)	33 kt-yr	$0.65 \pm 0.05^{stat} \pm 0.08^{syst}$ [10]
Kamiokande (sub-GeV)	8.2 kt-yr	$0.60^{+0.06}_{-0.05}{}^{stat} \pm 0.05^{syst}$ [12]
Kamiokande (multi-GeV)	8.2 kt-yr (FC) 6.0 kt-yr (PC)	$0.57^{+0.08}_{-0.07}{}^{stat} \pm 0.07^{syst}$ [12]
IMB ($E_{vis} < 0.95$ GeV)	7.7 kt-yr	$0.54 \pm 0.05^{stat} \pm 0.12^{syst}$ [13]
IMB ($E_{vis} > 0.95$ GeV)	7.7 kt-yr	$1.1^{+0.07}_{-0.12}{}^{stat} \pm 0.11^{syst}$ [14]
Soudan-2	3.9 kt-yr	$0.64 \pm 0.11^{stat} \pm 0.06^{syst}$ [15]
Fréjus	2.0 kt-yr	$1.00 \pm 0.15^{stat} \pm 0.08^{syst}$ [16]
NUSEX	0.74 kt-yr	$0.96^{+0.32}_{-0.28}$ [17]

Table 1.3: Summary of the measured R values in various experiments. (sub-GeV) and (multi-GeV) represent the energy range. In Super-Kamiokande and Kamiokande, they are defined that the visible energy is less and more than 1.33 GeV, respectively. In IMB, the events are separately analyzed with the threshold of 0.95 GeV in visible energy.

1.33 GeV. Each data sample is arranged to two energy ranges by their reconstructed momentum. The figures also show the simulation without any oscillation (hatched box), and the best fit with $\nu_\mu \to \nu_\tau$ oscillation (bold line). The interpretation of the low R value has two choices, one is the $\nu_\mu \to \nu_e$ oscillation, the other is the $\nu_\mu \to \nu_\tau$ oscillation. The results of the zenith angle distribution shows the deficit in upward-going μ-like events, while e-like events shows flat distributions. Therefore, latter $\nu_\mu \to \nu_\tau$ scenario is strongly favored. The allowed region of the mixing angle and Δm^2 are;

$$\sin^2 2\theta_{\mu\tau} > 0.88, \quad 1.5 \times 10^{-3} < \Delta m^2 < 5 \times 10^{-3}\ \mathrm{eV}^2 \quad \text{in two flavor oscillation,}$$

and

$$\begin{array}{c} 0.4 < \sin^2\theta_{23} < 0.7 \\ \sin^2\theta_{13} < 0.35 \end{array}, \quad 1.5 \times 10^{-3} < \Delta m^2_{23} < 5 \times 10^{-3}\ \mathrm{eV}^2 \quad \text{in three flavor oscillation,}$$

at 90% confidence level, as shown in Figure 1.1 (left).

In addition, the flux of upward-going muons has been analyzed in Super-Kamiokande [18] and MACRO experiment [19]. Since the upward-going muons are produced by the high energy ν_μ interaction in the underground, their zenith angle distribution also represents the ν_μ oscillation. Both experiments showed the deficit in vertical direction comparing to the horizontal direction, which gave the consistent parameter region in $\nu_\mu \to \nu_x$ oscillation.

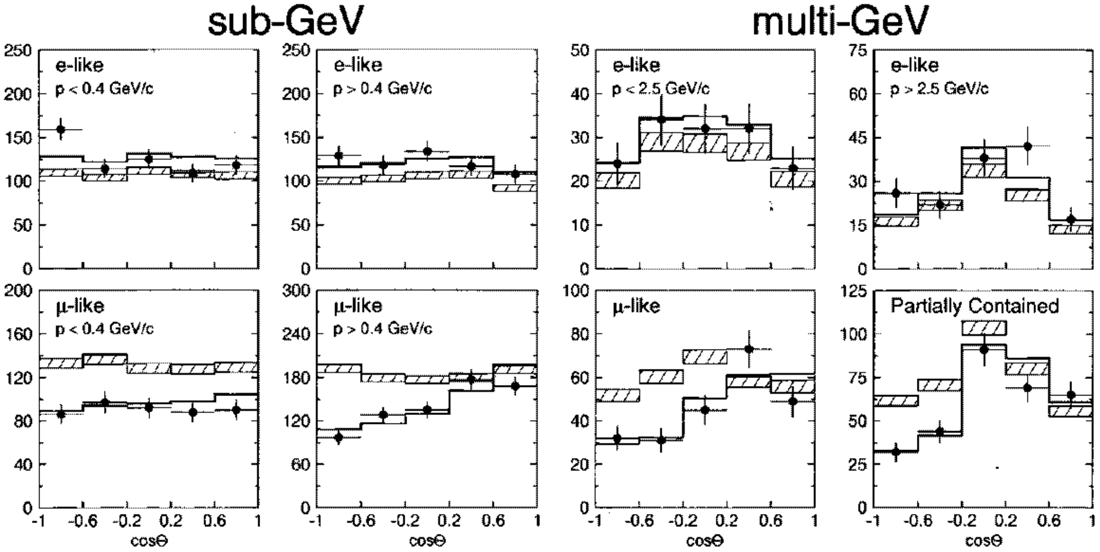

Figure 1.2: Zenith angle distribution of the μ-like and e-like events [10].

1.2.3 Solar neutrino observations

Solar neutrinos are produced by the nuclear interactions inside the sun. They are electron neutrinos with several 100 keV up to 15 MeV energy. Distance between the sun and the earth is 1.5×10^8 km. Therefore, the sensitivity of $\nu_e \rightarrow \nu_x$ oscillation reaches down to $\Delta m^2 \sim 10^{-11}$ eV^2. Two detection methods are used to analyze the solar neutrinos.

One is the measurement of the integrated amount of isotopes produced by the neutrino reactions as follows;

$$\nu_e + {}^{37}\mathrm{C}\ell \rightarrow e^- + {}^{37}\mathrm{Ar} \tag{1.17}$$

$$\tag{1.18}$$

in Homestake experiment [20], and

$$\nu_e + {}^{71}\mathrm{Ga} \rightarrow e^- + {}^{71}\mathrm{Ge} \tag{1.19}$$

in SAGE experiment [21], GALLEX experiment [22] and GNO experiment [23]. The results are summarized in Table 1.4. They show significantly lower neutrino flux comparing to the Standard Solar Model (SAM) of Bah call and Pinnsonneaut model (BP) [24].

Experiment	observation	$E_{thres.}$	Measured / BP2000
Homestake	Ar radioactivity	814 keV	0.34
SAGE+GALLEX+GNO	Ge radioactivity	233 keV	0.58
Kamiokande	water Cherenkov	7.0 MeV	0.55
Super-Kamiokande	water Cherenkov	6.5 MeV	0.48

Table 1.4: Results of the solar neutrino measurement, which are the measured flux over prediction given by BP2000. These comparisons are refereed from [24].

The other is the water-Cherenkov-type neutrino detector, which observe the Cherenkov photons from following elastic scattering.

$$\nu_e + e^- \rightarrow \nu_e + e^- \tag{1.20}$$

Kamiokande experiment [25] and Super-Kamiokande experiment [26] gave the results (Table 1.4) that also showed lower flux than expectation of SSM of BP model.

Recently, Super-Kamiokande has presented the energy spectrum of the recoil electrons and the flux difference between the daytime and the nighttime [27] which can be affected by the matter effect of the earth. They gave the constraint to the oscillation parameters. As a result, $\nu_e \rightarrow \nu_x$ oscillation with considering the MSW (Mikheyev-Smirnov-Wolfenstein) effect only could explain all the measurement. The allowed parameter region is $3 \times 10^{-5} < \Delta m^2 < 1 \times 10^{-4}$ eV^2 and $0.5 < \sin^2 2\theta < 0.9$, as shown in Figure 1.1 (right).

1.2.4 Reactor neutrino experiments

Several experiments [28, 29] have been performed to measure reactor-produced $\bar{\nu_e}$. The mean energy of $\bar{\nu_e}$ was about 3 MeV. The detectors were located with the distance of a few 10 m to 1 km far from the reactor core. $\bar{\nu_e}$ is interacted by the inverse β-decay reaction ;

$$\bar{\nu_e} p \rightarrow e^+ n \tag{1.21}$$

The detectors were filled with the liquid scintillator[1]. The events were identified by the coincidental detection of the prompt e^+ signal (boosted by the two 511-keV annihilation γ rays), and the delayed signal due to the n capture in the detector nuclei. The signal-to-background rate was estimated by comparing the data in reactor-ON and reactor-OFF.

All the experiments found no evidence of the $\bar{\nu_e}$ disappearance. The most sensitive result around $\Delta m^2 = 10^{-3} \sim 10^{-2}$ eV^2 was carried out by the CHOOZ experiment[28]. It

---

[1] In Krasnoyarsk experiment, the detector was a hexagonal prism filled with granulated polyethylene.

gave us the exclude region of $\bar{\nu_e} \rightarrow \bar{\nu_x}$ oscillation. With the assumption of Equation 1.12, parameters are restricted to approximately $\Delta m^2_{13} < 7 \times 10^{-4}$ eV^2 for maximum mixing, and $\sin^2 2\theta_{13} < 0.10$ for large Δm^2, as shown in Figure 1.1.

1.2.5 Accelerator neutrino experiments

$\nu_\mu(\bar{\nu_\mu})$ oscillation has been searched using the accelerator-produced neutrinos. The experiments which have the most sensitive results are listed below, and summarized in Table 1.2.

- $\nu_\mu \rightarrow \nu_\tau$, in $\Delta m^2 > 1$ eV^2 region.
  Two experiment, CHORUS and NOMAD has searched ν_τ events from the oscillation in the 800 m base line. Almost pure ν_μ beam with about 25 GeV average energy is produced from the π^+ decay in the production beam-line. In CHORUS detector, ν_τ events can be identified by the τ observation in the emulsion target. No τ candidate was found [30]. In NOMAD detector, ν_τ events can be analyzed by the kinematic distribution of the τ decay. An the result, there was no evidence for an oscillation signal [31]. Both experiments exclude the $\nu_\mu \rightarrow \nu_\tau$ oscillation down to $\sin^2 2\theta_{\mu\tau} < 4 \times 10^{-4}$ (90% C.L.) at large Δm^2.

- $\nu_\mu \rightarrow \nu_x$, in $\Delta m^2 > 0.3$ eV^2 region.
  Two old experiments, CDHSW and CHARM were performed using the ν_μ beam in CERN Proton-Synchrotron. The average energy of beam was 1 to 1.5 GeV. In each experiment, two similar detectors were placed on the near site (about 130 m from the π^+ production target) and the far site (about 900 m). Comparison of the observed events in near and far detector enable us the analysis of ν_μ oscillation. Both experiments reported no evidence of the oscillation was found [32, 33]. They excluded $0.3 < \Delta m^2 < 90$ eV^2 region for maximal mixing, and $\sin^2 2\theta > 0.05$ region at $\Delta m^2 = 2.5$ eV^2.

- $\bar{\nu_\mu} \rightarrow \bar{\nu_e}$, in $\Delta m^2 > 10^{-1}$ eV^2 region.
  Two experiments, LSND and KARMEN, has searched for μ^+ decay-at-rest $\bar{\nu_\mu} \rightarrow \bar{\nu_e}$ transitions by the reaction $\bar{\nu_e} p \rightarrow e^+ n$. Since the $\bar{\nu_\mu}$ is produced from stopped μ^+, it has a energy distribution according to Michel spectrum ($E_{\bar{\nu_\mu}} < 53$ MeV).

  The LSND neutrino detector is located 30 m far from the proton beam target. The detector consists of a large tank of mineral oil with a small admixture of scintillator, which enables us to tag the $\bar{\nu_e}$ interaction using the Cherenkov photons and the 2.2 MeV gamma rays from the subsequent neutron capture.

  The KARMEN detector is located at a distance of 17.7 m from the production target. The neutrinos are detected in a rectangular tank filled with a liquid scintillator, whose wall is coated Gd_2O_3 in order to detect efficiently thermal neutrons. The $\bar{\nu_e}$ event is identified by the delayed coincidence of the positron and γ emission of either of the two neutron capture process p(n,γ)d or Gd(n,γ).

Present results of these two experiments have fairly same sensitivity in the oscillation analysis. They show the opposite result each other. LSND reported the positive evidence of $\bar{\nu_e}$ appearance with a oscillation probability of $(0.25 \pm 0.06 \pm 0.04)\%$ [34]. On the contrary, KARMEN found no indication of the oscillation signal, and excluded many of the $(\sin^2 2\theta) - (\Delta m^2)$ space where LSND defined as an allowed region [35]. Assuming the exclusion from the KARMEN and reactor experiment result, the remaining allowed region is a narrow band shaped area between $(\sin^2 2\theta = 4 \times 10^{-2}, \Delta m^2 = 0.2\ \mathrm{eV}^2)$ and $(2 \times 10^{-3}, 1\ \mathrm{eV}^2)$, as shown in Figure 1.1.

1.2.6 Summary of the neutrino oscillation measurements

As shown in previous section, there are three positive measurement of the neutrino oscillation.

1	Atmospheric neutrino observations	$\Delta m^2 = 10^{-3} \sim 5 \times 10^{-3}\ \mathrm{eV}^2$
2	Solar neutrino observations	$\Delta m^2 \leq 10^{-4}\ \mathrm{eV}^2$
3	LSND	$\Delta m^2 = 0.2 \sim 1\ \mathrm{eV}^2$

If the neutrino has only three flavors (or closes with three generations), 3 neutrino mass eigenvalues can not explain these three different Δm^2. Or fourth generation or other exotic reduction scenario may be introduced to the Standard Model. Thus, these three cases must be carefully investigated as long as the fact is surely confirmed.

KamLAND experiment [36] will attempt to analyze the disappearance of $\bar{\nu_e}$ from nuclear power stations along the more than 100 km distance. It will cover the parameter range of case-2 ($\Delta m^2 >$ several $\times 10^{-6}\ \mathrm{eV}^2$).

The parameter range of case-3 will be investigated by the further measurement of KARMEN, and by MiniBooNE experiment [37] in Fermilab.

In order to confirm the parameter range of case-1, accelerator experiments, K2K experiment [38] has been performed since 1999. K2K experiment is the first terrestrial "long base-line" experiment with artificially produced ν_μ beam. If the Δm^2 exists over 2×10^{-3} eV^2, K2K is expected to provide significant evidence of the ν_μ oscillation, and to give constraint on the parameter space.

Entire understanding of the neutrino oscillation will imply the finite neutrino mass and the non-zero lepton mixing, which overtake the Standard Model.

This thesis is the report of the result for ν_μ disappearance in K2K experiment.

Chapter 2

Overview of the K2K Experiment

2.1 Concept of the Experiment

"K2K experiment" (KEK-PS-E362 [38]) was proposed and have been performed, in order to investigate the neutrino oscillation asserted by atmospheric neutrino observations. The experiment uses muon neutrinos, which are produced by the pion decay in flight as;

$$\pi^+ \rightarrow \mu^+ \nu_\mu \tag{2.1}$$

Large amount of pions are produced by hadron interactions of the high energy proton beam, provided by 12 GeV proton synchrotron (KEK-PS) in High Energy Accelerator Research Organization (KEK). Generated neutrinos travel through the 250 km distance and are observed at Super-Kamiokande detector (SK). Neutrinos are also measured just after the production by near neutrino detectors, which are located 300 m downstream of the target in KEK. Comparison of both observations gives us evidence (or exclusion) of the neutrino oscillation.

Main characteristics of K2K experiment are;

- **Sensitivity around $\Delta m^2 = 10^{-2} \sim 10^{-3}$ eV^2 range.**
  As described in previous chapter, atmospheric neutrino observations have asserted the oscillation parameter Δm^2 is in this range. Since the mean energy of the neutrinos is 1.3 GeV, 250 km base line is the appropriate (Formula 1.10).

- **Large far detector.**
  One of the difficulty of this type of experiment is low statistics due to the small cross section of neutrinos and due to the small acceptance for 250 km far site. The most massive neutrino detector, SK gains enough statistics of the events. In this experiment, expected events at SK is typically 0.4 events per day without oscillation.

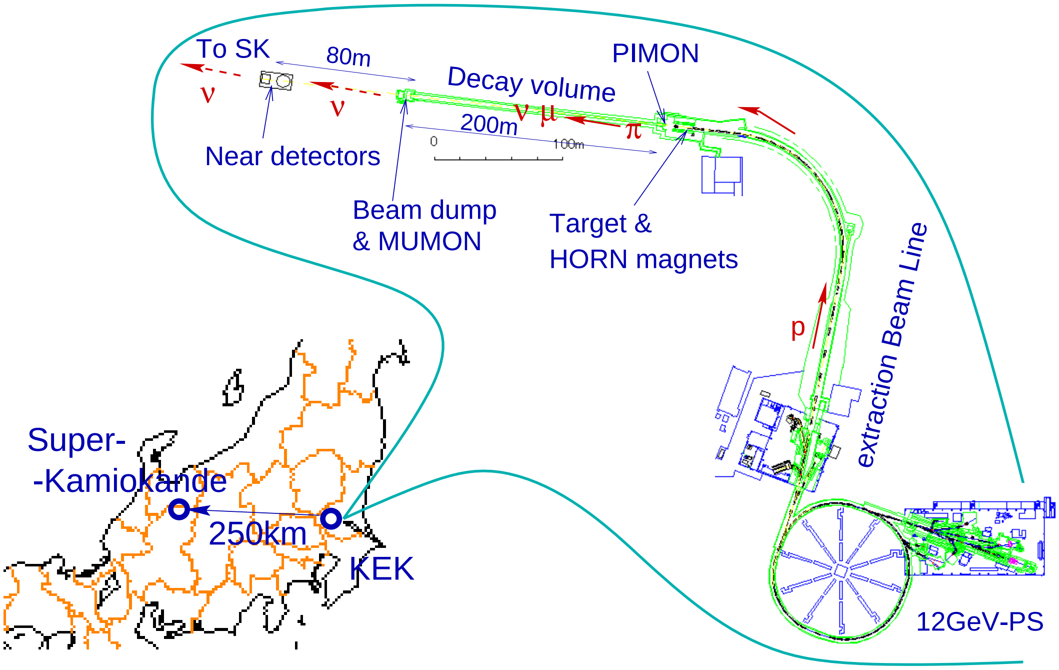

Figure 2.1: The schematic view of K2K experiment.

- **Simultaneous measurement at the neutrino production site and at the far site.**
  The neutrino beam properties can be experimentally measured before oscillation. Comparison of the observation in both site enable us to cancel most of the neutrino flux uncertainty as well as cross section uncertainty.
- **Accelerator-produced neutrinos.**
  Neutrino beam can be controlled and monitored by the measurement of protons, pions and secondary muons.

Basically the neutrino oscillation is studied by the comparison of the neutrino event distribution at near detector and the far detector. The analyzed quantities are mainly listed below;

- ◇ **Number of ν_μ events.**
  This (and next) kind of analysis is called "ν_μ disappearance". When deficit of the neutrino event rate is observed at the far site comparing to the observation at the near site, this proves the existence of the neutrino reduction mechanism, which is probably the neutrino oscillation (or some exotic scenario like neutrino decay).

◇ **Energy spectrum distortion of ν_μ events.**
When the observed neutrino reduction is caused by the neutrino oscillation, the reduction probability depends on the neutrino energy as shown in Formula 1.10. Therefore, measured energy spectrum of ν_μ at the far detector differ from the expected spectrum that is obtained from the measurement at the near site. This distortion pattern strongly proves the oscillation of $\nu_\mu \rightarrow \nu_x$ mode. By fitting the distortion pattern with Formula 1.10, the two oscillation parameters θ and Δm^2 can be determined.

◇ **ν_e event appearance.** [1]
When mixing angle between ν_μ and ν_e is not equal to zero, some ν_μ may oscillate to ν_e. This oscillation mode is studied by searching for the electron production by ν_e events at the far detector.

◇ **Events from neutral current (NC) interaction.**
When the ν_μ oscillation is observed, the study of the number of NC interaction gives the distinction of $\nu_\mu \rightarrow \nu_\tau$ or $\nu_\mu \rightarrow \nu_{sterile}$.

This thesis focused on the study of the number of event comparison between the near site and the far site. So far, event statistics is not enough to discuss about the energy spectrum.

2.2 Analysis of the Muon Neutrino Disappearance

As emphasized in previous section, ν_μ disappearance is investigated by means of the comparison of the observed number of ν_μ events in both sites. For the comparison, near detector measurement is expressed by following "number of expected event at SK";

$$N_{exp}^{SK} = \frac{N_{obs}^{near}}{\epsilon_{near}} \cdot \frac{\Phi_{far} \cdot \sigma_{far} \cdot M_{far}}{\Phi_{near} \cdot \sigma_{near} \cdot M_{near}} \cdot \epsilon_{SK} \tag{2.2}$$

where,

N_{obs}^{near} : number of observed events at near detector
ϵ_{near}, ϵ_{SK} : event selection efficiency
Φ_{near}, Φ_{far} : expected neutrino flux considering the angular acceptance difference
σ_{near}, σ_{far} : neutrino cross section
M_{near}, M_{far} : fiducial mass.

This expectation N_{exp}^{SK} and the observed number of events N_{obs}^{SK} are compared.

---

[1] Present studies and results of ν_e appearance mode is described in other thesis [39].

2.3 Components Design

K2K experiment was designed and constructed with satisfying following key issues.

- **Similar near detector to the far detector.**
  A water-Cherenkov-type detector named "1-kilo-ton detector (1kt)" was constructed as a near detector, to avoid uncertainty of the neutrino cross section. Then, σ_{near} and σ_{far} in Formula 2.2 are strictly canceled, and the large part of the uncertainty of ϵ_{near} and ϵ_{far} are also canceled.

- **Experimental measurement of Φ_{far}/Φ_{near}.**
  The flux ratio of Φ_{far}/Φ_{near} basically obeys the L^{-2} dependence where $L < 300$m at near site and $L = 250$km at far site from the production point of neutrinos. However, the decay point of pions depends on their energy and geometry of the decay volume. In addition, neutrinos are focused to the forward direction due to the Lorentz boost of pions, and the directional distribution depends on the pion direction and energy distribution. There has been large uncertainty in hadron interaction process at this energy range, and the simulation of pion production is not reliable enough to predict the neutrino flux.

  Then, the experimental measurement of pion energy and angular distribution is performed using the "pion monitor (PIMON)". The result can be compared to various Monte Carlo simulations with different hadron interaction models. The confirmed pion production model provides the neutrino energy and angular distribution. And finally, the flux ratio of Φ_{far}/Φ_{near} is obtained.

- **Neutrino beam pointing to SK.**
  The neutrino beam should be pointed to SK. The neutrino beam has a broad profile due to the pion divergence and the smearing by the pion decay. Figure 2.2 shows the expected profile broadness at SK site, and the energy spectrum estimated by Monte Carlo simulation (which is described in Chapter 4). According to these figures, the pointing accuracy of 3 mrad is needed to keep the neutrino flux and the spectrum shape.

  Direction of the neutrino beam is generally derived from the pion direction, which is determined by the two focusing magnets, named "HORN magnets". Direction of the neutrino beam is confirmed at the near detector. Muon Range Detector (MRD) with 7.6 m ×7.6 m of transverse area, effectively measure the spatial profile of ±10 mrad range. In addition, secondary muons are measured by Muon monitor (MUMON) on spill-by-spill basis. The muon profile center also confirms the neutrino beam direction.

  These components, that is, HORN magnets, MRD, and MUMON should be aligned with enough accuracy. Positions of SK and KEK were measured using Global Posi-

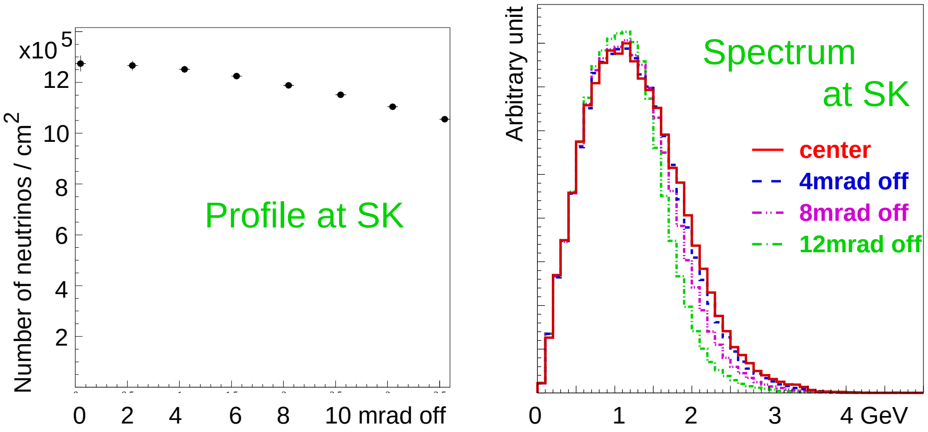

Figure 2.2: Left: Neutrino spatial profile at SK site. Right: Energy spectrum of the expected neutrino at SK site, without oscillation. Both figures are made by the Monte Carlo simulation.

tioning System (GPS) survey within 0.01 mrad accuracy [40]. Table 2.1 shows the position of the production target in the beam line (KEK) and center of the SK water tank. Following this survey point, these components were carefully aligned within 0.1 mrad accuracy.

- **Time synchronization.**
  Expected signal rate at SK is about 0.4 event per day (no oscillation), on the other hand, the fully-contained events from atmospheric neutrino is about 8 events per day. The most effective way to identify beam associated neutrino events is time synchronization with the KEK-PS. Simultaneous reception of GPS signal at both site

	Latitude	Longitude	altitude above sea
Target at KEK	$36^\circ09'14.9531''$ (N)	$140^\circ04'16.3303''$ (E)	70.218 m
SK center	$36^\circ25'32.5862''$ (N)	$137^\circ18'37.1214''$ (E)	371.839 m
distance from KEK to SK		249.83 km	
downward tilt		$1^\circ04'30''$	

Table 2.1: The positions of the production target at KEK and the center of SK water tank, measured by GPS survey [40].

provides the time calibration with the order of 100 ns precision. Two GPS receivers are prepared at each site. Since the proton beam is provided by fast-extraction with 1.1μs spill width, we obtain the order of μsec time window for event selection in every 2.2 sec repetition cycle. Thus, the background rate is suppressed to the order of 10^{-5} comparing to the signal rate.

Considering these issues, following components were designed and constructed.

- **KEK-PS and proton beam line,**
  which accelerate protons and bent them toward the direction of SK.
- **Proton beam monitors,**
  which measure the intensity and profile of the proton beam along the proton beam line, to monitor the beam stability.
- **Target and two HORN magnets,**
  where pions are produced by the hadron interaction, and are focused by toroidal magnetic field of two HORN magnets.
- 200 **m long decay volume,**
  where π^+ decay to ν_μ and μ^+. After the decay volume, an iron and concrete beam dump stops all charged particles and only neutrinos are pass through the earth to reach the near detectors and SK.
- **Pion monitor (PIMON),**
  which is occasionally put in the secondary beam line, in order to measure the pion momentum and angular distributions. The obtained distribution provides the energy spectrum shape of the neutrino beam and the flux ratio Φ_{far}/Φ_{near}.
- **Muon monitors (MUMONs),**
  which measure high energy muons above 5.5 GeV, in order to confirm the neutrino beam pointing on spill-by-spill basis.
- **Near neutrino detectors,**
  which consist of following detectors.
  - **1-kilo-ton water Cherenkov detector (1kt),**
    which is a miniature detector of SK. The obtained neutrino events are used for the comparison to the events in SK.
  - **Muon Range Detector (MRD),**
    which has a large coverage and a largest neutrino event rate, The results are used for the neutrino profile determination and also give the neutrino beam stability.

1995	Proposal [38] was approved at KEK.
	Components design was started.
1996	Civil construction was started.
1998	Detector components were placed.
	Civil construction finished.
Feb., 1999	Proton beam was extracted to the target.
Mar., 1999	Horn has been operated.
June, 1999	We started stable data taking with 200 kA. horn current
Oct., 1999	We started stable data taking with 250 kA. horn current

Table 2.2: The history of K2K experiment.

  - **Fine grained detector system (FGD),**
    which has a water tubes with scintillation fiber tracker as a neutrino interaction target. This is used for the neutrino energy reconstruction, and the study of the neutrino interaction.

- **Super-Kamiokande detector (SK),**
  which is used as the far neutrino detector.

Figure 2.1 shows the location of these components. In the next chapter, detailed structure and performance of them are described with this order.

2.4 History of K2K

Table 2.2 summarizes the history of K2K experiment. Stable data taking has been performed since June 1999. In this thesis, we analyzed the data with 100 days from June 1999 to June 2000 corresponding to 2.29×10^{19} protons on target.

Chapter 3

Experimental Components

K2K experiment consists of the accelerator, neutrino beam line, near detector systems, and 250km far site detector, Super-Kamiokande. The brief explanation of the purpose and performance in this experiment are described in following sections.

3.1 Neutrino Production Beam Line

3.1.1 Accelerator and proton beam line

KEK-12GeV Proton Synchrotron (KEK-PS) in High Energy Accelerator Research Organization (KEK) is used [41]. Its specifications are summarized in Table 3.1. More than 7×10^{12} protons per one cycle are accelerated up to 12 GeV in kinetic energy. Each extracted beam spill has 9 bunches in 1.1μs spill length. The repetition cycle is 2.2 second.

After protons are accelerated to 12GeV, they are extracted by the kicker magnet system at "EP1-A" section. Kicker magnets changed the proton orbits inside the PS and four septum magnets separate them to the extraction line. All the 9 bunches are extracted just in one cycle of 1.1μs, named "single turn extraction." This fast extraction is effective to our neutrino experiment to distinguish the beam-associated events from the backgrounds.

The extracted beams are collimated and lead to the target section by the proton beam line named "EP1 neutrino beam line" (shown in Figure 3.1). In this beam line, protons are bent about 90 degree to the West-North-West at the final section, pointing to SK [40]. 61 quadrupole magnets and 44 dipole magnets are used in this 400 m section.

3.1.2 Proton beam monitors

In order to control and monitor proton beam, beam monitor systems are used along the beam line, as shown in Figure 3.1. With these monitors, following issues are monitored;

Accelerator components	Pre-injector (750 keV, Cockroft-Walton acc.) LINAC (40 MeV) BOOSTER (500 MeV) Main ring (12 GeV in kinetic energy)
Operation mode for K2K	fast extraction (single turn) to EP1-A
Typical intensity in main ring	7×10^{12} protons per spill
Typical intensity after extraction	6×10^{12} protons per spill
Number of bunches	9
Bunch repetition	about 120 ns
Total spill length	1.1μs
Repetition cycle	2.2 sec

Table 3.1: Specification summary of KEK-PS for K2K experiment.

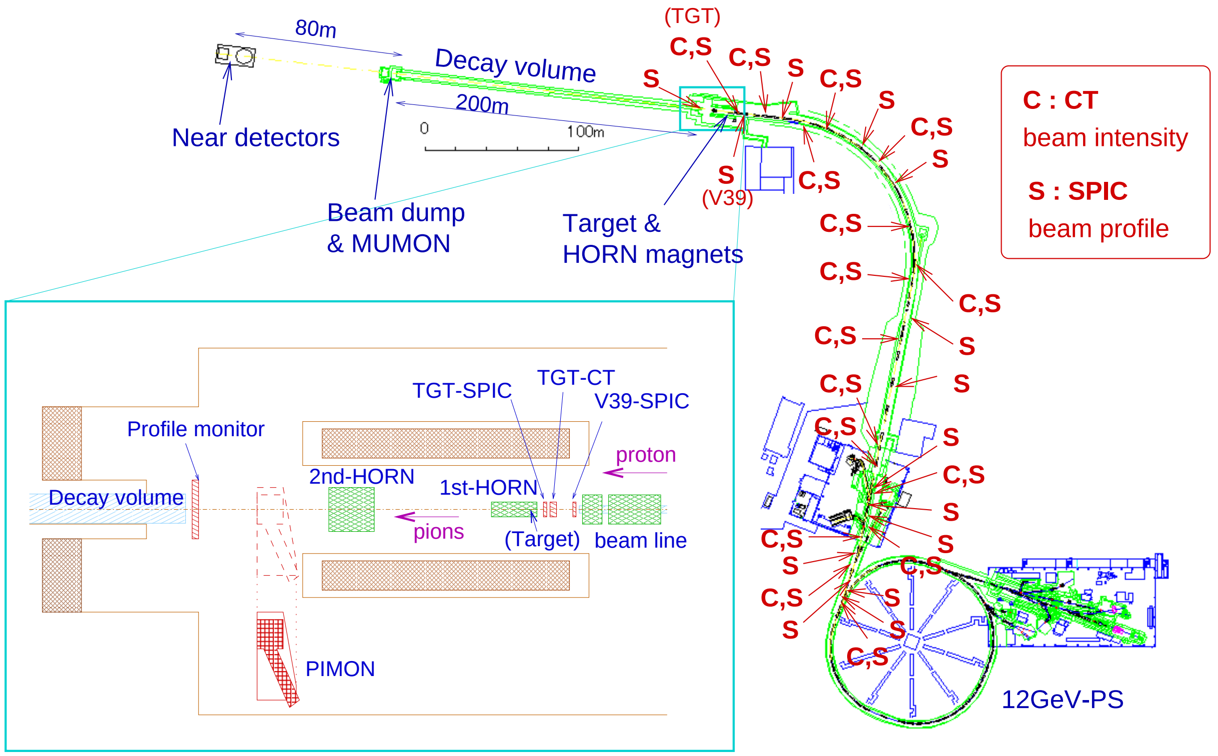

Figure 3.1: Location of the neutrino production beam line components and monitors. Lower-left figure shows a magnification view of the target area.

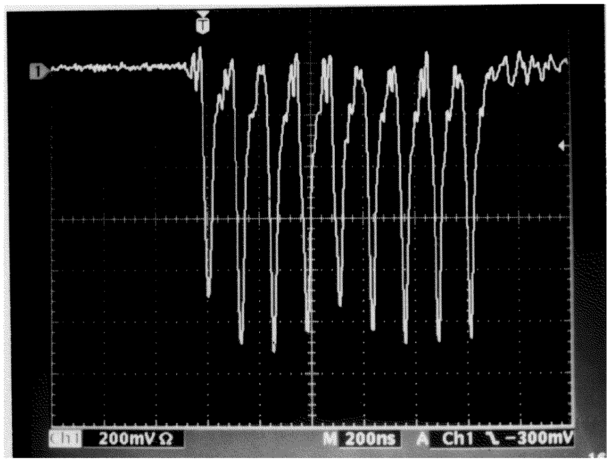

Figure 3.2: Oscilloscope photograph of the typical beam time structure from CT. Bunch structure is clearly shown while it is smeared due to the time constant of CT. Signals are usually measured with integration during the one spill gate time (1.3μs) by ADCs

- Proton beam intensity, and transport efficiency.
- Proton beam profile, in particular, at the target section.

Intensity monitors

Proton intensity is measured with 13 Integrated Current Transformers (CT), which picks-up the wake field when protons pass the coils. Figure 3.2 shows the typical signal shape of the proton beam. The signals are lead to the control room several 10 m to 100 m far out of the radiation area, and connected to the charge integration ADCs with full beam spill gate of 1.3μs. The CT's inner diameter is about 12cm, which is the same size as the beam pipe and large enough to contain the proton beam. Most of the CTs are placed along the vacuum pipe. One CT named "TARGET-CT" is placed in front of the target. The proton transport efficiency is monitored by CTs.

The CTs were calibrated by pulsed current source. The result shows the ±10% systematic error, due to the noise induced at 100 m long coaxial cables.

Profile monitors

Proton profiles are measured by 27 Segmented Plate Ionization Chambers (SPIC), shown in Figure 3.3. SPIC is the ionization chamber consist of three copper foiled capton sheets with 1 cm gap. Central plane is the anode (negative high voltage) and the outer ones are

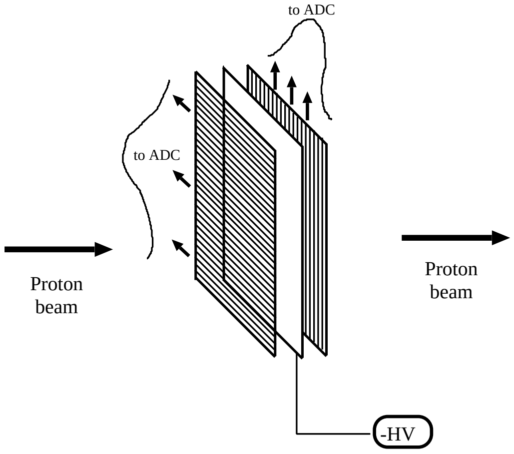

Figure 3.3: The schematic view of the Segmented Plate Ionization Chamber (SPIC).

the horizontal and the vertical readout cathodes. Size of the sensitive area of the SPICs is 4.1 cm square for one most downstream SPIC "TARGET-SPIC", and 16 cm square for other ones. They sufficiently cover whole proton profiles. The thickness of the sheet is 28μm. The gap is filled with helium. The electrons are collected by high voltage (typically -1000 V) between the copper cathodes and anodes. Cathodes are 32 of separated stripes with 1.27 mm and 5 mm pitch for "TARGET-SPIC" and others, respectively. The signals are read by charge sensitive ADCs.

Obtained proton profiles are continuously monitored. In particular, V39-SPIC and TARGET-SPIC which are located between final bending magnet "V39" and the target, are used to obtain proton emittance (profile and divergence), with 128 cm in free space (shown in Figure 4.1).

The further description about the SPIC is in [42].

3.1.3 Production target and focusing devices

Pions are generated from the hadron interaction of 12 GeV protons at the target. In order to focus these pions toward SK, two toroidal horn magnets provides the magnetic field as shown in Figure 3.4. "1st-HORN" has the aluminum target rod inside, in order to achieve high focusing efficiency, overcoming a rather large beam spot size. "2nd-HORN" is the reflector which is located at 10 m downstream of the 1st-HORN.

Electrical current is supplied along the beam axis between inner and outer conductors, which wakes the toroidal magnetic field between them, and also partially inside of the target rod. When current I_{horn} (kA) is supplied, the strength of the magnetic field B (kGauss) at

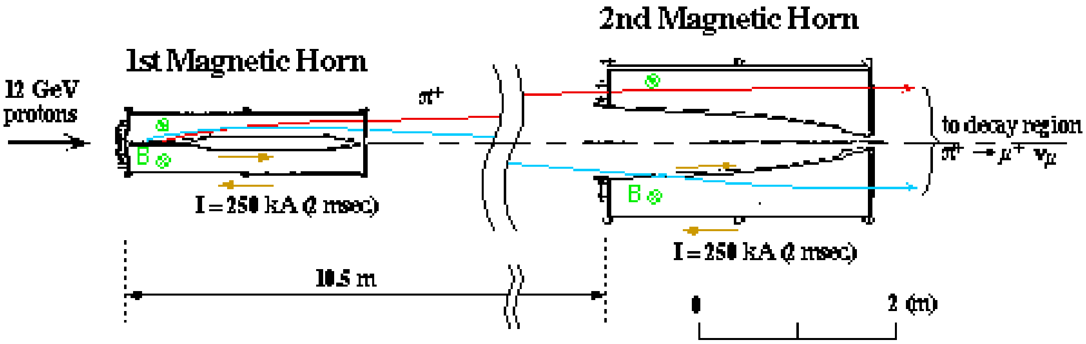

Figure 3.4: Schematic view of the two horn magnets.

radius r (cm) is given by;

$$B = \frac{I_{horn}}{5 \cdot r}, \qquad \text{where,}(r \geq R : \text{rod radius}) \tag{3.1}$$

Hence, the maximum magnetic field is 33 kGauss at $R = 1.5$ cm rod surface at $I_{horn} = 250$ kA. This field focuses the positive charged particles to forward direction and sweeps out the negative particles. Thus π^+ is selectively collected to get almost pure ν_μ. In addition, protons are also focused along the target, which improves the targeting efficiency. This two horn system enhances neutrino flux above 0.5 GeV by 22 times of one with no current case (see Figure 3.5).

1st-HORN is 0.70 m in diameter and 2.37 m in length. Target, inner, and outer conductors are made of aluminum alloy 6061-T, which is chosen for the reason of the light density, strength and electrical conduction. The length of the target rod is 66 cm. The diameter is 2 cm in June 1999 run, and 3 cm since Oct. 1999. The target corresponds to 1.7 interaction length [1]. Monte Carlo simulation (described later) shows almost all protons interact in the target, including elastic scattering. 2nd-HORN is 1.65 m in diameter and 2.76 m length, in order to focus spread low energy pions. Except the target, central region is vacant to avoid loss due to pion's secondary interaction. Both horn conductors are kept thin as much as strength requirement permitted.

Both horns have perfect cylindrical symmetry except four current feeders attachments at the front side. Pulsed electrical current is supplied to both horns. The peak current is 200 kA in June 1999 run and 250 kA since Oct. 1999. The pulsed cycle is synchronized with the beam extraction of 2.2 sec. repetition period. The total pulse length is about 3 ms and the timing of the current peak is adjusted to the beam timing, which is quite flat during the beam spill (1.1μs). The current is made by the HORN power supply with 6 mF

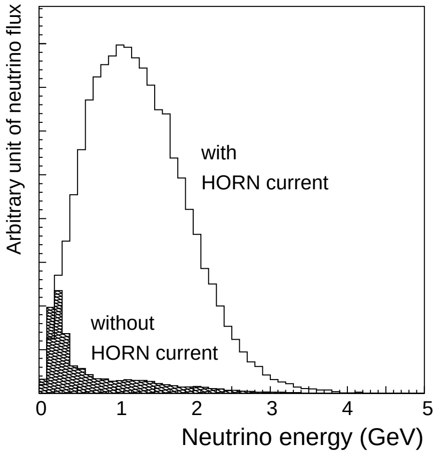

Figure 3.5: Expected neutrino flux at the Super-Kamiokande site in Monte Carlo simulation, with (solid) or without (hatched) horn current. Target diameter is 30 mm and current is 250 kA. Above 0.5 GeV, enhance factor is about 22.

capacitors and the thyristor switches. The pulsed operation is needed to avoid the thermal melt down and to reduce continuous electrical power. The current is measured by CTs put in the each power feeders, with Flash-ADC readout.

Magnetic field inside of the HORN was measured using coils for pro-to-type of the 1st-HORN (target rod is 2 cm diameter). The radial distribution is roughly consistent with the design and the azimuthal symmetry is confirmed within the measurement error of 15% [43]. The only non-symmetry structure in the azimuthal direction is four current feeders, which are commonly used both this pro-to-type HORN and the actually used one. Therefore, ±15% error is quoted as the azimuthal uniformity of the field in following analyses.

Further detailed issues about the horn systems are described in [44, 45].

Proton targeting and the pion focusing is also monitored by a large SPIC type ionization chamber, which is installed at the entrance of the decay volume (about 7 m downstream of 2nd-HORN). The coverage is $2(h) \times 1.5(v)$ m and it contains 192 and 160 channels for horizontal and vertical projection. It is used for monitoring to be kept the spatial symmetry of charged particles.

3.1.4 Decay volume

Focused pions (mainly π^+) are sent to the 200 m long decay volume which start at 19 m downstream from the target. The diameter is 1.5 m in the first 10 m section, 2 m in the following 90 m section, and 3 m for the remaining 100 m section. It is filled with helium at 1 atm. to avoid pion absorption loss and "un-controllable" pion production in the gas.

In the decay volume, π^+ decays to μ^+ and ν_μ.

$$\pi^+ \longrightarrow \mu^+ \nu_\mu \tag{3.2}$$

Because π^+ is strongly boosted, ν_μ is also emitted towards the Super-Kamiokande within some decay angle of several 10 mrad order. The neutrino profile is broad more than several km at Super-Kamiokande site.

Finally all the charged particles are stopped at the beam dump just after the end of the tunnel. The dump is consist of 3.5 m iron block, 2 m concrete and about 60 m soil (see Figure 3.15). Only the neutrino can pass through this shield to the near neutrino detector and SK.

3.2 Pion monitor (PIMON)

3.2.1 Goal of PIMON

Most of neutrinos come from well-known two-body decay of pions, as Formula 3.2. Therefore, neutrino flux in each acceptance can be predicted from the measurement of pion momentum and angular distributions.

When pions with momentum p_π decays to neutrinos, the energy of the neutrinos is;

$$E_\nu = \frac{m_\pi^2 - m_\mu^2}{2(E_\pi - p_\pi)(1 + \gamma^2\theta^2)} \tag{3.3}$$

where $\beta = p_\pi/E_\pi$ and $\gamma = E_\pi/m_\pi$ are the Lorentz factors, and θ is the polar angle of neutrino with respect to the pion direction in the laboratory flame. The neutrino flux $d\Phi$ in small solid angle $d\Omega$ is;

$$\frac{d\Phi}{d\Omega} = \frac{N}{4\pi\gamma^2(1-\beta\cos\theta)^2} \tag{3.4}$$

where, N is the number of decayed pions. The decay probability is basically given as a function of the pion velocity. In realistic case, the geometrical constraint of pion decay volume is considered. Pion flight and decay is traced using Monte Carlo simulation.

Pion monitor (PIMON) intends to measure 2-dimensional distribution of pion momentum (P_π) and divergence (θ_π) space just after the HORN magnets. From this (P_π, θ_π) distribution, the neutrino flux at both detector and their ratio can be obtained with previous formula.

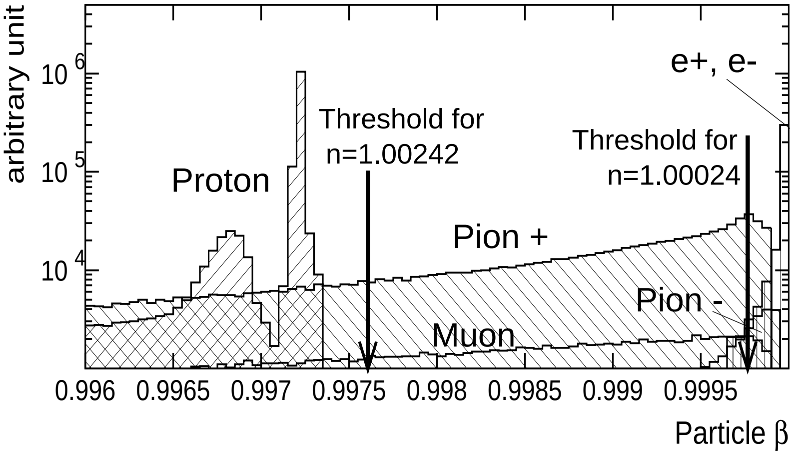

Figure 3.6: β distribution of protons, pions, muons and $e^{\pm}$ after the 2nd-HORN. In this figure, (radius) $<$ 60 cm, and $\tan\theta < 50$ mrad from the beam axis, are required.

3.2.2 Cherenkov technique for pion identification

The most severe requirement for PIMON is the pion identification from the large background of protons and electrons. Figure 3.6 shows the beta distribution of protons, pions, muons and $e^{\pm}$ after the PIMON site, in Monte Carlo simulation. Protons dominate over pions by about factor 2.

Cherenkov photon measurement distinguishes the pions from protons. Since our beam energy is 12 GeV in kinetic energy, proton momentum is naturally less than 13GeV/c. Then Cherenkov threshold is set at over the threshold of 13GeV/c protons. Electrons and positrons remain to the main background for high energy pions.

3.2.3 Cherenkov technique for simultaneous measurement of (p_π, θ_π)

Cherenkov photons is emitted as the corn shape with half opening angle of;

$$\cos\theta_c = \frac{1}{n\beta} \tag{3.5}$$

around the particle direction. Therefore, particle direction is obtained from the ring direction. And, Cherenkov ring radius gives the particle momentum.

In order to collect these Cherenkov photons, a spherical mirror is used. Figure 3.7 explains the characteristic of the spherical mirror. The spherical mirror focuses the light with an incident angle to a fixed position of the focal plane. That is, all the Cherenkov photons from the charged particles with certain momentum and certain direction gathers to the unique point on the focal plane, independent of its emission point. When a pion with velocity β $(= p_{pi}/E_{pi})$ and radial angle θ_π on the vertical direction, emitted Cherenkov photons are focused on y-axis of the focal plane at;

$$\begin{aligned} y &= L \cdot \tan(\theta_\pi \pm \theta_c) \\ &= L \cdot \left(\tan\theta_\pi \pm \sqrt{\frac{n^2}{1 + (m_\pi/p_\pi)^2} - 1} \right) \end{aligned} \tag{3.6}$$

where, L is the focal length, which is the half of the curvature radius of the spherical mirror.

Most of pions have only the radial divergence rather than the azimuthal angle, because the magnetic field of HORN does not give any azimuthal momentum. It is necessary to know only the radial divergence, in order to obtain neutrino flux with Formula 3.3. Therefore, PIMON can concentrate to measure radial divergence.

If simple circular spherical mirror is used, many Cherenkov rings with various central positions are overlapped, as shown in Figure 3.8-A. This image is hard to analyze. To avoid this difficulty, a "pie-shaped" mirror is used. The mirror is the part of the spherical mirror, as shown in Figure 3.8-B. Since the divergence of pions is dominated in vertical direction, the rings are aligned along the vertical axis. The photon distribution on vertical axis is measured to obtain $(p_\pi,\ \theta_\pi)$ distribution with Formula 3.6. It is assumed that obtained pion distribution is valid for all the azimuthal part, because the HORN magnets and beam line is designed azimuthal symmetric.

Cherenkov photon distributions are observed by photo detectors. They are vertically aligned at the focal plane. The photo detectors suffer hard radiation damage in the beam line area. Therefore, the photo detectors should be kept as far away from the beam line as possible. For this reason, the spherical mirror is placed with a 30 degree angle to the beam axis, to deflect Cherenkov photons to the photo detectors. This makes small spherical aberration acceptable for the analysis.

Considering these characteristics, PIMON was designed as shown in Figure 3.9. Using this mirror optics, observable Cherenkov photon distributions are simulated as shown in Figure 3.10. These distributions are obtained with certain refractive indices, and the realistic pion distributions simulated by our standard Monte Carlo simulation (this called "beamMC", described in Chapter 4).

Designed refractive indices are provided by gas. In order to obtain high refractive index, freon gas R-318 (C_4F_8) is used. The refractive index n of certain gas is given by following Lorentz-Lorenz formula;

$$\frac{n^2 - 1}{n^2 + 2} = \frac{N\alpha}{3\epsilon_0} \tag{3.7}$$

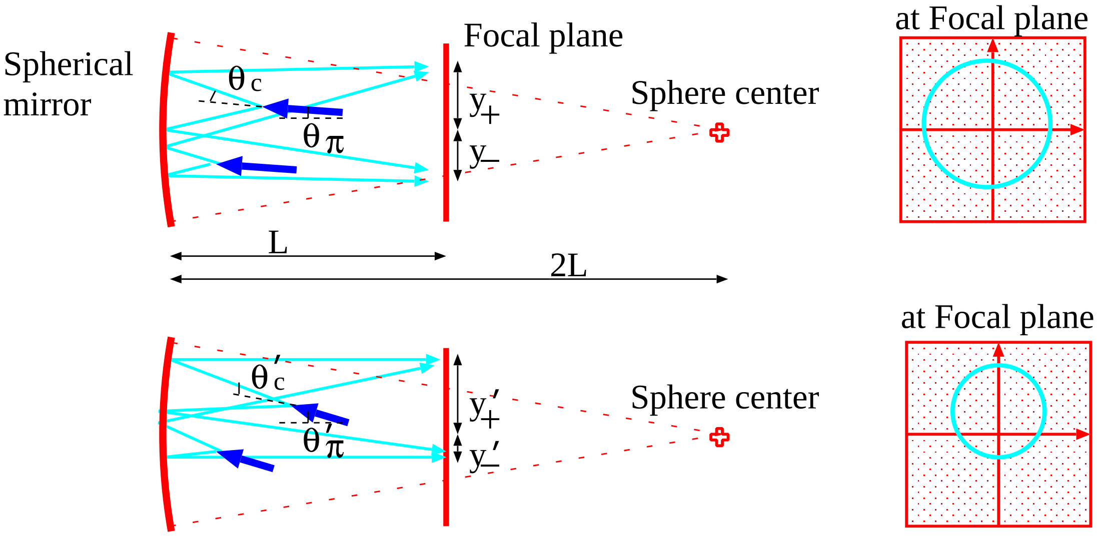

Figure 3.7: Focusing optics of the spherical mirror.

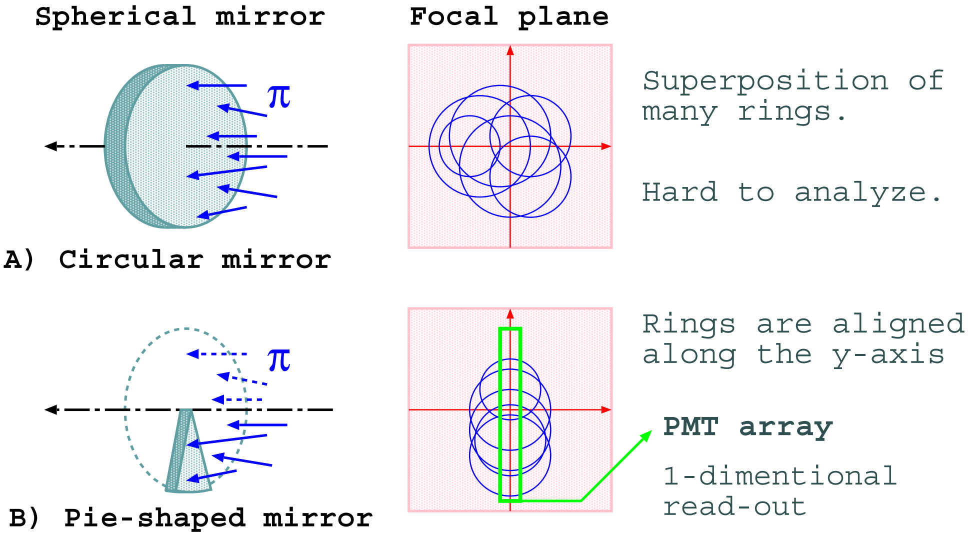

Figure 3.8: Advantage of the pie-shaped mirror.

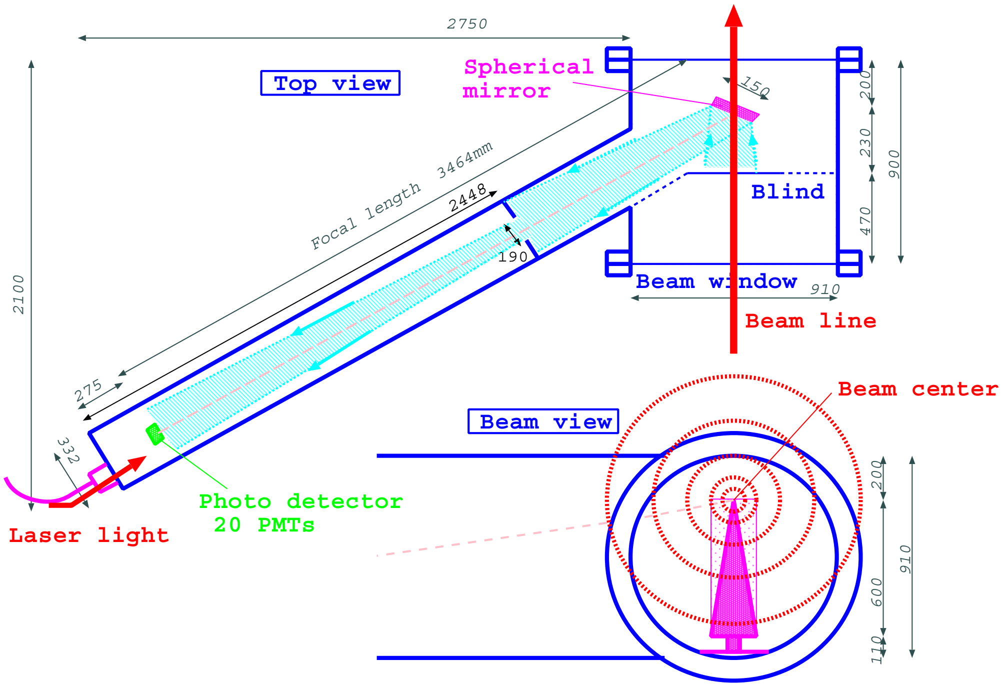

Figure 3.9: The schematic view of PIMON.

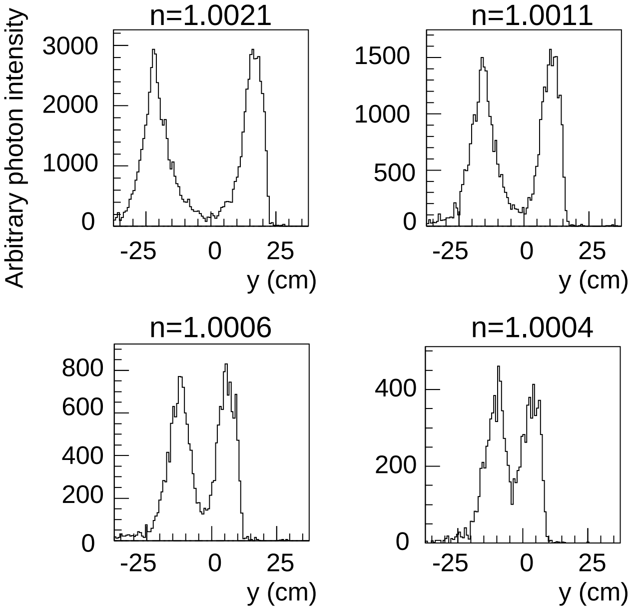

Figure 3.10: Y-directional slice of the typical Cherenkov photon distribution in Monte Carlo simulation, in various refractive indices. Horizontal axis of there figures is the vertical position at the focal plane. Only pions are simulated to emit the Cherenkov photons.

Pressure (atm.)	Refractive index	Cherenkov threshold for pion (GeV/c)
0.18	1.00024	6.4
0.31	1.00041	4.9
0.34	1.00048	4.5
0.42	1.00058	4.1
0.53	1.00074	3.6
0.68	1.00095	3.2
0.92	1.00129	2.7
1.24	1.00176	2.4
1.70	1.00242	2.0

Table 3.2: Freon gas pressure set in PIMON measurement in Nov. 1999. Refractive indices are calibrated by primary proton measurement described in Section 3.2.6.

where N is the number of molecules or atoms per unit volume, α is the polarizability of the molecules or atoms, and ϵ_0 is the dielectric constant of vacuum. N is given as $N = P/kT$ with the pressure P, the temperature T and the Boltzmann constant k. When $(n-1) \ll 1$, this formula is written as;

$$n - 1 = \frac{\alpha}{2\epsilon_0 k}\frac{P}{T} \tag{3.8}$$

After all, $n-1$ is proportional to the gas pressure P at fixed temperature.

Gas pressure can be controlled by an external gas system. Changing the gas pressure, Cherenkov photon distributions are measured with different Cherenkov threshold. Table 3.2 summarizes the freon gas pressure, refractive index, and the Cherenkov threshold, which are used in our measurement.

3.2.4 Analysis strategy

Observed Cherenkov photon distributions (typically shown in Figure 3.10) are superpositions of Cherenkov rings from particles of various momentums and divergences, as shown in Figure 3.11.

Reconstruction of the pion population in (p_π, θ_π) bins

Several Cherenkov photon distributions are obtained with various refractive indices listed in Table 3.2. They are fitted as weighted sum of the contributions from particular (p_π, θ_π)

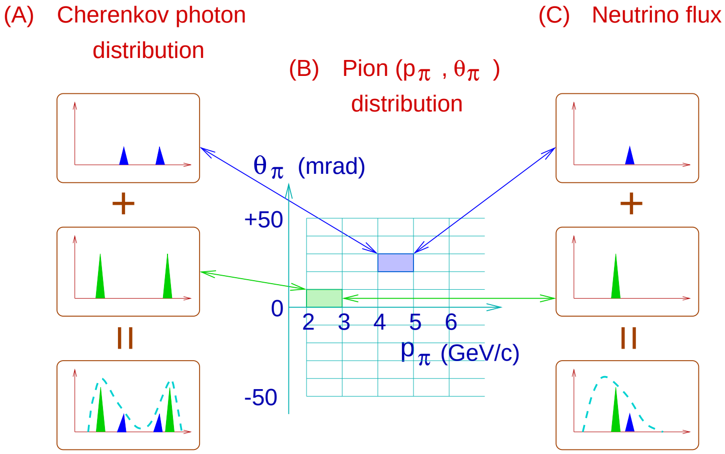

Figure 3.11: Analysis strategy of PIMON. It explains one-to-one correspondence between (p_{pi}, θ_π) plane and Cherenkov photon distribution, and (p_{pi}, θ_π) plane and neutrino energy spectrum.

bins, with considering following χ^2;

$$\chi^2 = \sum_k \left(\sum_{j=1}^{numberofPMT} \frac{(dist_j^{obs} - \sum_{n=1}^{50} W(n) \cdot dist(n)_j)^2}{\sigma_j^2} \right)_k \tag{3.9}$$

where, k is the identifier of the measurement with certain refractive index, j is the PMT number, n is the identifier of each pion kinematic bin, and $W(n)$ is a pion population in the $n-$th kinematic bin. By minimizing this χ^2, the best combination of pion populations $W(n)$ is obtained.

Prediction of the neutrino flux

Determined pion kinematic distribution gives the neutrino flux with Formula 3.3 and Formula 3.4. Neutrino flux from each (p_π, θ_π) is obtained using the pion tracing simulation with known decay volume.

Reconstruction test using Monte Carlo simulation

Monte Carlo study of our reconstruction method was performed [46]. The reconstructed results agreed well with the MC true distributions. Small discrepancies are assigned to the systematic errors of fitting method in Chapter 6.1.6.

3.2.5 Design of PIMON

As shown in Figure 3.1, PIMON is located at downstream of the 2nd HORN magnet, and in front of the decay volume. PIMON is designed to be retractable. It is rolled into the beam-line only during the PIMON measurement run. Otherwise, it is hidden at the escape position to avoid from disturbing the beam and its radiation damage.

To consider realistic circumstance of PIMON, the requirements are summarized;

- Measure pions in large background of protons and electrons.
- Measure (p_π, θ_π) distribution of a few 10^{12} pions per every spill.
- Measure intense photons with fast spill structure. The instantaneous photon intensity is up-to 10^9 photons in 1.1μs.
- Need large acceptance for the pion beam. Most of the pions are spread to 50 cm from the beam axis at the PIMON site.
- Keep minimum material along the beam line. To reduce the effect of beam interaction, beam window should be thin.
- Stand against severe radiation in the primary beam line.
- All systems and monitors are remotely controlled. Mechanical reliability of operation is needed. Because it is very hard to access to PIMON site due to the hard radiation during the running period.

Considering these issues, PIMON apparatus was designed and constructed. Figure 3.9 shows the schematic view of PIMON.

3.2.6 Hardware of PIMON

As shown in Figure 3.9, PIMON mainly consists of a gas volume and control system, a spherical mirror, photon detectors, a monitoring system, and a readout system. These sub-sections show the performance and calibration of them.

Gas vessel

Gas vessel is made from 5 mm thick stainless steel except for the beam window. The beam window is placed at the beam entrance and exiting point at the cylinder part of the vessel. The size is about 65 cm wide and 90 cm high. They are made from 1 mm aluminum (Al-6061), in order to reduce interaction in the window. This thickness corresponds to 0.01 radiation length and 0.0025 interaction length. PIMON must stand with the pressure

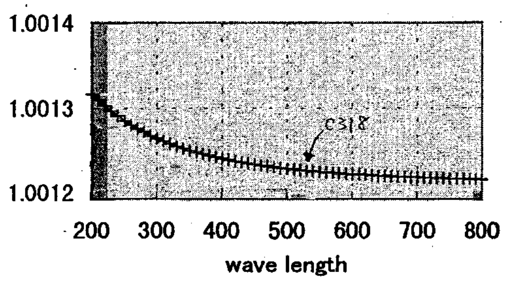

Figure 3.12: Wavelength dependence of the refractive index of freon R-318. The horizontal axis shows the wavelength, and the vertical axis shows the index at 1 atm. These data are referred from [47].

change between the −1 atm. (vacuum) and +1.1 atm. (maximum index). Resistance test of the window was performed using water. It was confirmed that they have enough strength [46].

A 50μm thick aluminum foil is set 23 cm in front of the mirror. This foil defines the fiducial area of the Cherenkov photon emission that is free from the beam window convex and concave.

All surface of the inner wall is painted black in order to reduce scattered light. An optical slit in the middle of the mirror and the PMTs also reduces the scattered light.

As described in previous section, PIMON is occasionally installed from the escape position. Gas vessel is set on a movable support. It is remote-controlled with a position meter. The alignment of the vessel and mirror optics is ensured by the geometrical survey within 1 mm accuracy.

Gas system

The gas supply system consists of freon gas bottles and a buffer tank, connected to PIMON by 100 m pipe with 1 inch diameter. Used gas is recirculated to the buffer tank using a recirculation pump. In addition, two vacuum pumps are prepared to set low pressure below 1 atm. The supply system is heated, because freon R-318 has low vapor pressure of about 2.3 atm. at 20 degree.

Refractive index of the freon gas is shown in Figure 3.12. There is wavelength dependence of the refractive index. Wavelength of the observed Cherenkov photon is determined by the emitted wavelength distribution (proportional to λ^{-2}), mirror reflectivity, transparency of the quartz window on PMT surface, and the quantum efficiency. In our case, it is assumed that 160 to 300 nm is the dominant wavelength range.

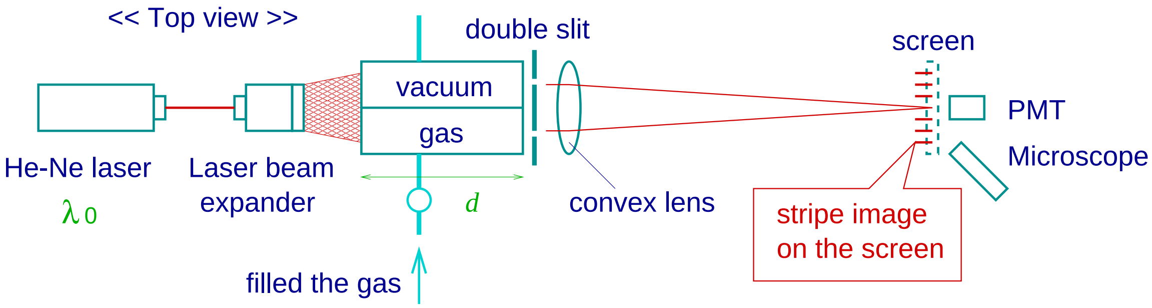

Figure 3.13: The schematic view of the interferometer.

The refractive index of freon gas is measured by two methods.

- One is the measurement using an interferometer as shown in Figure 3.13. He-Ne laser light is expanded through the beam expander. It goes to a vacuum vessel that is separated into two regions inside. One part of it is kept at vacuum (~ 1 torr) and the other is being filled with gas with a constant rate. Laser light passes a double slit and a convex lens to make stripe image on the screen in front of a microscope. The stripes slide proportional to the gas pressure. The number of stripes which pass through the one fixed point on the screen is counted by eyes or a photo-multiplier. This number N is related to the refractive index n by the following formula;

  $$N = \frac{n-1}{\lambda_0/d} \tag{3.10}$$

  where λ_0 is the wavelength of the laser (632.8 nm), d is the length of the vacuum vessel (16 cm).

  Obtained refractive index itself cannot be used for Cherenkov photon calculation, because wavelength of used laser light is different from that of Cherenkov photons. Although, this measurement is used to confirm the gas purity of the freon gas stored in the buffer tank.

- The absolute value of the refractive index is obtained by the measurement of the Cherenkov photons emitted by primary protons. Gas pressure of PIMON is set at 2.11 atm. and Cherenkov photon distribution is measured as Figure 3.14. It clearly shows the inner two steep peaks made by primary protons with 12 GeV kinetic energy, and two low peaks from pions. The refractive index is calculated from the distance of two peaks using the Formula 3.6. As a result, the refractive index is $n = 1.00294$ at 2.11atm.

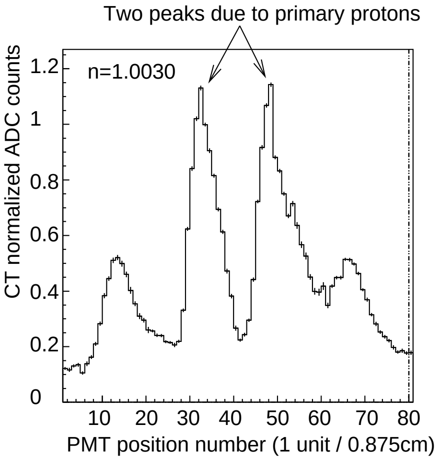

Figure 3.14: Cherenkov photon distribution measured by PIMON, in 2.11 atm. Two peaks around the center part is made from the 12 GeV proton.

Spherical mirror

The spherical mirror is shown in Figure 3.9. The radius of curvature is 6 m and the size is 60cm × 15 cm. The thickness is about 8 mm. It is made of Pyrex glass, which is partially coated with Al and frosted by sand to make a pie-shape. It covers about 12 degree of azimuthal part of the beam. The mechanical hardness for the radiation and heat-up of the mirror material was tested with intensive proton beam at KEK-Booster [46]. The optics of the mirror was confirmed using an LED [46]. The absolute reflectivity is assumed about more than 90% for Al coat, although the value is not used in the PIMON analysis because absolute pion intensity is not used for analysis.

PIMON has a mirror monitoring system using a dye laser to check the partial radiation damage. Light from a 410 nm dye laser is lead to the PIMON by quartz optical fiber. The light is directed towards the mirror and reflected to the PMT array. The reflectivity is monitored from the pulse height of the PMTs. We compared the reflectivity on the beginning of the run with that after first-year run. The result indicated that the partial reduction of the reflectivity suffered no damage within ±6% during 1999 run.

Photo detectors

Twenty photo-multiplier tubes (PMTs) are used as the photon detectors at the focal plane of the spherical mirror. Signal of each PMT is lead by a 100 m long cable to a charge sensitive ADC placed in the data acquisition room outside.

PMTs are Modified-R5600-01Q type made by HAMAMATSU Photonics Corporation. Notable characteristics are following;

- Small size.
  The size is 15.5 mm in diameter of the outer socket and 8 mm in diameter of the photo-cathode. This size enables us to align 20 PMTs along the vertical direction with 35 mm steps.

- Quartz window.
  This is adopted for radiation hardness instead of standard BK7 glass. The radiation hardness is tested by the exposure at KEK-PS-K3-beamline [46, 48].

- Multi-Alkali(Sb-Na-K-Cs) photo-cathode material.
  This is selected due to the wide dynamic range for intense light. An utilizing Multi-Alkali photo-cathode does not saturate up to 10μA, whereas a Bialkali photo-cathode saturates at 0.1μA [49].

- Low gain.
  PMTs should observe large amount of Cherenkov photon ($\sim 10^9$ photons instantly). Low gain PMT is required not only to adjust signal level to ADC but to avoid the signal saturation. The PMTs are modified to reduce the multiplication in each dynode step. Typical gain in our operation is 300 in Jun.99 run and $20 \sim 50$ in Nov.99 run.

Gain of PMT was relatively adjusted and calibrated using Xe lamp before the experiment. A Xe lamp with a diffuser was put in front of the PMT array. It provided isotropic light with order of 10^7 (10^5) photons in 500 ns per one PMT for Nov.(Jun.) run. Then, suitable high voltage was set by interpolation of the measurement with several high voltages. Relative ratio of this gain has 5%(10%) systematic error for Nov.(Jun.) run, mainly due to the uncertainty of the measurement of Xe light profile [46].

In addition, the gain ratio was also confirmed using Cherenkov photon during the run. Movable PMT holder enables each PMT to slide to the next PMT. Assuming Cherenkov photon intensities were stable after proton intensity normalization, the ratio of the signal gave us a gain ratio between the overlapped PMTs. The results were roughly agreed with the ratio from Xe lamp measurement, although this measurement have about 20% error due to the beam stability.

The linearity of each PMT was checked by the Cherenkov photon measurement with the correlation of the proton beam intensity and the observed signal. In Nov. run, no saturation was observed because of the low gain. In Jun.99 run set, PMT saturation was observed. The non-linearity was fitted with a 2nd polynomial function and corrected for measured signals. The uncertainty of the non-linearity correction of about 4% is compiled as a systematic error in June run.

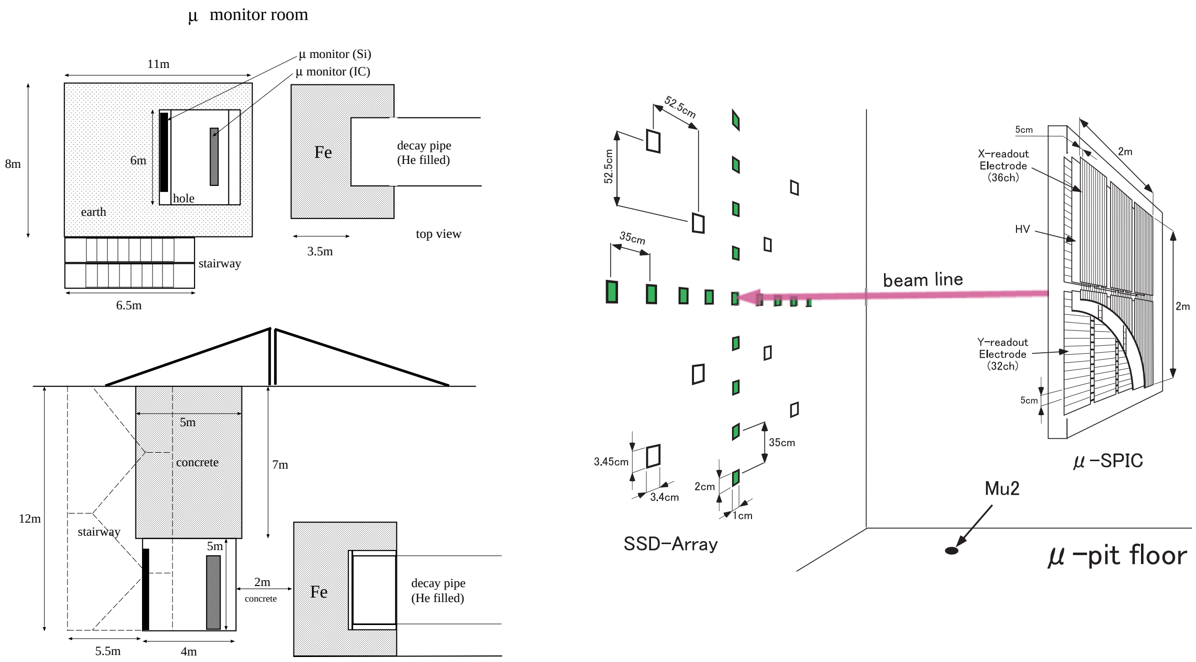

Figure 3.15: Left: the beam dump of the neutrino beam line and the muon monitor pit. Right: schematic view of muon monitors, Silicon Solid Detectors (SSD) array and ionization chamber (μ-SPIC in the figure)

3.3 Muon Monitors (MUMONs)

3.3.1 Goal of the MUMON

Muon monitors (MUMONs) measure the secondary muons after the beam dump. These muons are come from $\pi^+ \rightarrow \mu^+\nu_\mu$ decay in the decay volume. Since pion is a spin-less particle, muon profile center and neutrino's are same. This fact enables us to monitor the neutrino beam direction on spill-by-spill basis.

MUMONs are set at the downstream of the 3.5 m iron and 2 m concrete shields, as shown in Figure 3.15. These materials correspond to about 5.5 GeV energy loss for a minimum ionizing particle. Due to this energy loss in the shield, only 2.1% of muons can be reached at the MUMON site (see Figure 3.16), which are roughly 10^4 muons per 1cm^2. This amount of shield is needed to stop all the charged hadrons.

MUMON measurement reflects the properties of high energy pions and neutrinos. Figure 3.16 shows pions and neutrinos which is in the same kinematic region as high energy muons reached to the MUMON site. The corresponding pions are restricted at the forward ($\theta_\pi < 15$ mrad) and high energy ($p_\pi > 5.5\text{GeV/c}$) phase space. Its fraction is small due to the small spatial acceptance and high energy threshold. But the high energy pions are

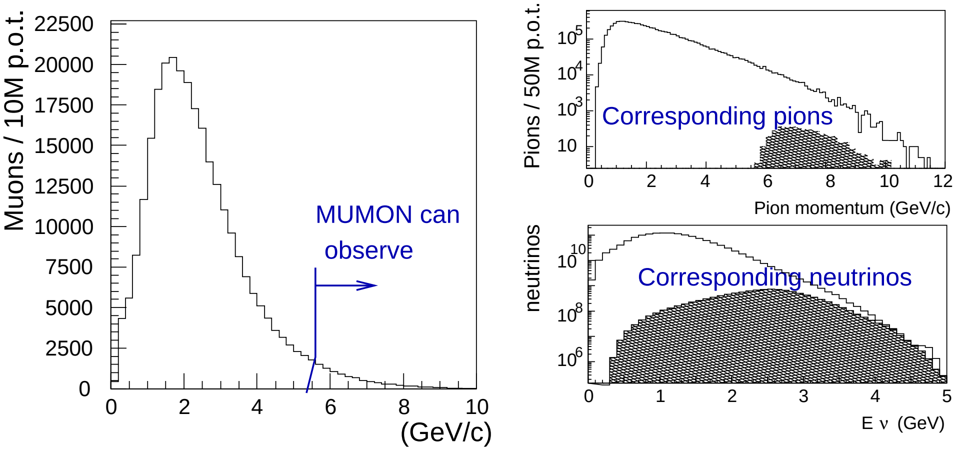

Figure 3.16: Left: Muon momentum distributions before the beam dump, with marking the threshold energy to survive to the MUMON site. Right-upper: Momentum spectrum of generated pions. Shaded area is the pions whose produced muons reach to the MUMON site. Right-lower: Energy distributions of generated neutrinos in the beam line. Shaded area corresponds to the shaded pions in right-upper figure. All the figures are based on the Monte Carlo simulation.

more sensitive to the overall beam direction than low energy ones. For example, when miss-steering caused by incident proton profile change, or horn trouble occurred, muon profile measured by MUMON always indicates the beam center movement. Thus, MUMON profile works as the good monitoring of the overall beam steering towards the Super-Kamiokande. In addition, intensity stability is also the confirmation of the proton targeting [50, 46].

In summary, objective purposes of the MUMON are mainly following two issues;

1. Monitor profile center to confirm neutrino direction on spill-by-spill basis. The requirement of the beam aiming is described in Chapter 6.3, that is ±1 mrad for 1% flux change. At the MUMON position of 220 m distance from the target, measurement must be done with a precision of better than 20 cm.

2. Monitor intensity stability to confirm neutrino beam production on spill-by-spill basis.

3.3.2 Hardware set up of the MUMON

Two type of MUMON detectors are prepared, as shown in Figure 3.15. One is a large Ionization chamber (ICH), and the other is a Silicon Pad Detector (SPD) array. ICH gives the horizontal and vertical projection of the muon profile of 1.9m × 1.75m area. SPD gives the 2-dimensional information of the muon profile of 2.8m × 2.8m area.

Ionization chamber (ICH)

ICH is a segmented ionization chamber like SPIC in the proton beam line. The cross section is 190cm × 175 cm square, in order to measure broad muon profile at the beam bump. From technical reason, the ICH consists of six modules of 60cm × 90 cm square plates. Three plates are in x and two plates are in y direction. Each module has parallel three copper-plated G10 board. Central one is the negative voltage anode in both side, and the outer ones are the x and y readout cathodes. The gap is 1 cm whose accuracy is 100μm kept by the insulated spacer. The supplied high voltage is 500 V (minus voltage). Each readout cathode is segmented to 5 cm strip lines to measure muon profile. Strips are connected to make 180 cm long strip in x and y. Since the electric field on edge strips are deformed in each modules, the edge strips are not used in the analysis. In the consequence, there are 30 available strips in x projection and 28 strips in y projection.

The whole modules are installed in gas vessel filled with argon gas. One minimum ionizing particle generates about 100 ion pairs in this 1 cm gap filled with argon gas. Average muon density is about a few $\times 10^4/\mathrm{cm}^2$, then, each 5cm × 180 cm strip has the order of 100 pC signal in every spill. Each signals are recorded by usual charge sensitive ADC in control room.

ICH is basically uniform conversion factor among each channel. Only the distortion of gap spacing may cause non-uniformity. The uniformity is calibrated using stable muon beam itself [46]. During the stable run, whole vessel of ICH is horizontally or vertically moved to place next parts where originally occupied by neighbor parts. Ratio of two observed signals gives the ratio of the conversion factor. First, rough distortion is calibrated, which is expressed as the relative factor of each sub-block with 6 (for x) or 8 (for y) channels. Next, the factor of each individual channel is calibrated. During the measurement, muon intensity is quite stable, monitored by SPD.

The obtained relative factors are shown in Figure 3.17. This calibration was performed several times during the long running period. They show the relative factor has been stable within several %. These factors are used to correct the observed muon distribution. With this correction, profile becomes continuous as shown in Figure 6.10.

Silicon Pad Detector (SPD) array

As shown in Figure 3.15, 17 small-type SPD (size: 1 cm × 2 cm, depletion layer 300μm, shaded in the figure) are installed along the horizontal and the vertical axis, and 9 large-type SPD (size: 3.4 cm × 3.05 cm, depletion layer 375μm) are installed as diagonal array.

When one muon make ionization loss in the depletion layer, 2.3×10^4 free electrons and

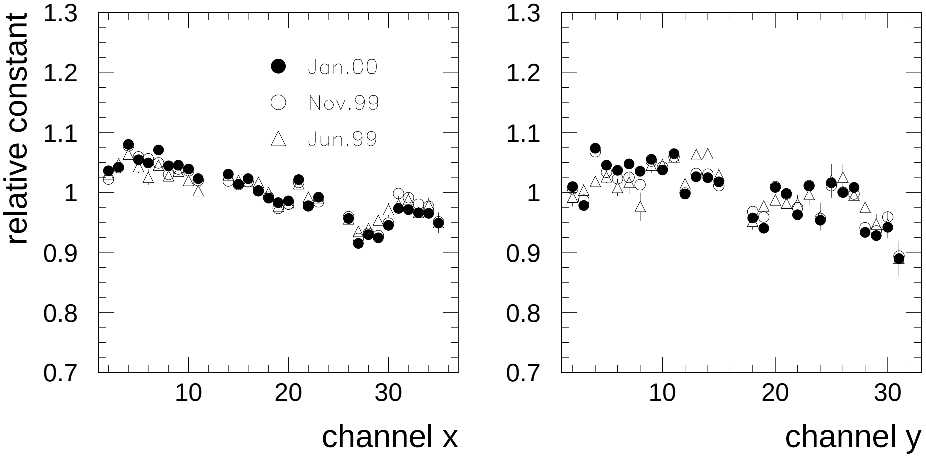

Figure 3.17: Relative constant of the gain of each ICH channel, for horizontal (left) and vertical (right) directions measured in June 1999, Nov. 1999, and Jan. 2000. Error bars are the spill-by-spill fluctuation only.

hole pairs are created in small-SPD and 2.9×10^4 pairs in large-SPD. They are collected by the bias voltage of 100 V for small-SPDs and 70 $\sim$ 80 V for large-SPD. Observed signals are order of 100 pC for small-SPD, and order of 1 nC for large-SPD, without any amplification. They are read out by charge sensitive ADCs.

Uniformity of the sensitivity of small-SPDs was measured using the LED light in the test bench. The result shows the uniformity is within ±6%.

For large-SPDs, the uniformity was measured using the muon beam. All the large-SPDs were once aligned along the beam axis. From the comparison of observed charge, relative factors are obtained, although they have 10% level uncertainty form the z dependence of the muon intensity [46].

3.4 Data Acquisition System of Beam Line Monitors

Data of all the detectors in beam line are taken with the common trigger signal of beam spill. Two trigger signals are provided from the accelerator. They are synchronized with the timing of the kicker magnet.

- One trigger signal comes 1.1 ms before the beam extraction. This signal is used for the timing on HORN magnet.

- The other signal comes 120μs before the beam extraction. This signal is used as the beam spill trigger for the data acquisition (DAQ) of beam line monitors and near detectors. Simultaneously 16-bit spill number is distributed to the each DAQ site to identify the each spill. The beam timing is recorded by the GPS time recording system described in Section 3.7, in order to take the time synchronization to the far detector measurement.

Signals from each detector, CTs, SPICs, (PIMON during the PIMON run), MUMONs are measured by charge sensitive ADCs on spill-by-spill basis. The gate width of ADCs are 1.2μs for CTs, and 2μs for other monitors. There are four DAQ system rooms and six front-end computers (PCs) along the beam line. One general DAQ program controls each data acquisition process in each computer. In total, about 10000 channels of the data are collected and recorded [45].

3.5 Near Neutrino Detectors

Near neutrino detector system is located at 80 m downstream of the beam dump (300 m downstream of the production target). The neutrino beam is tilted 18.8 mrad downward from the local horizontal plane, due to the curvature of the globe. Therefore, a detector hall of 16 m in depth and 24 m in diameter was excavated. The detector system consists of 1-kilo-ton water Cherenkov detector (1kt), Muon Range Detector (MRD), and Fine Grain Detector system (FGD) as shown in Figure 3.18. They are described in following sub-sections.

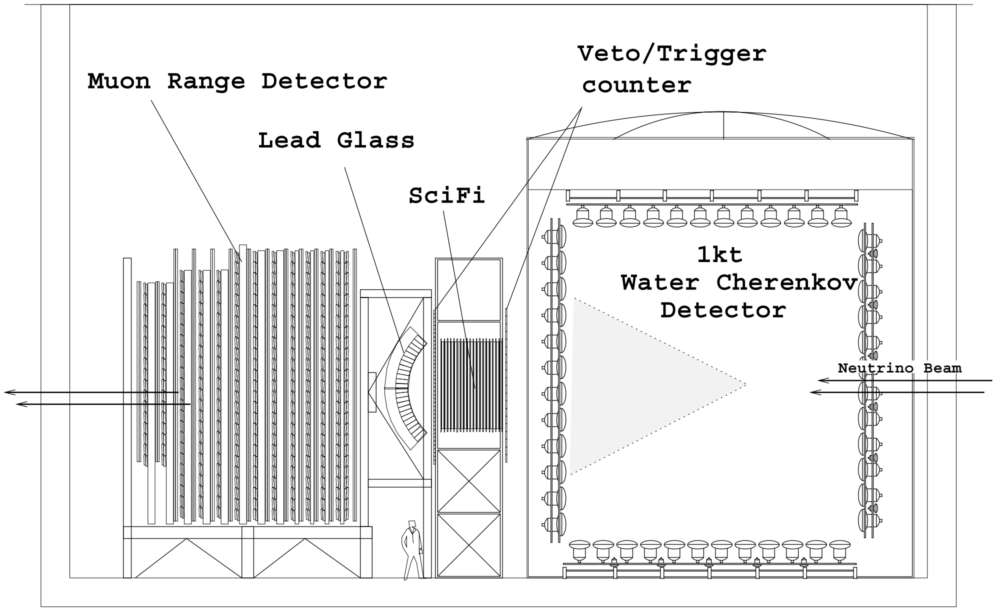

Figure 3.18: K2K near detector system. Neutrino beam direction is from right to left in this figure.

3.5.1 1kt water-Cherenkov detector (1kt)

Structure of 1kt

One-kilo-ton water Cherenkov detector (1kt) is located most upstream at the detector hall. It consists of the cylindrical tank of 10.8 m diameter and 10.8 m height, filled with 1000 ton pure water. The inside of the tank is optically separated for an inner volume of 8.6 m diameter and 8.6 m height, and an outer volume.

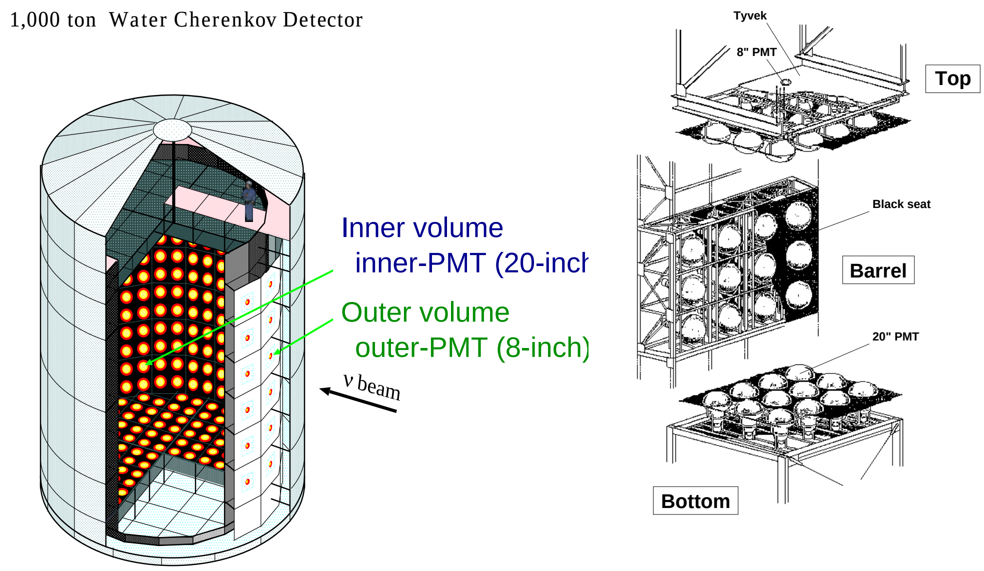

Figure 3.19: Left: The schematic view of 1kt barrel. Right: The schematic view of the inner structure.

The inner volume is used to detect neutrinos. In the inner volume, 680 photo-multiplier tubes of 20-inch diameter (inner-PMTs) are equipped. 456 PMTs are on the barrel wall, 112 PMTs are on the top and 112 PMTs are on the bottom. The PMTs with 70cm grid spacing are exactly same as those of SK. The photo-cathode of all 680 PMTs covers about 40% of the surface area of the inner volume. The remaining area of the surface is covered by black polyethylene sheet, which suppresses the reflection of Cherenkov photons.

The outer volume is used to veto the incoming particles from outside. Sixty-eight 8-inch PMTs (outer-PMTs) with 140cm spacing are placed on the outer surface of the inner structure. 42 PMTs are located upstream of the beam direction, and 26 PMTs are at the bottom. The surface of the outer volume is covered with the white polyethylene sheet (Tyvek), in order to collect Cherenkov photons effectively.

The 20-inch PMT has a long flight length of the multiplied photo-electron, which could be affected by a magnetic field. Therefore, 1kt detector equips "compensation coils" surrounding the water vessel, which compensate magnetic field of earth.

Cherenkov light

A neutrino interacts with Oxygen or Hydrogen nuclei in the water, and it generates muon, pion, electron and/or recoil nucleus (described in Chapter 4.2). Cherenkov photons are emitted by the charged particle traveling in the water at the velocity faster than the light velocity in water. They are emitted on a cone with respect to the particle direction. Its half

Particle	Threshold momentum (MeV/c)
$e^{\pm}$	0.57
$\mu^{\pm}$	118
$\pi^{\pm}$	155
p	1045

Table 3.3: The Cherenkov threshold momentum in the water.

opening angle θ is expressed with the particle velocity β and the refractive index $n = 1.34$ for water.

$$\cos\theta = \frac{1}{n\beta} \tag{3.11}$$

Table 3.3 shows the momentum of Cherenkov threshold in water.

The number of Cherenkov photons emitted by a single-charged particle per unit path length per unit wavelength is given by;

$$\frac{d^2N}{dxd\lambda} = \frac{2\pi\alpha}{\lambda^2}\left(1 - \frac{1}{n^2\beta^2}\right) \tag{3.12}$$

where α is the fine structure constant ($\sim 1/137$). The particle with $\beta = 1$ emits about 340 photons per 1cm in the wavelength from 300 to 600 nm, which is the sensitive range of our PMT.

20-inch PMT

The 20-inch PMTs are used to detect Cherenkov photons. Specifications of the PMTs are summarized in Table 3.4, and other documents [51]. The PMT can distinguish the single photo-electron. The timing resolution is typically 2 ns.

Gain calibration

A gain of each PMT is adjusted and calibrated using the scintillator that is flashed by Xe light with fiber (Scintillator ball) [52, 53]. The signal from each PMT is adjusted to give the same response after correcting the solid angle of each PMT and non-uniformity of Scintillator ball surface. The uncertainty on the gain of PMT is less than 5.7%, including the reproducibility [52].

The energy scale is calibrated by using the cosmic ray muons, which are triggered by a scintillation counter placed on the top of the tank. Muons emit Cherenkov photons, which

Photo-cathode area	50cm in diameter
Shape	Hemispherical
Window material	Pyrex glass, $4 \sim 5$ mm
Photo-cathode material	Bialkali (Sb-K-Cs)
Dynodes	11 stages, Venetian blind type
Quantum efficiency	22% at $\lambda = 390$ nm
Sensitive wavelength	300 nm to 600 nm, peak at 390 nm
Typical gain	10^7 at ~ 2000 V
Dark current	200 nA at gain 10^7
Dark pulse rate	3 kHz at gain 10^7
Cathode non-uniformity	less than 10%
Anode non-uniformity	less than 40%
manufactured	Hamamatsu Photonics K.K.

Table 3.4: The specifications of the 20-inch PMT.

can be calculated by the flight length in water by Formula 3.12. We made the Monte Carlo simulation of cosmic ray muons with suitable transparency, scattering, and the reflection of the water and PMT surfaces. The simulation gives the relation between the number of photo-electron and the energy deposit in the water. We analyzed two data samples. One is the data of through-going muons which is penetrated through the bottom of the tank. The other is the data of muons stopping inside of the tank. Figure 3.20 shows the comparison of the data and the simulation of both analyses, after adjustment of the energy scale. The discrepancy of the energy scale from both analyses is 5%. We adopt the energy scale from the analysis of through-going muons. These calibrations are performed by monthly basis. Time variation of these calibration results are within 5% level. From these results, ±5% error is assigned as the uncertainty of the energy scale in Chapter 8.2.3.

Water purification system

Cherenkov photons are attenuated and scattered by impurities like small dust, bacteria and metal ions in the water. These impurities are removed by a water purification system. The system supplies 20 t/hour of pure water. The water temperature is maintained around 10°C. Water purity is always monitored by the measurement of the electrical resistance ($\sim$ 10 MΩ/cm). The temperature and the purity were stable during the the running period.

Water transparency is directly obtained from the cosmic ray measurement several times in long running period. The attenuation length is measured to be over 50 m, and stable

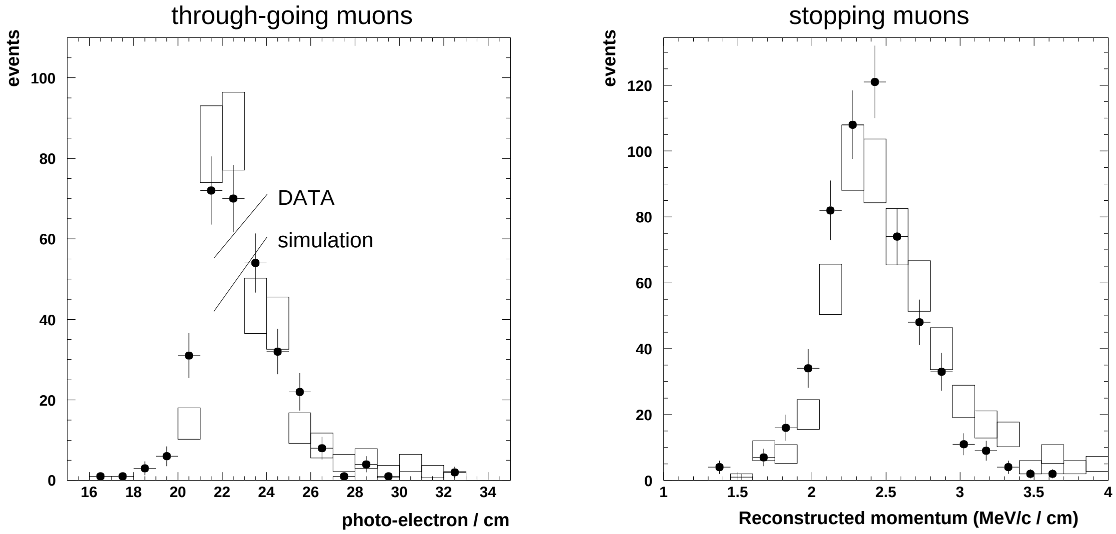

Figure 3.20: Result of the energy scale calibration using cosmic ray muons. The left figure is a distribution of the total number of photo-electron per 1 cm path length for through-going muons. The right figure is a distribution of the reconstructed momentum (calculated from the sum of ADC count), divided by the range, for muons which stop inside of the inner volume. In both figures, data (dots) and the simulation (boxes) are overlaid. Only statistical errors are shown.

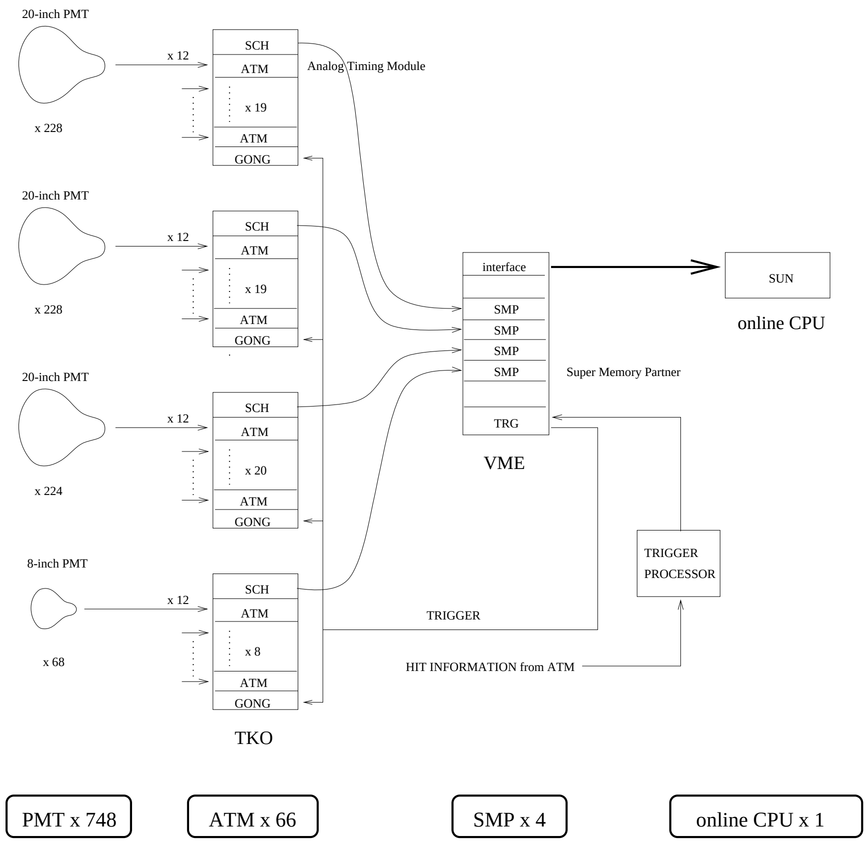

Figure 3.21: The schematic diagram of 1kt data acquisition system.

during the whole run. This good transparency causes negligible effect in 1kt measurement.

Data acquisition system

Figure 3.21 shows the diagram of the data acquisition system of 1kt detector. The data acquisition system consists of following four parts.

- Front-end electronics.
  The front-end electronics records the charge (ADC) and the timing (TDC) of the analog signals from inner and outer PMTs, and generates the discriminated pulses for trigger logics. At the front-end electronics, buffer-amplifiers have been used for impedance match since Jan. 2000. In 1999 run, the impedance mismatch caused the reflection pulse. Thus, 110 m long cable was used in order to delay the reflection signals to outside of the ADC gate, instead. Analog-to-digital conversion is performed by a specified TKO module named "ATM (Analog Timing Module)"[54], which is

also used at Super-Kamiokande detector. In the ATM, analog signal is divided to four. One of them is lead to a discriminator, two of others are lead to two ADCs, and the other is used to take the analog sum (called "PMTSUM") of all the signals in the module. The threshold of the discriminator is equivalent to typically 0.3 photo-electron equivalent signal. The discriminated pulse is sent to two independent TDCs, and also used for ADC gate. Two sets of TDC and ADC are prepared to handle multiple events. Both ADC and TDC have 12 bit data, and the conversion factor is about 0.4 ns/count and 0.15 pC/count for TDC and ADC, respectively.

Data are stored in FIFO memories in ATM, and sent to the rear-end electronics through SCH (Super-Control-Head) when GONG (GO/NotGo) module receives the trigger. In ATM, the signal "HITSUM" which corresponds to the number of hit channels is generated with voltage of about -10 mV per hit and with the width of 200 ns.

One ATM board has 12 channels, and in total 66 ATM are used.

In 1kt detector, all the PMTSUM signals of inner PMTs are summed-up and put into a Flash-ADC (FADC) module. Sampling frequency is 500 MHz and the dynamic range is 8 bit. This is used to identify multiple events in one beam spill by counting the number of steep peaks of the PMTSUM signals.

- Trigger electronics.
  The trigger is made by Trigger Processor module. When linear sum of HITSUM signals exceed to the threshold of -450 mV, which corresponds to about 40 hits at inner PMTs in 200 ns time window, the trigger pulse is distributed to each ATM through TRG module. In 1kt detector, the event trigger is permitted being sent during the beam spill. TRG module records the trigger type and the trigger time.

- Rear-end electronics.
  The read-end electronics save the digitalized data temporarily on four SMP modules in one VME crate. The data on SMP are read-out by the on-line computer with data on the TRG and data on the FADC.

- On-line computers.
  On the on-line computer, data are sorted to build an event, and sent to the host computer of near detector system.

Further details of the electronics are also described in [55].

Timing calibration

Hit timing information of PMTs are important to reconstruct the vertex point and the Cherenkov ring. Timing calibration was performed using a laser light [52]. Light from a dye laser ($\lambda \sim 390$ nm) was put into a optical fiber and lead to a diffuser ball, which was installed in the middle of the water tank. The light intensity was continuously changed using ND filters. We obtained the response of the hit timing as a function of the observed charge, which is called "T-Q map", for each of 680 PMTs. This T-Q map was used for the timing correction in the off-line analysis.

ATM calibration

ATM calibration gives a correction of non-linear response of TDC and ADC in ATM. With the correction, the responses of TDC and ADC are kept linear within 1 count for full range [55].

3.5.2 Muon Range Detector (MRD)

Design of the muon range detector

Muon range detector (MRD) is the range type calorimeter for neutrino-induced muons. It consists of 12 iron absorber sandwiched with 13 vertical and horizontal drift tube layers (see Figure 3.22). The size of the layer is approximately 7.6m × 7.6 m. In order to get a good energy resolution, 4 iron plates at the upstream side are 10 ± 0.17 cm thick, and 8 iron plates at the downstream side are 20 ± 0.2 cm thick. The total thickness of 2 m covers up to 2.8GeV/c muons. The total mass of iron amounts to 864 tons. When the materials of the drift tubes (mostly aluminum) are included, it amounts to 915 tons.

Figure 3.22 shows the schematic view of the drift-tube module used in MRD. These drift-tube modules are originally constructed and used in VENUS detector[56] at TRISTAN. There are 829 modules, which has 8 cells of 5cm × 7 cm cross section. One drift-tube layer is arranged by 25 modules of 7.6 m length with a 2 cm gap between two modules. For some layers two short modules are combined side-by-side to make 7.6 m sensitive length. Table 3.5 summarizes the detail order of drift-tubes and iron layers. In total, there are 6632 drift cells for charged particle detection. They are aligned as XX or YY pairs in one layer between iron plates. Therefore, in ideal case, the shortest track that penetrates one iron produces four hits in both X-view (top-view) and Y-view (side-view). Typical muon track is shown in Figure 7.1.

The drift-tubes are filled with P10 gas, which is the mixture of 90% argon and 10% methane. Gas circulation system [57] supplies purified P10 gas continuously. Gas quality has been measured using a gas chromatography every week, in order to keep lower noise rate. When the contamination level becomes higher, purifier is operated to regenerate the gas.

Each drift-tube has a 70μm diameter tungsten wire. Before construction, wire tension was measured by searching for the resonant frequency under a certain magnetic field [57].

Layer	z-pos(cm)	$H \times W \times t(\text{cm}^3)$	modules × length(cm)	modules × length(cm)
Tubes 1X			25×760	
Tubes 1Y				25×760
Iron 1	436.2	$763 \times 750 \times 10$		
Tubes 2Y				25×760
Tubes 2X			25×760	
Iron 2	478.5	$763 \times 750 \times 10$		
Tubes 3Y				25×760
Tubes 3X			25×760	
Iron 3	520.3	$763 \times 750 \times 10$		
Tubes 4Y				$25 \times (505 + 245)$
Tubes 4X			25×760	
Iron 4	562.6	$763 \times 750 \times 10$		
Tubes 5Y				$25 \times (505 + 245)$
Tubes 5X			25×760	
Iron 5	609.8	$763 \times 750 \times 20$		
Tubes 6Y				25×760
Tubes 6X			25×760	
Iron 6	662.0	$763 \times 750 \times 20$		
Tubes 7Y				$25 \times (290 + 474)$
Tubes 7X			25×760	
Iron 7	713.6	$780 \times 755 \times 20$		
Tubes 8Y				$25 \times (290 + 474)$
Tubes 8X			25×760	
Iron 8	764.5	$710 \times 755 \times 20$		
Tubes 9Y				$23 \times (474 + 290)$
Tubes 9X			25×760	
Iron 9	815.2	$709 \times 755 \times 20$		
Tubes 10Y				$23 \times (474 + 290)$
Tubes 10X			25×760	
Iron 10	867.0	$709 \times 755 \times 20$		
Tubes 11Y				$6 \times (300 + 474) + 9 \times (290 + 474)$ $+8 \times (474 + 290)$
Tubes 11X			25×760	
Iron 11	917.9	$674 \times 755 \times 20$		
Tubes 12Y				$1 \times (760) + 16 \times (300 + 505)$
Tubes 12X			25×505	
Iron 12	968.6	$674 \times 755 \times 20$		
Tubes 13Y				$1 \times (760) + 16 \times (300 + 505)$
Tubes 13X			25×505	

Table 3.5: Arrangement of the drift-tubes and iron layers in MRD.

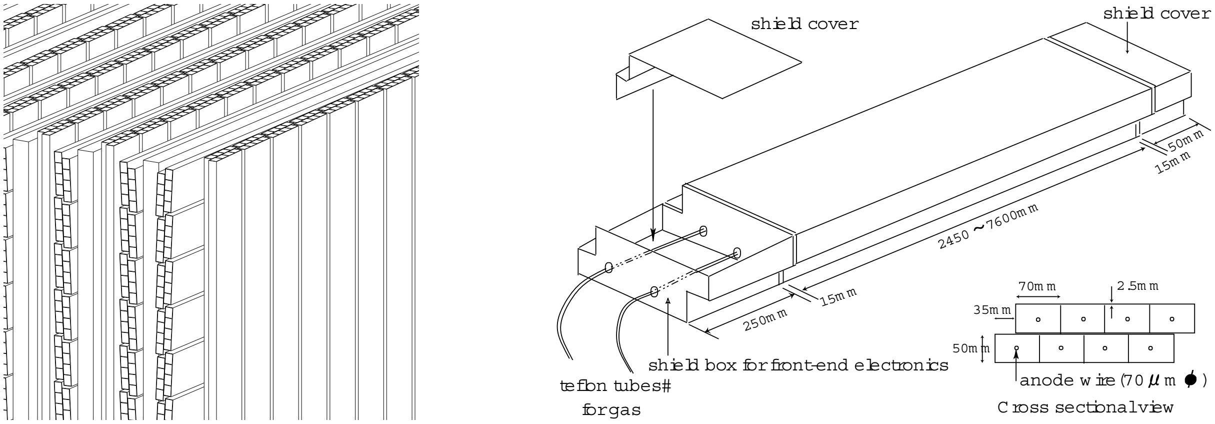

Figure 3.22: The schematic view of Muon Range Detector (left) and its drift-tube (right, [58]).

In addition, a cosmic ray test was performed as a whole test of the drift-tube system at the assembly hall.

In MRD, 2.7 kV negative high voltage is supplied to each wire. The efficiency plateau is around 2.5 kV [57]. The time-to-drift-distance relation was investigated by using cosmic ray data. This study confirmed the VENUS parameterization of the relation:

$$x = 2.11 \times t^2 + 2.72 \times t \tag{3.13}$$

where x is the drift length in cm and t is the drift time in μsec.

Data acquisition electronics

Wires are connected to 6-bit single-hit TDCs with 20 MHz clock generator, equipped by a front-end electronics board at each tube. The start signal is made from the beam spill timing, which is commonly delivered to the near detector system. Stop signal is provided if the wire signal surpasses the threshold voltage after amplifier. Therefore hit informations in 3.2μs time range are recorded with the TDC count form 0 to 63 count. Maximum eight of front-end electronics boards are connected to one module-address-generator. Maximum eight module-address-generators are connected to one main-address-generator. Finally all the hit information is transfered to 16 memory-buffer-modules in TKO (TRISTAN-KEK-ONLINE) crate and accessed from the data acquisition computer. These data acquisition electronics were also used in VENUS experiment[58]. All the electronics are tested before construction.

More details about MRD components and the construction are described in [57].

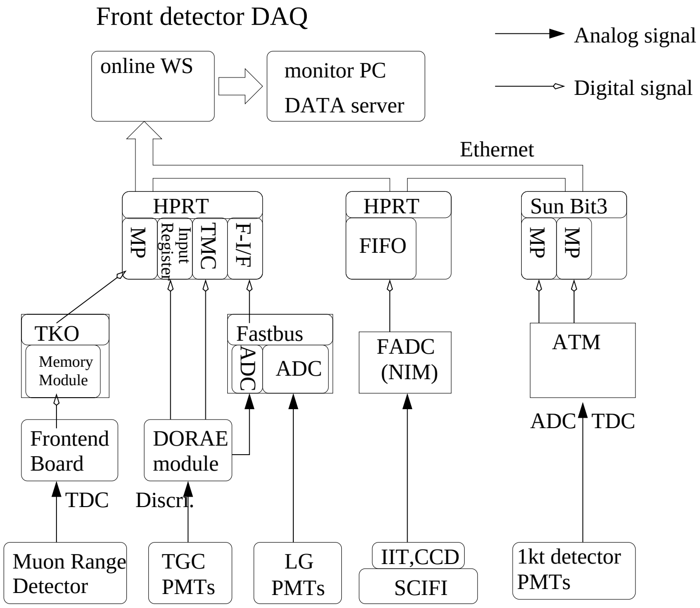

Figure 3.23: DAQ system of the near detector.

3.5.3 Fine grain detector (FGD) system

Further precise study about neutrino interaction has been performed using the events interacted in the water target of SCIFI.

SCIFI [59] consists of 20 layers of scintillating fiber modules and 19 layers of water targets. Hit information of fiber modules enables us to reconstruct the particle's track induced by the neutrino interaction. Total mass of SCIFI is 8.7 ton, including 6 ton water and 1.4 ton of aluminum structure. At the both side of SCIFI, Trigger Scintillating Counter (TGC) planes provide the timing information of penetrating particles. At the downstream of SCIFI/TGC, Lead Glass calorimeter (LG) is prepared to measure the energy of electromagnetic shower, and to identify electrons, positrons or gammas from muons [39]. Many of muons penetrate LG to reach MRD, and are measured their energy.

In this thesis, FGD data are not used for the analysis.

3.5.4 Data acquisition system of near neutrino detector

The data of each detector is continuously taken on spill-by-spill basis, with the beam spill trigger described in Section 3.4. Figure 3.23 shows the data acquisition (DAQ) system of the near detector.

Near detector DAQ has three front end computers. A SUN computer collects 1kt data from ATMs and TRG module by the VME-TKO interface. One VME on-board computers reads the data from SCIFI, and the other on-board computer collects the data of MRD, LG, TGC.

A event builder computer collects and sorts all of these data using the spill number recorded in each data. The data size of the near detector is about 1 MB per spill.

3.6 Far neutrino detector

Super-Kamiokande detector (SK) is used as the far detector for our experiment. SK is a large underground water Cherenkov detector. It is located in the Mozumi zinc mine at 1000 m (2700 m water-equivalent) below the peak of Mt. Ikenoyama in Kamioka, which is 250 km west of the KEK [40]. Figure 3.24 is the schematic view of the SK detector and the experiment site.

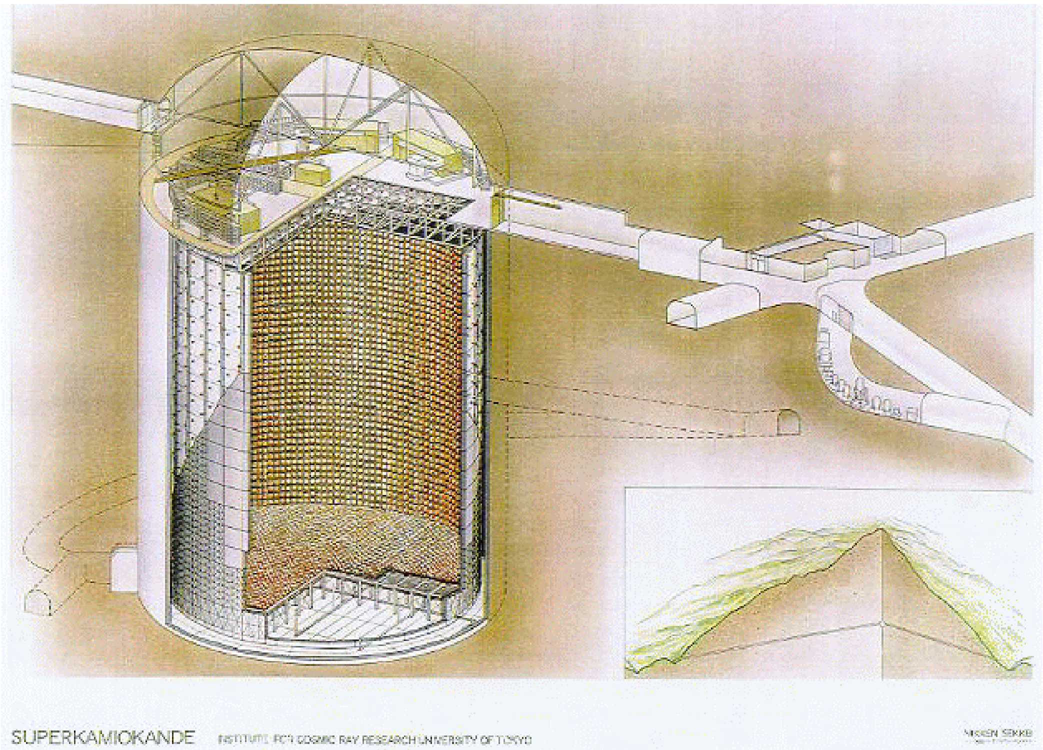

Figure 3.24: The schematic view of Super-Kamiokande detector and the experiment site.

SK have been running since 1996, for the various physical motivation, nucleon decay search [60], atmospheric neutrino and upward muon measurement [9, 10, 18], solar neutrino measurement [27, 26], and Supernova neutrino observation *etc.*.

The detector is designed with similar detection schemes to Kamiokande detector. SK and 1kt uses fairly the same hardware and software components, which are PMTs, water purification systems, data acquisition electronics, and many online/off-line software codes. The hardware components are described in following sections (and also described in [61]).

3.6.1 Detector features

Detector structure

The detector holds 50 kt of ultra pure water contained in a cylindrical stainless steel tank measuring 41.4 m in height and 39.3 m in diameter. The water is optically separated into three concentric cylindrical regions.

The inner region is 36.2 m in height and 33.8 m in diameter and is viewed by 11146 20-inch PMTs, which are same PMTs used in 1kt (see Table 3.4). Each PMT is installed every 70 cm on the wall, which is covered by black-sheet to avoid photon reflection. The photo-coverage is about 40%.

The outer region completely surrounds the inner detector. It is $1.95 \sim 2.2$ m thick, and is viewed by 1885 outward pointing 8-inch PMTs (outer-PMTs) with 60cm square wavelength shift plates. The walls of the outer detector are lined with white Tyvek sheet. The primary function of the outer detector is to veto cosmic ray muons and to help containment identification.

The middle region (dead space) is 0.55 m thick between the inner and outer detectors. In the middle region, there is a support structure made of stainless steel. Along with the outer detector the dead space acts as a shield against radioactivity from the surrounding rock.

Gain calibration of the PMTs

Gain of each PMT is adjusted and calibrated using the scintillator ball light [62]. A Xe lamp with UV-pass filter is used as a light source. The light is guided by the optical fiber to the scintillator ball in the tank. The scintillator ball consists of a BBOT wavelength shifter, which emits light around 450 nm wavelength, and a MgO diffuser. Comparing the observed charge in each PMT considering the distance and PMT acceptance, relative gain constant is obtained, and used for the correction of the observed photo-electrons in physics analysis. Accuracy of this correction is about 7% including the reproduceability and the imperfect isotropy of the scintillator ball. Since the number of hit PMTs are mainly more than 1000 for neutrino events, the ambiguity in the energy measurement is estimated to be less than 1% [61].

The gain uniformity is also confirmed by the direction dependence of the momentum distributions of decay electrons [61]. The result shows that the gain is uniform within ±1% level.

The absolute scale of gain is calibrated using the gamma emission from thermal neutron capture of Nickel, with ^{252}Cf as a neutron source. The energy of the gamma is so low ($6 \sim 9$ MeV) that the expected number of hit photons for each fired PMT is one. The mean of 1 photo-electron distribution is 2.055 pC and the absolute gain is determined as $\sim 6 \times 10^6$ [61].

Water purification system

The source of the water filled in SK is the clean spring water flowing in the mine. In order to reduce radioactive materials and to keep good transparency, ultra-pure water is filled in the tank using a water purification system. It supplies about 50 ton of ultra-pure water per hour. The water temperature is kept at 13°C to prevent the growth of bacteria.

The water quality is calibrated using laser light and cosmic ray muons [61].

- A dye laser provides the light with 337 to 580 nm wavelength to a diffuser ball, which is installed into the tank. Using the CCD camera on the top of the detector, the light intensity is measured at several distances.
- The Cherenkov photons from cosmic ray muons are always measured for the calibration. The travel length dependence of the observed number of photon is fitted with the absolute gain G and the attenuation length L_{att} with following formula;

  $$Q_{corr}(\ell) = G \times \exp\left(-\frac{\ell}{L_{att}}\right) \tag{3.14}$$

  Where, Q_{corr} is the sum of the observed charge after acceptance correction, and ℓ is the travel length between the emission point and the each PMT.

The measured attenuation length from these measurements agrees well and the attenuation length is about 100 m. Obtained water parameters are put in the detector simulation.

3.6.2 Data acquisition system

The data acquisition system for inner detector is almost same as that of 1kt described in previous Section 3.5.1. Figure 3.25 shows the system. 946 of ATM are used for the function of TDC/ADC and records an amount of hit timing and charge of each PMT signal. TDC/ADC data are read separately by 8 on-line-computers through 48 SMP modules. Trigger information recorded by TRG module are also read by another server computer. The data are transfered to the on-line host computer by FDDI network and merged to make complete events.

These electronics and computers are placed in one central hut and 4 electronics huts, where room temperature are controlled to around 27°C and is kept within ±0.5°C. The estimated inaccuracies coming from the temperature dependence is less than 0.4 ns and 0.3 pC for the timing and charge measurements, respectively [61].

Outer detector data are processed by a different electronics system. Signals of outer PMTs are sent to QTC (Charge to Timing Converter) modules which generates rectangular pulses with a width proportional to the input charge. They are digitalized by LeCroy 1877 multi-hit TDC modules in a FASTBUS crate. The dynamic range of the TDC is set to

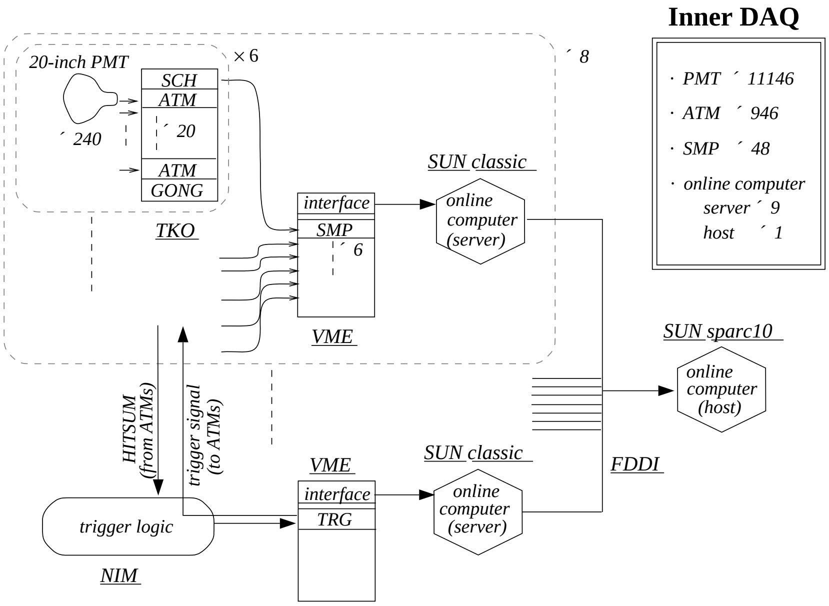

Figure 3.25: The data acquisition system for the inner detector.

be 16μs with the minimum time unit of 0.5 ns. The TDC data are read by VME memory modules by a separate on-line server computer and then sent to the on-line host computer.

The rectangle HITSUM signals from ATMs are separately summed up to generate grand HITSUM signal of inner detector. The HITSUM signals from QTC modules are also summed up separately to make grand HITSUM of the outer detector. They are sent to trigger logic and recorded by TRG module. For normal neutrino data taking, three kinds of trigger levels are prepared. One of them is High Energy Trigger (HE trigger) which is requiring -340 mV inner HITSUM signals corresponding to 31 hits in inner PMTs, in 200 ns time window. Another one is Low Energy Trigger (LE trigger) whose threshold level is -320 mV (29 hits), and the other is the series of Super Low Energy Trigger (SLE trigger) with lower threshold level than LE trigger. Since our neutrino beam have 1.3 GeV energy in average, HE triggered events are used in our analysis (in Chapter 9.1).

3.7 Global Positioning System (GPS)

The neutrino beam has a time structure of 1.1μs width in every 2.2 s. The time synchronization effectively work for the event selection from the continuous background.

Proton extraction time is recorded at KEK site, and at SK, the triggered time of neutrino event is independently recorded. Clocks in both site should be synchronized within μs accuracy. Global Positioning System (GPS) is used for this purpose [63].

3.7.1 Mechanism

GPS consists of 27 satellites maintained by the US Department of Defense (DOD). Each satellite has an atomic clock and the clock time and the position information of the satellite are regularly calibrated by communicating each other. A GPS receiver always receives the position and time information of the $4 \sim 6$ satellites. The receiver calculates the precise position of the latitude, the longitude and the altitude, and also the calibrated time, named Universal Time Coordinated (UTC) time stamp. The resolution is 40 ns in average and 150 ns in maximum fluctuation.

Figure 3.26 shows the time synchronization system. At each site, two GPS clocks run in parallel, providing hardware backup as well as data quality check. In KEK site, the two receivers are placed at the beam line control room and the antennae are mounted on the room roof. In SK site, GPS receiver is located at an external building near the mine entrance. It is connected to a VME receiver at the central electronics hut by 2 km optical fiber, and send the UTC time stamp signals every 1 sec. The VME receiver decodes the signals to UTC time, and sends the calibration trigger signals to a LTC module. The LTC module has a 50 MHz clock and it is synchronized to the calibration trigger signals. The LTC module gets the timing signal, that is the timing signal of beam extraction in KEK, or the event trigger in SK. An online computer records the LTC count of the event triggered time and the calibration triggered time, and the UTC time provided by the VME module. The UTC time of the triggered events are calculated with interpolation of the calibrated UTC time by off-line analysis, as shown in Figure 3.26.

3.7.2 Stability check

In KEK, two independent GPS were compared for check. The results shows the agreement to each other within 100 ns (half-width-half-maximum) [63].

In SK site, stability of the system is continuously monitored comparing UTC and LTC. Figure 3.27 shows the difference of $(N_n - N_{n-1})$ from the nominal count $(= 5 \times 10^7)$, from the beginning of June 1999 to the end of June 2000. This "cross check" proves the stable running of both UTC and LTC within the measurement accuracy of 200 ns.

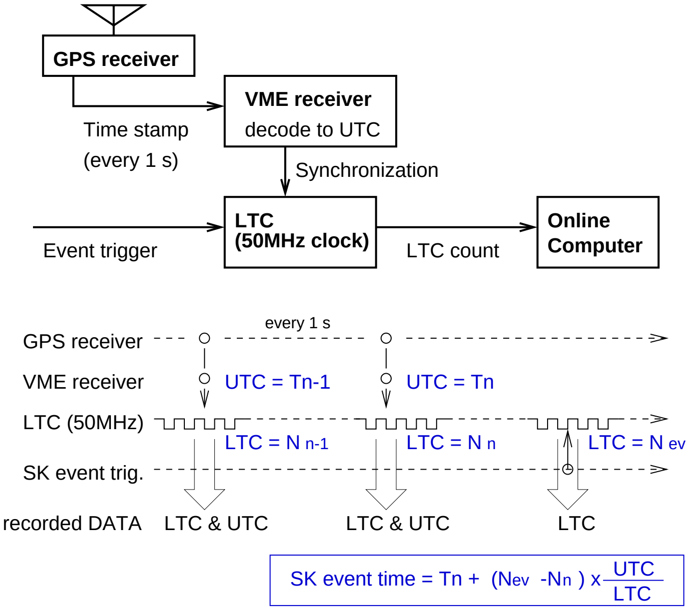

Figure 3.26: Overview of the GPS in SK. Block diagram (upper) and the timing chart (lower) are shown.

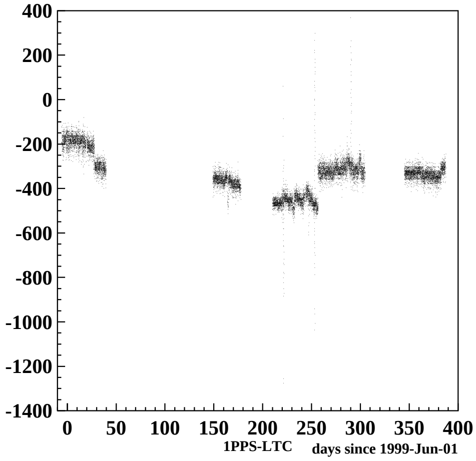

Figure 3.27: History plot of the LTC count during the each 1 sec of UTC time stamp. The vertical axis shows the difference of the LTC count from the nominal count, expressed by nsec unit. Horizontal axis shows the integrated days since June 1, 1999.

Chapter 4

Monte Carlo Simulations

In order to study our detection scheme and evaluate various systematic uncertainties, Monte Carlo simulation is used. The Monte Carlo simulation consists of following three modules;

1. Neutrino beam generation; **"beamMC"**.
   This simulates from the proton injection on the production target, produces pions, focuses and tracks them until they decay to neutrino or dumped, and provides neutrino flux at near and far site.

2. Neutrino interaction; **"neutMC"**.
   This simulates interaction and provides the individual information of produced particles.

3. Detector simulation.
   This simulates the passage of particles and the detector response.

In following sections they are described in this order.

4.1 Pion Production and Decay to Neutrino (beamMC)

4.1.1 Proton injection to the target

Proton profile, as a in-put of the simulation, is measured using V39-SPIC and TGT-SPIC (Figure 6.7). As shown in 4.1, fitted profile width on both SPIC is extrapolated to the width and the divergence on the target front-face, with the assumption of the ideal emittance description as;

Parameters	for Jun.99	for Nov.99 to Jun.00
Beam spread σ_x	1 mm	3.4 mm
Beam spread σ_y	6 mm	7.2 mm
Slope k_x	-8 mrad/mm	-2.5 mrad/mm
Slope k_y	-0.4 mrad/mm	-0.14 mrad/mm
Target rod	Al	Al
Rod diameter	2 cmϕ	3 cmϕ
HORN current	200 kA	250 kA

Table 4.1: Parameters for our standard simulation. Definitions are noted in text.

- Proton beam spreads by a 2-dimensional Gaussian with the width σ_x and σ_y. The width is determined by the SPIC measurement as follows;

  $$\begin{aligned}\sigma_x &= \sigma_{x2} + (\sigma_{x2} - \sigma_{x1}) \cdot (\ell/L) \\ \sigma_y &= \sigma_{y2} + (\sigma_{y2} - \sigma_{y1}) \cdot (\ell/L) \qquad (4.1)\end{aligned}$$

  where, $\sigma_{x1,y1}$ and $\sigma_{x2,y2}$ are the x or y profile width measured at V39-SPIC and TGT-SPIC, respectively. $L = 128$ cm is the distance between V39-SPIC and TGT-SPIC, and $\ell = 37$ cm is the distance between TGT-SPIC to the target front-face.

- In (x, dx) plane (x: distance from beam axis, dx: divergence), following linear correlation is assumed between them;

  $$dx = k_x \cdot x, \qquad and \qquad dy = k_y \cdot y \qquad (4.2)$$

  where k_x and k_y are the parameters which were also determined by the measurement as follows;

  $$\begin{aligned}k_x &= \frac{1}{\frac{\sigma_{x2}}{\sigma_{x2}-\sigma_{x1}} \cdot L + \ell} \\ k_y &= \frac{1}{\frac{\sigma_{y2}}{\sigma_{y2}-\sigma_{y1}} \cdot L + \ell} \qquad (4.3)\end{aligned}$$

For our standard simulation, proton beam center is at the center of the target rod. Table 4.1 summarizes the parameters which is used in beamMC. Studies of these parameter dependences are discussed in Chapter 6.2.

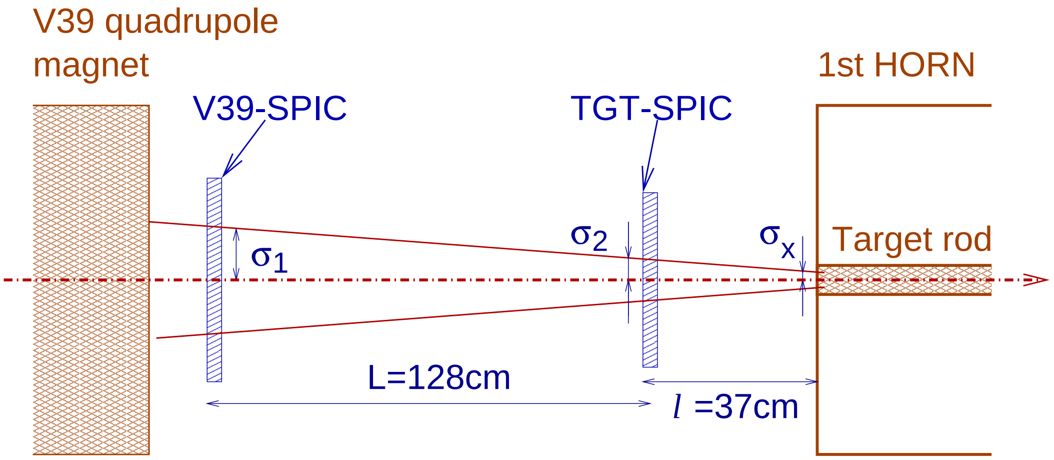

Figure 4.1: The schematic view of the proton emittance calculation.

4.1.2 Pion production in the target rod

There are some hadron interaction models to simulate pion production in the target material. This is one of the largest ambiguities of the Monte Carlo simulation. There have been various pion production experiments around this energy range. However results of these experiments are inconsistent with each other.

We compare following two models;

1. GCALOR/FLUKA model [64, 65].
   GCALOR/FLUKA is one of the hadron simulation package prepared for GEANT simulation [66]. This model has larger p-Al cross section than other models.

2. Cho model [67].
   This is a pion production model with a experimental parameterization of Sanford-Wang [68]. The differential yield of the secondary particle ($d^2n/d\theta dp$) is expressed as follows;

   $$\frac{d^2n}{d\theta dp} = C_1 \cdot p^{C_2}\left(1-\frac{p}{p_B-1}\right)\exp\left(-\frac{C_3\cdot p^{C_4}}{P_B^{C_5}} - C_6\cdot\theta\left(p - C_7\cdot p_B\cos^{C_8}\theta\right)\right) \tag{4.4}$$

   where, p_B, p is the momentum of the primary and the secondary particle, respectively, and θ is the angle between the secondary particle and the initial beam axis.

   The eight parameters $C_1 \sim C_8$ are obtained from the global fit with their own measurement and other experimental results [69, 70]. The values of the parameters are listed in Table 4.2. Figure 4.2 shows the comparison of the experimental measurements and the fitting of this Cho model.

Cho model is used only for primary interaction of protons. For secondary interaction of hadrons, GCALOR/FLUKA is always used. Kaon production is calculated using [71].

model	C_1	C_2	C_3	C_4	C_5	C_6	C_7	C_8
Cho	196	1.08	2.15	2.31	1.98	5.73	0.137	24.1

Table 4.2: Parameters of Sanford-Wang Formula 4.4, for Cho model.

As described in Chapter 6.1, the pion distribution obtained by PIMON measurement strongly favored the simulation using Cho model. Thus we adopt the simulation with Cho model as a standard simulation, while GCALOR/FLUKA simulation is used for a comparison.

4.1.3 Simulation of the particle tracing through the magnetic field and the decay section.

Scattered protons and generated secondary particles are traced by Monte Carlo simulation GEANT with GCALOR hadron simulation [66, 64], through the two HORN magnets and decay section.

The magnetic field of 1st-HORN is given as follows;

$$\text{In air}(r > R) : B(r) = B_{max} \cdot \frac{R}{r} \tag{4.5}$$

$$\text{In rod}(r \leq R) : B(r) = B_{max} \cdot \frac{r}{R} \tag{4.6}$$

where R is the target radius, and B_{max} is the maximum magnetic field at the surface of the rod, given by Formula 3.1. We ignored the skin effect inside the target rod, and assumed the static approximation for all the area. The uncertainty of the asymmetric field is considered at the error estimation in Chapter 6.1.6.

These simulations are also used for PIMON analysis. When pions pass the PIMON gas vessel, Cherenkov photons are emitted. The photons are ray-traced to simulate the Cherenkov photon images on the focal plane. Since Cho model does not treat the production of electro-magnetic components, simulation of their contribution is always simulated by GCALOR/FLUKA model.

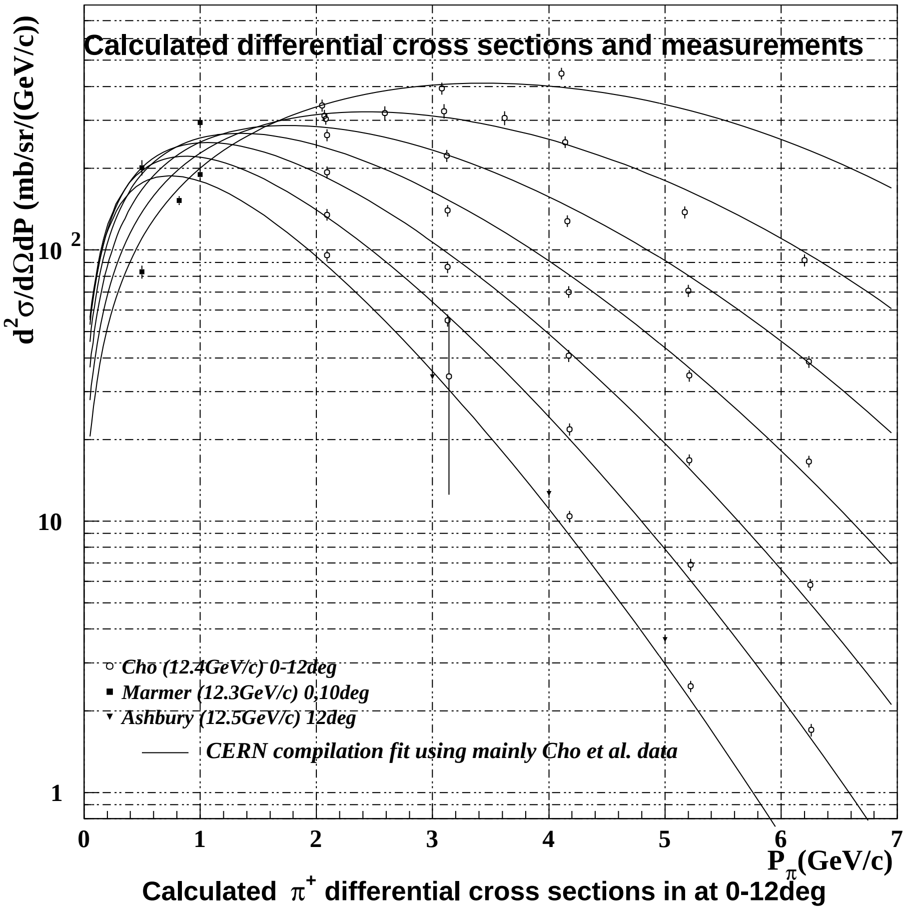

Figure 4.2: Pion yield of experimental results [67, 69, 70] and the fit by Cho model.

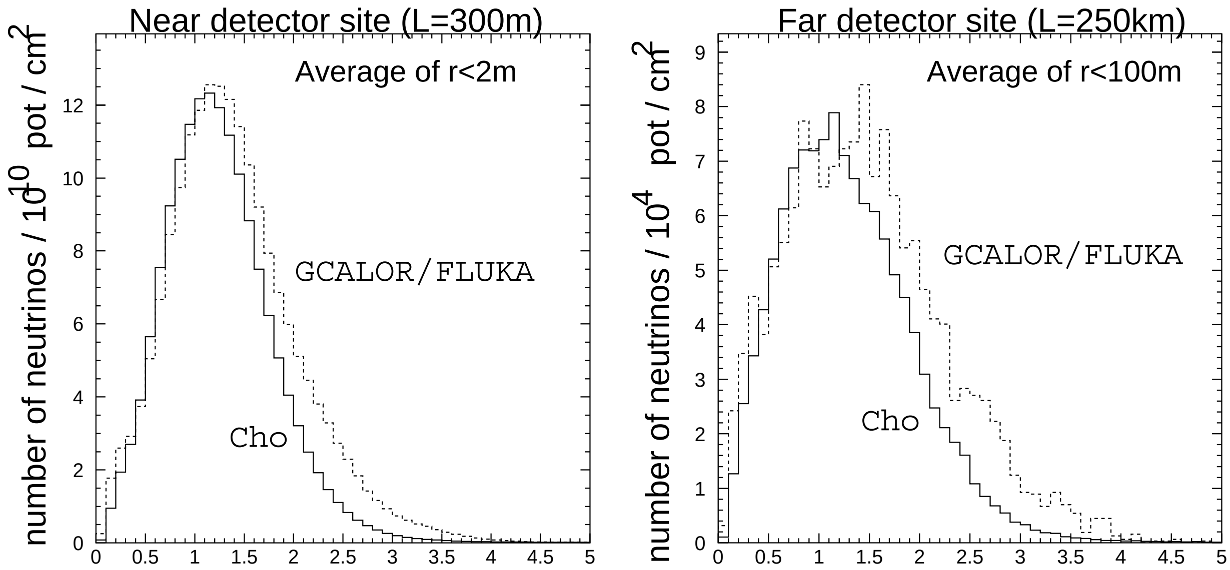

Figure 4.3: Simulated ν_μ flux at near site (left) and far site (right), using the standard 250kA Monte Carlo simulation with Cho model (solid), and GCALOR/FLUKA model (dashed).

4.1.4 Simulated neutrino beam

Neutrinos are produced mainly from the pion decay,

$$\pi^\pm \rightarrow \mu^\pm \overset{(-)}{\nu_\mu} \tag{4.7}$$

Since HORN magnets enhance π^+ rather than π^-, the fraction of ν_μ dominates over that of $\bar{\nu_\mu}$. A little fraction of the neutrinos comes from muon decay in the decay volume, and from kaon decay around the target section. According to the beamMC, about 98% of neutrinos flying toward SK are ν_μ. ν_e is 1.3% of ν_μ, $\bar{\nu_\mu}$ is 0.5%, and $\bar{\nu_e}$ is 0.02%.

Figure 4.3 shows the simulated ν_μ flux at the near neutrino detector area (300 m from the target) and the far site (250 km from the target). The near flux is the average of 2 m in radius, and the far flux is the average of 100m in radius. In these figures, simulation with GCALOR/FLUKA model and that with Cho model are compared.

4.2 Neutrino interaction simulation (neutMC)

Neutrino interaction is generated with the simulated neutrino flux as an input. The simulator of the neutrino interaction is called "NEUT", which is originally developed and used at the atmospheric neutrino analysis in Super-Kamiokande experiment [72]. NEUT mainly consists of three parts, the part to calculate all of differential cross section, the part to simulate individual interaction, and the part to simulate nuclear interaction for outgoing hadrons.

4.2.1 Neutrino interaction around 1 GeV

Neutrino interacts with target material by $W^{\pm}$ exchange and Z^0 exchange. First one is called charged current interaction (CC) and latter one is called neutral current interaction (NC). Around 1 GeV neutrino, have following interactions;

• CC quasi-elastic scattering	$\nu N \rightarrow lN'$	$(\sim 30\%)$
• NC elastic scattering	$\nu N \rightarrow \nu N$	$(\sim 13\%)$
• CC single-meson production	$\nu N \rightarrow lN' + m$	$(\sim 29\%)$
• NC single-meson production	$\nu N \rightarrow \nu N' + m$	$(\sim 10\%)$
• CC multi-pion production	$\nu N \rightarrow lN' + n\pi (n \geq 2)$	$(\sim 13\%)$
• NC multi-pion production	$\nu N \rightarrow \nu N' + n\pi (n \geq 2)$	$(\sim 4\%)$
• CC coherent-pion production	$\nu ^{16}O \rightarrow l ^{16}O + \pi^{\pm}$	$(\sim 2\%)$
• NC coherent-pion production	$\nu ^{16}O \rightarrow \nu ^{16}O + \pi^{0}$	$(\sim 1\%)$

where, N is a nucleon (proton or neutron), l is a charged lepton and m is a meson, mostly a pion. The percentage of each interaction mode is shown at the end of each line. These values are obtained with the expected flux at 1kt and the target material is water (H_2O). Figure 4.4 shows the cross section for water target and iron target, provided by our NEUT simulation.

The cross section of neutrino with atomic electron is roughly 1/1000 of above interactions. Thus, it is neglected.

4.2.2 CC quasi-elastic, and NC elastic scatterings

This interaction has the largest cross section in our energy region. This interaction is two-body scattering on the nucleon. Therefore, the differential cross section is described by the initial energy and 4-momentum transfer ($Q^2 = -q^2 = -(p_\nu - p_\mu)^2$, where p_ν, p_μ are injected ν and out-going lepton momentum, respectively). Since target hadron has internal structure, vector and axial vector form factors are taken into account. The hadron current is expressed as follows [73];

$$< N\prime|J_{had}|N >= cos\theta_c \bar{u}(N\prime)\Big[\gamma_\lambda F_V^1(Q^2) + \frac{i\sigma_{\lambda\nu}q^\nu \xi F_V^2(Q^2)}{2m_N} + \gamma_\lambda\gamma_5 F_A(Q^2)\Big]u(N), \tag{4.8}$$

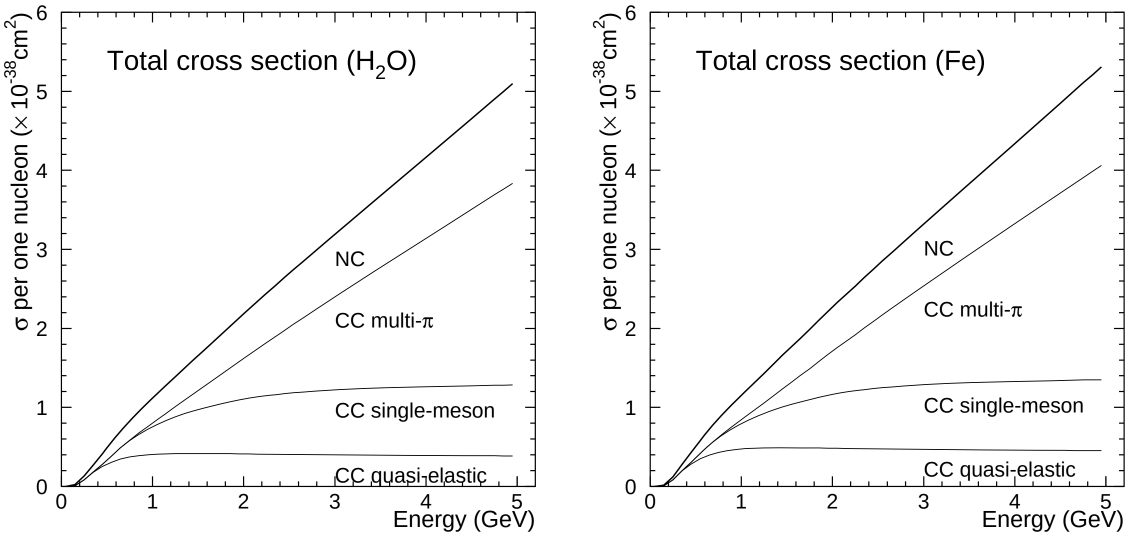

Figure 4.4: Neutrino cross section for water target (left) and iron target (right). The plot shows the cross section of each interaction mode. CC coherent-pion interaction is assorted to CC single-meson interaction, in this plot. Horizontal axis is the injected neutrino energy. Cross sections are normalized per one nucleon.

where, F_V^1,F_V^2,F_A are the vector and axial vector form factors and represented as follows.

$$F_V^1(Q^2) = \Big(1 + \frac{Q^2}{4m_N^2}\Big)^{-1}\Big[G_E^V(Q^2) + \frac{Q^2}{4m_N^2}G_M^V(Q^2)\Big], \tag{4.9}$$

$$\xi F_V^2(Q^2) = \Big(1 + \frac{Q^2}{4m_N^2}\Big)^{-1}\Big[G_M^V(Q^2) - G_E^V(Q^2)\Big], \tag{4.10}$$

$$G_E^V(Q^2) = \frac{1}{\Big(1 + \frac{Q^2}{M_V^2}\Big)^2}, \quad G_M^V(Q^2) = 1 + \frac{\xi}{\Big(1 + \frac{Q^2}{M_V^2}\Big)^2}, \quad \xi \equiv \mu_p - \mu_n = 3.71 \tag{4.11}$$

$$F_A(Q^2) = \frac{-1.23}{\Big(1 + \frac{Q^2}{M_A^2}\Big)^2}, \qquad M_V = 0.84(GeV^2/c^2), \quad M_A = 1.01(GeV^2/c^2) \tag{4.12}$$

where, θ_c, m_N, M_V and M_A represent the Cabbibo angle, nucleon mass, the vector mass, and the axial vector mass, respectively. The vector mass was determined by $e-p$ scattering experiments by CVC hypothesis. The axial vector mass was determined by neutrino experiments with about 10% uncertainty [74].

Finally the cross section is expressed by following formula;

$$\frac{d\sigma^{\nu}}{dQ^2} = \frac{m_N^2 G_F^2 \cos^2\theta_c}{8\pi E_\nu^2}\Big[A(Q^2) \mp B(Q^2)\frac{(s-u)}{m_N^2} + C(Q^2)\frac{(s-u)^2}{m_N^4}\Big] \tag{4.13}$$

where, G_F is the Fermi coupling constant, $(s-u) = 4m_N E_\nu - Q^2 - m_l^2$ when m_l is the lepton mass, and;

$$\begin{aligned} A(Q^2) &= \frac{(m_l^2+Q^2)}{4m_N^2}\Big[\Big(4+\frac{Q^2}{m_N^2}\Big)|F_A|^2 - \Big(4-\frac{Q^2}{m_N^2}\Big)|F_V^1|^2 + \frac{Q^2}{m_N^2}|\xi F_V^2|^2\Big(1-\frac{Q^2}{4m_N^2}\Big) \\ &\quad + \frac{4Q^2 F_V^1 \xi F_V^2}{m_N^2} - \frac{m_l^2}{m_N^2}\Big(|F_V^1+\xi F_V^2|^2 + |F_A|^2\Big)\Big], & (4.14) \\ B(Q^2) &= \frac{Q^2}{m_N^2}F_A\Big(F_V^1+\xi F_V^2\Big) & (4.15) \\ C(Q^2) &= \frac{1}{4}\Big(|F_A|^2 + |F_V^1|^2 + \frac{Q^2}{m_N^2}|\frac{\xi F_V^2}{2}|^2\Big) & (4.16) \end{aligned}$$

Figure 4.5 shows the quasi-elastic cross section as a function of initial neutrino energy calculated using our simulation. It gives a consistent result to various bubble chamber measurements round 1 GeV [75, 76, 77, 78]. Uncertainty of the axial vector mass M_A changes the overall scale of the cross section, as shown in Figure 4.5. However, it hardly change the differential distribution, like Q^2 dependence.

For the NC elastic scattering, following relations are used according to [79].

$$\begin{aligned} \sigma(\nu p \rightarrow \nu p) &= 0.153 \times \sigma(\nu n \rightarrow e^- p) & (4.17) \\ \sigma(\nu n \rightarrow \nu n) &= 1.5 \times \sigma(\nu p \rightarrow \nu p) & (4.18) \end{aligned}$$

When target nucleons are bounded in the nuclei, Fermi motion and Pauli blocking effect must be taken into account. Fermi gas model is adopted to simulate Pauli blocking, by requiring the final nucleon momentum to be over Fermi surface momentum. This calculation uses a nucleon-nucleus potential distribution which is derived from the e^{-12}C (e$^-$Ni) scattering experiment [80] for oxygen (iron) nuclei. The measured value of Fermi surface momentum is 217MeV/c for oxygen and 237MeV/c for iron nuclei. Figure 4.5 exhibits the comparison by changing the Fermi surface momentum to 237, 217, 250MeV/c.

4.2.3 Single-meson production

Single-meson production is the next dominant interaction mode to the quasi-elastic scattering. This interaction consists of following reactions;

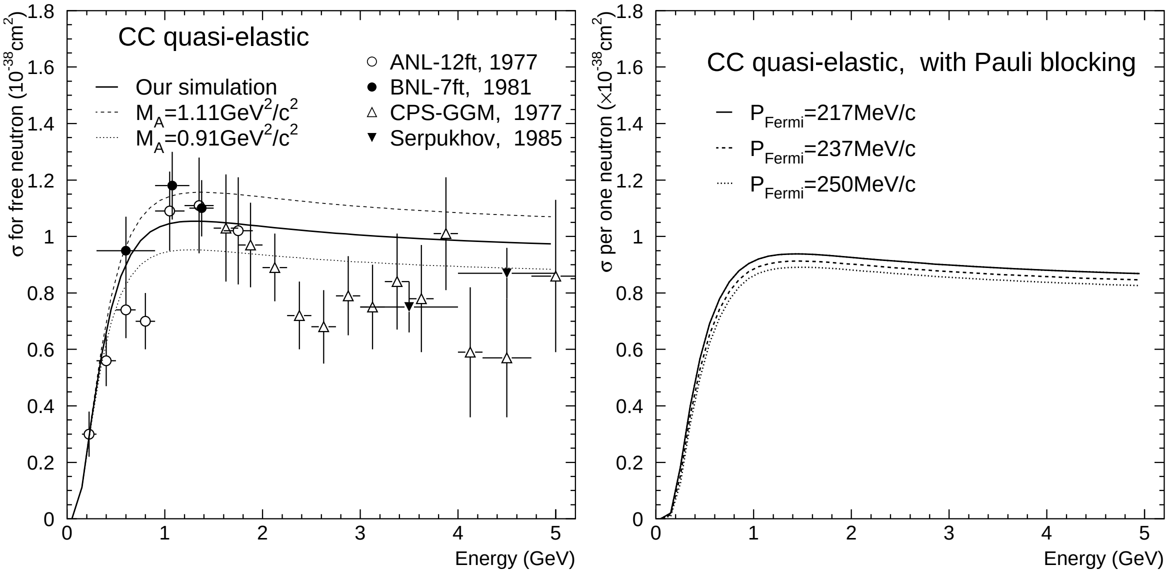

Figure 4.5: (Left figure) Cross section of CC quasi-elastic scattering to one free neutron in our simulation. The standard one with $M_A = 1.01\mathrm{GeV}^2/c^2$ is shown by solid line, whereas the dashed(dotted) line shows the simulation with $M_A = 1.11(0.91)\mathrm{GeV}^2/c^2$. Horizontal axis is the injected neutrino energy in Lab. frame. Measurements from various experiments (ANL:[75], BNL:[76], GGM:[77], and Serpukhov:[78]) are overlaid. Error bars on the marks mean the error quoted in their papers. (Right figure) CC quasi-elastic cross section with Pauli blocking effect. The unit is cm^2 per one neutron.

- Charged Current (CC)

$$\nu n \rightarrow l^- p m^0 \tag{4.19}$$
$$\nu n \rightarrow l^- n \pi^+ \tag{4.20}$$
$$\nu p \rightarrow l^- p \pi^+ \tag{4.21}$$

- Neutral Current (NC)

$$\nu n \rightarrow \nu n m^0 \tag{4.22}$$
$$\nu p \rightarrow \nu p m^0 \tag{4.23}$$
$$\nu n \rightarrow \nu p \pi^- \tag{4.24}$$
$$\nu p \rightarrow \nu n \pi^+ \tag{4.25}$$

where, m^0 is the neutral meson (mainly π^0, and a little fraction of η, and K^0). These interactions are simulated using the method by Rein and Sehgal[81]. In their method, the single-meson production is mediated by a certain baryon resonance states as;

$$\begin{array}{ll} \text{resonance production} & \nu N \rightarrow l N^* \\ \text{resonance decay} & N^* \rightarrow m N\prime \end{array}$$

where, N^* is one of the baryon resonances. When this interaction occurred through one resonance state, the differential cross section is expressed by following formula;

$$\frac{d^2\sigma}{dQ^2 dE_\nu} = \frac{1}{32\pi m_N E_\nu^2} \cdot \frac{1}{2} \cdot \sum_{spins} |T(\nu N \rightarrow l N^*)| \cdot \chi_{E_\nu} \cdot \delta(W^2 - M^2) \tag{4.26}$$

where, E_ν is the neutrino energy, m_N is the nucleon mass, W is the invariant mass of hadronic system, and χ_{E_ν} is the decay probability of resonance. The last δ-function is calculated for each resonance with given mass M and width Γ, using following Breit-Wigner formula:

$$\delta(W^2 - M^2) \rightarrow \frac{1}{2\pi} \cdot \frac{\Gamma}{(W - M)^2 + \Gamma^2/4} \tag{4.27}$$

In our case, dominant resonance is $\Delta(1232)$ and other 17 higher resonance states are also considered, until W is less than 2 GeV. Figure 4.6 compares our calculated cross sections with the experimental data [82, 83, 84].

Angular distribution of mesons from $\Delta(1232)$ is calculated using this Rein-Sehgal's method. For the decay of other resonance states, the meson direction is assumed to be isotropic in the resonance rest frame.

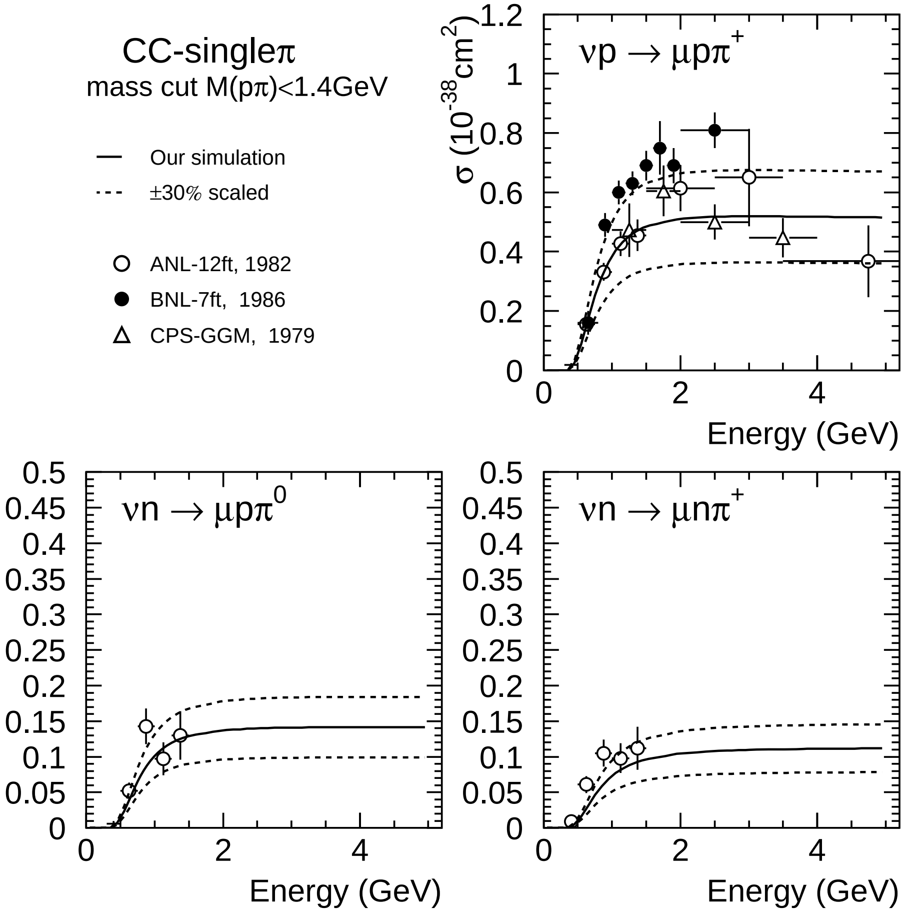

Figure 4.6: Cross section of CC single-pion production (solid), with experimental data (ANL:[82], BNL:[83], GGM:[84]). ±30% scaled ones (dashed) are also shown as a reference.

4.2.4 Multi-pion production

In higher energy region, deep in-elastic scattering dominates to the elastic or resonance interaction. The cross section of CC deep in-elastic scattering is calculated based on Bjorken scaling, and expressed as;

$$\begin{aligned} \frac{d^2\sigma^\nu}{dxdy} &= \frac{G_F^2 m_N E_\nu}{\pi} \cdot \Big[(1-y+\frac{1}{2}y^2+C_1)F_2(x)+y(1-\frac{1}{2}y+C_2)[xF_3(x)]\Big] \quad (4.28) \\ C_1 &= \frac{m_l^2(y-2)}{4m_N E_\nu x} - \frac{m_N xy}{2E_\nu} - \frac{m_l^2}{4E_\nu^2} \\ C_2 &= -\frac{m_l^2}{4m_N E_\nu x} \end{aligned}$$

where, $x = Q^2/(2m_N(E_\nu - E_l) + m_N^2)$ is Bjorken scaling variable, in low energy, $y = (E_\nu - E_l)/E_\nu$ is the fractional energy transfer to the hadron system, m_N (m_l) is nucleon (lepton) mass and E_ν (E_l) is initial neutrino (final lepton) energy. The nucleon structure functions F_2 and xF_3, as a function of x and Q^2, are given by GRV-94[85].

In our simulation, the events are generated from $W > 1.4$ GeV according to this formula. In $1.4 < W < 2$ GeV range, pion multiplicity is calculated using the measurement at Fermilab bubble chamber experiment [86]. It is found to be $(0.06\pm0.06)+(1.22\pm0.03)lnW^2$. Assuming $\langle n_{\pi^+}\rangle = \langle n_{\pi^-}\rangle = \langle n_{\pi^0}\rangle$ and $< n_{\pi^+} >= 1/2 < n_c >$, mean multiplicity including neutral pion is estimated as follows;

$$\langle n_\pi \rangle = 0.09 + 1.83lnW^2 \qquad (4.29)$$

When the pion multiplicity is determined to one, the event is ignored, in order to avoid double counting with resonance (single-meson) contribution. For an individual Monte Carlo event, pion multiplicity is finally determined KNO(Koba-Nielsen-Olesen) scaling [87], which well reproduce the previous experimental data. The charge of each hadron is randomly chosen keeping the charge conservation. Forward-backward asymmetry of the produced pions is also taken into account in the hadronic center of mass system as [88];

$$\frac{\text{“}forward\text{''}}{\text{“}backward\text{''}} = \frac{0.35 + 0.41lnW^2}{0.50 + 0.09lnW^2} \qquad (4.30)$$

For the events with $W > 2$ GeV, kinematics are determined by JETSET/PYTHIA [89].

For the NC multi-pion production, ratio of NC/CC is estimated in [90] for less than 3 GeV neutrinos, and in [91] for greater than 3 GeV neutrinos. Then following relations are used;

$$\frac{\sigma(\nu N \to \nu X)}{\sigma(\nu N \to l^- X)} = \begin{cases} 0.26 & (\mathrm{E}_\nu < 3 \text{ GeV}) \\ 0.26 + 0.04(E_\nu/3 - 1) & (3 \text{ GeV} < \mathrm{E}_\nu < 6 \text{ GeV}) \\ 0.30 & (6 \text{ GeV} < \mathrm{E}_\nu) \end{cases} \qquad (4.31)$$

4.2.5 Coherent pion production

Coherent interaction occurs as whole nucleus, instead of the individual nucleon. They interact without any change of charge or isospin for recoil nucleus. Since the transferred momentum is very small, angular distribution of recoil leptons and produced pions have sharp peaks in the forward direction.

The cross section for oxygen nucleus is calculated employing the Rein-Sehgal model [92], which is expressed by following formula;

$$\begin{aligned}\frac{d^3\sigma}{dxdyd|t|} &= \frac{G_F^2 m_N E_\nu}{2\pi^2} f_\pi^2 A^2 (1-y) \frac{1}{16\pi} \left[\sigma_{tot}^{\pi N}\right]^2 (1+r^2) \Big(\frac{M_A^2}{M_A^2+Q^2}\Big)^2 e^{-b|t|} F_{abs} \quad (4.32)\\ r &= \frac{Ref_{\pi N}(0)}{Imf_{\pi N}(0)}\end{aligned}$$

where, $f_\pi = 0.93 m_\pi$ is the decay constant, A is atomic number (oxygen:$A = 16$), $b = \frac{1}{3}(R_0 A^{1/3})^2$ is of the order of traverse dimensions of the nucleus ($\sim 80(\mathrm{GeV})^{-2}$ for oxygen), and t is the square of 4-momentum transfered to the nucleus. F_{abs} is the considerable term for pion absorption in the nucleus. For iron nucleus, coherent cross section is scaled proportional to $A^{1/3}$ from the cross section of oxygen nucleus.

4.2.6 Experimental constraint of the CC total cross section

CC-total cross section is also compared with the measurement of bubble chamber experiment [93, 94, 95]. In Figure 4.7, left figure shows the CC-total cross section, and right figure shows $\sigma(\nu n)$ over $\sigma(\nu p)$. In these figures, cross section is corrected to the water target by the ratio of proton and neutron. Coherent interaction is neglected in this comparison. Ambiguity of ±30% of in-elastic / elastic cross section ratio covers most of the experimental data.

4.2.7 Nuclear effect for hadrons

Since neutrino interaction occurs inside of the nucleus, produced hadrons often interact before leaving the nucleus. This "nuclear effect" has been studied for oxygen nuclei. For iron nuclei, the nuclear effect is known to be larger than that for oxygen nuclei, because the density of iron nuclei is large. However, our standard simulation of iron interaction assumed same nuclear effect and the uncertainty of the effect is assigned to the systematic error.

Following interactions are considered;

- For pions, an in-elastic scattering, a charge exchange, and an absorption are considered. The cross section of each interaction is calculated by the model of Oset *et. al.*

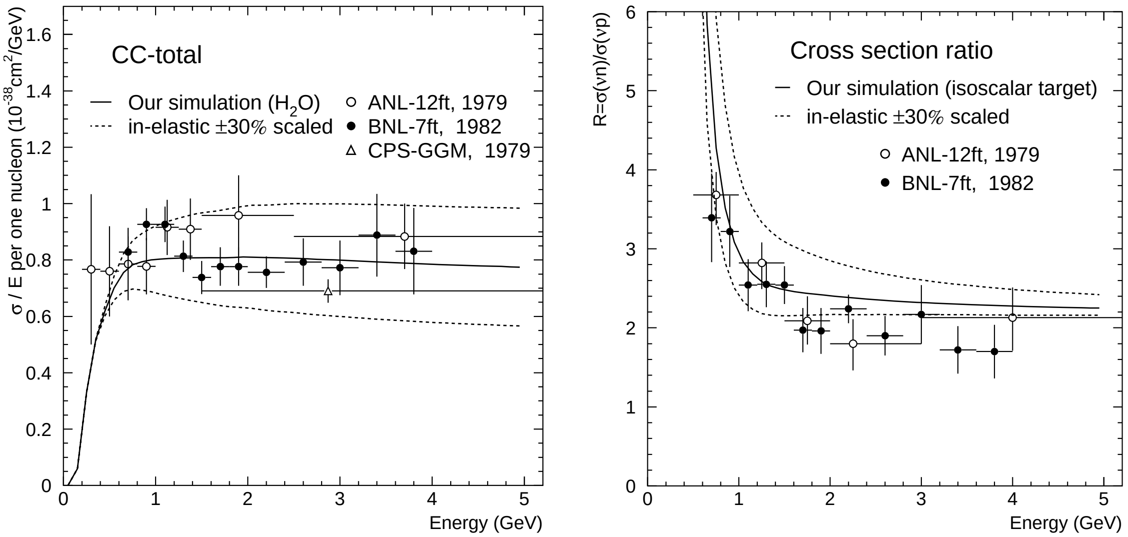

Figure 4.7: $\sigma(\text{CC-total})/E_\nu$ (left) and $\sigma(\nu n)/\sigma(\nu p)$ (right) as a function of the neutrino energy. The absolute values are normalized to the water target case. Dotted lines show the cases with scaled single-meson and multi-pion cross section by ±30%. Other experiments (ANL: [93], BNL: [94], GGM: [95]) are overlaid.

[96]. In the cross section calculation, nuclear density in oxygen nucleus is assumed to be the Wood-Saxon form, which is typically expressed for protons;

$$\rho_p(r) \ = \ \frac{Z}{A}\rho_0 \frac{1}{1+\exp(\frac{r-c}{a})} \tag{4.33}$$

where r is the distance from the center of the oxygen. In our simulation, $\rho_0 = 0.48 m_\pi^3$, $a = 0.41$fm, and $c = 2.69$fm for ^{16}O.

Figure 4.8 shows the cross section of each interaction for π^+, and the interaction probability for π^0, as a function of the pion momentum. Measurements of other experiments are also shown there.

- The absorption of resonance baryon (Δ) is considered. 20% of produced Δ is absorbed [97].

Protons and neutrons contribute a little for our event in 1kt, MRD, and SK. Therefore, nuclear effect of protons and neutrons are neglected.

4.2.8 Uncertainty of the neutrino interaction

Considering the ratio of the near and far observation, absolute scale of the cross section is canceled. Remaining uncertainties are arranged into following two items.

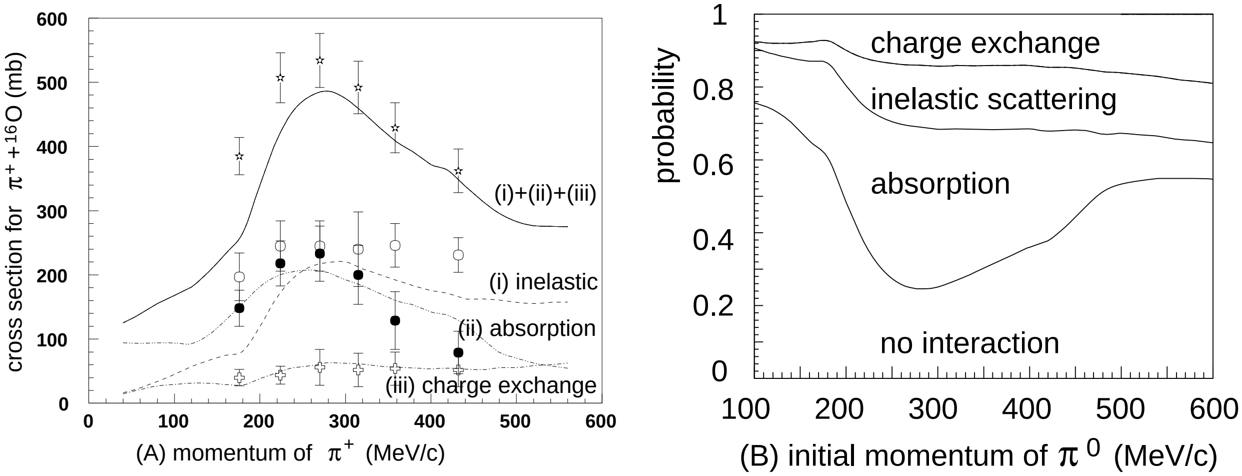

Figure 4.8: Cross section for pi^+ (left) and π^0 (right) on oxygen nuclei.

- Cross section ratio between Charged current (CC) and Neutral current (NC). We change the NC cross section by ±30%, and estimate the effect for the analysis.

- Cross section ratio of in-elastic cross section relative to CC quasi-elastic and NC elastic scattering. We change the cross sections of single-meson production, multi-meson production, and coherent-pion production mode of both CC and NC by ±30%, simultaneously, and estimate the effect.

These assigned uncertainties are suitable to cover the experimental data (as shown in Figure 4.6 and 4.7).

For iron nuclei, following two uncertainties are also taken into account.

- Uncertainty of the Pauli blocking threshold.
  We simulate with different Fermi surface momentum of 217, 237, and 250MeV/c.

- Uncertainty of the nuclear effect.
  We prepare two simulations. One is assumed to have same nuclear effect as the oxygen nuclei. The other is the simulation with 100% absorption of hadrons.

4.3 Detector simulation

After neutrino interaction occurs, passage of generated particles is simulated using GEANT simulation [66]. GCALOR package is used for the hadron interaction simulation Validity of the simulation is experimentally checked by the measurement of proton range in iron [98]. The results show the simulation with GCALOR well reproduces the measurements.

Simulated events are saved with the same data format as real data. This enables us to use the same analysis codes which is used for real data.

4.3.1 Simulation of MRD

Full structure of irons, drift-tube modules, and gas in MRD are taken into account. When charged particles pass the each cell, hit information is saved after conversion to TDC count. For each hit, 97.5% hit efficiency is applied. Noise hits are generated according to the estimation from the real data, although our noise rate is small enough not to affect for our track identification.

4.3.2 Simulation of water Cherenkov detector (1kt, SK)

Same water Cherenkov detector simulation is used at 1kt and SK. The water volume works as a neutrino target and also a radiator of the Cherenkov photon. The simulator emits photons according to Formula 3.11 and 3.12.

Emitted photons are tracked with considering the absorption and scattering in the water. At the black sheet on the wall and at the surface of PMTs, reflection is considered as a function of the incident angle [61].

For simulating PMT response in photon detection, measured quantum efficiency is used. Obtained photo-electron signals are smeared according to measured 1 photo-electron distribution and timing resolution. Finally detected photo-electrons are converted to TDC and ADC information.

Chapter 5

Analysis Strategy

5.1 Overview of the Analysis

In the following chapters, study of the ν_μ disappearance is discussed. As described in Chapter 2.2 and Formula 2.2, the study was performed by comparing the observed neutrino events in SK (N^{SK}_{obs}) to the expected number (N^{SK}_{exp}) derived from the near detector measurement.

The discussion is described in following order.

1. **Proton intensity measurement.**
   Neutrino beam intensity can be normalized by proton intensity measured by CTs, in particular, TGT-CT. The accumulation of protons on the target (p.o.t.) is used for the normalization of rate, to correct the live spill difference between each detector measurement.

2. **Pion distribution measurement using PIMON.**
   PIMON measurement provides the pions' (p_π, θ_π) distribution before decaying to neutrinos, by measuring the Cherenkov photon distribution. This confirms beamMC, which predicts the neutrino energy spectrum and the flux ratio Φ_{far}/Φ_{near}. The results and the systematic errors are described.

3. **Proton beam and secondary muon measurement.**
   Proton beam profile and its stability is continuously measured using SPICs. Secondary muons are measured using MUMON after the beam dump. They work as the spill-by-spill monitors of the beam. The results of these stability measurements and the effect for our analysis are discussed.

4. **Neutrino beam measurement using MRD.**
   Neutrino beam is continuously measured with the iron interacted events in MRD. The

neutrino beam direction and profile width are measured during the whole running period. Stability of the event rate and the muon distributions confirms the neutrino beam stability. The event selection and the results are described.

5. **Neutrino event rate measurement using 1kt.**
   Number of near events is extracted from the events measured in 1kt. The event selection, results and the related systematic errors are described.

6. **Neutrino event measurement at SK.**
   Neutrino event selection and the results at SK are presented.

7. **Comparison of near and far event rate.**
   The comparison between the observed number of events at SK and the expected number is discussed. The quantitative discussion of probability of the neutrino event reduction is discussed.

5.2 Operation of the Experiment

During the experiment, the proton beam had been controlled to get best targeting efficiency and best pointing to SK. The muon profile center at MUMON had been kept to the designed direction to SK. And we continuously monitored the intensity ratio of MUMON and CT, which is the indicator of pion production efficiency.

5.3 Good Beam Spill Selection

Proton intensity was measured by CTs. We used the measurement of TGT-CT as the normalization of accumulated protons on target. Figure 5.1 shows the accumulated number of protons on the target (p.o.t.) measured by TARGET-CT. The averaged number of protons per one beam spill (ppp) was typically $4 \sim 6 \times 10^{12}$ as also shown in Figure 5.1. In total, 2.6×10^{19} p.o.t. was injected to the target since May 1999.

This accumulated p.o.t. includes some fraction of the unusable periods, for example, beam tuning, fail of the data acquisition. "Good beam spill" is defined to be used for our analysis, with following criteria.

- We use the data from June 1999 to June 2000.
- Exclude the machine study, beam tuning, or PIMON measurement.
- Exclude the period of beam line component trouble.
- Proton intensity is greater than 1×10^{12}ppp (proton per pulse).

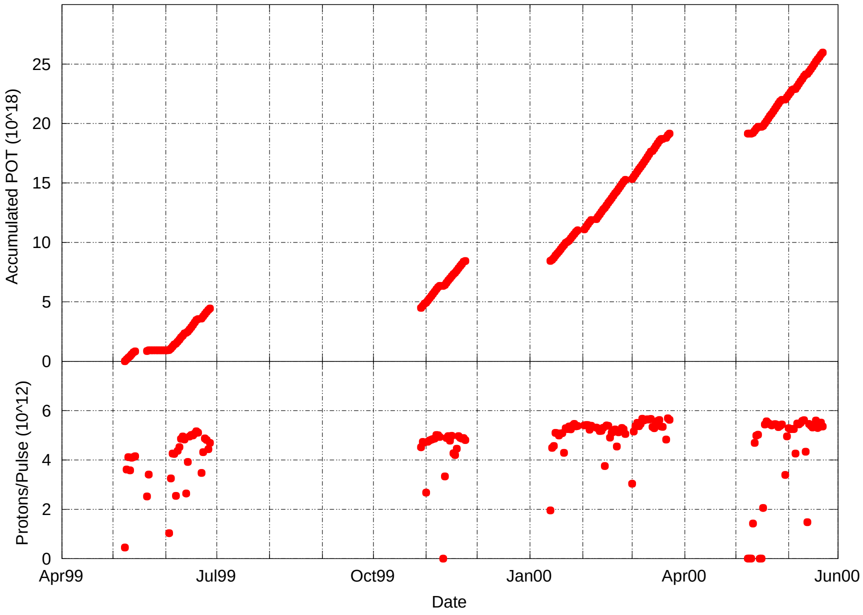

Figure 5.1: Accumulated number of proton on the target (upper) and the averaged proton intensity (lower), measured by TARGET-CT.

- Horn current is greater than 240(190) kA where nominal current is 250(200) kA from Nov. 1999 to June 2000 (in June 1999).
- SK is alive.

In short, we used the period as long as SK is alive and beam line is properly running, as shown in Table 5.1. Table 5.2 summarizes the used p.o.t.s for each near detector analysis in each month. We have about 2.29×10^{19} p.o.t. for SK analysis, whereas 2.10×10^{19} p.o.t. and 1.97×10^{19} for MRD and 1kt, respectively.

	1kt alive	1kt dead
SK alive	used (19.7×10^{18}p.o.t.)	used, need correction (3.2×10^{18}p.o.t.)
SK dead	not used	not used

	MRD alive	MRD dead
SK alive	used, (21.0×10^{18}p.o.t.)	used, need correction (1.9×10^{18}p.o.t.)
SK dead	not used	not used

Table 5.1: Chart of the used spill definition. Values are the accumulation from June 1999 to June 2000.

Period	Jun.99	Nov.99	Jan.00	Feb.00	Mar.00	May.00	Jun.00
From	Jun.4	Oct.29	Jan.14	Feb.2	Mar.1	May 11	May.31
To	Jun.26	Nov.24	Jan.29	Feb.26	Mar.23	May 28	Jun.21
Target diameter	20mmϕ	30mmϕ					
HORN current	200kA	250kA					
POT_{SK} ($\times 10^{18}$)	3.10	3.57	2.22	4.04	3.71	2.56	3.75
POT_{1kt} ($\times 10^{18}$)	2.60	2.62	1.81	3.74	3.35	2.42	3.16
POT_{MRD} ($\times 10^{18}$)	2.93	2.72	2.04	3.81	3.49	2.51	3.54

Table 5.2: Summary of the used p.o.t. (protons on the target) for each detector analysis.

Chapter 6

Proton and Secondary Particle Measurement

6.1 Pion Distribution Measurement using PIMON

6.1.1 PIMON measurement

PIMON measurements have been done in the special run in June 1999 ($I_{horn} = 200$ kA) and Nov. 1999 ($I_{horn} = 250$ kA). Special beam time is occupied by PIMON measurement because materials of PIMON structure affect to the secondary beam, and because the low intensity beam is needed to avoid PMT saturation. Low intensity operation is achieved by the adjustment of the Booster injection. In June run, data are taken with typically 7×10^{10} ppp of 1 bunch operation. After studying the lower gain operation of PMTs, data is taken with typically 7×10^{11} ppp of full (= 9) bunch operation in Nov. run. The operation parameters are summarized in Table 6.1.

This chapter presents mainly the results in Nov. run. Results of June run is presented in Appendix E.1 and other documents [46].

6.1.2 Cherenkov photon distribution

Figure 6.1 shows the typical signal distribution of the observed ADC counts in each PMT, after pedestal subtraction. Pedestal value of each PMTs are provided from the off-spill data. The observed signals contain the “background” Cherenkov photons and the beam associated radiation noises, as much as the “signal” Cherenkov photons emitted at the fiducial area in the beam line. In order to subtract these “background” signals and noises, the MIRROR-OFF run is taken, where mirror is set to the wrong direction. Figure 6.1 shows the typical result of MIRROR-ON data, and MIRROR-OFF data, and the subtracted result. In order to obtain fine photon distribution, PMTs are slid by half channel and data

Parameter	June 1999	Nov. 1999
Target diameter	20mmϕ	30mmϕ
HORN current	200 kA	250 kA
Proton intensity (during PIMON run)	7×10^{10} ppp	7×10^{11} ppp
Proton beam bunch	1	9
Number of refractive indices	9	9
PMT gain	300	20 or 50
PMT saturation	exist	none

Table 6.1: Summary of the beam condition and PIMON operations in June and Nov. run.

are taken. Accordingly, 40 data points of the Cherenkov photon distribution are taken for each refractive index. In these subtraction and combination process, data are normalized by the proton intensity, measured by TGT-CT.

Figure 6.2 shows the Cherenkov photon distribution after MIRROR-OFF subtraction, with various refractive indices. Following systematic errors are considered in these distributions.

- The error due to spill-by-spill fluctuation, which is estimated by $\frac{(r.m.s.)}{\sqrt{n\text{spill}}}$.
- Uncertainty of the gain adjustment for each PMTs. 5% error is quoted for each PMT (see Chapter 3.2.6).
- Uncertainty of lower gain operation estimated by the difference between two data with different gain (gain= 20 and gain= 50) at same refractive index of $n = 1.00129$.

6.1.3 Subtraction of electro-magnetic shower contribution

There is non-negligible contribution from the electro-magnetic shower. Electro-magnetic shower is caused by the converted γ from π^0. Subtraction of this background is performed using beamMC, which is normalized in lowest index measurement of $n = 1.00024$. Absolute normalization is determined by the lowest index case. As shown in Figure 3.6, high momentum pions above 6.4 GeV/c are negligible compared to electro-magnetic components. Electro-magnetic components make broad distribution.

Figure 6.2 proves that the electro-magnetic component (shaded area) estimated by beamMC with one normalization factor well reproduces the broad background distribution at all refractive indices.

The obtained Cherenkov photon distributions are compared to beamMC. Figure 6.3 shows the comparison to the distribution predicted by beamMC, based on Cho model (left)

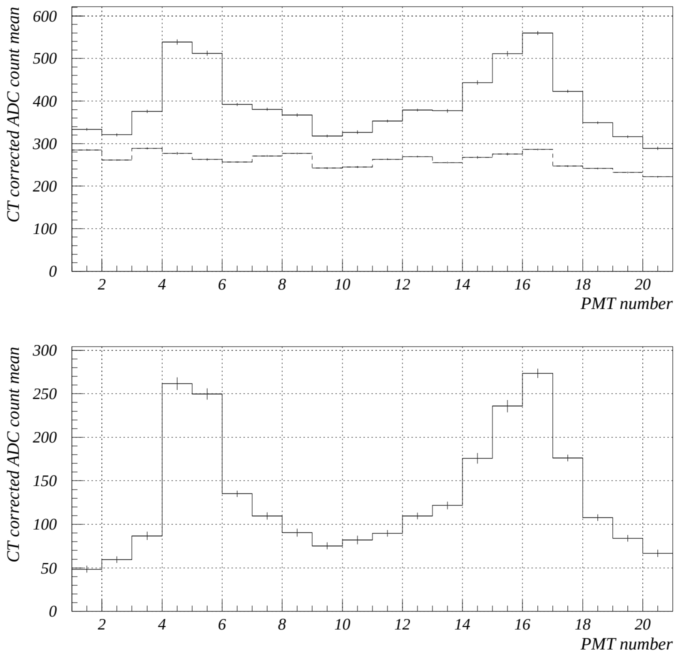

Figure 6.1: Typical example of the MIRROR-OFF subtraction at $n = 1.000243$, in June 1999. Signal of MIRROR-ON and MIRROR-OFF (top) and subtracted result (bottom) are shown. Horizontal axis shows the PMT number, which are vertically aligned at the focal plane with 3.5 cm repetition. PMT-1 is at the top, and PMT-20 is at the bottom.

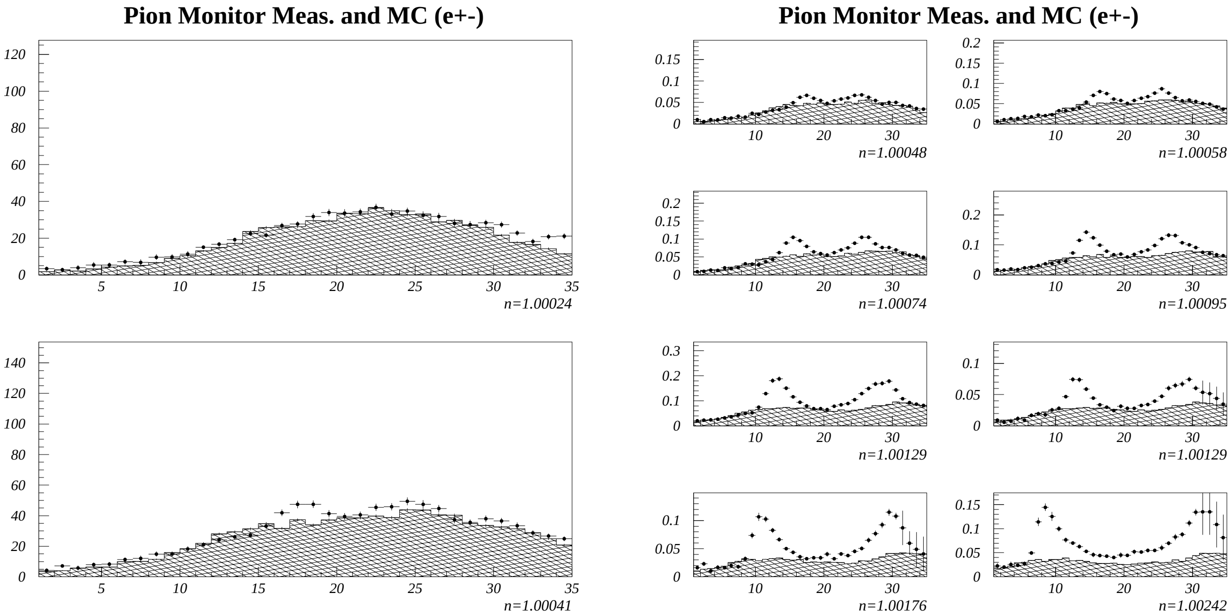

Figure 6.2: Measured cherenkov photon distribution in various refractive indices in Nov. 1999 run ($I_{horn} = 250$ kA), shown with the systematic error bars. Horizontal axis means the PMT position number (1 unit corresponds to 1.75 cm) with respect to the y-axis at focal plane. Large number in the horizontal axis means the bottom PMT, which measures relatively large divergence angle with respect to the beam axis. Vertical axis shows the ADC count. Pedestal and MIRROR-OFF distribution (see text) are already subtracted. PMT gain correction is applied. Shaded area is the estimated Cherenkov photons from the electro-magnetic shower components, normalized to the lowest pressure data (see text).

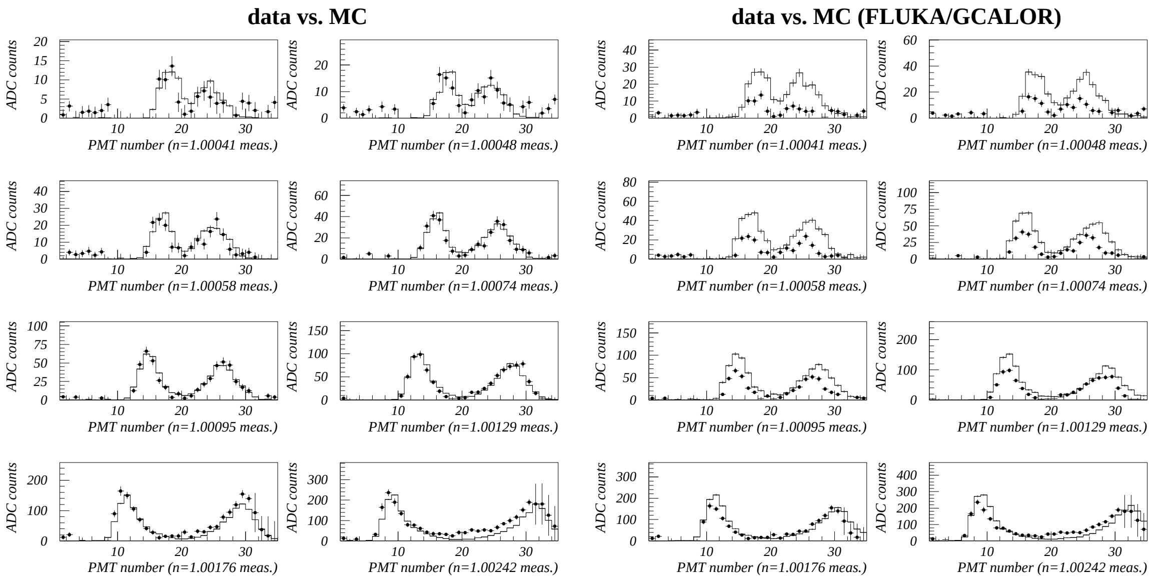

Figure 6.3: Cherenkov photon distribution measured in Nov. (dots) and two sets of beamMC (histograms). The simulation in left figures is based on Cho model and the simulation in right figures is based on GCALOR/FLUKA model. Error bars are quoted in previous Section6.1.2.

or GCALOR/FLUKA model (right). These figures clearly show that the simulations using Cho model have good agreement to the data, while the simulation using GCALOR/FLUKA model has some difference.

6.1.4 Extraction of the pion energy and angular distribution

Obtained Cherenkov photon distributions are fit with the pion distribution on (p_π, θ_π) plane, as described in Chapter 3.2.4. Figure 6.4 shows the fitted answer and its error on (p_π, θ_π) plane.

6.1.5 Prediction of the neutrino energy spectrum

Basically the neutrino flux from pions with (p_π, θ_π) is calculated by the Formula 3.3. Each neutrino flux at the near or the far site is made from corresponding (p_π, θ_π) bin, with following two assumptions;

- Flat population inside the each (p_π, θ_π) bin.
- The same spatial distribution of the pion as the one from beamMC.

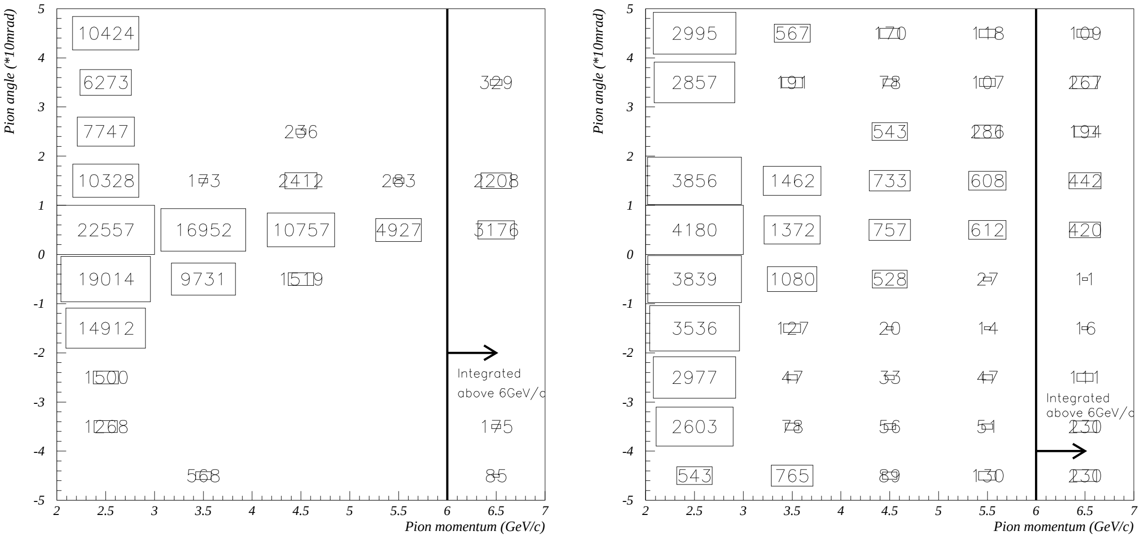

Figure 6.4: Fitted results of pion kinematic distribution, the center value (left figure) and their error (right figure) in Nov. run. These values are arbitrary numbers.

Systematic errors from these assumptions are discussed in next Section 6.1.6. Then, all the contributions from (p_π, θ_π) are summed up to predict the neutrino spectrum at near and far site, and lead to the flux ratio.

The neutrino flux contribution from the decay before PIMON, are added. This is estimated by beamMC. Amount of this is about 7% and 10% of the total flux in the near site and the far site, respectively. The uncertainty is also discussed in next Section 6.1.6.

Left figure of Figure 6.5 shows the predicted neutrino energy spectrum in Nov. run. The simulated spectrum based on beamMC with Cho model (see Chapter 4.1.2) is overlaid. Although absolute scale is arbitrary, beamMC well reproduced the predictions based on PIMON reconstruction above 1 GeV.

Right figure of Figure 6.5 shows the ratio of far and near flux (Φ_{far}/Φ_{near}) as a function of the neutrino energy. This energy dependence is explained by following reasons.

- Low energy neutrinos are produced from low energy pions, which decay at relatively upstream of the decay section. On the contrary, high energy pions decay at relatively downstream. It gives the larger acceptance of neutrinos for near detector.

- High energy pions have small decay angle. It gives the larger acceptance of neutrinos for far site.

Energy integration of these ratio gives the total flux ratio (Φ_{far}/Φ_{near}) used in Formula 2.2.

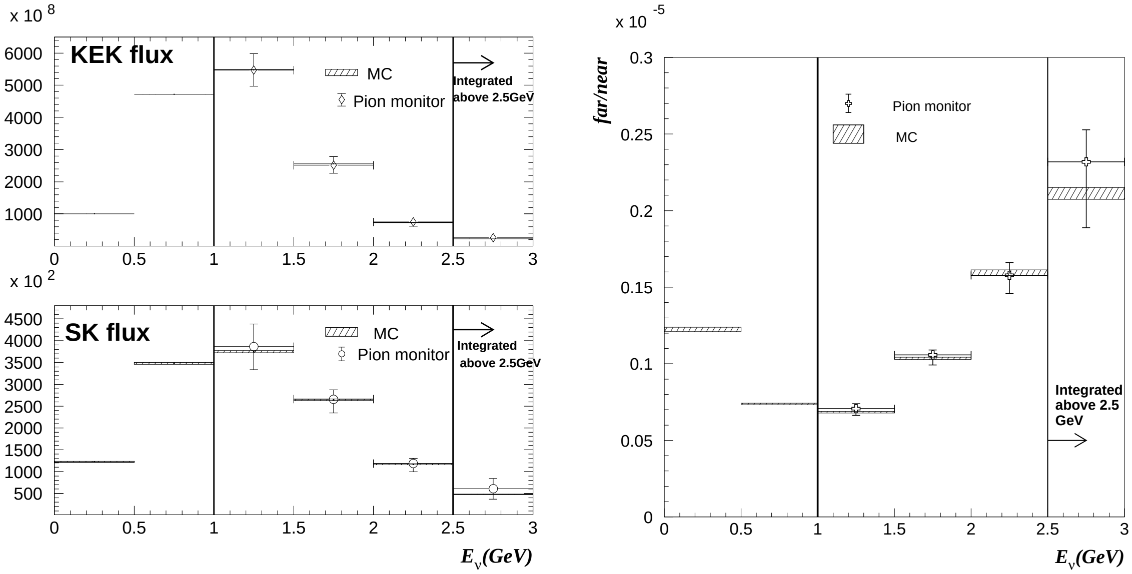

Figure 6.5: Left: Prediction of the neutrino energy spectrum at near and far site in Nov. ($I_{horn} = 250$ kA). Neutrino flux above 2.5 GeV is integrated. Standard beamMC based on Cho model is overlaid. Normalization is done by the entry above 1 GeV, which are arranged to the expected number of "neutrinos/cm^2/10^{20}p.o.t." Right: Prediction of the flux ratio of far and near (Φ_{far}/Φ_{near}) as a function of energy, in Nov. run. Standard beamMC based on Cho model is overlaid. In both figure, error bars include all the systematic errors, which are described later.

These figures again show the agreement between PIMON prediction and the beamMC. Hereafter we use the flux ratio and the energy spectrum shape estimated with this simulation, for the analysis in following chapters.

Figure 6.6 shows the neutrino spectrum and ratio compared with the simulation based on GCALOR/FLUKA model. This model gives fairly different spectrum and flux ratio from Cho model. PIMON measurement strongly suggests the Cho model.

We also emphasize that the difference of the flux ratio below 1 GeV is small because it is mainly determined by the geometry of the decay section. Therefore, the uncertainty of the flux ratio in this range is assigned from the difference of these expectations from the beamMC.

6.1.6 Systematic error of the energy spectrum and Far/Near ratio

Various systematic errors were estimated on these PIMON analysis. They are summarized in Table 6.2 and 6.3 for Nov. run. They are explained in following section.

Nov. 1999		Errors on spectrum at near			
	Energy bin (GeV)	1 − 1.5	1.5 − 2	2. − 2.5	> 2.5
1	Fitting error	±6.2%	±4.8%	±7.7%	±12%
2	Mirror reflectivity	−2.0%	+2.9%	+3.4%	+0.6%
3	Refractive index uncertainty	−5.1%	+7.3%	+4.6%	+37%
4	Low and high beam intensity	−1.2%	+0.6%	+4.0%	+5.0%
5	Beam stability (PIMON run)	—	—	—	±5.5%
6	ϕ asymmetry of the HORN field	−3.6%	+5.2%	+0.7%	+10.6%
7	PIMON alignment	—	—	—	—
8	Proton injection point	—	−2.0%	—	−4.8%
9	MIRROR-OFF subtraction	—	—	—	—
10	Electro-magnetic subtraction	—	—	—	—
11	Fitting method	+6.8%	−7.7%	−15.3%	$^{+12\%}_{-21\%}$
12	Pion decay before PIMON	—	±0.8%	±0.5%	—
13	Radial distribution of pions	±0.5%	±1.0%	±4.3%	±20%
14	Kinematic bin of pions	+2.7%	−2.4%	−7.0%	−10.0%
		+9.1%	+10.7%	+11.3%	+47.3%
	Total	−9.5%	−9.7%	−17.7%	−33.8%

Nov. 1999		Errors on spectrum at far			
	Energy bin (GeV)	1 − 1.5	1.5 − 2	2. − 2.5	> 2.5
1	Fitting error	±8.1%	±4.9%	±7.6%	±12%
2	Mirror reflectivity	−3.1%	+1.8%	+4.0%	—
3	Refractive index uncertainty	−8.6%	+5.4%	+1.1%	+33%
4	Low and high beam intensity	−2.1%	−1.5%	+3.1%	+7.8%
5	Beam stability (PIMON run)	—	—	—	±4.8%
6	ϕ asymmetry of the HORN field	−5.7%	+2.5%	+0.7%	+9.8%
7	PIMON alignment	—	—	—	—
8	Proton injection point	—	—	—	−4.9%
9	MIRROR-OFF subtraction	—	—	—	—
10	Electro-magnetic subtraction	—	—	—	—
11	Fitting method	+11.0%	−10.2%	−12.3%	$^{+1.6\%}_{-32\%}$
12	Pion decay before PIMON	±0.5%	±1.5%	±1.1%	—
13	Radial distribution of pions	±0.5%	±0.5%	±3.1%	±10%
14	Kinematic bin of pions	+0.5%	−2.4%	−5.4%	−15.4%
		+13.7%	+8.1%	+9.8%	+38.9%
	Total	−13.6%	−11.8%	−15.7%	−39.5%

Table 6.2: Systematic errors of neutrino spectrum at near and far detector in Nov. run.

Errors on flux ratio (Nov. 1999, HORN current 250 kA)

	Energy bin (GeV)	$0 - 0.5$	$0.5 - 1$	$1 - 1.5$	$1.5 - 2$	$2. - 2.5$	> 2.5
1	Fitting error			$^{+2.2\%}_{-2.9\%}$	$^{+2.2\%}_{-2.1\%}$	$^{+3.2\%}_{-2.9\%}$	$^{+1.0\%}_{-0.9\%}$
2	Mirror reflectivity			-1.2%	-1.1%	$+0.5\%$	—
3	Refractive index uncertainty			-3.7%	-1.8%	-3.3%	-2.6%
4	Low and high beam intensity			-1.9%	-3.7%	-1.9%	$+2.9\%$
5	Beam stability (PIMON run)			—	—	—	$\pm 0.5\%$
6	ϕ asymmetry of the HORN field			-2.6%	-2.4%	-2.4%	-1.0%
7	PIMON alignment			—	—	—	—
8	Proton injection point			—	$+1.2\%$	—	—
9	MIRROR-OFF subtraction			—	—	—	—
10	Electro-magnetic subtraction			—	—	—	—
11	Fitting method			$+4.0\%$	$^{+1.4\%}_{-3.0\%}$	$^{+3.2\%}_{-4.6\%}$	-14.5%
12	Pion decay before PIMON			$\pm 0.7\%$	$\pm 0.7\%$	$\pm 1.7\%$	$\pm 0.5\%$
13	Radial distribution of pions			—	$\pm 0.5\%$	$\pm 1.3\%$	$\pm 8.5\%$
14	Kinematic bin of pions			$\pm 2.1\%$	—	$+1.7\%$	-7.1%
15	Hadron model (MC)	$^{+5.1}_{-9.5}\%$	$^{+7.3}_{-2.5}\%$				
		$+5.1\%$	$+7.3\%$	$+4.6\%$	$+2.9\%$	$+5.3\%$	$+9.1\%$
	Total	-9.5%	-2.5%	-6.2%	-6.2%	-7.4%	-16.2%

Table 6.3: Systematic errors of neutrino flux ratio (Φ_{far}/Φ_{near}) in Nov. run.

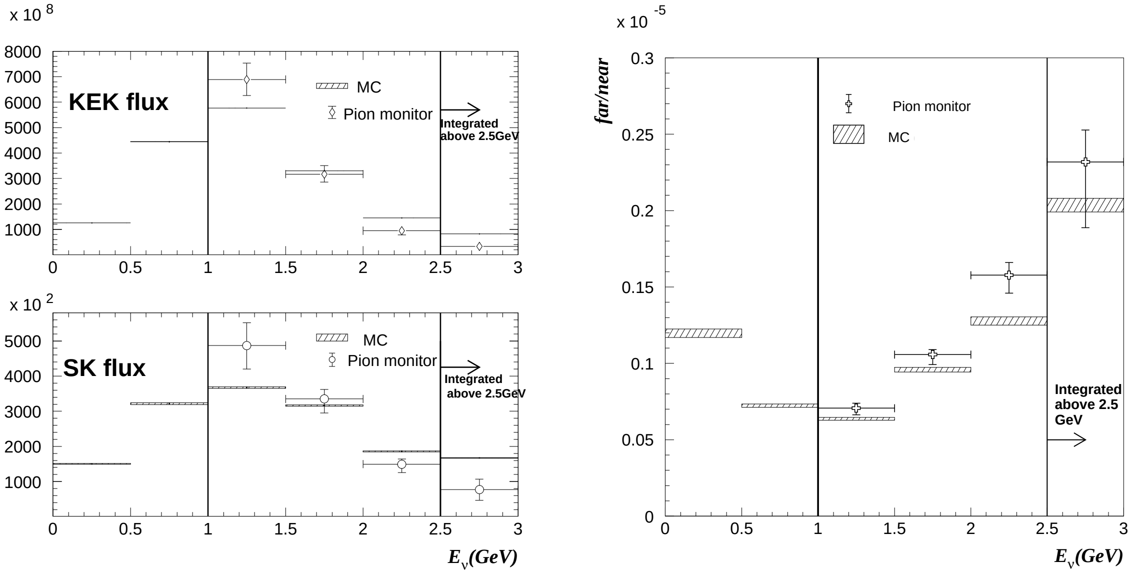

Figure 6.6: Comparison with the simulated neutrino spectrum and Far/Near ratio using GCALOR/FLUKA model, in Nov. run ($I_{horn} = 250$kA). Notations are same as Figure 6.5.

1. **Fitting error.**
   The error listed in Section 6.1.2 are assigned for each data point of the Cherenkov distributions. The fit of Cherenkov distributions gives the fitting errors on the (p_π, θ_π) distribution (shown in Figure 6.4). For the error estimation, we randomly change the (p_π, θ_π) distribution within the fitting errors, and predict the neutrino spectrum and the flux ratio from various (p_π, θ_π) distribution. The differences of the results are quoted as the systematic errors of the fitting error.

2. **Mirror reflectivity.**
   The laser system confirms the mirror reflectivity suffered no damage within ±6% during both 1999 run. The systematic error is assigned based on the difference of the results considering a few percent deterioration around the beam center.

3. **Refractive index uncertainty.**
   The major uncertainty of the refractive index comes from the wavelength dependence as shown in Figure 3.12. Two simulations are compared. One includes this wavelength dependence down to 160 nm, and the other is the standard one with particular index calibrated by the primary proton threshold (Figure 3.14). The difference is quoted as the systematic error.

4. **Difference between the low and high beam intensity.**
   In Nov. run, both of the horizontal and vertical profile of proton beam were about

20 $\sim$ 30% narrower from the normal run. Systematic errors are assigned based on the comparison between these simulations with two profiles.

5. **Beam stability during the PIMON measurement.**
   Proton beam was monitored using two SPICs (V39-SPIC and TARGET-SPIC). The fluctuation of the proton beam center is about 0.1 $\sim$ 0.2 mm during the PIMON run. Secondary muon yield was also monitored by SPDs. They show the rate stability was 1.4% and the profile center was stable within ± 1 cm. Various simulations are performed with the various proton injection according to these fluctuation. They provide the systematic error.

6. **Azimuthal angular symmetry (ϕ symmetry) of the magnetic field inside the HORN magnet.**
   Since the spherical mirror samples small (12 degree) azimuthal region, PIMON analysis is affected by the azimuthal asymmetry of the pion distributions.

   Systematic errors are assigned based on the comparison between the beamMC with 15% of 4-fold asymmetric field and the original one.

7. **Alignment of the PIMON with respect to the beam line center.**
   PIMON is well aligned to the beam line. An optical survey ensures that, the height of the mirror is aligned within 1 mm, and the horizontal position is precisely adjusted within a few hundred μm from the designed beam axis. Systematic errors from this are negligible.

8. **Proton injection point to the target.**
   Secondary beam axis in normal neutrino run is monitored by the proton profile center measured by SPICs and the muon profile center at MUMON. For PIMON run, the profile center of the proton is same within 1 mm compare to the normal run. Muon profiles measured by SPD have less than 10 cm shift compared to the normal run, which confirms that the proton injection point is within 1 mm in Nov. The systematic error is estimated by the beamMC study in both case.

9. **Systematic error of MIRROR-OFF subtraction.**
   We took the data with the mirror rotation up to 14.5 degree off from the nominal direction. It proves that the background components are uniform. Estimated systematic errors are negligibly small.

10. **Electro-magnetic component subtraction.**
    BeamMC well reproduces the shape of contributions from electro-magnetic components. Therefore the systematic error is estimated by changing the normalization factor by $+1\sigma$ of χ^2 from the best fit. This error mainly affects to the distribution of

high momentum pions, which corresponds to high energy neutrino flux. The error is negligibly small in Nov.

11. **Fitting method.**
    Monte Carlo test is performed to confirm the analysis method. Simulated Cherenkov photon distributions are analyzed to extract the (p_π, θ_π) distribution, and to predict the neutrino spectrum and the flux ratio. These "results" are compared with fully-simulated distributions by same beamMC as Cherenkov photon simulation.

    For this Monte Carlo test, three beamMC is used. One is the standard beamMC with Cho model, with the HORN current of 250 kA. Another is the beamMC with GCALOR/FLUKA hadron model, with 250 kA. The other is the beamMC with Cho model, with the HORN configuration of Jun.99 run (200 kA). The largest difference is quoted as the error due to the fitting method.

12. **Decayed pions before PIMON.**
    Uncertainty of the contribution of pion decay before PIMON, is estimated by comparison between the beamMC with Cho and GCALOR/FLUKA model.

    Neutrinos from kaons are order of 10^{-2} of these from pions. Thus the error from the kaon contributions is neglected.

13. **Radial distribution of pions.**
    Radial distribution of the pions affects to the decay probability due to the finite decay volume. The difference of neutrino prediction from the beamMC with Cho and GCALOR/FLUKA models is assigned as the systematic error.

14. **Kinematic bin size in (p_π, θ_π).**
    Inside of the (p_π, θ_π) bin, flat population is assumed. Systematic bias from this assumption is estimated by comparing the spectrums of full simulation with the spectrums which are predicted from the (p_π, θ_π) distribution given by same beamMC.

15. **Uncertainly of the neutrino flux below 1 GeV.**
    BeamMC is used for the neutrino flux and flux ratio below 1GeV. Error of the neutrino spectrum is quoted as ±100% which is well within 1kt measurement (see Chapter 8.3.1). Error of the flux ratio is estimated by the beamMC by changing the parameters at the formula 4.4 within 90% C.L. of pion production experiments.

6.2 Stability of the Proton Beam

6.2.1 Proton beam profile measurement

Proton targeting are continuously monitored by two SPICs; V39-SPIC and TARGET-SPIC, which are located in front of the target (Figure 3.1 and Figure 4.1). Typical proton profile measured by these SPICs are shown in Figure 6.7. Transported proton beam has Gaussian like distribution in x and y projection, with certain offset caused by pedestal level fluctuation.

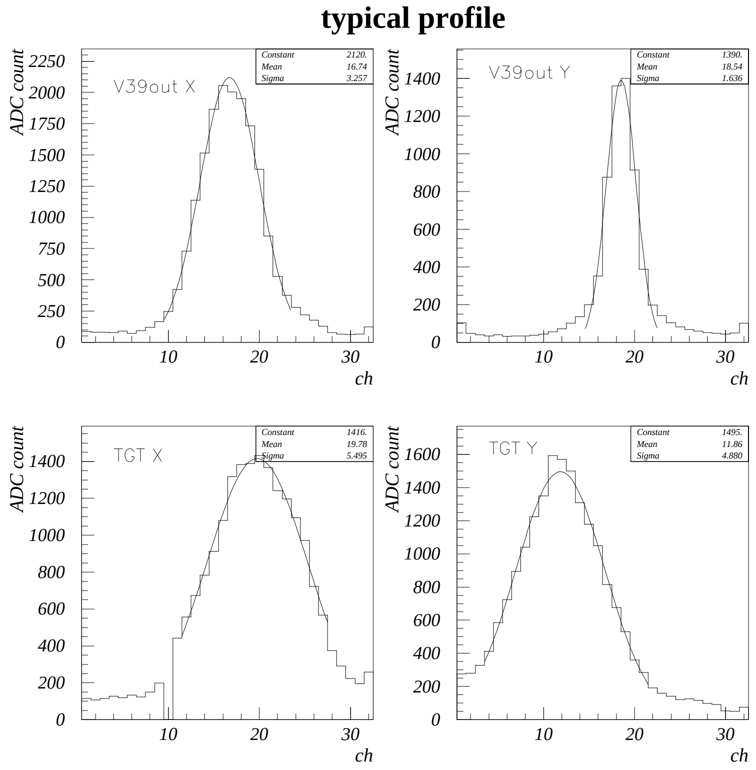

Figure 6.7: Typical proton profile measured at V39out-SPIC (upper) and TARGET-SPIC (lower) in Nov. 1999 run. Gaussian fit is also shown. 1 channel corresponds to 5 mm for V39out-SPIC and 1.27 mm for TARGET-SPIC. For these SPIC, small channel number corresponds to the Southern or bottom side.

Stability of these proton profiles is studied by following two steps.

1. **Spill-by-spill fluctuation.**
   Analysis procedure is explained in Figure 6.8. Simple mean position and r.m.s. of the

proton profile are studied on spill-by-spill basis. When the proton beam is shifted, the mean value changed. The mean and r.m.s. of V39-SPIC and TGT-SPIC are analyzed on each 100 spills (which correspond to one sub-run of beam line DAQ). Figure 6.8 exhibits the spill-by-spill fluctuation is small enough to deal with summed profile of one sub-run.

2. **Periodical fluctuation.**
   The profile summed over each sub-run (100 spills) are fitted with Gaussian function plus linear offset. The fluctuation of these profile center (width) is less than ±5 mm (±25%) at V39-SPIC and less than ±3 mm (±20%) at TGT-SPIC during the whole run.

   Stability of the proton targeting is obtained from the extrapolation of these proton beam profiles. Proton beam width and the divergence at the target are calculated with Formula 4.1 and 4.3, as described in Chapter 4.1.1, in each period. And the fluctuation of the beam center δx and the injection angle $\Delta\theta_x$ are calculated with following formula;

   $$\begin{aligned} \text{center shift} : \delta x &= \Delta x_2 + (\Delta x_2 - \Delta x_1) \cdot (\ell / L) && (6.1) \\ \text{angle shift} : \Delta\theta_x &= (\Delta x_2 - \Delta x_1)/L && (6.2) \end{aligned}$$

   where, Δx_1 and Δx_2 are the center shift from the nominal point, for V39-SPIC and TGT-SPIC, respectively. With same formula, δy and $\Delta\theta_y$ are also calculated.

   Figure 6.9 shows the time variation of these proton beam properties, and their projection.

The effect to the analysis, that is the event ratio of each detectors, from these targeting uncertainty is studied using beamMC in following sub-sections.

6.2.2 Injection angle dependence

Neutrino flux is simulated with pencil-like proton beam (no profile spread, and no divergence) with injection angle of 0, 2, 4, and 6 mrad with respect to the nominal beam axis. Table 6.4-A shows the relative numbers of observed events in 1kt, MRD, and SK, and their ratio. The fluctuation of the injection angle is ±1.8 mrad and ±0.8 mrad by r.m.s. of x and y, shown in Figure 6.9. And the typical emittance spread which is neglected in Chapter 4.1.1 is also several mrad. The study proves that the injection angle of several mrad makes negligible effect for the event ratio of Far/Near.

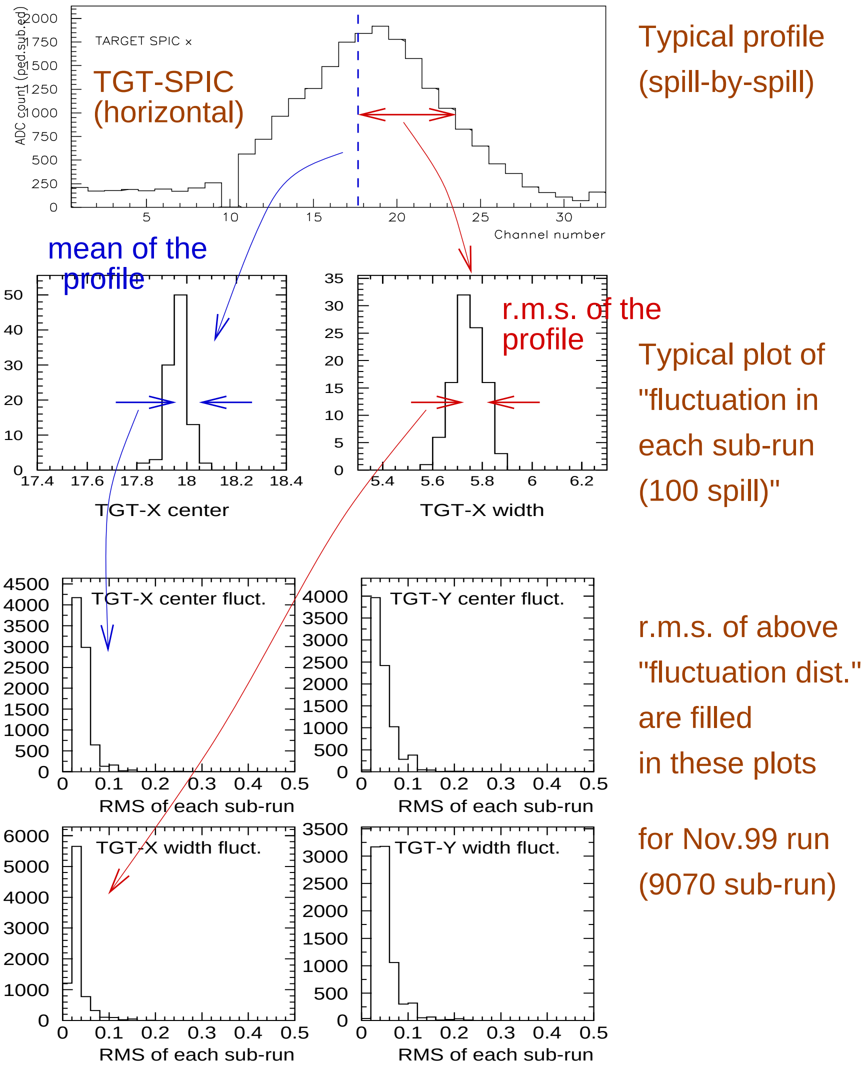

Figure 6.8: Spill-by-spill stability of the profile center and width of TGT-SPIC. Top figure is the typical proton profile measured by TGT-SPIC (horizontal). The mean and standard deviation (r.m.s.) of this plot is filled to the second histograms of "fluctuation distribution" in each sub-run. Then, r.m.s. of these "fluctuation distribution" means the spill-by-spill stability of profile center and profile width, analyzed for each sub-run. This values in Nov.99 run are filled to the lower four histograms. They are x-profile center (left-top), width (left-bottom), y-profile center (right-top), and width (right-bottom) of TGT-SPIC data. Unit of horizontal axis is channel, which is 1.27 mm spacing. These results show the proton profile is quite stable in each sub-run (100 spills).

(A) Injection angle dependence

Injection angle (mrad)	0	2	4	6
1kt	1.	1.01	1.01	0.99
MRD	1.	1.01	1.01	0.99
SK	1.	1.00	1.00	1.00
MRD/1kt	1.	1.00	1.00	1.00
SK/1kt	1.	1.00	0.99	1.01
SK/MRD	1.	1.00	0.99	1.00

(B) Injection point dependence

Center shift (mm)	0	2	4	6
1kt	1.	0.99	0.96	0.94
MRD	1.	0.99	0.96	0.94
SK	1.	0.98	0.95	0.94
MRD/1kt	1.	1.00	1.00	1.00
SK/1kt	1.	0.99	0.99	1.00
SK/MRD	1.	0.99	0.99	1.00

(C) Profile width, divergence dependence

	config-1	config-2
Width σ_x (mm)	3.4	2.3
Width σ_y (mm)	7.2	5.0
Slope k_x (mrad/mm)	-2.5	-4.0
Slope k_y (mrad/mm)	-0.14	-0.36
1kt	1.	1.04
MRD	1.	1.07
SK	1.	1.06
MRD/1kt	1.	1.02
SK/1kt	1.	1.02
SK/MRD	1.	1.00

Table 6.4: Proton targeting dependence of the observed events.
Proton targeting dependence of the observed events, estimated by beamMC. These numbers are the relative number of observed events in each detector and their ratio. For injection angle dependence study (A), monochromatic pencil proton beam was injected to the target, whereas, for other studies, standard beamMC was used. In Table-C, config-1 means the default beamMC, and config-2 is the configuration which is based on another profile estimation (see text).

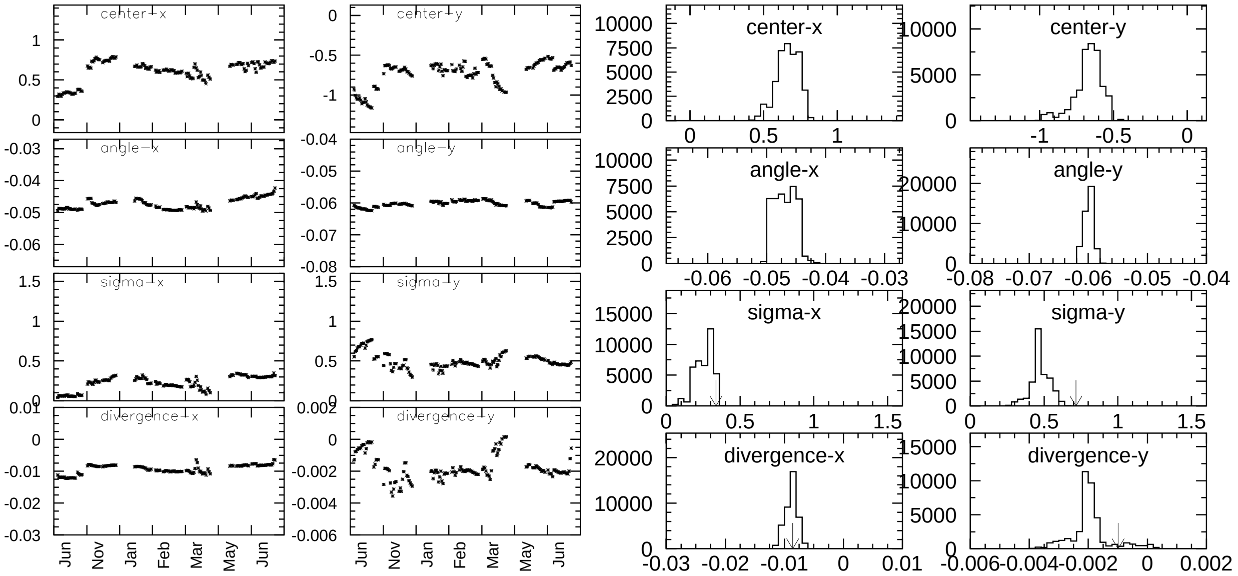

Figure 6.9: Stability of the proton profile in front face of the target from 1999 to 2000. Left figures are the history plot. One data point means the average of half day. In Jun.99, relative geometry of TGT-SPIC was a little different from the other period. Right figures are their projection from Nov.99 to Jun.00. Every fitted result is filled in the histograms.

6.2.3 Injection point dependence

This is studied with beamMC with standard profile (Table 4.1) and the several injection point of 0, 2, 4, and 6 mm shift from the nominal center of the target. Table 6.4-B shows the result of the relative number of events. The fluctuation of the injection center is 0.8 mm and 0.9 mm by r.m.s. of x and y shown in Figure 6.9. This causes negligible effect within 1% for the event ratio of Far/Near.

6.2.4 Profile width and divergence dependence

As described before, profile width and the divergence are calculated from the observed proton profile width at V39-SPIC and TGT-SPIC, typically shown in Figure 6.7. Two analyses are performed to fit the proton profile.

1. configuration-1
   One is the fit with Gaussian function. Fitted profiles give us the parameter set of proton width and the divergence at the target, which are shown as ”config-1” in Table 6.4-C. These parameters are used for standard beamMC (Table 4.1).

2. configuration-2
   The other is the fit with Gaussian plus linear offset as noted above. This fitting

function is attempted to eliminate the flat background due to the electrical noise. The obtained parameters are called "config-2" as shown in Table 6.4-C.

Two simulations are performed with these two parameter sets. The results are also shown in Table 6.4 (lower table). They shows the difference of the event ratio Far/Near is $\pm 1 \sim 2\%$ level, which is quoted as the systematic error due to the fitting method.

The periodical fluctuation of the profile width and the divergence shown in Figure 6.9 is smaller than this discrepancy from the fitting method difference. Therefore, fitting method error is adopted as the systematic error of the profile width and the divergence.

6.2.5 Systematic errors due to the proton targeting

Proton is transported along the designed trajectory. Therefore, the injection angle is given with the accuracy of comparable to the time fluctuation. When proton injection point is 1 mm shifted, the muon profile at MUMON is about 10 cm shifted, due to the magnetic field in side of the HORN [50]. Proton beam is controlled being monitored the muon profile (described in next subsection), in addition to the proton profiles at SPICs. Therefore, the injection point is confirmed with the accuracy of comparable to the time fluctuation. In addition, neutrino profile center is continuously measured by MRD in Chapter 7.3, and the systematic error of the neutrino beam direction is estimated there. Hence, systematic errors due to the injection angle and the injection point are assigned from their time fluctuation estimated in this section.

In summary, estimated systematic errors from the proton targeting are shown as follows;

systematic errors	for MRD/1kt	for SK/1kt	for SK/MRD
Injection angle	$\pm 0.0\%$	-0.3%	-0.3%
Injection center	$\pm 0.0\%$	-0.8%	-0.8%
width, divergence	$+2.1\%$	$^{+1.6\%}_{-1.0\%}$	$^{+0.9\%}_{-1.4\%}$
Quad.-sum	$^{+2.1\%}_{-0.0\%}$	$^{+1.6\%}_{-1.3\%}$	$^{+0.9\%}_{-1.6\%}$

6.3 Stability of the Muon Profile Center

Muon profile information measured by MUMON is used for beam steering during the whole run. Stability of the muon profile center gives the spill-by-spill stability of the neutrino beam direction, which supports the neutrino beam measurement at MRD. Figure 6.10 shows the typical profiles measured by MUMON-SPD and MUMON-ICH, after pedestal subtraction and gain correction.

The time variation of this fitted center is analyzed in following two steps like proton profile case in previous section.

1. First, spill-by-spill fluctuation of the mean of the profile in every 100 spill (one subrun) is analyzed. Although this simple mean has less than half sensitivity of fitted center motion, it follows the actual shift. Figure 6.11 shows no obvious fine fluctuation. This fact confirms the next step of Gaussian fit after the integration of 100 spills.

2. After taking 100 spill average of the profile, ICH profile is fitted with Gaussian function, while SPD is fitted with asymmetric Gaussian function, in order to obtain profile center. Figure 6.12 shows time variation of the fitted center from Jun.99 to Jun.00. They show profile center is always distributed around the designed direction within 1 mrad. Fitted center of SPD profile is also directed to the expected direction within 1 mrad in all the time period, while SPD pad information may be different from the x,y projections of profile in ICH.

These results confirm that neutrino is continuously pointed to the intended direction to Super-Kamiokande.

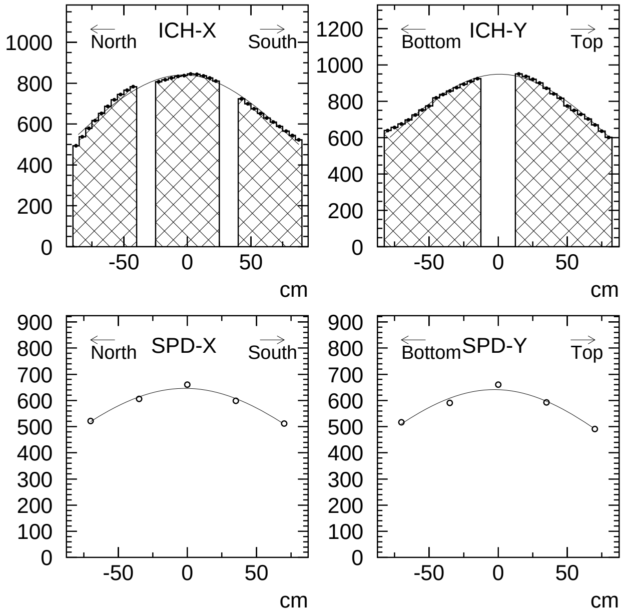

Figure 6.10: Typical muon profile of MUMON-ICH (top) and MUMON-SPD (bottom) in Jan. 2000 run. Left two show the horizontal direction and right two show the vertical direction. Vertical axis is the corrected ADC count, which is already applied pedestal subtraction and gain correction. This profile is averaged over 100 spill. Both profiles are fitted with Gaussian function, in order to obtain profile center.

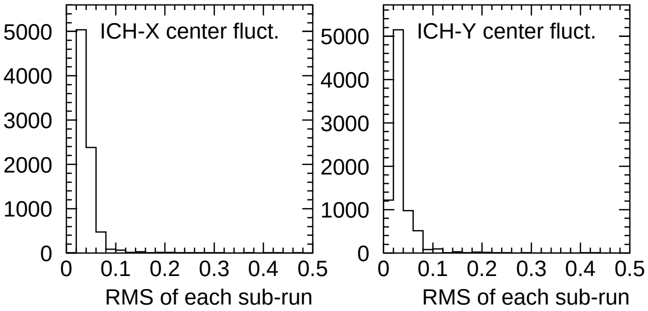

Figure 6.11: Spill-by-spill fluctuation of the mean of MUMON-ICH profile in Nov.99 run.

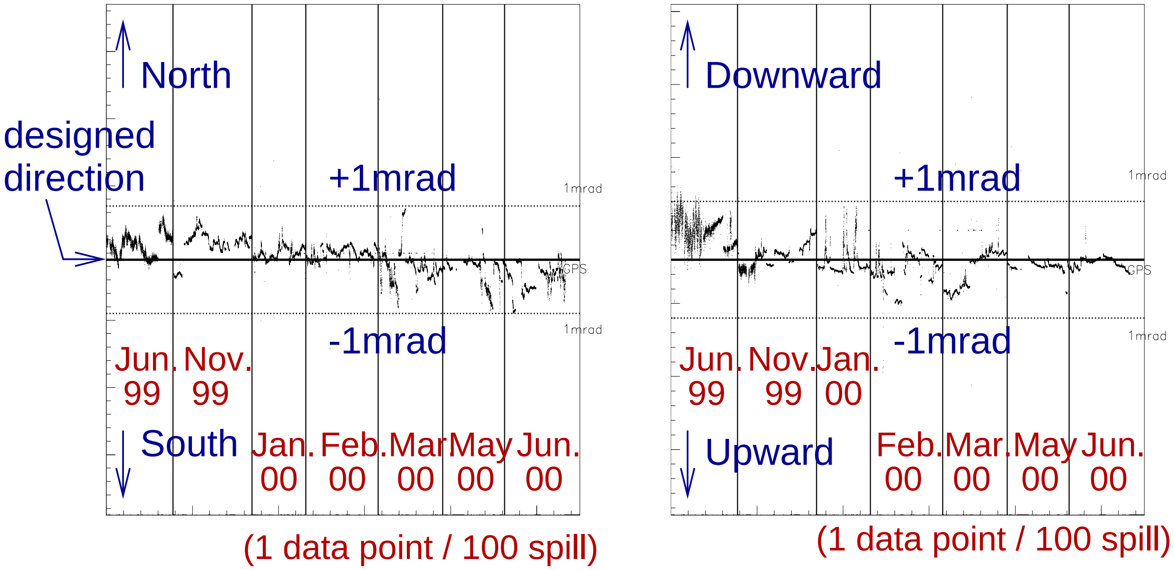

Figure 6.12: Time variation of the muon profile center measured by MUMON-ICH. Left figure shows the center of horizontal (x) direction. Right figure shows the center of vertical (y) direction. Middle solid line is the designed center toward Super-Kamiokande. Two dotted line means ±20 cm (1 mrad from the target) shift. One data point corresponds to the every 100 spill integration.

Chapter 7

Neutrino Beam Measurement

7.1 Neutrino Event Selection at MRD

7.1.1 Overview of the MRD analysis

Neutrino events in Muon Range Detector (MRD) is analyzed to confirm the neutrino beam direction and the stability of the neutrino flux. For these purposes, vertex profile, event rate and the produced muon distribution are analyzed throughout the whole run.

Figure 7.1 shows the typical neutrino event interacted in the iron plate in MRD. Such a neutrino induced muon track is reconstructed by a track finder.

7.1.2 Overview of the track finder

The track finder consists of the four part, "Cell fit", "Fragment fit", "2-D fit", and "3-D fit", working in this order. They are summarized as follows, and detailed algorithm is described in Appendix A.

1. First, noise hits are rejected which is mainly caused by the electronics. This removes typically 20 of noise hits per each one spill data.

2. Cell fit connects all the combination of two hits in X-view (top view) or Y-view (side-view) independently, and makes evaluation of the track to select reliable ones.

3. Fragment fit divides the "cell-fit track" into "fragments" which have more than 3 hits in 4 drift-tube planes[1] Each fragment is fitted with a linear line, considering the drift time from the reconstructed time of particle arrival (called "Time-zero": T_0).

---

[1] The word "plane" means the transversely aligned cells in the given z-position. That is, there are two X-planes and two Y-planes between the neighboring iron plates.

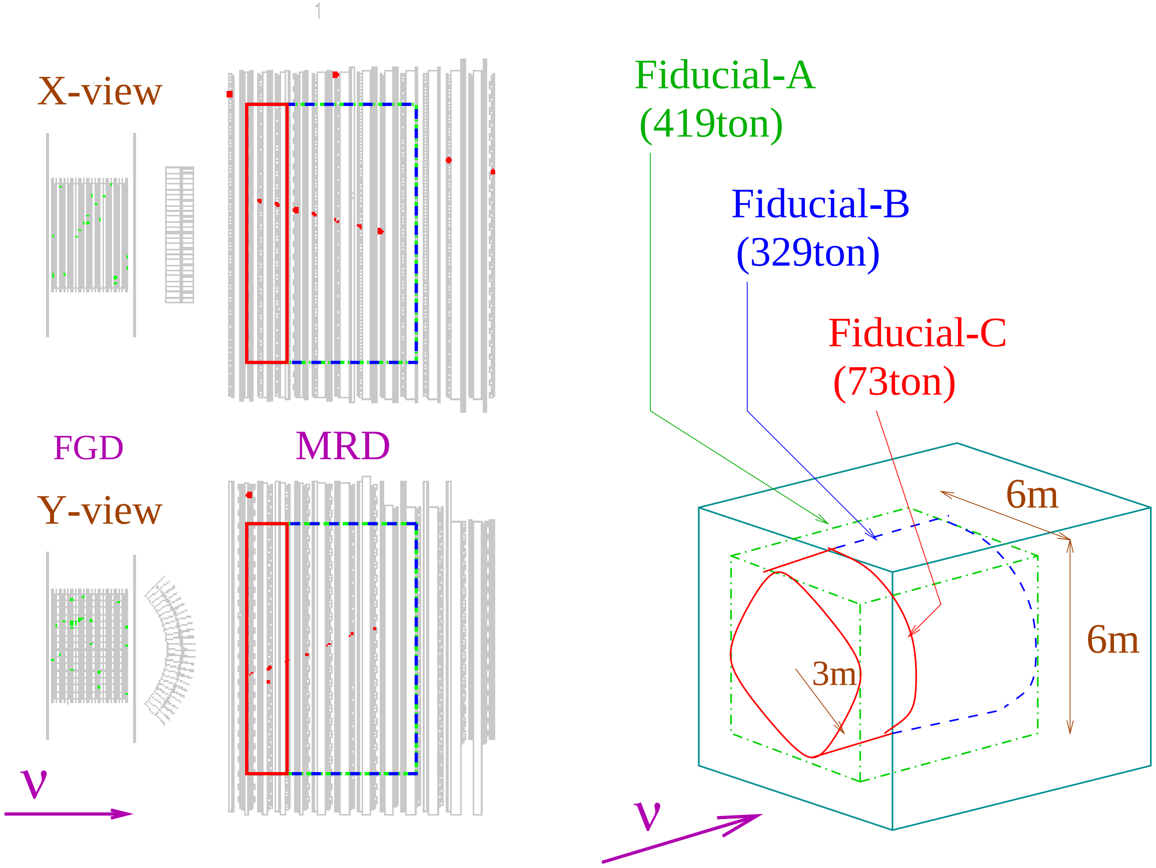

Figure 7.1: The typical MRD event. Hit channels are expressed by closed circles. Noise hits are already removed. Three fiducial volumes are also indicated.

4. 2-D fit connects these fitted fragments from the most upstream fragment to the downstream fragments, with adopting the best combination based on the distance and angle between each fragments.

5. 3-D fit combines a 2-D track in X-view and another 2-D tracks in Y-view. It selects from the longest overlap length along the beam axis. Finally these 3-D tracks are used to various analysis as the muon track candidate in MRD. Start point, end point, path length and track directions are also calculated. Muon energy is calculated from the path length in the iron.

Fitted tracks are good agreement with the eye scan. As a result, typically 0.2 tracks are found in one spill. Tracking efficiency is discussed in latter section.

7.1.3 Neutrino event selection

The fitted tracks are mainly neutrino-induced muons. For quantitative study of the event rate and the muon distribution, we have to select muon tracks contained in the MRD, and whose vertices are in the fiducial volume.

Three fiducial volumes of the iron target are defined inside of MRD. Figure 7.1 shows their geometry.

- **Fiducial-A.**
  The largest cubic volume is used for neutrino profile measurement. This has 6m × 6 m transverse area and from 1 to 9-th iron plate longitudinally (1.4 m total thickness). Total amount of iron mass is 419 ton.

- **Fiducial-B.**
  This large volume is used for the neutrino beam stability monitor. This is the cylinder of 6 m diameter and 1 to 9-th plate longitudinally. Total amount of iron mass is 329 ton.

- **Fiducial-C.**
  Quantitative analysis of the number of events and the muon distribution are performed using this upstream fiducial, in order to attain better efficiency. The 6 m diameter is same as Fiducial-B and the longitudinal length is limited from 1 to 3-rd iron plate (10cm thickness × 3 plate). Total amount of iron mass is 73 ton.

Figure 7.2 is the flow chart of the selection. Selection efficiencies of observed data and the Monte Carlo simulation (neutMC) are summarized in Table 7.1

1. **Consistency between X-view and Y-view.**
   First, some badly fitted tracks are rejected by considering the between a 2-D track in X-view and another 2-D track in Y-view. We require;

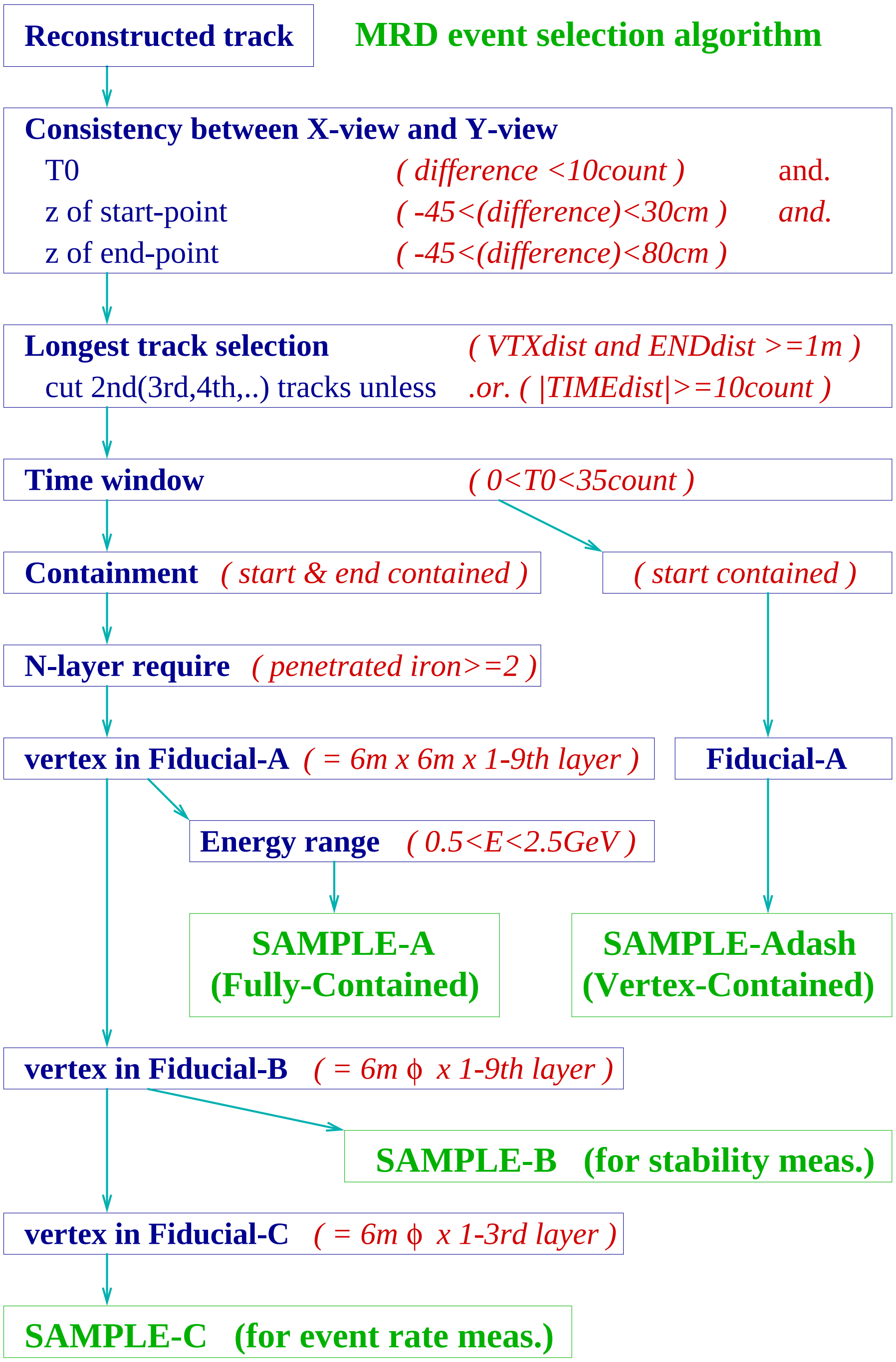

Figure 7.2: Flow chart of the event selection scheme. The selection of SAMPLE-A, SAMPLE-B, and SAMPLE-C are described in this section, while the SAMPLE-A-dash is explained in Appendix B.

- Difference of T_0 in X-view and in Y-view to be within 10 count (= 500 ns, Figure 7.3-A).
- Difference of the z-coordinate of the start point to be within -45 and 30 cm (Figure 7.3-B).
- Difference of the z-coordinate of the end point to be within -45 and 80 cm (Figure 7.3-C).

The effects of these cuts are about 10% and can be reproduced by neutMC.

2. **Longest track selection.**
When data are selected at least one track in one spill, about 14% of these spills have two or more tracks in same spill. Some of them are due to the multiple neutrino interactions. Others are considered to have associated short tracks near the long track. This is considered mainly due to the hadron activity around the vertex. In order not to count as the double neutrino interactions, such associated tracks are removed.

When two or more tracks remain in one spill, following three parameters are checked for all the two track combinations.

- Distance from start point of the second track to the first track ($VTXdist$).
- Distance from end point of the second track to the first track ($ENDdist$).
- Difference of T_0 ($TIMEdist$).

When

$$(VTXdist < 1 \text{ m or } ENDdist < 1 \text{ m }) \text{ and } |TIMEdist| < 10 \text{ count},$$

the shorter track[2] is removed. Figure 7.4 shows the typical distribution of the three parameters for data and neutMC which have two tracks in one spill. The simulation does not include multiple event in one spill. Therefore, in the simulation, more than 99% of the second tracks are removed. On the other hand, data can have some fraction of multiple events in one spill. Hence, 66% of the second tracks remain. The miss-rejection rate of the multi-event is estimated to be 13% by the study of random matching test of the selected tracks.

This cut acts as the conversion from number of tracks to number of neutrino interactions.

---

[2] In correct definition, the track with shorter overlap length between X-view and Y-view is removed. This track has mostly the shorter total length than the other track.

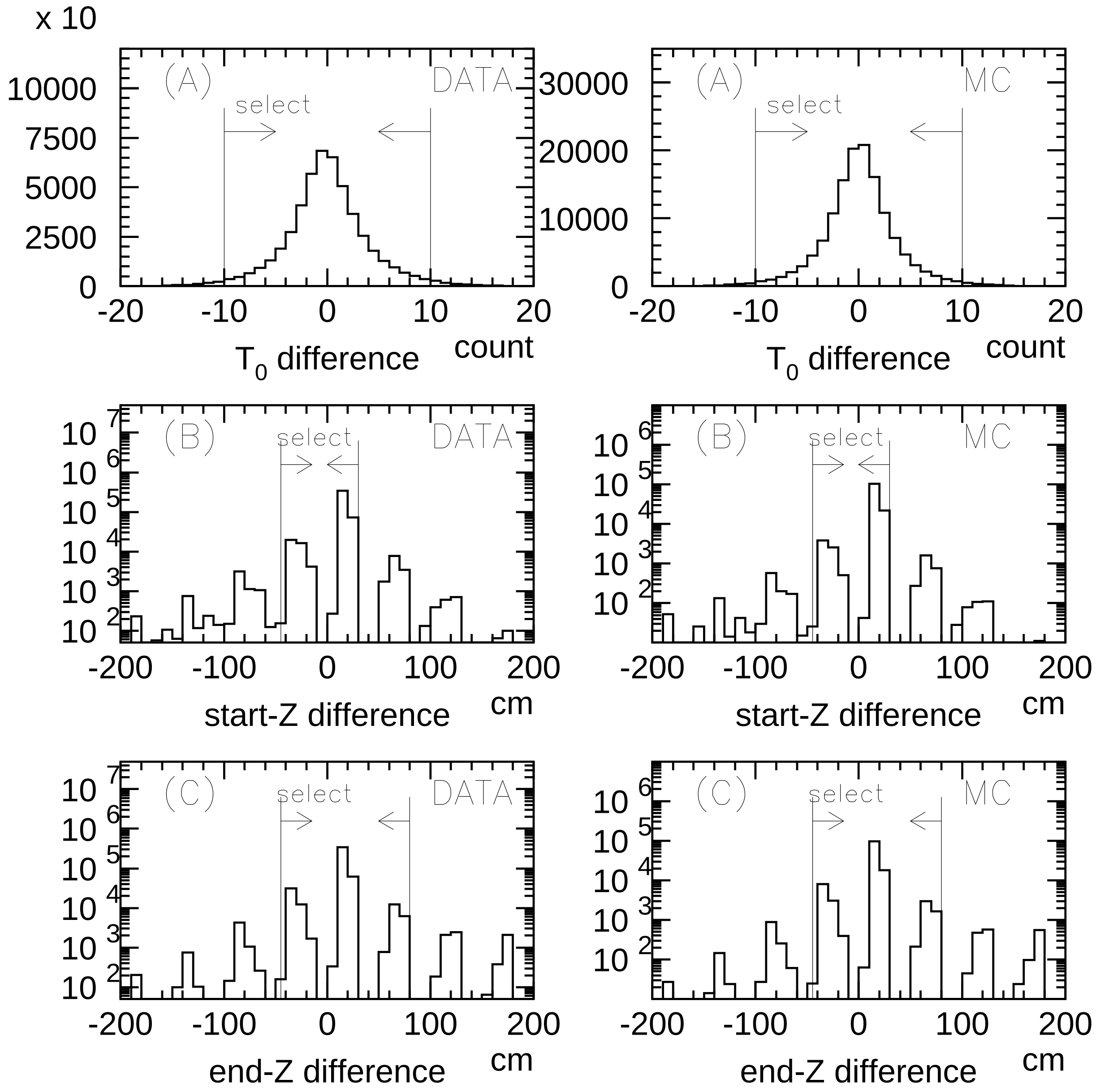

Figure 7.3: A: Difference of T_0 in X-view and in Y-view. B: Difference of z-coordinate of the start point in X-view and in Y-view. C: Difference of z-coordinate of the end point in X-view and in Y-view. In each plot, data (left) and neutMC (right) are compared. In these distributions, the events are already selected with requiring the vertex containment.

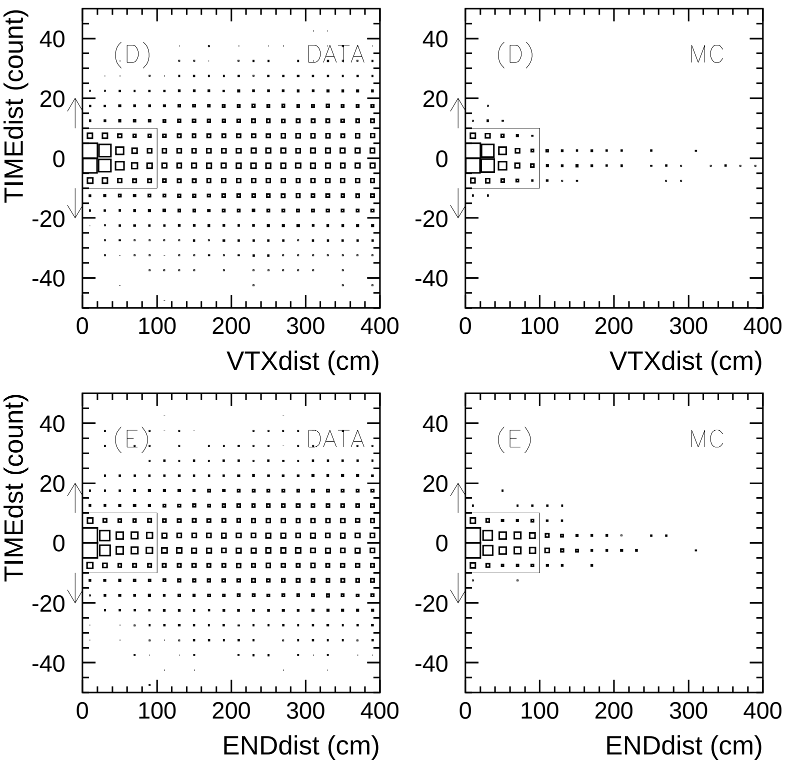

Figure 7.4: 2-dimensional distribution of $VTXdist$ or $ENDpoint$ and $TIMEdist$ for two track sample. Data and neutMC are compared.

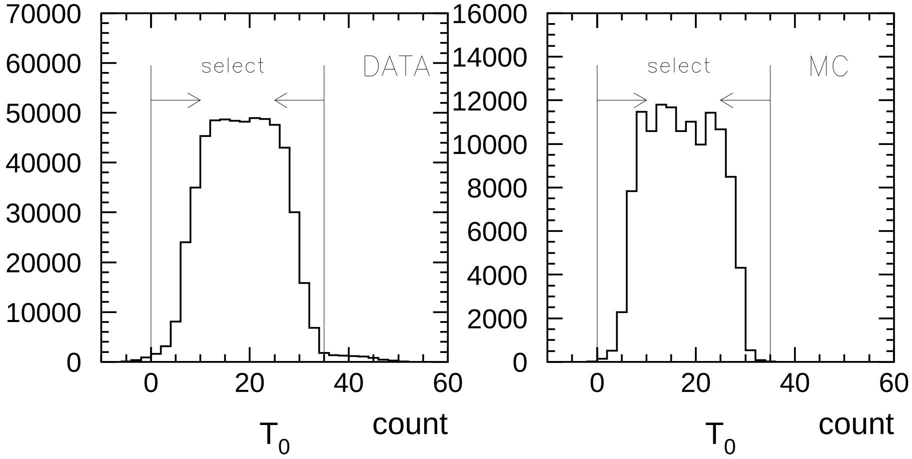

Figure 7.5: Reconstructed T_0 distribution.

3. **Time window**
   Because the data acquisition is synchronized with beam extraction timing, time window is adopted as $0 < T_0 < 35$ count (1.75μs width) to reject cosmic ray backgrounds and late timing activities supposed to be the sky-shine neutron activities. Figure 7.5 shows the T_0 distribution.

4. **Containment requirement.**
   Muon energy can be reconstructed only when its start and end points contain in the MRD, which is called "fully-contained" track. Therefore, fully-contained tracks are used for the analysis. When an associated hit exists at the first or last drift-tube layer, the track is discarded. To check entering or exiting from the side of MRD, start and end points are extrapolated one layer further in front side and back side. When the extracted point is more than 5 cm away from the any wire position, this track is judged as entering or exiting, and is excluded from the analysis.

5. **Number of penetration layer $N^{iron}_{layer} \geq 2$.**
   N^{iron}_{layer} is defined as the number of penetrated iron plates. In some portion of the short tracks contains the hit of hadron (p and π) activity. Then, tracks with $N^{iron}_{layer} \geq 2$ are used to keep safety side.

6. **SAMPLE-A,** for profile study.
   Large coverage is effective to analyze the profile center and the width. Therefore, Fiducial-A is adopted as the fiducial volume for profile study. The events whose vertices are in Fiducial-A are selected. This cubic Fiducial-A has relatively uniform

	selection	DATA		neutMC	
0	number of track	687599		141778	
1	Consistency of T_0	664244	(0.97)	138471	(0.98)
1	Consistency of start/end-point	600575	(0.90)	130137	(0.94)
2	Longest track selection	561321	(0.93)	123416	(0.95)
3	Time window	552853	(0.98)	123383	(1.00)
4	Containment requirement	274713	(0.50)	83450	(0.68)
5	$N_{layer} \geq 2$	192664	(0.70)	55700	(0.67)
6	Vertex in Fiducial-A	165125	(0.86)	47903	(0.86)
6	$0.5 < E_\mu < 2.5$ GeV				
	Sample-A	164935	(1.00)	47876	(1.00)
7	Vertex in Fiducial-B				
	Sample-B	144091	(0.87)	42056	(0.88)
8	Vertex in Fiducial-C				
	Sample-C	53294	(0.37)	15274	(0.36)

Table 7.1: Summary of the event selection process. DATA is the observed event from Nov.1999 until Jun.2000 run. MC event is only generated inside the iron plate, although DATA contains many beam-induced events from outside.

series of iron-drift-tube structure and enables us to avoid an inefficient area near the side of the detector. Tracks with less than 0.5 GeV energy or more than 2.5 GeV are not used, because their selection efficiency is low. For low energy muons, they do not pass more than 2 iron plates. For high energy muons, they do not contain inside of the detector.

7. **SAMPLE-B**, for the stability study of event rate and muon distributions.
   Since the neutrino flux has a radial dependence, cylindrical Fiducial-B and Fiducial-C are used for the event rate study and the muon distribution study. For the stability study, larger Fiducial-B is used, in order to gain the event statistics. The events whose vertices are in Fiducial-B are called "SAMPLE-B".

8. **SAMPLE-C**, for the event rate and muon distribution study.
   In order to obtain lower threshold energy and better acceptance, upstream Fiducial-C is used for quantitative study of the event rate, the muon energy spectrum, and the muon angular distribution. SAMPLE-C is required as whose vertex is in the first three iron plates with 10 cm thickness.

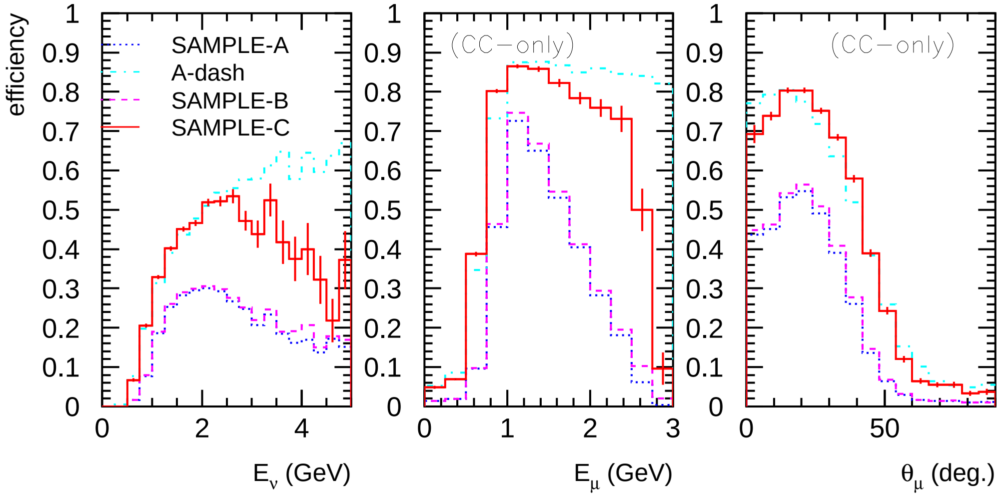

Figure 7.6: Selection efficiency of the function of E_ν, E_μ, and θ_μ. Solid line shows the efficiency for SAMPLE-C, dashed line is for SAMPLE-B, and dotted line is for SAMPLE-A. Dot-dashed line means the efficiency for SAMPLE-A-dash, which is described in Appendix B.

7.1.4 Selection efficiency

Event selection efficiency is estimated using neutMC. For SAMPLE-C, overall efficiency, which is number of selected events divide by number of generated neutrino events in the fiducial, is 0.36. The efficiency of each interaction type is summarized in Table 7.2. Figure 7.6 shows the neutrino energy dependence, and muon distribution dependence.

type		generated	selected	efficiency
CC	quasi-elastic	14309	7942	0.56
CC	single-meson	11277	4815	0.43
CC	multi-π	6149	2305	0.37
NC	all	11208	212	0.019
	all	42943	15274	0.36

Table 7.2: Summary of the selection efficiency for each interaction type, in Fiducial-C. they are estimated by Monte Carlo simulation.

7.2 Check of MRD Performance and its Stability

The performance of MRD is experimentally checked, and its stability is monitored during the running period. Following items are discussed in this Section.

- Hit efficiency of the drift-tubes.
- Tracking efficiency.
- Reconstruction resolution.

Finally, the distribution of cosmic ray muons is analyzed for overall confirmation of the detector stability.

7.2.1 Hit efficiency

Each drift-tube has a little inefficiency for detecting charged particles inside the cells. In addition, the gaps between the tubes and the masked noisy channels contribute to the inefficiency of the detector. Effective hit efficiency have been monitored by counting number of hits on the long tracks during the whole run. Number of included hits divided by passed drift-tube planes defines the effective hit efficiency.

The analysis use muon tracks which passed longer than 10 planes (passed 4 iron plates), whose $\tan\theta_x$ and $\tan\theta_y$ were less than 0.5, and requiring the time window of $5 < T_0 <$ 35count.

The results of the effective efficiency from June 1999 to June 2000 are shown in Figure 7.7. Average efficiency is 93.9% for x-tube and 93.2% for y-tube. Monte Carlo simulation is performed with various intrinsic cell hit efficiency from 97% to 100%, which are also shown in Figure 7.7. The result indicates 97.5% to 98.5% efficiency MC has the best agreement with data. Intrinsic cell hit efficiency of 97.5% is adopted for standard neutMC. The inefficiency of 2.5% includes the geometrical effect coming from a possible miss-alignment of the drift-tube modules, as well as the real hit efficiency. According to the Monte Carlo study, 1% uncertainty of the hit efficiency yields about 1% difference of the selection efficiency of SAMPLE-C. Although, this uncertainty also affects the tracking efficiency estimated in next sub-section. Hence, this uncertainty of the hit efficiency is taken into account as the difference of the tracking efficiency, and provides the systematic error for the event rate at MRD.

Uniformity of the hit efficiency is analyzed in this way applying to tracks in various area. The result says the non-uniformity of the hit efficiency is estimated to be less than 1%. Therefore, effects on the neutrino profile determination are negligible.

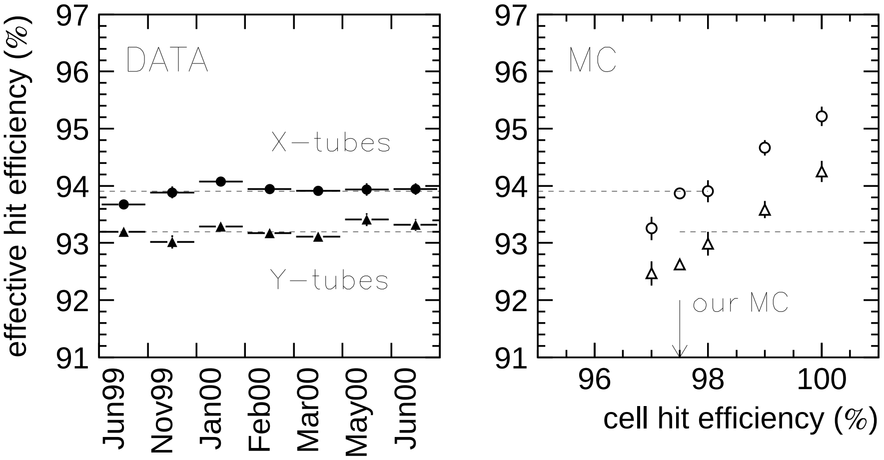

Figure 7.7: Left: The effective hit efficiency for each month. closed circles show the hit efficiency of X-tubes, while closed triangles show that of Y-tubes. Right: The effective hit efficiency by neutMC, with various hit efficiencies of each cell itself (horizontal axis).

7.2.2 Tracking efficiency

Tracking efficiency is analyzed with performing a re-tracking test. The test is schematically explained in Figure 7.8. The test checks whether the track is reconstructed with restricted hits in "test area", from the already "known" long muon tracks. It corresponds to the test of SAMPLE-C tracks with penetrating iron layers of $N^{iron}_{layer} = 2 \sim 4$. The method and the results are described as follows.

1. Data sample.
   Following two data samples are used for this re-tracking test.

   - Neutrino induced long tracks.
     (typically shown in Figure 7.8) Their vertex is contained in 1st or 2rd iron plates. They passes the Fiducial-C. And they reaches at least one layer downstream of the test area. The test area is set with 3, 4, or 5 drift-tube layers (which corresponds to N^{iron}_{layer} = 2,3, or 4) from the 3rd or 4th drift-tube layer.
   - Cosmic ray muon tracks.
     (typically show in Figure 7.9) They passes the Fiducial-C, and which leave hits at least one layer downstream of the test area. The test area starts from 2nd, 3rd or 4th drift-tube layer, and have length of 3, 4, or 5 drift-tube layers. These tracks are taken with a coincidence trigger of upstream- and downstream-TGC hits in both side of SCIFI.

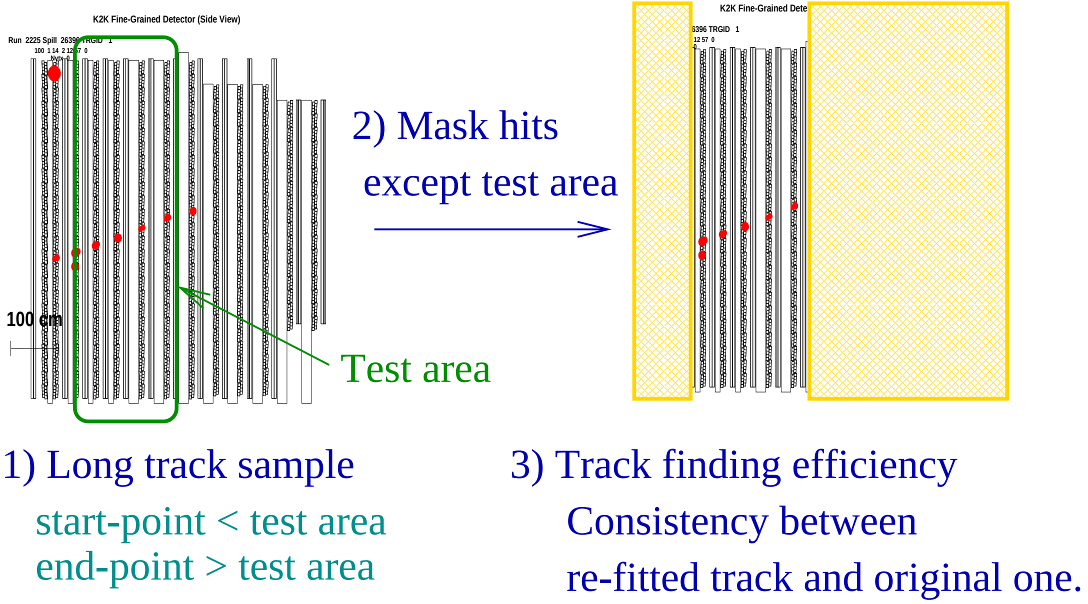

Figure 7.8: Method of the re-tracking test.

Due to the geometry of the experimental site, the tracks are distributed as two groups, as shown in Figure 7.9. One is due to the muons which enter at the lower part of the MRD 1st plane and go downward. The other is due to the muons which enter at the top of MRD detector and exit from the upper part of the MRD 1st plane.

2. Hit mask.
   All the hit informations are masked except the test area.

3. Re-tracking
   The track finding routine is applied to the remaining hits. The re-fitted tracks are counted when they match to the original tracks within (start and end point difference)< 20 cm, and (T_0difference) < 4 count.

Figure 7.10 shows the results of the tracking efficiency, as a function of N^{iron}_{layer}, using neutrino induced tracks or cosmic ray muons. Monte Carlo simulations of neutrino events (neutMC) and the cosmic ray muons are generated and analyzed with same procedure. The results are overlaid with dashed line in Figure 7.10. The efficiency is more than 90%, and consistent with simulation a few %. A difference is found at $N^{iron}_{layer} = 2$ in analysis of

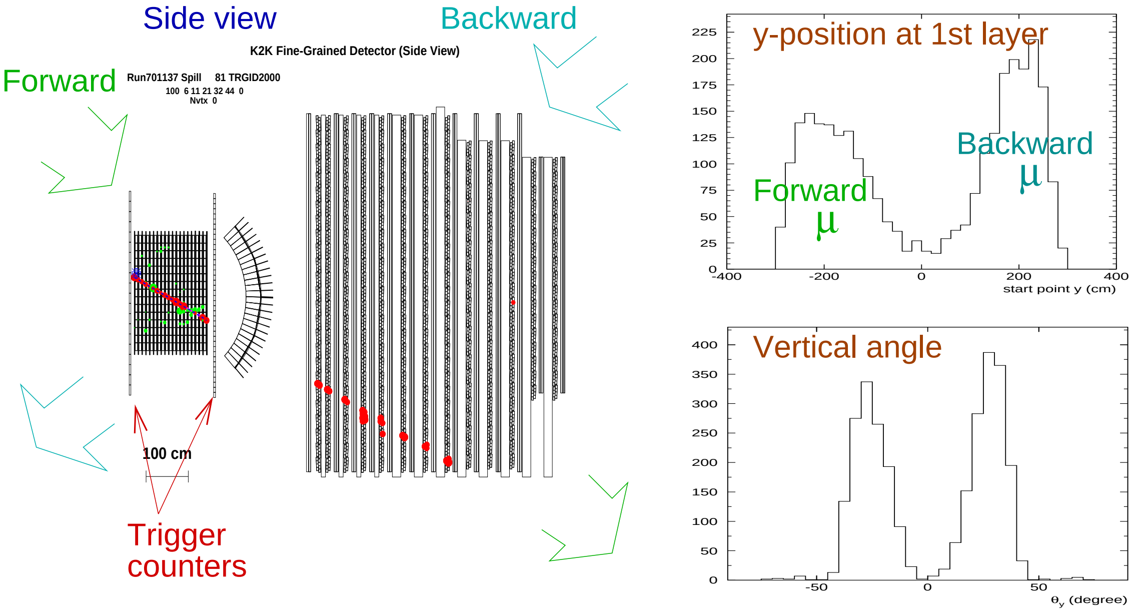

Figure 7.9: Typical event display of the cosmic ray muon (left). Distributions of the vertical position at 1st drift-tube layer (right-top) and the vertical angle (right-bottom) of the cosmic ray sample.

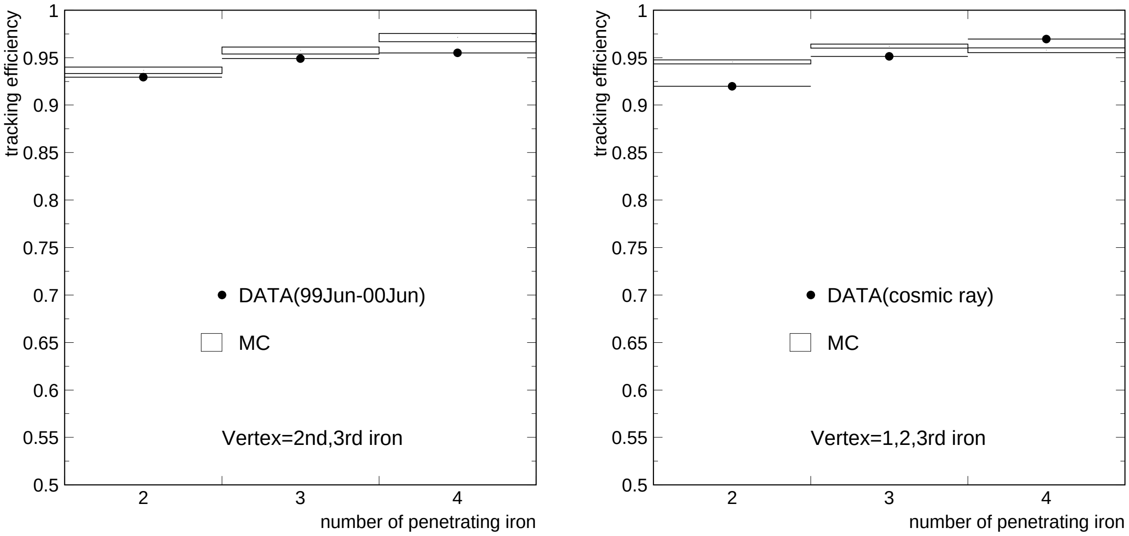

Figure 7.10: Tracking efficiency obtained from the re-tracking test. The left figure is the result using the neutrino induced tracks. The right figure is the one using the cosmic ray muons. Horizontal axis means the number of penetrating iron plates (N^{iron}_{layer}). The results from Monte Carlo simulation are overlaid (box).

cosmic ray muons, in particular, for tracks with large angle. This difference is taken into account for the systematic error, and the effect for the total number of event is estimated to be less than 1%, as described in Section 7.5.3.

7.2.3 Reconstruction resolution

Reconstruction resolution is experimentally checked by following two methods.

- **Residual of the fit.**
  Residual of the 2-D fit is investigated. Figure 7.11 shows the results. Width (sigma) of the residual distribution is 8 mm for data, and 7 mm for neutMC. These residuals mainly come from the multiple scattering of muons in the iron.

- **Difference between the re-fitted track and the original one.**
  In the re-tracking test in previous sub-section, the reconstruction difference of them is investigated. Figure 7.12 shows a typical result. These distributions suggest us the intrinsic vertex and end point determination of typically 5 cm and 1 count (50 ns), Re-tracking test of neutMC gives the consistent results.

These agreement of the data and neutMC allows us to estimate the resolution using neutMC.

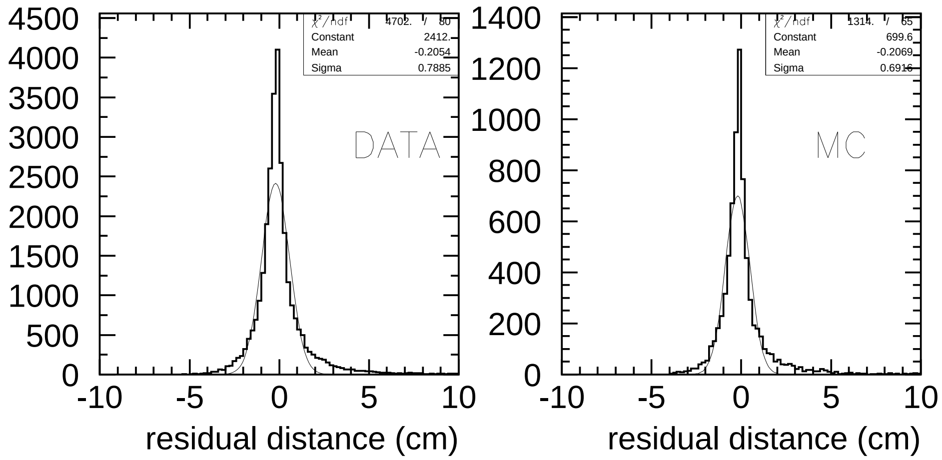

Figure 7.11: Residual distribution of the 2-D tracks for data (left) and for neutMC (right).

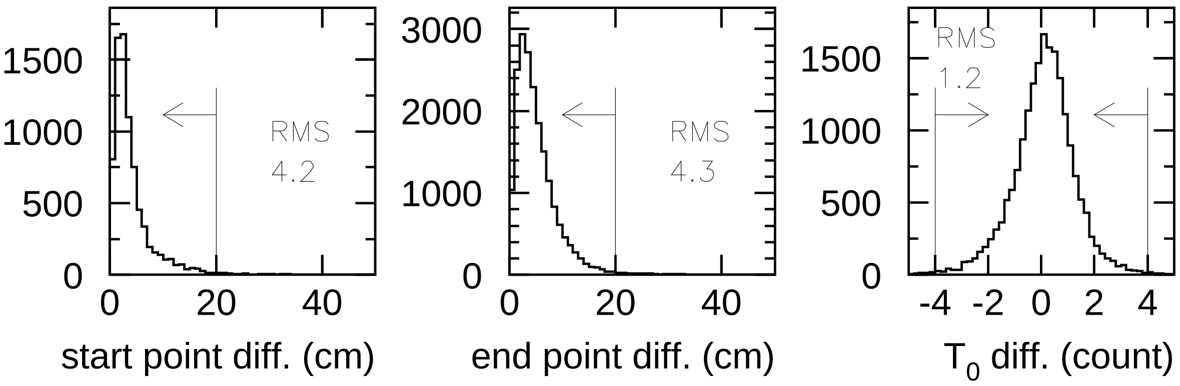

Figure 7.12: Distributions of the difference of the start point (left), end point (center), and T_0 (right), between the re-fitted track and the original one. Start (end) point difference means a 2-dimensional distance between the re-fitted start (end) point and the interpolated penetrating point at same z-position from the original track information.

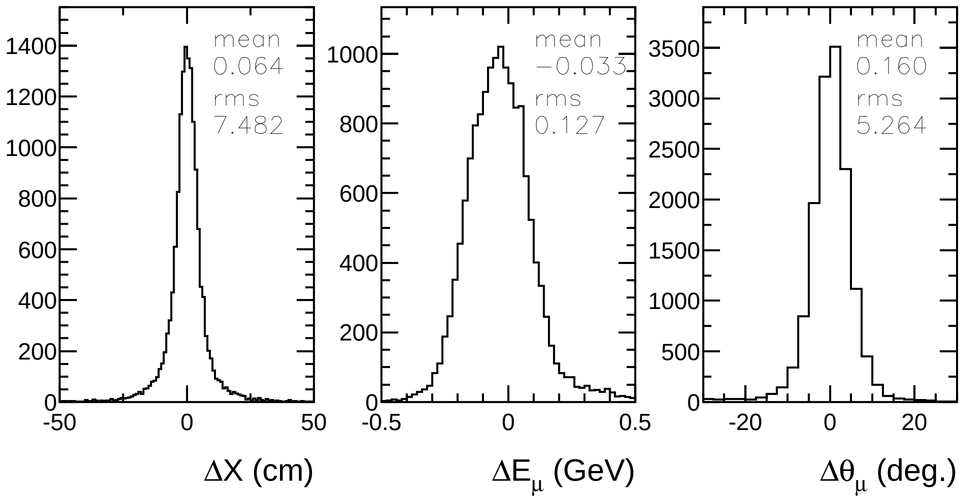

Figure 7.13: Reconstruction resolutions of the vertex, energy and angle for SAMPLE-C, which are estimated with neutMC.

- **Comparison between reconstruction and the MC true information.** Difference from the MC true value of the muon energy and the polar angle of the reconstructed tracks are estimated for SAMPLE-C. Figure 7.13 shows the result. Their r.m.s. are 127 MeV and 5.3 degree for the energy and the angle, respectively.

  The x-vertex reconstruction of the neutrino events is also estimated. The reconstructed start point is, by our definition, on the drift-tube plane, although the "true" vertex position is inside the iron. Including this systematic smearing, the vertex can be determined within 7cm by r.m.s. as shown in Figure 7.13.

  Extend to the case of SAMPLE-A and SAMPLE-B, these resolutions are almost the same.

7.2.4 Cosmic ray measurement

Cosmic ray muons are measured for the demonstration of the stable operation of the detector. The data are taken by the off-spill trigger, which is 1 sec after the on-spill trigger. Only the cosmic ray muons contribute to the off-spill data as tracks. The same track finder is applied to find the muon tracks. Figure 7.14 shows the time variation of the reconstructed 3-D track rate. The average number of tracks is about 11 per 1000 triggers and has been stable within the statistical error. The N_{layer}^{iron} distribution and angular distributions are also analyzed on a monthly basis. The results show no time variation is observed over the

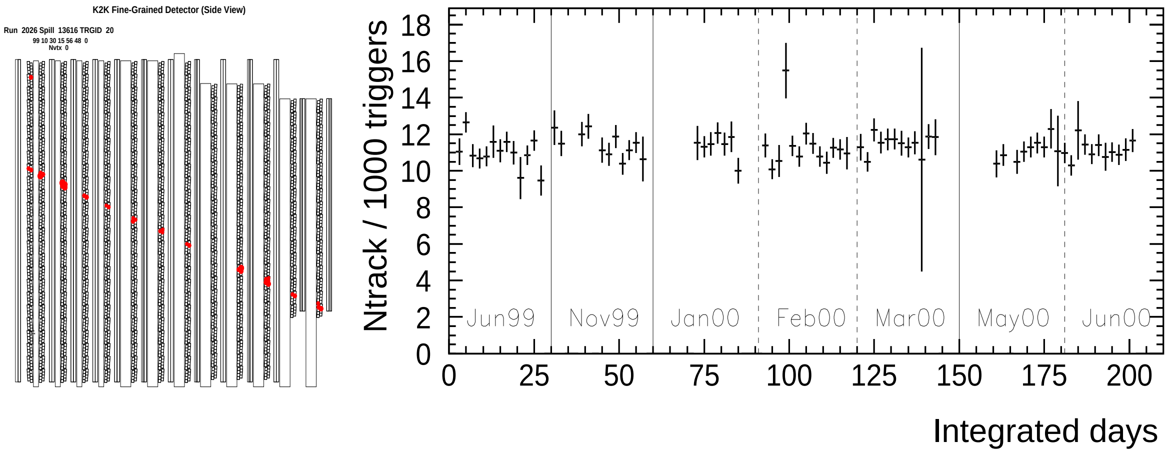

Figure 7.14: Number of reconstructed 3-D tracks from the off-spill data as a function of time. The horizontal axis shows the integrated days. The vertical axis shows the number of tracks per 1000 triggers.

statistical fluctuation [57]. The stability of these distribution show the detector has been working in these period.

7.3 Neutrino Profile at MRD

Neutrino beam profile is obtained by measuring the vertex distribution in MRD. In our standard analysis in this section, fully-contained (FC) events are analyzed. In addition, another profile analysis is performed using vertex-contained (VC) events, for the cross-check. This is described in Appendix B.

7.3.1 Vertex profile of fully-contained (FC) events

SAMPLE-A is used for this analysis. It is defined as the event whose start point is in Fiducial-A, (6m × 6 m) and whose end point is contained inside of the MRD. The distributions are corrected with the geometrical acceptance as follows.

1. SAMPLE-A is arranged to be a distribution of X-vertex, Y-vertex, and the reconstructed energy. In this analysis, there are 12 bins (50cm × 50 cm bin) in X-vertex and Y-vertex, and 4 bins (0.5 GeV bin, from 0.5 GeV to 2.5 GeV) in energy.

2. Acceptance for the muon track has a dependence on the vertex position and the energy. Thus, the acceptance of each bin is estimated by Monte Carlo simulation for each X, Y, and energy region. Only for this estimation, neutrino event is uniformly generated with flat spectrum, in order to avoid the position dependent bias and to acquire enough statistics for high energy muons.

3. The corrected distributions in all the energy bins are summed up. Obtained 2-dimensional distribution is taken to the projection of x and y direction.

Three profile distributions are obtained with different muon energy range.

- **FC-All-Energy** ($0.5 < E_\mu < 2.5$ GeV).
  All the energy bins are summed.

- **FC-Low-Energy** ($0.5 < E_\mu < 1.0$ GeV).
  Lower energy muons mainly come from lower energy neutrinos. Typical neutrino energy is 1.4 GeV in average.

- **FC-High-Energy** ($1.0 < E_\mu < 2.5$ GeV)
  High energy muons mainly come from high energy neutrinos. Typical neutrino energy is 1.7 GeV in average.

Figure 7.15 shows the corrected profile of FC-Low-Energy (top) and FC-High-Energy (bottom), for Nov.99 to Jun.00 run. (The obtained profile for Jun.99 run is presented in Appendix E.2.) They prove that neutrino is well pointed to the designed direction to the Super-Kamiokande. The neutMC with same reconstruction procedure are overlaid. Their width of distribution agrees well with the observation.

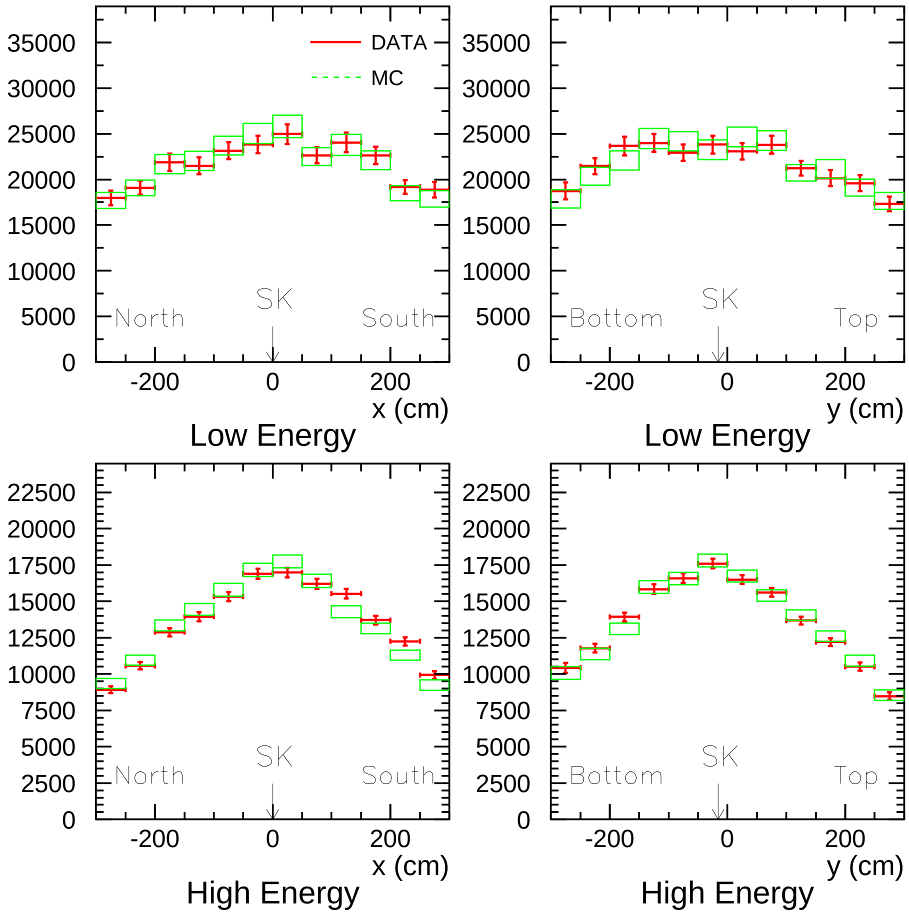

Figure 7.15: Corrected vertex profile of fully-contained (FC) events in MRD, for Nov.99 to Jun.00 run. Number of contained events is corrected with acceptance. DATA (cross) and neutMC (box) are overlaid, with normalization by the area under the histograms. Error bars are due to data statistics and also MC statistics of the applied efficiency correction. In these profiles, 30 cm shift corresponds to 1 mrad off from the nominal direction.

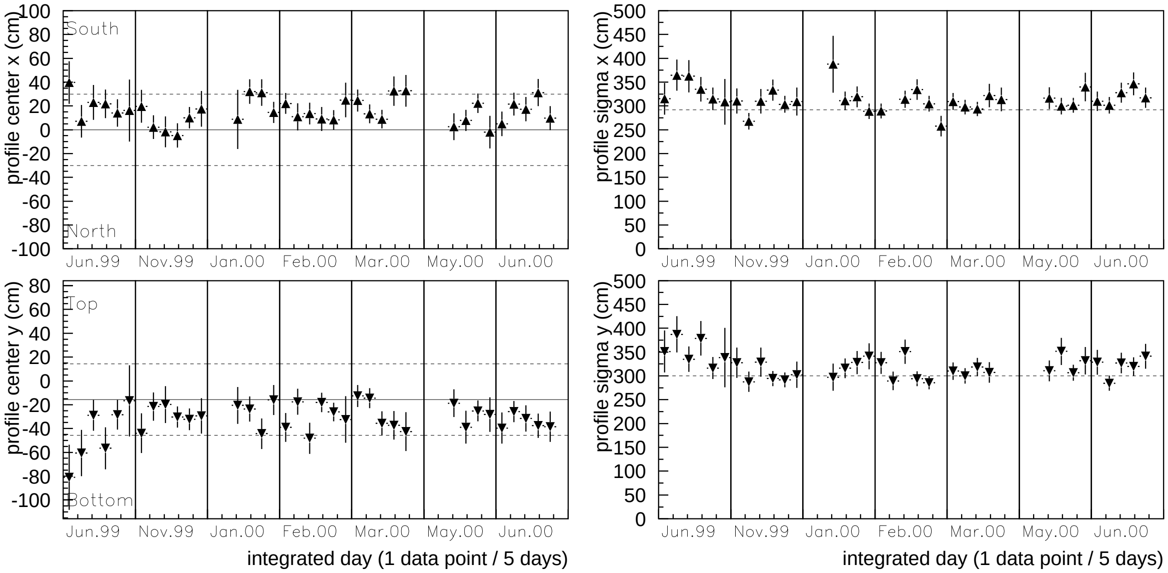

Figure 7.16: Stability of the neutrino profile center (left figure) and width (Gaussian sigma, in right figure) from June 1999 to June 2000, obtained from FC-all analysis. DATA is analyzed every five days integration. The error bars mean the Gaussian fitted error. They mainly come from the statistics of DATA and Monte Carlo event used for acceptance correction. Designed beam direction is $x = 0$ cm and $y = -15.8$ cm (solid line in left figure). Dashed line in left figure means the ±1 mrad (= ±30 cm) boundary. Dashed line in right figure means the width estimated by neutMC.

7.3.2 Stability of the neutrino profile

Long-term stability of the profiles is studied as follows. Vertex profiles are integrated every five days, to obtain enough statistics for reconstruction. Short time stability within five days are monitored and confirmed to be stable, by the proton measurement (SPIC) and the secondary muon measurement (MUMON) as discussed in Chapter 6.2 and 6.3.

Each profile is fitted with Gaussian function to obtain the profile center and the width. Gaussian function is proper because reduced chi-square is always equal to or less than 1. Figure 7.16 shows the results of fitted center and its width (Gaussian sigma) in whole run. Since MRD is located at about 300 m away from the target, 30 cm shift corresponds to 1 mrad-off direction. The result show the profile center of both X and Y have been always distributed around the nominal direction (solid line) within 1mrad (dashed line).

Stability of FC-Low-Energy profile and FC-High-Energy profile are also analyzed. Profile center of FC-High-Energy analysis is always pointed to nominal direction to SK within 1 mrad. While the center of FC-Low-Energy analysis is confirmed with 2 mrad accuracy. This is because low energy events have broad profile as shown in Figure 7.15. Although,

	center x	(cm)	center y	(cm)	width x	(cm)	width y	(cm)
nominal center	0.		−16					
Jun.99	+18	±8	−45	±10	340	±17	354	±19
Nov.99	+5	±6	−30	±6	308	±12	301	±11
Jan.00	+24	±7	−28	±8	311	±13	325	±15
Feb.00	+13	±6	−29	±6	307	±11	308	±11
Mar.00	+20	±6	−25	±6	305	±11	313	±12
May.00	+11	±6	−28	±7	312	±13	322	±14
Jun.00	+17	±6	−34	±7	322	±13	320	±13
Nov.99 to Jun.00	+14	±5	−29	±5	311	±9	314	±10

Table 7.3: Summary of the fitted center and width of the neutrino profile by FC-all analysis, on monthly basis from June 1999 to June 2000. Fitting errors are also shown.

this broad profile means the direction determination of low energy event is less important than that of high energy event. Profile width of both analyses is agreed with that of neutMC.

Fluctuation of the neutrino beam direction is discussed.

1. The fitted center distribution is made by projection of the each point in Figure 7.16-left, with weighted by its number of observed events in this period. R.M.S. of this distribution shows the degree of fluctuation of the neutrino beam direction.
2. On the other hand, the average of the fitted error in each data point of Figure 7.16-left is calculated.

The results are as follows.

		x	y
1	R.M.S. of the profile center	11 cm	13 cm
2	average of the fitted error	11 cm	12 cm

The agreement of these two values proves that the distribution is explained by the statistical fluctuation, no other unexpected instability is observed.

The stability allows us to fit an integrated profile by each month. The fitted center and the width for each month are summarized in Table 7.3. The neutrino beam direction is stable within the fitting error, again.

7.3.3 Profile reconstruction test by Monte Carlo simulation

The profile reconstruction is tested by neutMC with shifted beam axis. Same analysis routine is applied for $x + 50$ cm shifted and $y \pm 50$ cm shifted MC sample. The fitted

beam shift	method	center	x (cm)	center	y (cm)	width	x (cm)	width	y (cm)
Center	(nominal)	(0)		(-16)					
	FC-all	+1	±5	-16	±5	292	±9	300	±10
X +50cm	(nominal)	(+50)		(-16)					
	FC-all	+54	±9	-17	±9	275	±14	293	±16
Y +50cm	(nominal)	(0)		(+34)					
	FC-all	+1	±7	+57	±11	266	±12	291	±16
Y -50cm	(nominal)	(0)		(-66)					
	FC-all	+5	±9	-62	±11	296	±17	294	±17

Table 7.4: Reconstruction test of FC profile, with neutMC with shifted beam axis.

results are summarized in Table 7.4. The results almost agree with the nominal input axis. But, in some case, the reconstructed center is outside of the true position. Therefore, the systematic errors of these methods are quoted from the largest discrepancy among this test, as follows;

$$\text{for FC-all analysis :} \quad -23\text{cm} \times (\text{center shift})/50\text{cm}$$

This error is adopted instead of the fitting error, only for the near side to the nominal center.

7.3.4 Conclusion of the neutrino beam direction

Finally, the neutrino beam direction is concluded as following precision;

period	direction	profile center at MRD	angle
Jun.99	x	$+18^{+8}_{-8}$ cm (South)	0.6 mrad
	y	-29^{+13}_{-10} cm (Down)	1.0 mrad
	$\sqrt{x^2+y^2}$	35^{+12}_{-15} cm	1.1 mrad
Nov.99 to Jun.00	x	$+15^{+5}_{-7}$ cm (South)	0.5 mrad
	y	-13^{+6}_{-5} cm (Down)	0.4 mrad
	$\sqrt{x^2+y^2}$	20^{+7}_{-9} cm	0.7 mrad

In addition, the analysis results with vertex-contained (VC) events are presented in Appendix B. They show consistent results with above results. We conclude that the neutrino beam is stably directed to SK within 1 mrad accuracy.

When the neutrino beam is shifted from the designed direction, neutrino flux is decreased at both near site and far site simultaneously. Monte Carlo simulation is performed with 1.7

Off-direction	0	$x + 1.7$ mrad	$y - 1.7$ mrad	$x + 1.7, y - 1.7$ mrad
1kt	1.	0.99	0.98	0.97
MRD	1.	0.98	0.98	0.96
SK	1.	0.99	0.99	0.99

	(Jun.99)	(Nov.99 to Jun.00)
Off-direction	1.1 mrad	0.7 mrad
MRD/1kt	1.00	1.00
SK/1kt	1.01	1.01
SK/MRD	1.01	1.01

Table 7.5: Relative rate at 1kt, MRD and SK when beam is off-direction, which are estimated by the Monte Carlo simulation. Normalization is done by the number of injected proton.

mrad off-centered flux and obtained the observed event rate at Near detector (1kt, MRD) and Far detector (SK). The results are summarized in Table 7.5. The change of the event rate ratio due to the 1 mrad miss-direction is expected to be about 1%. This is negligibly small comparing to other systematic errors.

In this thesis, center value of the event rate is kept to the case of perfect direction, and the difference due to the off-direction is assigned as the systematic error. This error amounts to 0.6% (1.1%) for SK/1kt event ratio, in Nov.99 to Jun.00 run (Jun.99 run).

7.4 Muon Distribution at MRD

7.4.1 Observed muon spectrum and angular distribution

When a ν_μ interacts to a nucleon by CC quasi-elastic scattering, the neutrino energy can be reconstructed by measuring the out-going muon energy E_μ and the polar angle θ_μ with respect to the neutrino direction, as follows[3];

$$E_\nu = \frac{m_N \cdot E_\mu - m_\mu^2/2}{m_N - E_\mu + p_\mu \cos\theta_\mu} \tag{7.1}$$

where, $m_N(\sim 0.94$ GeV) and $m_\mu(\sim 0.106$ GeV) are nucleon and muon mass. Therefore, distributions of the muon energy and polar angle are the confirmation of the neutrino energy spectrum. In this sub-section, observed distributions are compared with those of neutMC. SAMPLE-C is used for this study.

Figure 7.17 is the E_μ spectrum and the θ_μ distribution in Nov.99 to Jun.00 run. Observed data is plotted by solid cross. The dashed line shows the distribution of neutMC, which assumes the same hadron interaction inside the iron nucleus (nuclear effect) as in the oxygen nuclei, as noted in Chapter 4.2.7. The dotted line shows the "muon-only" simulation, in which only muons are put to the detector simulation. This corresponds to 100% nuclear absorption of hadrons. Figure 7.17 shows that the observed distributions are between these two simulations. Therefore, the difference of these two simulations is assigned as the systematic error for comparison of $\nu -$ Fe and $\nu - H_2O$ interaction. The results of Jun.99 run are presented in Appendix E.3.

7.4.2 Stability of the muon distribution

The time variation of the muon energy spectrum and angle distribution are studied. Stability of the muon distribution is the evidence of the stable neutrino spectrum. It is already shown that MRD responses; they are efficiency and noise, have been stable during the whole period.

SAMPLE-B is used for this stability analysis. Due to the large mass of MRD iron target, contained events of every five days have enough statistics to be compared each other. Figure 7.18 clearly proves the monthly stability from Nov.99 to Jun.00. Figure 7.19 shows the reduced chi-square of the shape of the muon energy and angle distribution from the averaged ones, in every five days. Comparison is done after the normalization with its number of observed event. The variation is consistent with the statistical fluctuations.

These muon distribution stabilities imply the neutrino energy spectrum is stable throughout this experimental period.

---

[3] Fermi motion of the target nucleon is neglected in this formula.

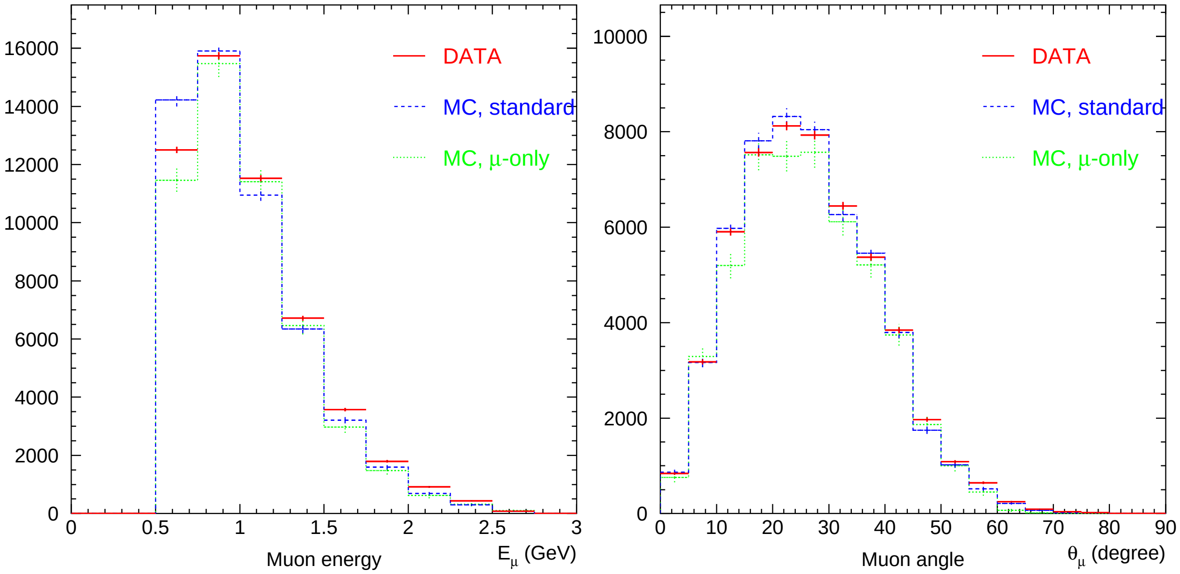

Figure 7.17: E_μ spectrum and θ_μ distributions observed in MRD, for Nov.99 to Jun.00 run. Observed data (solid) and standard neutMC (dashed) are overlaid, with normalization by their entry. Dotted line shows the muon-only Monte Carlo, in which produced hadrons are killed (see text). Normalization of the dotted histogram is done by its generated event relative to the standard neutMC (dashed). Difference of the selected event is 5.6% which is correspond to the difference of their area.

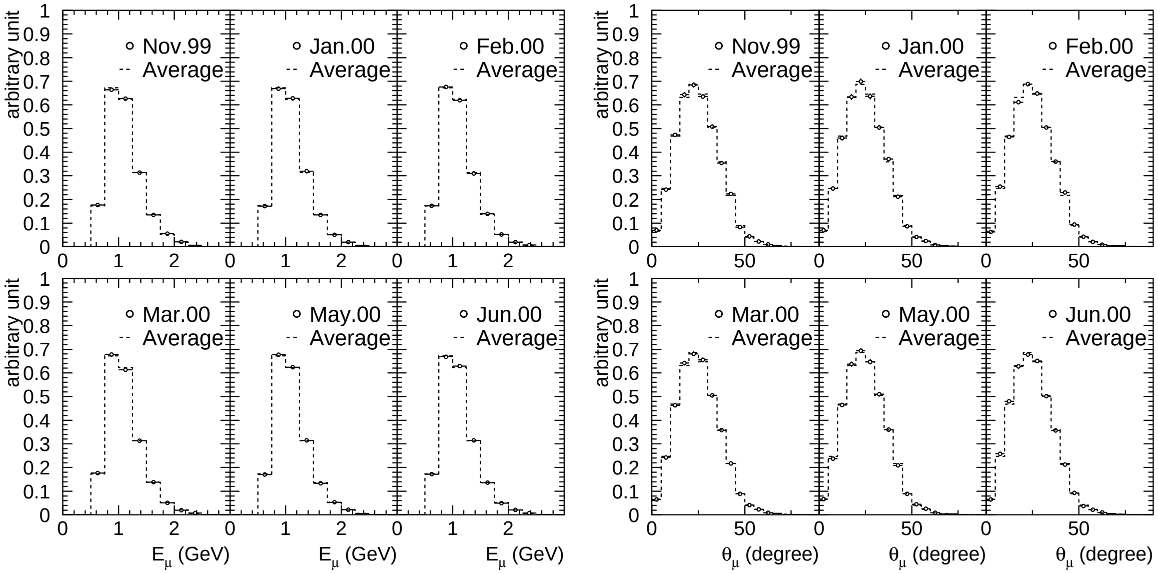

Figure 7.18: Monthly plot of E_μ and θ_μ distributions (solid), overlaid with the average of Nov.99 to Jun.00 (dashed). Normalization is done by its number of observed event. Error bars mean statistical errors only.

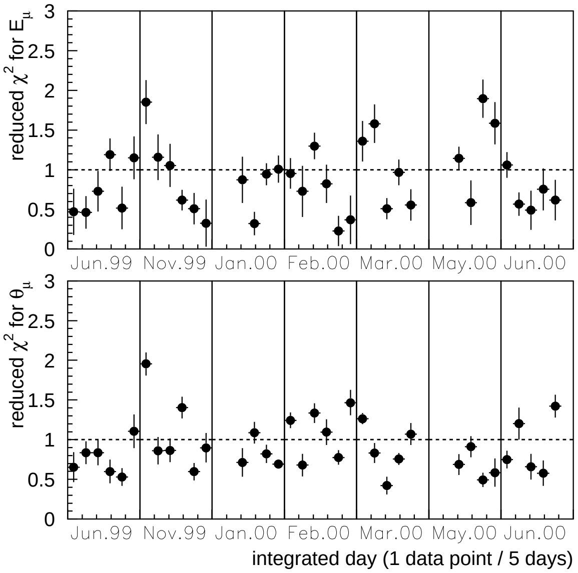

Figure 7.19: Reduced chi-square of the E_μ spectrum and θ_μ distortion from the averaged ones. The data are analyzed in every 5 days. Vertical axis are already divided by the degree of freedom, which is typically 9 and 14, for E_μ and θ_μ, respectively.

Period	Jun.99	Nov.99	Jan.00	Feb.00	Mar.00	May.00	Jun.00
Target diameter	20mmϕ	30mmϕ					
HORN	200kA	250kA					
Number of spill	615896	552335	390715	724648	627875	467142	649740
P.O.T. ($\times 10^{18}$)	2.93	2.72	2.04	3.81	3.49	2.51	3.54
Observed SAMPLE-C	7417	8140	5997	11228	10306	7464	10159
N_{corr}	21516	22886	16861	31568	28975	20985	28562
Event rate ($/10^{15}$pot)	7.4	8.4	8.3	8.3	8.3	8.3	8.1

Table 7.6: Summary of the number of observed event (SAMPLE-C) in MRD. Efficiency corrected number of interactions N_{corr} and the event rate are also shown.

7.5 Neutrino Event Rate at MRD

7.5.1 Event rate stability

Table 7.6 summarizes the number of observed events. The number is normalized by accumulated number of targeting protons measured by TGT-CT, and summarized by every half days and two days. Figure 7.20 shows the time variation of the event rate of SAMPLE-B (upper solid) and SAMPLE-C (lower solid). Each point corresponds to the two days average rate. In Jun.99, experiment was running with different HORN system. Thus, the event rate is different from other period by factor of 0.86 for SAMPLE-B and 0.89 for SAMPLE-C.

No fluctuation is observed except for statistical ones either in half days integration plot or in two days plot. Right figures of Figure 7.20 show the difference distribution from the averaged rate for SAMPLE-B and SAMPLE-C. Standard deviation (r.m.s.) of each plot is 5.5% and 6.8% for SAMPLE-B and SAMPLE-C, respectively. These are completely explained by the statistical fluctuation. For another verification, chi-square is calculated from the average rate. Total chi-square of the period is summarized at the bottom table in Figure 7.20. They show the chi-square value is almost equal to the degree of freedom. It is concluded that the MRD events is stable within the statistical error.

7.5.2 Calculation of the neutrino interaction rate at MRD

Neutrino interaction rate presents the product of the neutrino flux and the cross section. Number of observed SAMPLE-C events is corrected by the event selection efficiency (ϵ_{MRD}) of 0.356 (0.345) for Nov.99 to Jun.00 (Jun.99), estimated by neutMC. And it is normalized by p.o.t. to obtain the interaction rate r_{corr}^{MRD}. The results are shown in Table 7.6.

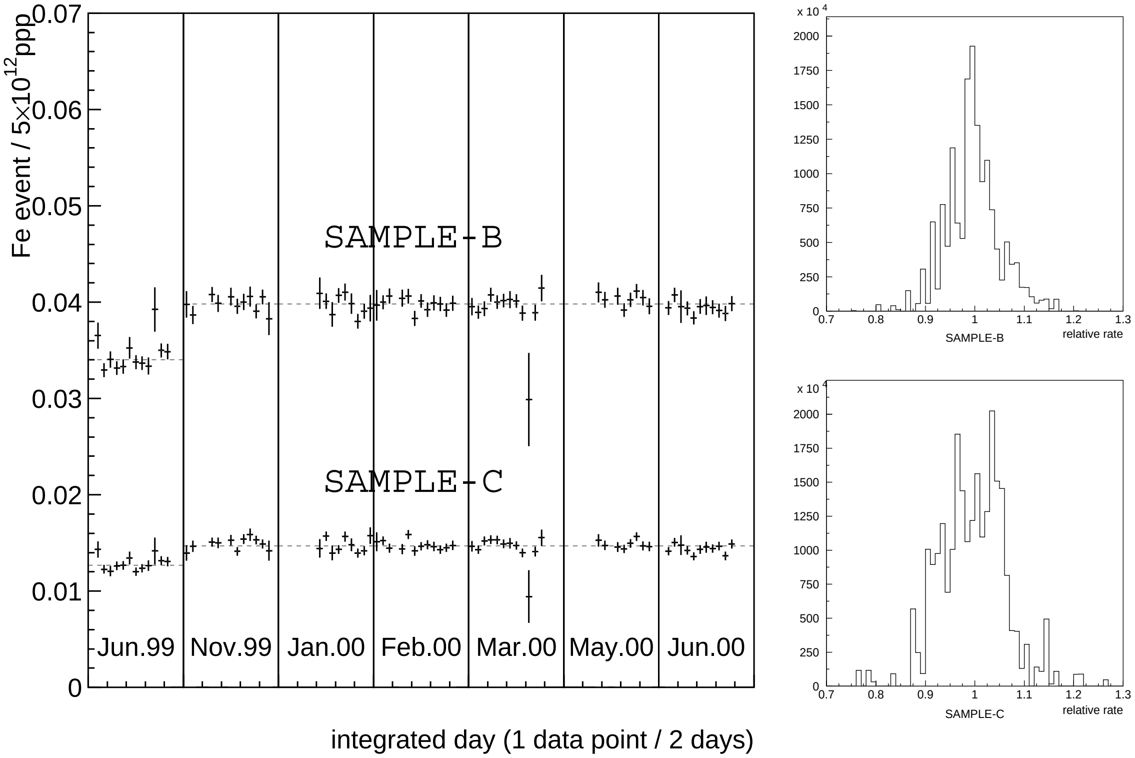

	period	Jun.99	Nov.99 to Jun.00
SAMPLE-B	average rate	0.034	0.040
	χ^2	57 (39 d.o.f.)	234 (220 d.o.f.)
SAMPLE-C	average rate	0.013	0.015
	χ^2	43 (39 d.o.f.)	260 (220 d.o.f.)

Figure 7.20: Left figure shows stability of the MRD event SAMPLE-B (upper solid) and SAMPLE-C (lower solid), from Jun.99 to Jun.00. One data point corresponds to the averaged rate of each two days. The event rate is normalized to 5×10^{12} protons on target, which is the typical proton intensity per one spill. Error bars are statistical error only. Right two figures are their projection. Right-upper figure is the event rate distribution of SAMPLE-B, which is divided by the average rate of corresponding horn configuration. In this figure, the event rate is calculated on every half days. Right-bottom figure is the corresponding distribution of SAMPLE-C. Bottom table summarizes the average event rate and the chi-square from the average.

Item	Systematic error		
Fiducial volume	+1.2	−2.1	%
Selection criteria	+1.0	−4.5	%
Tracking efficiency	+1.0	−1.0	%
Background contamination		−0.3	%

Table 7.7: Systematic errors from MRD event detection scheme. This is used for the observed MRD event rate per unit proton intensity, that is, the normalization factor of the neutrino flux determination.

7.5.3 Systematic errors at MRD

Table 7.7 shows the systematic errors from MRD detection scheme, except the physics uncertainty.

1. **Fiducial volume error.**
   Fiducial volume is defined by the x, y and z coordinate of the tracks start point. The tracking residual shows no systematic bias for the miss-vertex reconstruction produced by the tracking algorithm.

   We compare the event rate with different fiducial definition as shown in Table 7.8. Radial dependence is within $^{+0.8\%}_{-2.1\%}$ and z-dependence is within $^{+0.9\%}_{-0\%}$. Quadrature sum is taken to be concluded the systematic error of the fiducial volume definition is $^{+1.2\%}_{-2.1\%}$.

2. **Selection criteria error.**
   Estimation of the event selection errors is summarized in Table 7.9.

   Errors from "consistency between X-view and Y-view" and "time window" are estimated by changing the cut value. Maximum difference between data and simulation appears when start point difference limits to $0 < (diff.) < 30$ cm instead of $-45 < (diff.) < 30$ cm. This tight cut prohibits the situation that: two y-tubes have no hits and more than one of the x-tubes has a hit. One reason is that neutrino interaction in the chamber of x-tube makes hits only at x-tube. In the neutMC, the chamber mass is considered, but the events were generated in the iron.

   Uncertainty of the "longest track selection" is considered from the rejection probability of a coincidental two events. This "over-killing" probability is 13%, which is described in Section 7.1.3. The probability of the multi-events occurs in one spill is about 0.05. Then, 0.7% of the neutrino events are rejected by this cut. This number is quoted as the systematic error of this cut.

Fiducial volume		Number of events		
radius	iron plate	DATA	MC	difference
< 3m	1 to 3rd	1.	1.	default
< 2m	1 to 3rd	0.53	0.54	-2.1%
< 4m	1 to 3rd	1.33	1.32	$+0.5\%$
all the iron	1 to 3rd	1.39	1.38	$+0.8\%$
< 3m	4 to 9rd	1.70	1.69	$+0.9\%$
< 3m	1 to 9rd	2.70	2.69	$+0.6\%$
Quadrature sum				$^{+1.2\%}_{-2.1\%}$

Table 7.8: Event rate comparison with different fiducial volume definition. DATA and MC means the relative number of events in their own fiducial volume, for Nov.99 to Jun.00 data and the neutMC, respectively.

Selection	cut value change	maximum difference		
Difference of T_0	±1 count	$+0.2$	-0.0	%
Difference of start/end-point	various combination	$+0.7$	-4.5	%
Time window	loosen 10 count	$+0.1$	-0.0	%
Longest track selection (see text)		$+0.7$	-0.0	%
Quadrature sum		$+1.0$	-4.5	%

Table 7.9: Error estimation of the MRD event selection.

To summarize, quadrature sum of these errors is $^{+1.0\%}_{-4.5\%}$, as the systematic error due to MRD event selection.

3. **Systematic error from tracking efficiency.**
Tracking efficiency is estimated by the re-tracking test for long track sample described in Section 7.2.2. This re-tracking test is the overall test including physics process (energy deposit, multiple scattering), detector simulation (hit efficiency) and tracking.

Figure 7.10 shows the tracking efficiency as a function of N^{iron}_{layer} and track slope for each vertex iron plate. We apply the efficiency correction to observed neutrino event with the estimated efficiency from data or neutMC as follows;

$$N_{corr} = \sum^{V_z} \sum^{\theta_\mu} \sum^{nlayer} \frac{N_{obs}(V_z, \theta_\mu, nlayer)}{\epsilon(V_z, \theta_\mu, nlayer)} \tag{7.2}$$

	N_{obs}	N_{corr}^{DATA}	N_{corr}^{MC}	difference
All	53295	55985	56021	-0.1%
1st layer	19144	19947	19912	$+0.2\%$
2nd layer	18622	19715	19771	-0.3%
3rd layer	15529	16323	16338	-0.1%

Table 7.10: Comparison corrected number of track with estimated tracking efficiency from data and simulation. N_{obs} is the observed number of track from 1999 June to 2000 June.

where V_z means the vertex iron plate number, N_{obs} is observed number of events, and ϵ is the estimated efficiency. The results are summarized in Table 7.10. Considering the statistical error of the tracking efficiency study and the discrepancy of the hit efficiency estimation (Section 7.2.1), the systematic error of the tracking efficiency is quoted ±1%.

4. **Background contamination.**
Three probabilities of the background event are considered.

   - One probability is due to the cosmic ray tracks, miss-reconstructed as the contained events. Another probability is due to drift-tube noise. These probability is estimated by analyzing the off-spill-timing data (same data as used for the cosmic ray measurement in Section 7.2.4). The data are analyzed with same procedure as neutrino data. The result is; 18 events are satisfied the criteria of SAMPLE-C, per $2,067,886$ trigger. They are mainly made by cosmic ray muons with large scattering inside of MRD. This selection rate is about 0.06% of the typical neutrino event rate.
   - The other probability is due to beam-induced muons. They enter from upstream, but the track finder fails to identify the entering points. This probability is estimated by analyzing the cosmic ray muons entering or exiting from the upstream. The cosmic ray data are triggered by TGC hits, same as Section 7.2.2 (see Figure 7.9). The entering point to MRD is calculated by extrapolation of both TGC hits. Total 5904 events are analyzed. The track finder identifies most of them to "incoming muons". Only 10 events (0.2%) are miss-reconstructed to be the contained tracks.

     Using this miss-reconstruction probability, the contamination rate of the upstream muon is estimated. In the neutrino data of Nov.99 run, 9128 events are coming from the upstream, when 8140 events are in SAMPLE-C. Thus, the contamination rate is less than 0.2% for SAMPLE-C.

Consequently, probability of the background contamination is estimated to be negligibly small ($< 0.3\%$).

Chapter 8

Measurement of the Neutrino Event Rate at 1kt Detector

8.1 Neutrino Event Selection

8.1.1 Overview of the 1kt analysis

Neutrino events in 1kt water Cherenkov detector (1kt) are analyzed in order to measure the event rate N_{obs}^{1kt} in the near site. Comparison of the neutrino event rate in 1kt and SK is the better than the comparison of MRD and SK, because of same interaction target (water), and same detection techniques. The systematic errors on the comparison of the event rate are almost canceled by adopting the similar selection criteria to SK. For this reason, the activities are counted, when total Cherenkov photons exceed the detection threshold, and the interaction vertex are in the fiducial volume.

Figure 8.1 shows the typical neutrino event. Event selection is explained in the following sub-section. Table 8.1 shows the typical number of selected events in each step in Jan.00 run, and Table 8.2 summarizes the numbers of all the period.

8.1.2 Event selection

1. **Good beam selection.**
   The commonly-defined good beam spills are used, as described in Chapter 5.3.
2. **Triggered on-spill data.**
   Events occurred in beam time of 1.2μs are recorded by HITSUM trigger described in Chapter 3.5.1
3. **Without pre-activity.**
   The events with pre-activity within 1.2μs before beam timing are rejected with TDC

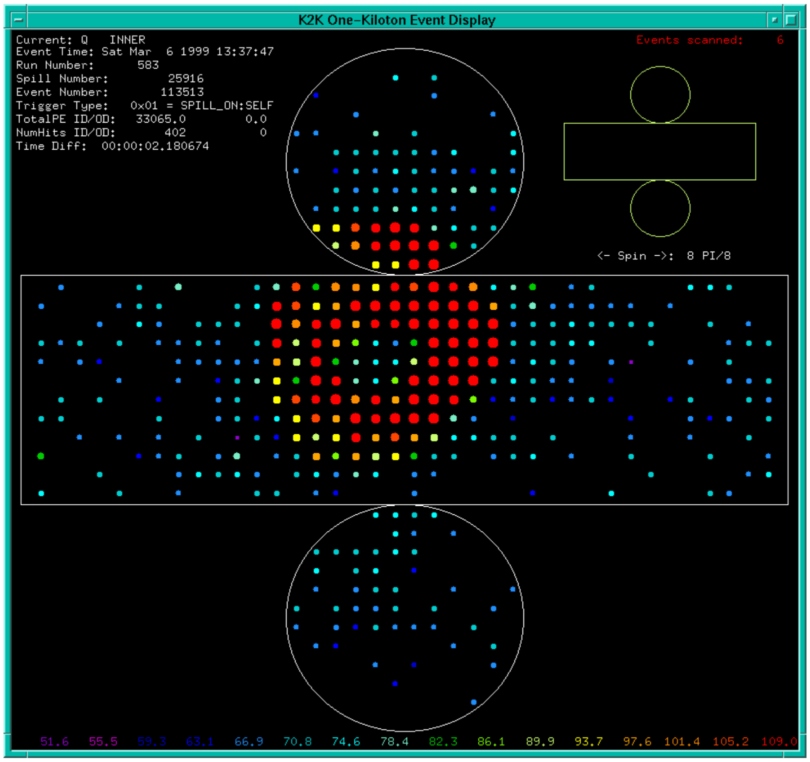

```
Current: Q   INNER
Event Time: Sat Mar  6 1999 13:37:47
Run Number:      583
Spill Number:          25916
Event Number:         113513
Trigger Type:   0x01 = SPILL_ON:SELF
TotalPE ID/OD:   33065.0         0.0
NumHits ID/OD:       402           0
Time Diff:  00:00:02.180674
```

Figure 8.1: A typical neutrino event in 1kt detector.

		DATA	MC
1	number of used spills	346158	
	P.O.T. ($\times 10^{18}$)	1.81	
	(MC) generated in Fiducial-C		125616
2	triggered spills	91864	
	total peak in FADC (N_{peak}^{total})	85238	
5	1 peak in FADC (N_{peak}^{1})	67641	
6	Vertex in Fiducial-B	6513	175352
6	Vertex in Fiducial-C	3505	90300

Table 8.1: Summary of the number of events at each selection stage, in Jan.00 run. Presented number of spills are after pre-activity cut (3).

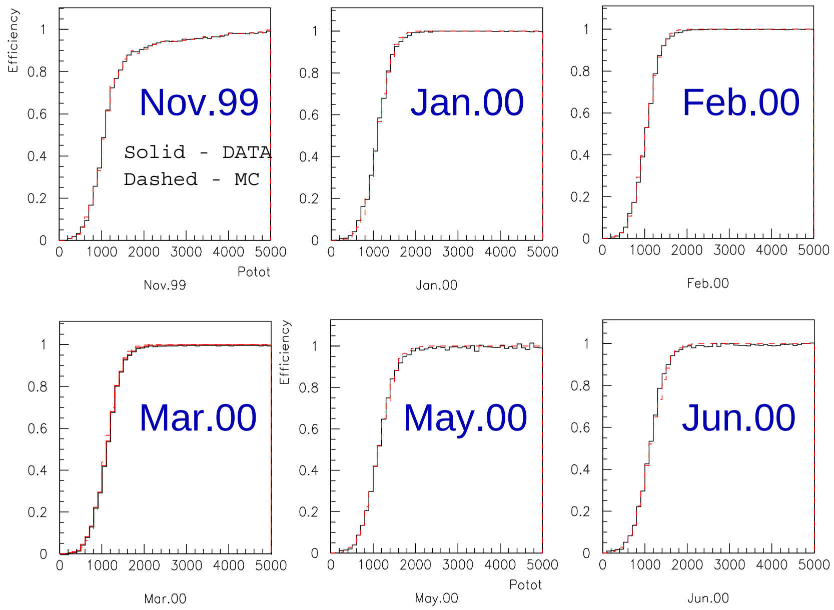

Figure 8.2: Efficiency curve of the total photo-electron selection around the threshold height. The efficiency estimated from data (solid line) and from MC simulation (dashed line) are overlaid. In Nov.99, the efficiency curve was distorted by the disconnection of one of PMTSUM cables (see text).

information recorded in TMC module. The source of the pre-activities are mainly cosmic ray muons, which could cause fake in-time events by reflection signal on the cables. The fraction of the spills with the pre-activity event is about 1.9% (3% in 1999 run, before the buffer-amplifiers were installed). Those spills are not counted in the accumulated number of spills and p.o.t.

4. **Total photo-electron threshold.**
   Analyzed events are required to have more than about 1000 photo-electron of PMTSUM (sum of all the inner PMTs) in Flash-ADC (FADC). This threshold is equivalent to visible energy deposit of about 100 MeV. Figure 8.2 shows the efficiency curve as a function of total photo-electron for data and Monte Carlo simulation. This threshold is set to avoid electron signals from muon decay in the vessel.

5. **Single event selection.**
   In 1kt detector, the rate of the neutrino-induced activity is about $0.2 \sim 0.3$ events per spill. Therefore, more than two neutrino events sometimes occur in the same spill. In these "multiple-events," it is hard to reconstruct the real vertex position.

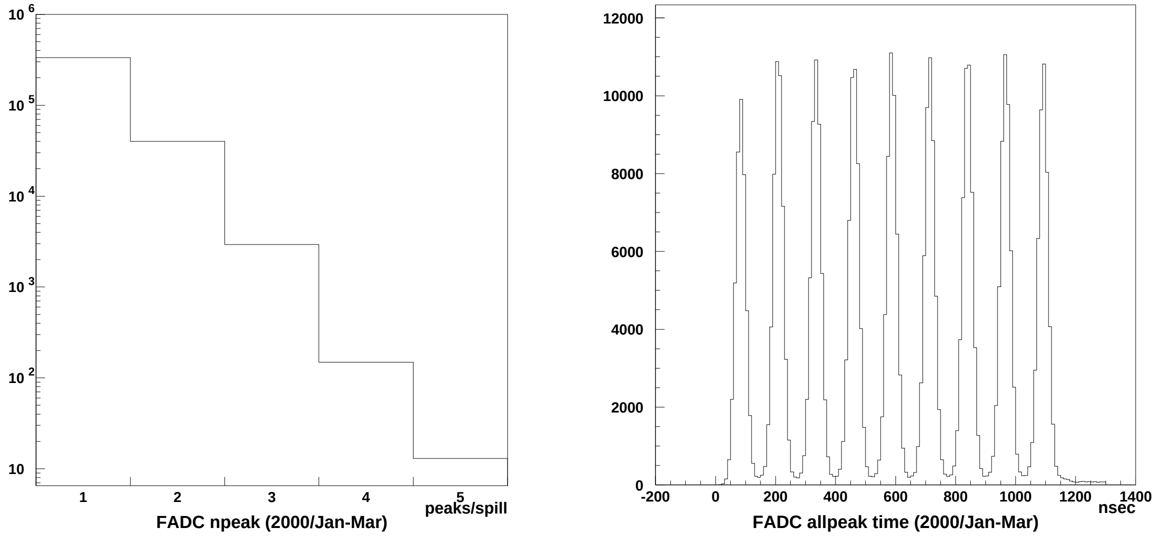

Figure 8.3: Left: Number of peaks in one spill. Right: Timing distribution of selected peaks.

In addition, several quantities are distorted by overlapping of the events. Therefore, only the events with single interaction are used for this analysis.

The number of the events in one spill is measured by counting the number of peaks in PMTSUM signals in FADC, within 1.1μs of beam time window. Figure 8.3 shows the distribution of number of peaks in one bunch, and the timing distribution of of the selected peaks.

The effect of multiple-events is taken into account to the number of events. The correction factor of multiple-events $\left(N_{peak}^{total}/N_{peak}^{1}\right)$ is simultaneously calculated. This is the ratio of the number of total peaks at FADC signal (N_{peak}^{total}) divided by the number of events that have only one peak in each spill (N_{peak}^{1}).

6. **Fiducial volume cut.**
In order to distinguish neutrino interactions from incoming background events from outside, the following three fiducial volumes are defined inside of the detector. The fiducial volumes are shown in Figure 8.4.

- **Fiducial-A**, for neutrino profile analysis.
  Perpendicular cylinder with 3 m radius, and 6 m length.
- **Fiducial-B**, for the event rate stability.
  Horizontal cylinder with 2 m radius, and 4 m length. Total mass is 50 ton.

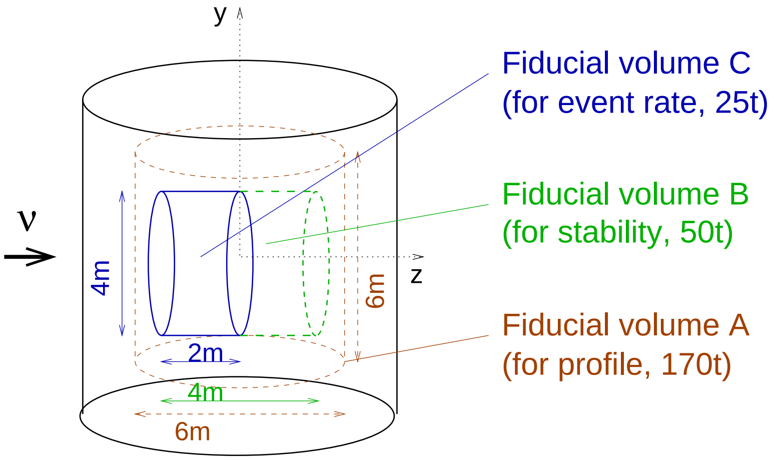

Figure 8.4: Definition of the fiducial volume in 1kt.

- **Fiducial-C**, for the measurement of the number of event N_{obs}^{1kt}.
  Horizontal cylinder with 2 m radius, and $-2 < z < 0$ m length, where the tank center is $z = 0$. Total mass is 25 ton.

  The vertex point is reconstructed by the "TDC fit", which is explained in Appendix C, using the TDC information of PMTs. When the fitted vertex point is in this fiducial volume, the event is selected as a neutrino event candidate.

In Nov.99 run, one of four PMTSUM cables was disconnected by mistake. The missing of one cable decreased the event selection efficiency by 1%, and distorted the efficiency curve as shown in Figure 8.2. The effect is included in the detector simulation of this period.

In May.00 and Jun.00 run, the stop-timing signal to FADC were sometimes drifted and the 8-th and 9-th bunches sometimes went outside of 1.1μs gate time window. To avoid this gate timing uncertainty, we analyzed the neutrino data in 1 to 7-th bunches. Then, the correction factor of (7-bunch)/(9-bunch) $\equiv k_{7\rightarrow 9bunch}$ is applied to measure the neutrino event rate. The $k_{7\rightarrow 9bunch}$ was calculated based on the real data in which the stop signal was not drifted in this period. The $k_{7\rightarrow 9bunch}$ has been quite stable during the running period. The instability of $k_{7\rightarrow 9bunch}$ are assigned as a systematic error of ±1.2%.

8.1.3 Selection efficiency

Figure 8.5 shows the selection efficiency for the Fiducial-C as a function of neutrino energy and vertex position. The efficiency is 88% for CC events and is 56% for NC in-elastic

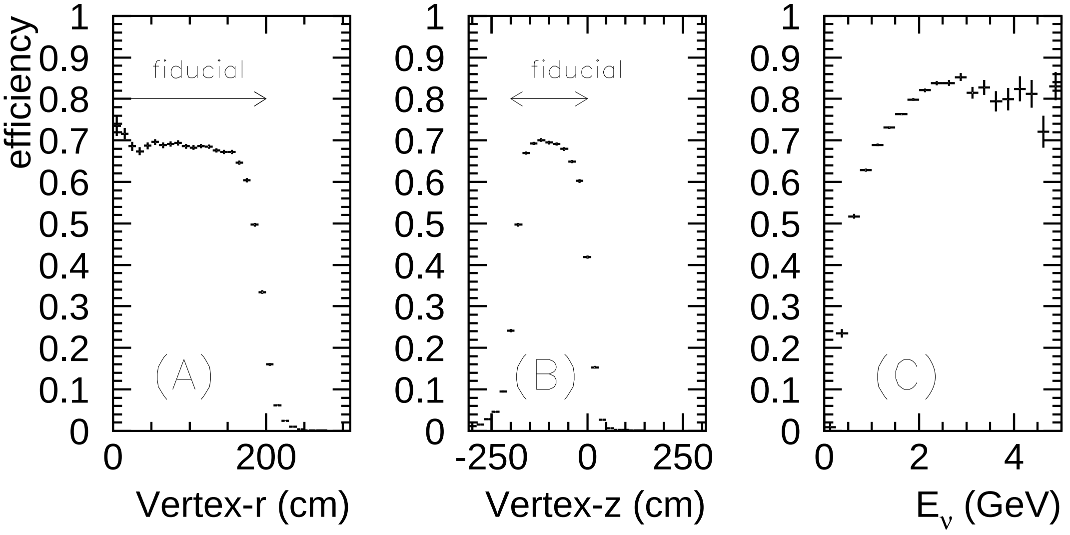

Figure 8.5: Selection efficiency for events in fiducial-C, as a function of its vertex position (A,B) and neutrino energy (C). For figure (A), horizontal axis is the radius from the z-axis (beam direction). For figure (B), horizontal axis is the z-position.

events. The expected ratio of CC to NC gives an overall efficiency of 72%. The main source of inefficiency is the 1000 photo-electron threshold.

8.1.4 Background estimation

The fiducial cut rejects most of the cosmic ray muons and neutrino induced incoming muons from outside. The contamination rate of the remaining background events is estimated as follows.

- **Cosmic ray muons.**
  The rate of cosmic ray muons is estimated by the random-triggered data. The data are analyzed with the same selection. As the result, the cosmic ray contamination is 1.0% of the neutrino candidates in the Fiducial-C. In Jun.99 and Nov.99 run before the installation of the buffer-amplifiers, the reflection pulse in a signal cable sometimes caused fake events miss-identified as the Fiducial-C events. During this period, the contamination was estimated to be 2.6%.

- **Neutrino induced incoming muons.**
  The random-triggered data do not include in-coming muons from the neutrino interaction in surrounded materials. Most of them are injected from the upstream of

Period		Jun.99	Nov.99	Jan.00	Feb.00	Mar.00	May.00	Jun.00
Target diameter		20mmϕ	30mmϕ					
HORN		200kA	250kA					
P.O.T. ($\times 10^{18}$)		2.60	2.62	1.81	3.74	3.35	2.42	3.16
total peak in FADC	N_{peak}^{total}	109119	118321	85238	177437	155778	88558	114739
1 peak in FADC	N_{peak}^{1}	89782	96304	67641	140740	122651	74135	95652
Observed events	N_{obs}	4282	4923	3505	6986	6080	3574	4745
Efficiency	ϵ_{1kt}	0.706	0.708	0.719	0.724	0.719	0.718	0.718
Background	R_{BKG}	0.031	0.031	0.015	0.015	0.015	0.015	0.015
7-bunch correction	$k_{7\rightarrow 9}$	–	–	–	–	–	1.282	1.283
Total interactions	N_{corr}	7150	8286	6052	11985	10581	7510	10021
Event rate (/10^{15}pot)		2.76	3.17	3.34	3.21	3.17	3.10	3.17

Table 8.2: 1kt event summary.

> the tank and they penetrate the front side of outer-detector. Some of the selected neutrino candidates in Fiducial-C, with outer-detector hit were visually scanned by physicists. It was found about 1/4 of them are identified to the incoming muons from the upstream, which amounts to 0.5% of the total neutrino candidates.

Therefore, $R_{BKG} = 1.5\%$ (3.1% for 1999 run) of the neutrino candidates are considered as the incoming muons. The number of neutrino events are corrected with this factor R_{BKG}.

8.2 Neutrino Event Rate

8.2.1 Event rate calculation

In order to obtain the number of events in 1kt, the events in Fiducial-C (Figure 8.4) are selected. The results are summarized in Table 8.2.

The total number of neutrino interactions are calculated as;

$$N_{corr} = N_{obs}^{1} \cdot \left(\frac{N_{peak}^{total}}{N_{peak}^{1}}\right) \cdot \left(\frac{1}{\epsilon_{1kt}}\right) \cdot \left(\frac{1}{1+R_{BKG}}\right) (\cdot k_{7\rightarrow 9bunch}) \tag{8.1}$$

Where,

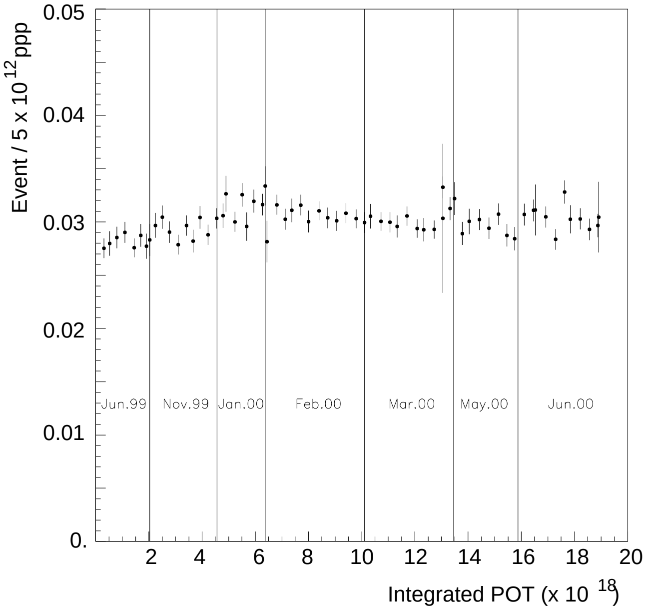

Figure 8.6: Stability of the 1kt event in Fiducial-B, from Jun.99 to Jun.00. Number of events are efficiency corrected by Formula 8.1. Data point is summarized by every 2 days, and plotted by integrated proton on target in horizontal axis. Vertical axis is the event rate per 5×10^{12} protons. Error bars are only the statistical error.

N_{corr} : The number of neutrino interactions in Fiducial-C.
N^1_{obs} : Number of observed events in Fiducial-C.
$\left(\frac{N^{total}_{peak}}{N^1_{peak}}\right)$: Correction factor of multiple-event (Section 8.1.2). Typically $1.2 \sim 1.3$.
ϵ_{1kt} : Event selection efficiency (Section 8.1.3). Typically $0.71 \sim 0.72$.
R_{BKG} : Background contamination rate (Section 8.1.4).
$k_{7\rightarrow 9bunch}$: Correction factor for 7-bunch analysis, only in May.00 and Jun.00 run (Section 8.1.2).

In total, 34095 events are observed during the corresponding period of 1.97×10^{19} p.o.t. This number is corrected to be $N_{corr} = 61585 \pm 335(stat.)$ events.

8.2.2 Event rate stability

Stability of the 1kt event rate is studied. Fiducial-B are used to increase the statistics. Figure 8.6 shows the observed rate of every two days. There are no obvious time variations

<table>
<tr><th colspan="2">Period</th><th>Jun.99</th><th>Nov.99</th><th>Jan.00</th><th>Feb.00</th><th>Mar.00</th><th>May 00</th><th>Jun.00</th></tr>
<tr><td>1</td><td>Fiducial volume</td><td colspan="7">±4.0%</td></tr>
<tr><td>2</td><td>Multi-event treatment</td><td colspan="7">±3.0%</td></tr>
<tr><td>3</td><td>FADC threshold</td><td>±1.0%</td><td>±1.4%</td><td colspan="5">±1.0%</td></tr>
<tr><td>4</td><td>Energy scale</td><td colspan="7">±1.0%</td></tr>
<tr><td>5</td><td>Background rate</td><td colspan="2">±1.0%</td><td colspan="5">±0.5%</td></tr>
<tr><td>6</td><td>7-bunch/9-bunch</td><td colspan="5">–</td><td colspan="2">±1.2%</td></tr>
<tr><td colspan="2">Total</td><td>±5.3%</td><td>±5.4%</td><td>±5.2%</td><td>±5.2%</td><td>±5.2%</td><td>±5.4%</td><td>±5.4%</td></tr>
</table>

Table 8.3: Systematic errors of 1kt measurement.

except for the statistical fluctuation.

8.2.3 Systematic errors at 1kt

Systematic errors of the event rate are summarized in Table 8.3 and described as follows;

1. **Fiducial volume error.**
   The vertex reconstruction of TDC fit is experimentally studied using cosmic ray, as described in Appendix D and [52]. The result proves that the vertex reconstruction is much better for transverse direction with respect to the particle direction than that for longitudinal direction. The neutrino events are dominantly directed to z-axis. therefore, z-vertex distribution is compared.

   Vertex profile is analyzed with the selected event in the Fiducial-A. Due to the cylindrical shape of the volume, target mass correction is applied to the horizontal profile. Figure 8.7 shows the reconstructed vertex distribution of horizontal (X), vertical (Y) and longitudinal (Z) direction. Monte Carlo simulations (neutMC) are overlaid in the figures.

   In principle, the z-vertex distribution should be flat. However, the observed distribution is systematically uneven structure, due to the effect of the vertex reconstruction. Therefore, the event rate of data and neutMC are compared with various fiducial volume definition of z-vertex. Table 8.4 shows the results. The largest discrepancy between the data and the neutMC is 3%. The X and Y profiles show good agreement between data and neutMC. The difference of the event rate of data and neutMC along the X and Y direction is within 1%. In consequence, ±4% error is assigned for fiducial volume related uncertainty.

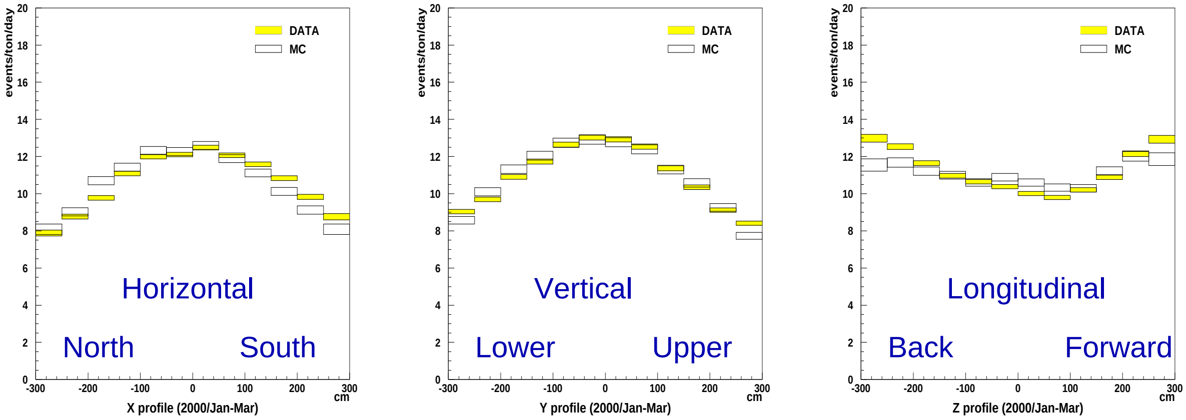

Figure 8.7: Vertex profile of horizontal, vertical, and longitudinal direction in 1kt detector, after target mass correction.

z-vertex	DATA	neutMC	relative DATA/MC
$-2 < z < 0$ m (Fiducial-C)	16571	13223	1.
$-3 < z < 0$ m	24990	19418	1.03
$-2 < z < +2$ m (Fiducial-B)	31290	25720	0.97
$-2 < z < +3$ m	39330	32139	0.98
$-2 < z < +4.5$ m	49449	38425	1.03

Table 8.4: Event rate comparison (DATA/MC) with various fiducial volume definition of z-vertex. DATA means the observation from Jan.00 to Mar.00.

FADC threshold change	number of events	relative rate
Default	90300	1.
-10%	91081	1.01
-5%	90723	1.01
$+5\%$	89838	0.99
$+10\%$	89320	0.99

Table 8.5: Effects for the event rate caused by the FADC threshold change. "Event" means the selected events in Fiducial-C. This is estimated by neutMC.

2. **Multiple-event treatment error.**
   The FADC peak search algorithm cannot distinguish multiple-events occurred at one bunch in the spill from a single neutrino interaction. The probability of the multiple-events in one bunch is estimated to be 3%. This 3% is assigned as the systematic error due to the multiple-event treatment.

3. **FADC threshold error.**
   The threshold of FADC is set at about 1000 photo-electron as shown in Figure 8.2. The threshold is stable within 10% for full period. The 10% change on the threshold causes 1% change on the event rate, as shown in Table 8.5.

   In Nov.99 run, the analog-summed cable is disconnected as described in Section 8.1.2. An additional error 1% was estimated the difference between the obtained efficiency curve from the data and the simulation with multiple-event consideration. The error was assigned to be 1.4% by the quadrature sum of these errors.

4. **Energy scale error.**
   The absolute energy scale of 1kt detector is calibrated within 5% accuracy, as described in Chapter 3.5.1. If the energy scale is 5% shifted, FADC threshold is effectively changed. Table 8.5 shows that 5% change causes less than 1% changes for the event rate. The energy scale error is conservatively assigned to be 1%.

5. **Background rate uncertainty.**
   Estimation of the background rate (R_{BKG}) is described in Section 8.1.4. The uncertainty of the estimation is ±1% in 1999 and 0.5% to the other period.

6. **Correction factor for 7-bunch analysis.**
   Correction factor of 7-bunch/9-bunch ($k_{7\rightarrow 9-bunch}$) is described in the previous Section 8.1.2 and its error is quoted to be ±1.2%.

8.2.4 Summary of the neutrino event rate at 1kt

In summary, the total number of neutrino interactions from Jun.99 to Jun.00 (1.97×10^{19} p.o.t.) are;

$$N_{corr} = 61585 \pm 335(stat.) \pm 3261(syst.)$$

8.3 Constraint of the Low Energy Neutrino Spectrum

Neutrino energy spectrum is well predicted only above 1 GeV by PIMON analysis as described in Section 6.1. However, beamMC says about 16% of the observed events at SK are expected to come from the neutrinos below 1GeV in case there is no neutrino oscillation. Then, the neutrino flux below 1 GeV should be confirmed. For this purpose, total photo-electron distribution of 1kt is studied.

8.3.1 Total photo-electron distribution

Total photo-electron basically corresponds to the total energy deposit of the muons in the 1kt water. Charged pions and gamma conversion from π^0 emit additional photons if in-elastic interaction occurs. Proton has small contribution due to the high Cherenkov threshold.

Figure 8.8 is the comparison of the total photo-electron distributions between observed data and the neutMC in Fiducial-C. There is a discrepancy between the observation and the neutMC, which may be explained by the detector systematics (absolute energy scale, scattering parameters, or other systematic differences), or physics reason (cross section, or neutrino spectrum shape). It is hard to solve this discrepancy, but we can conservatively exclude some extreme cases to take the constraint to the neutrino flux below 1 GeV.

Figure 8.8-right shows the comparison of the observed total photo-electron distribution with MC with changing the flux below 1GeV by ±100%. The histograms are normalized by the total entry in $7000 <$ (total p.e.) < 20000, because they definitely come from the neutrinos with more than 1GeV energy. From this figure, ±100% is the rather conservative estimation of the flux uncertainty below 1 GeV, and used for the number of event comparison.

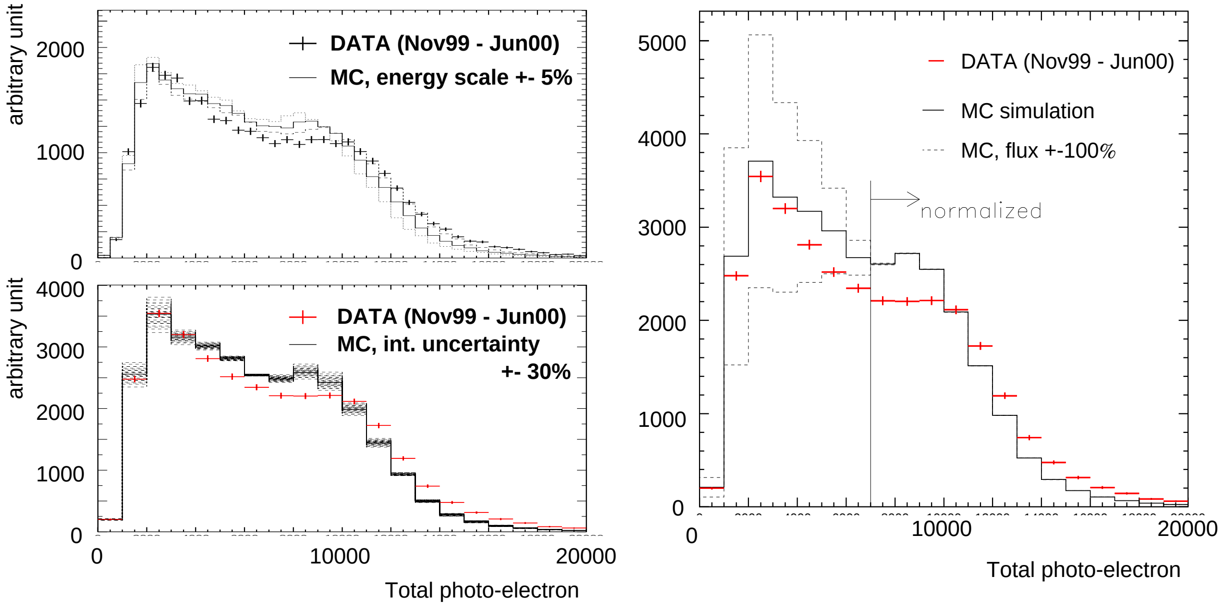

Figure 8.8: Comparison of observed total photo-electron distribution (bold cross) overlaid with the neutMC (histogram). In left-top figure, the MC with ±5% shifted energy scale are also overlaid. Left-bottom figure shows the various MC with changing both the NC cross section by ±30% and the in-elastic cross section by ±30%. For both figure, normalization is done by the entry of each histogram over 2000 p.e. In right figure, the MCs which are changed the neutrino flux below 1GeV by ±100%, are overlaid. These histograms are normalized by the area of $7000 <$ (total p.e.) < 20000.

Chapter 9

Neutrino Event Measurement at Super-Kamiokande

9.1 Neutrino Event Selection

”K2K candidate” is selected from a large amount of cosmic ray background, radioactive background and natural neutrino activities in Super-Kamiokande (SK). Figure 9.1 shows a typical neutrino event observed in SK.

The best mark of our neutrino event is the time matching to the beam spill time, based on GPS. The dime difference $\Delta(T)$ is defined as follows;

$$\Delta(T) \equiv T_{SK} - T_{KEK} - TOF \tag{9.1}$$

where, T_{SK} is the observed time in SK, T_{KEK} is the start time of the beam spill in KEK, and $TOF(= 833\mu\text{s})$ is the time-of-flight from KEK to SK. After then, contained neutrino events are selected with similar selection algorithm to the atmospheric neutrino observation in SK [61].

The selection criteria are briefly described as follows, and the number of selected events are summarized in Table 9.1.

1. **Good beam spill definition.**
   The good beam spills are defined in Chapter 5.3.

2. **Rough GPS time cut.**
   From all of the triggered events in SK, we select the events with the criteria of $|\Delta(T)| < 500\mu\text{s}$ matching to each of the good beam spill.

3. **High energy (HE) trigger.**
   HE-triggered events are used for K2K candidate search. Threshold of the HE trigger

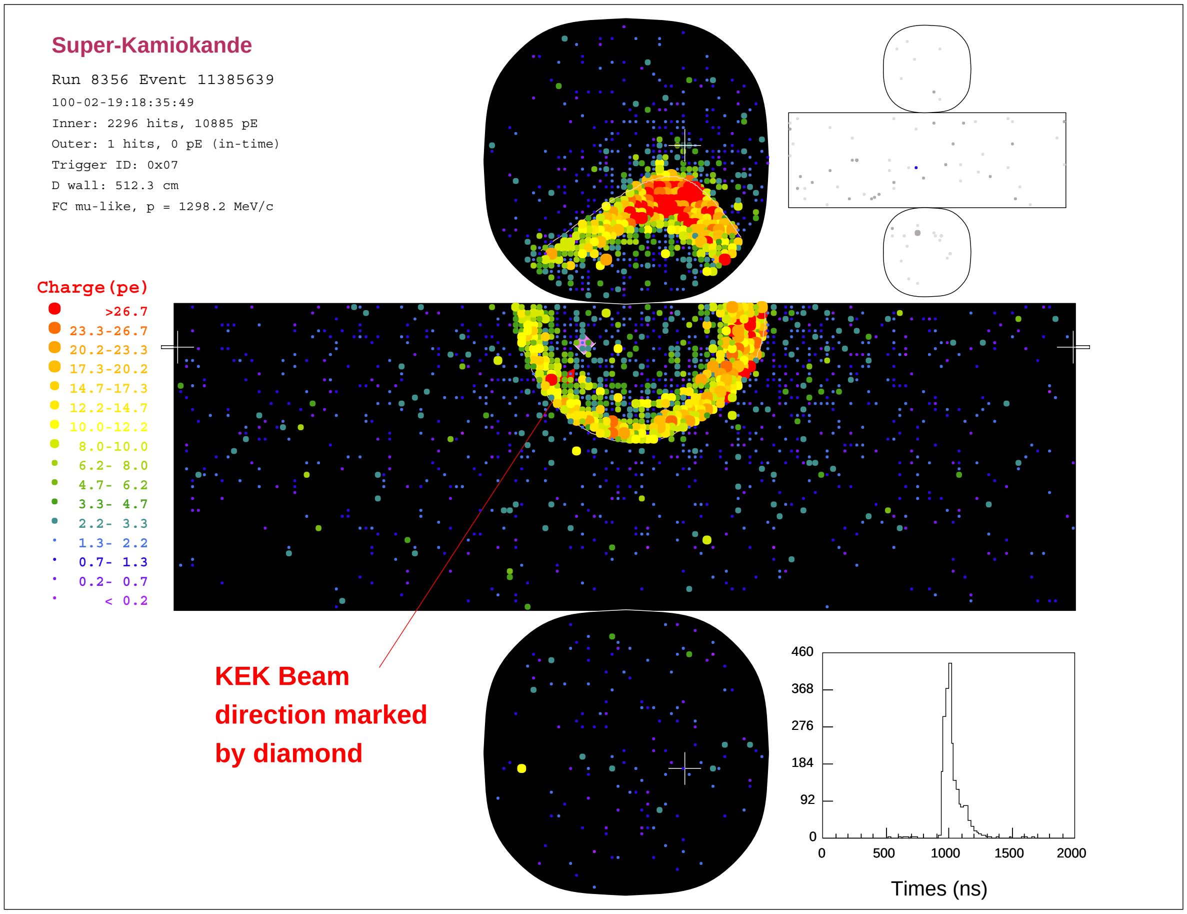

Figure 9.1: Typical neutrino event in Super-Kamiokande, observed on Feb. 19, 2000. Observed charge (photo-electron) in each PMT is indicated by color scale. The large map shows the inner PMTs and upper-right figure shows the hit map of the outer PMTs. Lower-right figure shows the corrected timing distribution. This event passes the following selection criteria and fitted as a contained event with 1 μ-like ring.

	Selection	DATA	MC
1	Analyzed number of spill	4404180	
	(MC) generated in the tank		30495
	(MC) generated in fiducial		(13938)
2	$\|\Delta(T)\| < 500\mu$s		
3	HE-trigger		
4	Decay electron cut	17102	↓
5	Total photo-electron cut	8944	18739
6	Flasher cut	8797	18190
7	Outer detector cut	51	15917
8	Fitting goodness cut	50	15907
9	Visible energy cut	46	15448
10	Fiducial volume cut	29	10937
11	$-0.2 < \Delta(T) < 1.3\mu$s	28	↓

Table 9.1: Summary of the number of selected events in each step.

is given by requiring more than about 31 hits in inner PMTs (described in Chapter 3.6.2). This is equivalent about to $50 \sim 100$ photo-electrons.

4. **Decay electron cut.**
   If muons stop inside the tank, decay electrons make Cherenkov rings, which often miss-identified to the neutrino events. Therefore, events which have activities before 30μs are removed. Dead time factor caused by this selection is less than 1/1000, since the total trigger rate (except SLE trigger) is typically ~ 10 Hz.

5. **Total photo electron cut.**
   Since the HE trigger threshold is smeared by PMT relative gain fluctuation, more conservative cut is applied after gain correction. Number of total photo-electrons (p.e.) in 300 ns time window is calculated from the reformatted data. The threshold is set at 200 p.e. This threshold is equivalent to 20 MeV deposited energy. Figure 9.2 shows this cut for data and neutMC. Rejected events in the first peak around 100 p.e. is mainly the events interacted by NC elastic scattering.

6. **Flasher cut.**
   It is already known that there are some "flasher PMTs" in SK. They are caused by sparks inside of the PMTs. They sometimes make similar ring hit patterns like Cherenkov light. To inhibit such fake events, "flasher cut" is applied. First, (maximum photo-electron)/(total photo-electron)≤ 0.2 is required as Figure 9.3. Next,

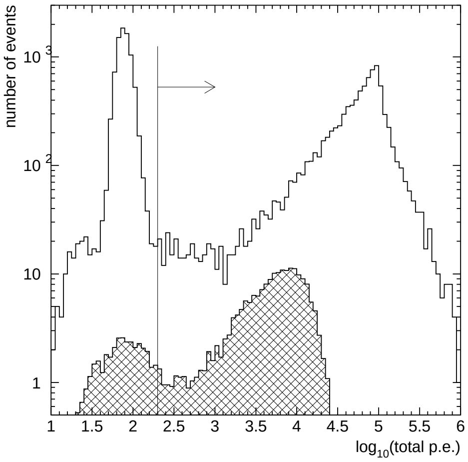

Figure 9.2: Distribution of total photo-electron (p.e.) in 300 ns time window. The horizontal axis is log_{10} p.e., and the vertical axis is entry. The hatched area is neutrino event of neutMC, normalized by its expected number of event by equivalent POT. Greater than or equal as 200 p.e. is required.

two identical flasher cut is applied for the fake event cut. One of this cut eliminates continuous flashing events after 1200 to 1700 ns. The other cut uses ring pattern identification after low energy ring fitting.

7. **Outer detector cut.**
   The events which have more than 10 PMT hits in the largest hit cluster in outer detector arrays are rejected as shown at Figure 9.4. This cut effectively selects fully-contained events from the large background of cosmic ray activities. Also the events which have more than 50 hits within 800 ns time window in outer detector are eliminated.

8. **Fitting goodness cut.**
   In order to define vertex point of the interaction, TDC fit (described in Appendix C) is applied to the remaining events. Little fraction of badly fitted events are reduced when the fitting goodness shows less than 0.

9. **Visible energy cut.**
   In order to avoid the threshold uncertainty of the total photo-electron cut, more conservative energy cut is applied. Electron-equivalent energy E_{vis} is calculated from the sum of the observed signal belonging to the Cherenkov ring, considering the attenuation correction. $E_{vis} \geq 30$ MeV is required.

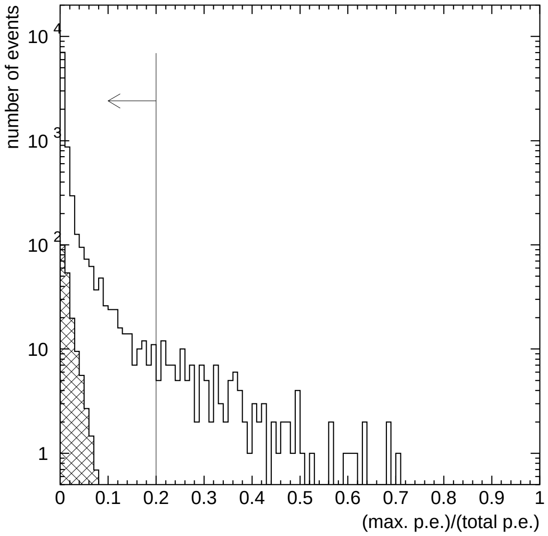

Figure 9.3: Ratio of maximum photo-electron in one PMT over total photo-electron. The hatched area is neutrino events of neutMC.

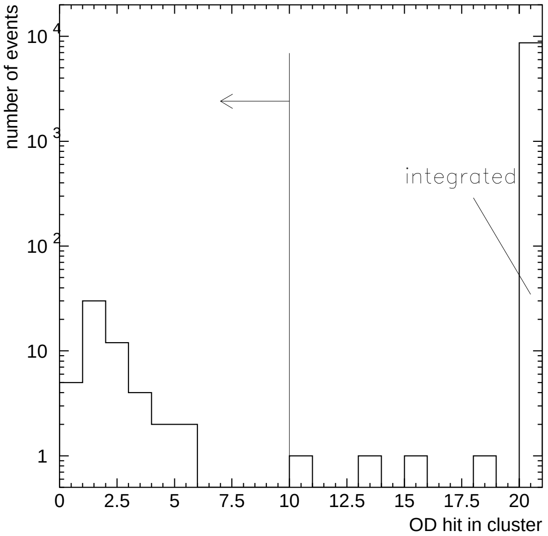

Figure 9.4: Number of outer PMTs in largest hit cluster. The highest bin contains the events with number of PMTs $\geq .20$.

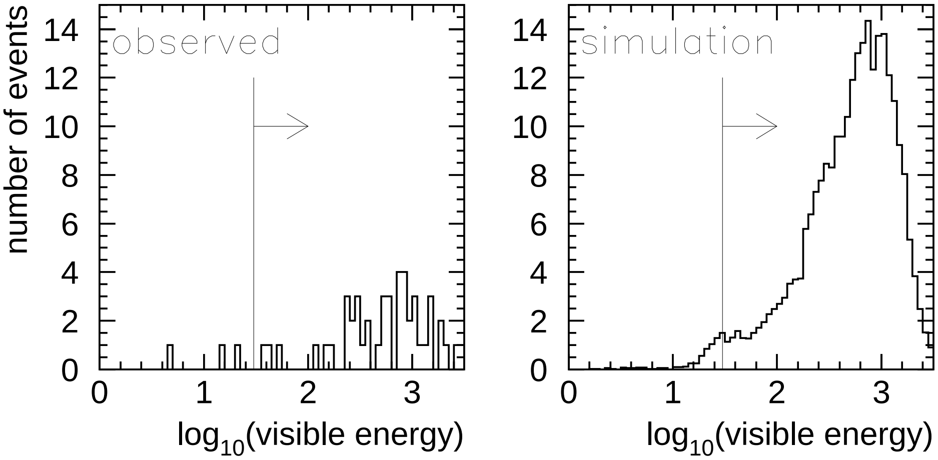

Figure 9.5: Visible energy distribution for observed data (left) and neutMC (right). Threshold is set at 30 MeV of electron equivalent energy.

10. **Fiducial volume cut.**
    The event is required to have its reconstructed vertex point 2 m from the tank wall. This requirement avoids the event reconstruction uncertainty near the PMTs. As a consequence, a fiducial volume of 22.5 kt water is defined in the SK tank.

11. **Fine GPS timing cut.**
    Tighter timing cut is applied using GPS time stamp. The resolution and the uncertainty of the time stamp is about 0.2μs. Therefore, time window of $-0.2 < \Delta(T) < 1.3\mu$s is the suitable cut for timing requirement. Figure 9.7 shows the precise timing distribution. The events are clearly identified in the expected time window.

Figure 9.8 shows the selection efficiency of the neutrino events interacted in the fiducial volume, as a function of the neutrino energy, estimated by neutMC. The efficiency for CC interactions is 93%, and for NC in-elastic interactions it is 68%. The efficiency for all the interactions is 78%.

9.2 Observed events

After these event selection, 28 fully-contained events are observed during the whole running period from June 1999 to June 2000. Figure 9.7 clearly shows that observed events were accumulated at the expected arrival time. The figure also exhibits that the background events due to the atmospheric neutrinos are very rare, as expected.

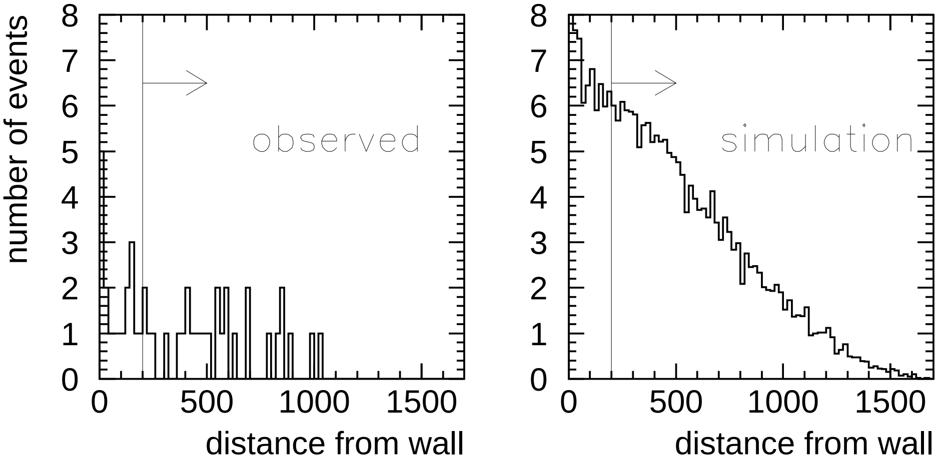

Figure 9.6: Reconstructed vertex distance from the tank wall. The events with (distance) $\geq$ 2 m away are selected. Left figure is for observed events, and right figure is for neutMC.

Figure 9.9 shows the reconstructed vertex distributions. This figure shows that neutrino events are uniformly distributed and no obvious bias is observed with this statistics. Reconstructed direction and momentum for each Cherenkov ring are expressed by the line direction and their size. They are obtained after the ring-counting routine which is used for the atmospheric neutrino analysis in SK [9, 61]. The momentum and angular distributions are shown in Appendix G, without any quantitative discussion.

An expected background is atmospheric neutrino interactions. Typical rate of the fully-contained events in SK is 8 events per day [9]. Considering the 1.5μs time window, the accidental contamination of atmospheric neutrino events are estimated to be order of 10^{-3} events during the whole period.

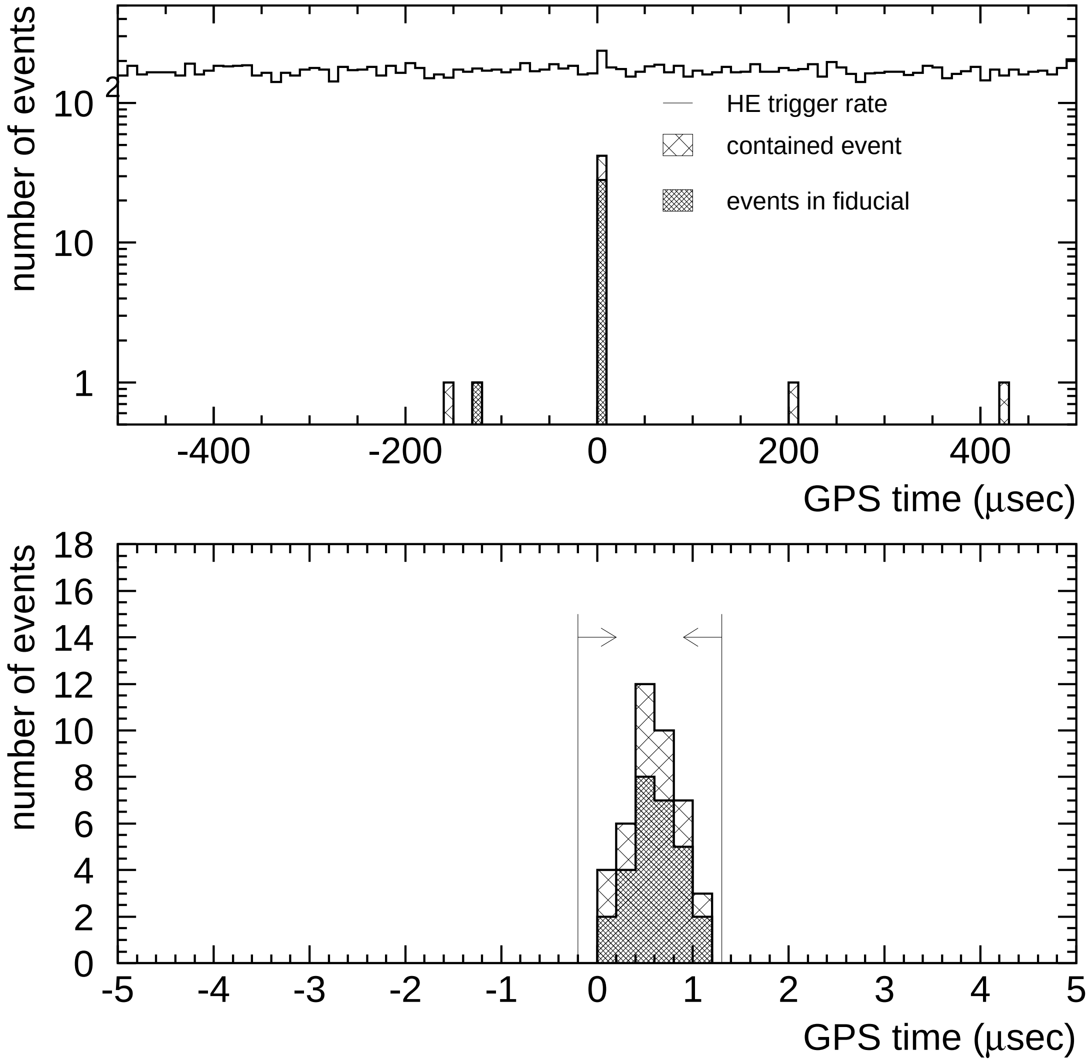

Figure 9.7: Time difference distribution of HE triggered events(solid line), fully contained events after visible energy cut(hatched), and selected events in fiducial volume(dark hatched). Upper figure is ±500 ns and lower figure os ±5 μs. We can see clear peak at just within 1.1 μs of beam spill width and ±0.2 μs of GPS precision.

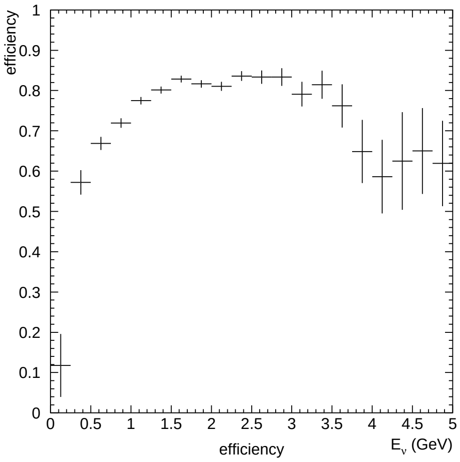

Figure 9.8: The selection efficiency at Super-Kamiokande, as a function of neutrino energy. This is estimated using neutMC.

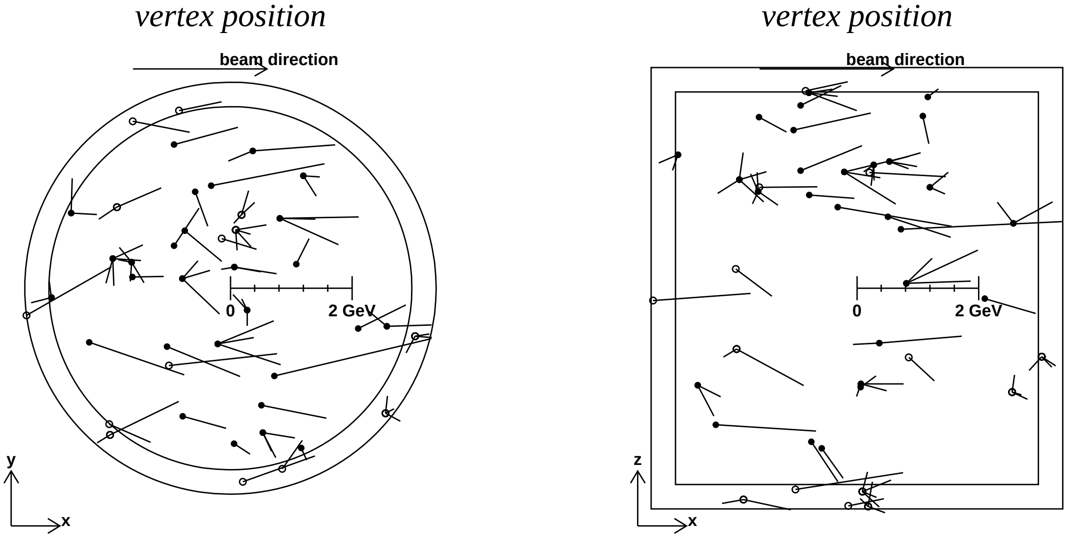

Figure 9.9: Reconstructed vertex distribution in SK. Left figure shows the top view and the right figure is the side view with respect to the beam direction. Outer circle and box represent the inner detector wall, and the inner circle and the box represents the boundary of the fiducial volume. Each circle point shows the reconstructed vertex position and the line represents the reconstructed particle momentum along the Cherenkov ring. Closed circles correspond to the events whose vertices are in the fiducial volume. Open circles are the events whose vertices are out of the fiducial volume.

Chapter 10

Comparison of Near and Far Event Rate

In this chapter, a comparison of the number of events between the near and the far site is discussed.

10.1 Key Issues of the Near Site Measurement

Following neutrino beam properties are measured and confirmed;

- PIMON measures the distributions of Cherenkov photons emitted by pions. They correspond to the momentum and angular distribution of pions. The result is well reproduced by the Monte Carlo simulation (beamMC) with hadron interaction parameterized by Cho experiment. Therefore, the neutrino energy spectrum and the flux ratio Φ_{far}/Φ_{near} are obtained from beamMC and their systematic errors are estimated using PIMON results.

- Neutrino profile is measured by MRD. It confirms that neutrino beam is continuously pointed to Super-Kamiokande within 1 mrad accuracy. The profile width is reproduced by the Monte Carlo simulation (neutMC) with the neutrino beam prediction from beamMC. Muons from pion decay are measured using MUMON. It also supports the neutrino beam direction on spill-by-spill basis.

- Neutrino beam stability is continuously monitored by MRD. The distributions of the profile width, the muon spectrum, and the event rate are analyzed. These distributions are quite stable through the whole run, which confirms the neutrino beam stability. The event rate at 1kt is also stable during the whole run.

These facts allow us to compare the event rate at the near site with that at the far site. The number of expected neutrino events in SK is estimated based on the number of observed events in the near detector. The 1kt measurement is used for the estimation, because the target nuclei is same and the detection technique is similar to SK.

10.2 Estimation of the Expected Number of Events

10.2.1 Extrapolation formula

The number of expected neutrino events N_{exp}^{SK} at SK is derived by extrapolation the number of observed events N_{obs}^{1kt} at 1kt by following formula;

$$N_{exp}^{SK} = N_{corr}^{1kt} \cdot R_{SK/1kt} \cdot \frac{POT_{SK}}{POT_{1kt}} \cdot \epsilon_{SK} \tag{10.1}$$

where, N_{corr}^{1kt} is the number of neutrino interaction defined by Formula 8.1, ϵ_{SK} is the event selection efficiency, POT_{1kt} and POT_{SK} is the number of proton on target (p.o.t.), and $R_{SK/1kt}$ is the ratio of the number of neutrino interaction at SK and 1kt. The values are explained as follows;

Number of neutrino interaction at 1kt: N_{corr}^{1kt}

N_{corr}^{1kt} is the total number of neutrino interactions in 1kt, which is obtained with Formula 8.1. In the formula, N_{obs}^{1kt} is the observed events in the Fiducial-C of 1kt. Table 8.2 summarizes the result of the observation and the correction.

Ratio of the number of neutrino interaction: $R_{SK/1kt}$

$R_{SK/1kt}$ is given as follows;

$$R_{SK/1kt} = \frac{k \cdot \Phi_{SK} \cdot \sigma_{H_2O} \cdot M_{SK}}{k \cdot \Phi_{1kt} \cdot \sigma_{H_2O} \cdot M_{1kt}} \tag{10.2}$$

where, Φ_{SK} and Φ_{1kt} are the neutrino flux per unit P.O.T, per unit area, averaged over their fiducial area, σ_{H_2O} is the cross section, M_{SK} and M_{1kt} are the fiducial mass, and k is a normalization factor corresponding to Avogadro constant N_A. After cancellation, $R_{SK/1kt}$ represents the flux ratio Φ_{SK}/Φ_{1kt} multiplied by the fiducial mass difference $M_{SK}/M_{1kt} \sim 900$. Since the beamMC well reproduces the PIMON measurement (Chapter 6.1), the energy integrated ratio $R_{SK/1kt}$ is provided by the beamMC. That is 6.81×10^{-4} for Jun.99 run, and 6.71×10^{-4} for other periods.

Live time correction: $\frac{POT_{SK}}{POT_{1kt}}$

As shown in Table 5.1, 1kt data was not taken (or not used) in 14% of SK live time. Neutrino events in these periods are extrapolated with p.o.t. normalization.

Selection efficiency at Super-Kamiokande: ϵ_{SK}

Selection efficiency of SK is estimated using Monte Carlo simulation. Efficiency curve as a function of neutrino energy is shown in Figure 9.8. The integrated efficiency is 0.781 for Jun.99 run, and 0.785 for other periods.

10.2.2 Result

Table 10.1 summarizes the results of N_{exp}^{SK}. In total,

$$\begin{aligned} N_{exp}^{SK} &= 37.8 \pm 0.2(stat.)^{+3.8}_{-4.0}(syst.) \\ &= 37.8^{+3.8}_{-4.0}(stat. + syst.) \end{aligned}$$

events are expected when a neutrino oscillation does not occurred, for 2.29×10^{19} p.o.t. Statistical error ($stat.$) comes from the number of observed events in 1kt. The systematic error ($syst.$) is described in the next section.

10.2.3 Systematic error for N_{exp}^{SK}

Systematic errors on N_{exp}^{SK} are estimated in Table 10.2. The largest systematic error is due to the uncertainty of $R_{SK/1kt}$ (6(b)), which is derived from the PIMON analysis. The second dominant error is related to the 1kt measurement (1), described in Chapter 8.2.3. The third dominant error comes from the uncertainty of the neutrino energy spectrum (6(a)). This is due to the difference of the energy threshold of SK and 1kt.

The systematic errors are explained as follows.

1. **1kt measurement.**
   The error on the event rate at 1kt is already discussed in Chapter 8.2.3.

2. **P.O.T. normalization.**
   The analysis extrapolates the event rate to the 1kt dead time, normalized by accumulated P.O.T. The uncertainty of the number of events in this period comes from the stability of the event rate with P.O.T. normalization. The error is expressed by;

   $$\text{(r.m.s. of event rate stability in 1kt)} \times \text{(percentage of the 1kt dead time)} \quad (10.3)$$

   Using this formula, the error is calculated on monthly basis.

Period	Jun.99	Nov.99	Jan.00	Feb.00	Mar.00	May.00	Jun.00
Target diameter	20mmϕ	30mmϕ					
HORN	200kA	250kA					
N_{obs}^{1kt}	4282	4923	3505	6986	6080	3574	4745
N_{corr}^{1kt}	7150	8286	6052	11985	10581	7510	10021
POT_{1kt} $(\times 10^{18})$	2.60	2.62	1.81	3.74	3.35	2.42	3.16
POT_{SK} $(\times 10^{18})$	3.10	3.57	2.22	4.04	3.71	2.56	3.75
$R_{Far/Near}$ $(\times 10^{-4})$	6.81	6.71					
ϵ_{SK}	0.781	0.785					
N_{exp}^{SK}	4.54	5.95	3.90	6.83	6.17	4.17	6.27
Stat. error	±0.07	±0.09	±0.07	±0.09	±0.08	±0.07	±0.10
Syst. error	+0.75	+0.55	+0.35	+0.62	+0.56	+0.38	+0.58
	−0.64	−0.61	−0.39	−0.68	−0.61	−0.42	−0.63

Total: $N_{exp}^{SK} = 37.8 \pm 0.2(stat.)^{+3.8}_{-4.0}(syst.)$

Table 10.1: Calculated number of expected event at SK from 1kt measurement.

	Item	Jun.99	Nov.99	Jan.00	Feb.00	Mar.00	May.00	Jun.00
1	1kt measurement (Table 8.3)	±5.3	±5.4	±5.2	±5.2	±5.2	±5.4	±5.4
2	P.O.T. normalization	±1.0	±1.9	±1.1	±0.4	±0.7	±0.3	±1.0
3	Neutrino profile (direction)	+1.0	+0.6					
4	Proton targeting stability	$^{+1.6}_{-1.3}$						
5(a)	NC/CC uncertainty	$^{+0.6}_{-0.7}$						
5(b)	in-elastic cross section	$^{+0.3}_{-0.5}$						
6(a)	Neutrino energy spectrum	$^{+6.7}_{-7.9}$	$^{+3.9}_{-3.6}$					
6(b)	$R_{SK/1kt}$ ratio	$^{+13.6}_{-9.8}$	$^{+5.1}_{-6.8}$					
7	SK selection efficiency	±3.0						
	Total	$^{+16.5}_{-14.1}$	$^{+9.3}_{-10.2}$	$^{+9.0}_{-9.9}$	$^{+9.0}_{-9.9}$	$^{+9.0}_{-9.9}$	$^{+9.1}_{-10.0}$	$^{+9.2}_{-10.0}$

Table 10.2: List of systematic error for N_{exp}^{SK} from 1kt measurement. Unit is %.

3. **Neutrino profile error.**
   Uncertainty of the neutrino beam direction is discussed in Chapter 7.3. There, Table 7.5 presents the change of the number of events, due to the off-pointing.

4. **Errors from proton targeting stability.**
   The uncertainty of the monitor of proton targeting is discussed in Chapter 6.2. Most of the systematic error comes from the uncertainty of the proton profile measurement.

5. **Uncertainty of the neutrino interaction.**
   Neutrino interaction is described and its uncertainty is discussed in Chapter 4.2.8. Since the target material is water in both detectors, uncertainty of the absolute cross section is canceled. However, the selection efficiency for each interaction mode in SK is different from that in 1kt. Therefore, the uncertainty of the neutrino interaction model causes the uncertainty of the ratio of the event rate at SK and 1kt. They are following two issues;

   (a) The ratio between the Neutral Current (NC) and the Charged current (CC) cross section.
   This uncertainty is estimated by changing the NC cross section by ±30% comparing to CC interaction in neutMC. Table 10.3 shows the change of the selection efficiency. The difference of $\epsilon_{SK}/\epsilon_{1kt}$ from the default one is quoted as the systematic error due to "NC/CC uncertainty".

   (b) The cross section of the in-elastic interaction compare to (quasi-)elastic scattering.
   This uncertainty is estimated by changing the in-elastic (single-meson production, multi-pion production, and coherent-pion production of both CC and NC) cross section by ±30% comparing to (quasi-)elastic scattering cross sections, in neutMC. The results are also shown in Table 10.3. The difference of $\epsilon_{SK}/\epsilon_{1kt}$ from the default one is quoted as the systematic error due to "in-elastic cross section uncertainty".

6. **Errors from neutrino energy spectrum and $R_{SK/1kt}$ uncertainty.**
   The selection efficiency of 1kt and SK have energy dependence as shown in Figure 8.5 and 9.8). The flux ratio Φ_{SK}/Φ_{1kt} also have energy dependence as shown in Figure 6.5. In Formula 10.1, and Formula 10.2, the selection efficiency ϵ_{1kt}, ϵ_{SK}, and the ratio of number of interaction $R_{SK/1kt}$ are calculated as a integration of these plots over the all energy range. Therefore, the uncertainty of the neutrino energy spectrum affects to these values; ϵ_{1kt}, ϵ_{SK}, and $R_{SK/1kt}$. Then, it provides the systematic error of N_{exp}^{SK}. This systematic error is estimated.

σ_{NC}	1.	1.3	0.7	1.	1.
$\sigma_{inelastic}$	1.	1.	1.	1.3	0.7
ϵ_{1kt}	1.	0.96	1.05	1.01	0.98
ϵ_{MRD}	1.	0.93	1.08	0.98	1.02
ϵ_{SK}	1.	0.96	1.04	1.02	0.98
$\epsilon_{MRD}/\epsilon_{1kt}$	1.	0.97	1.03	0.97	1.03
$\epsilon_{SK}/\epsilon_{1kt}$	1.	1.01	0.99	1.00	1.00
$\epsilon_{SK}/\epsilon_{MRD}$	1.	1.03	0.96	1.03	0.95

Table 10.3: The event selection efficiency =(selected)/(generated) change for each detector, when the NC cross section and in-elastic cross section change by ±30% relative to CC quasi-elastic scattering. "In-elastic" includes single-meson production, multi-pion production, and coherent-pion production, of both CC and NC.

The values ϵ_{1kt}, ϵ_{SK}, and $R_{SK/1kt}$ are provided by neutMC, as follows;

$$\epsilon_{1kt} = \left(\frac{N^{1kt}_{obs}}{N^{1kt}_{gen}}\right)_{MC} \qquad \epsilon_{SK} = \left(\frac{N^{SK}_{obs}}{N^{SK}_{gen}}\right)_{MC} \qquad R_{SK/1kt} = \left(\frac{N^{SK}_{gen}}{N^{1kt}_{gen}}\right)_{MC}$$

where, N_{gen} is the number of generated events, and N_{obs} is the number of observed events in neutMC. Then, N^{SK}_{exp} is expressed as;

$$N^{SK}_{exp} \quad = \quad N^{1kt}_{obsDATA} \cdot \left(\frac{N^{SK}_{obs}}{N^{1kt}_{obs}}\right)_{MC} \tag{10.4}$$

In this formula, other corrections are neglected.

When the neutrino flux of each energy bin i at 1kt changes by $\Delta\phi_i$, change of the the neutrino flux at SK is expressed by the sum of the correlated change and the un-correlated change as $(\Delta\phi_i + \Delta r_i)$. Then, N^{SK}_{exp} changes to $N\prime_{exp}$ as follows;

$$\begin{aligned} N\prime_{exp} &= N^{1kt}_{obsDATA} \cdot \left(\frac{N^{SK}_{obs} + \sum_i(\Delta\phi_i + \Delta r_i) \cdot n^{SK}_i}{N^{1kt}_{obs} + \sum_i(\Delta\phi_i) \cdot n^{1kt}_i}\right)_{MC} \\ &\simeq N^{SK}_{exp} \cdot \left[1 + \left(\sum_i \Delta\phi_i \left(\frac{n^{SK}_i}{N^{SK}_{obs}} - \frac{n^{1kt}_i}{N^{1kt}_{obs}}\right)\right) + \left(\sum_i \Delta r_i \frac{n^{SK}_i}{N^{SK}_{obs}}\right)\right]_{MC} \end{aligned} \tag{10.5}$$

where, n_i is the number of observed events from the neutrinos in i-th energy bin $(\sum_i n_i = N_{obs})$, in neutMC. The second expression is valid when ($\Delta\phi_i \cdot (n^{1kt}_i/N^{1kt}_{obs}) \ll 1$), and $((\Delta\phi_i + \Delta r_i) \cdot (n^{SK}_i/N^{SK}_{obs}) \ll 1)$. The second term and the third term express the “(a) error from the near spectrum” and “(b) error from the flux ratio”, respectively.

Changeable range of $\Delta\phi_i$ and Δr_i is given by the uncertainties of the energy spectrum at the near site $\left(\frac{\Delta\Phi}{\Phi}\right)_i$ and the flux ratio $\left(\frac{\Delta R}{R}\right)_i$, which are estimated by PIMON analysis in Chapter 6.1. These uncertainties are shown in Table 6.2, and Table 6.3. We estimate the systematic error with considering following correlation,

- Errors are estimated in 6 energy bins $(0-0.5, 0.5-1, ..., 2.5-$ GeV). Errors between different energy bin have large correlation each other. Thus, linear sum of the errors in each energy bin is taken.
- The error from “(a) near spectrum” does not correlated to “(b) error from the flux ratio”. Thus, quadrature sum of these two errors is quoted as the total systematic error of these uncertainties.

Then, the systematic error of N_{exp}^{SK} is estimated as follows,

$$\begin{aligned}
\Delta N_{exp}^{SK} &= N_{exp}^{SK} \cdot \sqrt{(A)^2 + (B)^2} && (10.6)\\
A &\equiv \left(\begin{array}{c}\text{Sum of errors from}\\ \text{the near spectrum}\end{array} \right) = \sum_{i=1}^{6} \left(\frac{\Delta\Phi}{\Phi}\right)_i \cdot \left(\frac{n_i^{SK}}{N_{obs}^{SK}} - \frac{n_i^{1kt}}{N_{obs}^{1kt}}\right)_{MC} && (10.7)\\
B &\equiv \left(\begin{array}{c}\text{Sum of errors from}\\ \text{the flux ratio}\end{array} \right) = \sum_{i=1}^{6} \left(\frac{\Delta R}{R}\right)_i \cdot \left(\frac{n_i^{SK}}{N_{obs}^{SK}}\right)_{MC} && (10.8)
\end{aligned}$$

The validity of this error estimation is checked as follows. We prepare various beamMCs with various pion distributions within the quoted error. Each of these beamMC gives the energy spectrum at near site, and the flux ratio in each energy bin. The differences of these values from the standard beamMC are summed-up according to the Formula 10.6 to 10.8, to obtain the “predicted” uncertainty of (N^{SK}/N^{1kt}). On the other hand, the beamMC gives the actual difference of (N^{SK}/N^{1kt}) from the standard one. As the result, the “predicted” error range conservatively covers most of the actual difference. Then, this error estimation is proper for our experiment.

Table 10.4 summarizes the estimation with this formula. The limit of the neutrino flux below 1GeV is obtained as $\left(\frac{\Delta\Phi}{\Phi}\right)_{1,2} = \pm 100\%$ by 1kt analysis described in Chapter 8.3.1.

7. **Errors from SK selection efficiency.**
   Following systematic errors are considered in the selection efficiency at SK;

   - Event selection described in Chapter 9.1 is obvious and there are negligible systematic uncertainties except for the vertex reconstruction.

E_ν bin (GeV)	$0.0-0.5$	$0.5-1.0$	$1.0-1.5$	$1.5-2.0$	$2.0-2.5$	$2.5-$
Nov.99 to Jun.00 (250 kA) run						
n_i/N_{obs} (1kt, MC)	0.00	0.15	0.36	0.29	0.13	0.06
n_i/N_{obs} (SK, MC)	0.01	0.15	0.29	0.29	0.16	0.09
$\left(\frac{\Delta\Phi}{\Phi}\right)_i$	$\pm100\%$	$\pm100\%$	$^{+9.1\%}_{-9.5\%}$	$^{+10.7\%}_{-9.7\%}$	$^{+11.3\%}_{-17.7\%}$	$^{+47.3\%}_{-33.8\%}$
$\left(\frac{\Delta R}{R}\right)_i$	$^{+5.1\%}_{-9.5\%}$	$^{+7.3\%}_{-2.5\%}$	$^{+4.6\%}_{-6.2\%}$	$^{+2.9\%}_{-6.2\%}$	$^{+5.3\%}_{-7.4\%}$	$^{+9.1\%}_{-16.2\%}$
(a) Error from $\left(\frac{\Delta\Phi}{\Phi}\right)_i$	$\pm0.9\%$	$\mp0.2\%$	$^{-0.6\%}_{+0.7\%}$	$\mp0.1\%$	$^{+0.4\%}_{-0.6\%}$	$^{+1.6\%}_{-1.2\%}$
(b) Error from $\left(\frac{\Delta R}{R}\right)_i$	$\pm0.1\%$	$^{+1.1\%}_{-0.4\%}$	$^{+1.4\%}_{-1.8\%}$	$^{+0.8\%}_{-1.8\%}$	$^{+0.9\%}_{-1.2\%}$	$^{+0.9\%}_{-1.5\%}$

(a) Sum of errors from near spectrum = +3.9% −3.6%
(b) Sum of errors from flux ratio = +5.1% −6.8%

Jun.99 (200kA) run
(a) Sum of errors from near spectrum = +6.7% −7.9%
(b) Sum of errors from flux ratio = +13.6% −9.8%

Table 10.4: Errors on N_{exp}^{SK} from (a) the near spectrum and (b) the flux ratio uncertainty.

GPS timing cut is applied with 1.5 μs time window. As shown in Figure 9.7, the systematic error from the uncertainty of the timing information is negligible.

- The observed events in SK are required to originate in the 22.5 kt fiducial volume. The vertex position is reconstructed using "TDC-fit". For the confirmation, another vertex reconstruction method so called "MS-fit" is applied to fully-contained single ring events, after ring counting and particle identification. MS-fit is the vertex fitter with particle type (muon-type or electron-type) dependent fitting parameters, which is recently used for atmospheric-neutrino analysis in Super-Kamiokande experiment [61]. In the Monte Carlo simulation, the two results show ±2% difference.
- Statistical error of Monte Carlo event sample is about ±1%.

Therefore, total systematic error of SK selection efficiency is assigned to be ±3%.

10.3 Cross-check of the Expected Number of Events From MRD.

The number of expected neutrino events at SK N_{exp}^{SK} is also estimated based on the MRD measurement, a cross-check. N_{exp}^{SK} is estimated using same Formula 10.1, from the number of observed event in MRD N_{obs}^{MRD}. The results are summarized in table 10.5. In total,

$$N_{exp}^{SK} = 41.0 \pm 0.2(\text{stat.}) \pm 6.3(\text{syst.})$$

Estimated systematic error is summarized in 10.6.

Since the target nuclei is Fe, the uncertainty of the cross sections difference is additionally estimated as follows;

8. **Uncertainty of the Fe cross section, comparing to the H_2O target.** They are already described in Chapter 4.2.8.
    (a) In quasi-elastic and elastic scattering, we compared different iron interacted neutMC with Fermi surface momentum (correspond to Pauli blocking threshold) $P_{Fermi} = 217$ MeV/c and 250 MeV/c instead of 237MeV/c in default. The change in the observed number of events in MRD is +3.4% and −1.7%, respectively.
    (b) Hadron interaction uncertainty inside of the iron nuclei. Since the hadron interaction in iron nuclei is assumed to be larger than that in oxygen nuclei, the default neutMC, which has the same interaction as oxygen, gives the minimum estimation of the hadron interaction effect inside of the iron nuclei. On the other

Period	Jun.99	Nov.99	Jan.00	Feb.00	Mar.00	May.00	Jun.00
Target diameter	20mmϕ	30mmϕ					
HORN	200kA	250kA					
N_{obs}^{MRD}	7417	8140	5997	11228	10306	7464	10159
N_{corr}^{MRD}	21516	22886	16861	31568	28975	20985	28562
POT_{MRD} ($\times 10^{18}$)	2.93	2.72	2.04	3.81	3.49	2.51	3.54
POT_{SK} ($\times 10^{18}$)	3.10	3.57	2.22	4.04	3.71	2.56	3.75
$R_{Far/Near}$ ($\times 10^{-4}$)	2.81	2.80					
ϵ_{SK}	0.781	0.785					
N_{exp}^{SK}	5.00	6.59	4.03	7.34	6.76	4.68	6.64
Stat. error	± 0.06	± 0.07	± 0.05	± 0.07	± 0.07	± 0.05	± 0.07
Syst. error	$+1.00$	$+0.97$	$+0.59$	$+1.08$	$+0.99$	$+0.69$	$+0.98$
	-0.91	-1.00	-0.61	-1.11	-1.02	-0.71	-1.00

Total: $N_{exp}^{SK} = 41.0 \pm 0.2(stat.) \pm 6.3(syst.)$

Table 10.5: Calculated number of expected events at SK from MRD measurement. This estimation is for the cross-check of the N_{exp}^{SK} from 1kt measurement in Table 10.1.

	Item	Jun.99	Nov.99 to Jun.00
1	MRD measurement (Table 7.7)	$^{+1.9}_{-5.1}$	
2	P.O.T. normalization	$< \pm 0.1$	
3	Neutrino profile (direction)	$+1.4$	$+0.8$
4	Proton targeting stability	$^{+0.9}_{-1.6}$	
8	$\sigma_{Fe}/\sigma_{H_2O}$ including p and π int. in nuclei	$^{+7.3}_{-3.4}$	
5(a)	NC/CC uncertainty	$^{+3.3}_{-3.7}$	
5(b)	in-elastic cross section	$^{+3.3}_{-4.8}$	
6(a)	Neutrino energy spectrum	$^{+11.1}_{-12.0}$	$^{+9.8}_{-9.5}$
6(b)	$R_{SK/MRD}$ ratio	$^{+13.6}_{-9.8}$	$^{+5.6}_{-7.1}$
7	SK selection efficiency	± 3.0	
	Total	$^{+20.0}_{-18.1}$	$^{+14.7}_{-15.1}$

Table 10.6: List of systematic errors for N_{exp}^{SK} from MRD measurement. Unit is %.

hand, we also analyze with "muon-only" simulation, which gives the 100% nuclear absorption of hadrons. Figure 7.17 shows the difference The 5.7% difference is quoted as the systematic error.

Linear sum of these two errors is assumed as the systematic error of the cross section difference between Fe and H_2O.

Obtained N_{exp}^{SK} from MRD is consistent with the N_{exp}^{SK} from 1kt measurement, within the systematic errors.

10.4 Observed Number of Events at SK

Neutrino events in 22.5 kt fiducial volume in Super-Kamiokande is analyzed as described in Chapter 9.1. As the result of the whole running period of 2.29×10^{19} P.O.T., number of observed fully-contained events N_{obs}^{SK} is;

$$N_{obs}^{SK} = 28$$

10.5 Discussion

10.5.1 Statistical significance

Twenty-eight of fully-contained events are observed, when $37.8^{+3.8}_{-4.0}$ events are expected. In order to obtain statistical judgment, following purely statistical "Monte Carlo test" is performed.

Poisson distributions are generated repeatedly which have the average around 37.8 smeared by a Gaussian function with the attached error ± 4.0 (small difference between 3.8 and 4.0 is neglected). The probability of this observation is calculated as the integration of the probability of less than or equal to 28 events. This definition is expressed as follows;

$$P(x \leq n; \mu_0 \pm \Delta\mu) = \frac{\int_0^\infty \sum_{x=0}^{n} \frac{e^{-\mu}\mu^x}{x!} \cdot e^{\frac{-(\mu-\mu_0)^2}{2\Delta\mu}} d\mu}{\sqrt{2\pi\Delta\mu}} \tag{10.9}$$

where n, μ_0, and $\Delta\mu$ are the number of observed events, a center value of the number of expected events, and its error. In our case, $n = 28$, $\mu_0 = 37.8$, and $\Delta\mu = 4.0$.

This test is performed 10^6 times. The obtained probability is 9.6% for this observation of 28 event. The null oscillation hypothesis is excluded with more than 90% C.L. (confidence level) by one side (lower side) test.

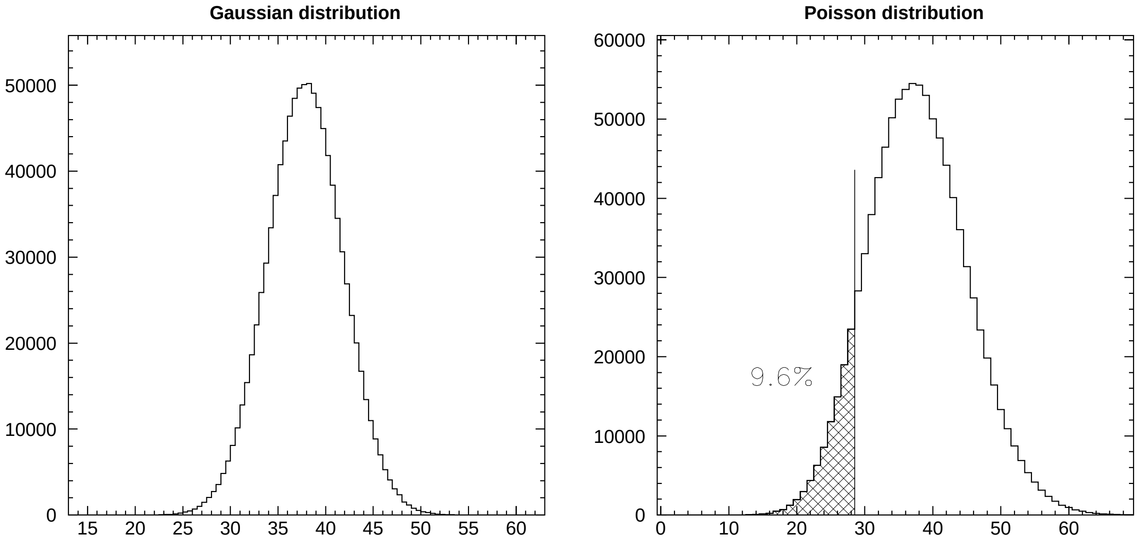

Figure 10.1: Results of the statistical test. The left figure shows the Gaussian distribution with mean 37.8 and sigma 4.0. This gives the probability of the mean of the Poisson distribution in the right figure. The area less than or equal to 28 event occupies 9.6% of the total right histogram. These are the results with 10^6 trials of the random number generation.

10.5.2 Physics Conclusion

An evidence of the neutrino disappearance is obtained. The most likely explanation is the neutrino oscillation. Assuming the neutrino oscillation between 2 flavors, ν_μ and ν_x, the oscillation probability is expressed as Formula 1.10. Though one measurement of the “number of events” cannot simultaneously solve two parameters $\theta_{\mu\mu}$ and Δm^2_{23}, the best favored area is drawn in the (Δm^2)-(θ) contour. When $\theta_{\mu\mu}$ is assumed to be 1, the best estimation of Δm^2_{23} is around 2.5×10^{-3} eV^2. This point is close to the best fit of recent atmospheric neutrino observation in Super-Kamiokande experiment [10], which is shown in Figure 1.1.

The neutrino oscillation will be concluded when the ν_μ energy spectrum at SK will differ from the expected one. The distortion pattern will be analyzed according to Formula 1.10. For this purpose, the ν_μ energy spectrum will be reconstructed by the analysis of near neutrino detectors, in particular, 1kt and FGD.

Further accumulation of the neutrino events in SK will enable us to analyze the ν_μ disappearance with smaller statistical error, and also enable us to analyze the ν_μ spectrum distortion.

Chapter 11

Conclusion

In order to investigate neutrino oscillation using well-monitored neutrino beam, the neutrino oscillation experiment with 250 km long base line has been performed.

Neutrino energy spectra and the ratio of the flux of far/near sites are obtained by measuring the (P_π, θ_π) distribution of pions before decaying to neutrinos. Neutrino beam itself is carefully measured by Muon Range Detector at the near site. The results confirm the stability of the neutrino flux, spectrum shape and the pointing accuracy toward Super-Kamiokande, throughout the whole run. The beam stability is kept, on spill-by-spill basis, by proton monitors and secondary muon monitors in the beam line. The neutrino event rate, which is the product of the neutrino flux and the cross section, is measured at 1kt detector.

These measurements at near site allow us to extrapolate the event rate from the near detector to the far detector, Super-Kamiokande. During the whole run of 2.29×10^{19} protons on target, the expected number of event at Super-Kamiokande is $37.8\pm0.2(stat.)^{+3.8}_{-4.0}(syst.)$. It is cross checked by the event rate at Muon Range Detector.

In Super-Kamiokande, the neutrino events are clearly distinguished by the time synchronization to the accelerator using GPS system. Twenty-eight fully-contained events are observed during the corresponding period of 37.8 expected events.

The probability of the observation without oscillation or any reduction is discussed. Comparing the expected number from 1kt detector and the observation at Super-Kamiokande, the result shows 9.6% probability of no change. The most likely explanation is the neutrino oscillation. Assuming the hypothesis of $\nu_\mu \rightarrow \nu_x$ oscillation with large mixing angle, the best estimation of Δm^2 is around sevral of 10^{-3} eV^2. This is consistent with the recent assertion of the atmospheric neutrino observations.

Appendix A

MRD Track Finder

A muon that penetrates MRD deposits several drift-tube hits along the particle trajectory. In order to reconstruct the muon track, MRD "track finder" code is used. The track finder consists of four parts, "Cell fit", "Fragment fit", "2-D fit", and "3-D fit". Figure A.1 shows the flow chart of these track finding algorithm. They are explained in following sub-sections.

> In this chapter, the word "layer" means the one iron plate (10 cm or 20 cm thickness), or one series of X-tubes and Y-tubes inserted between the given two iron plates. The word "plane" means the transversely aligned cells in the given z-position. That is, two X-planes and two Y-planes make one drift-tube layer. MRD has 12 iron layers and 13 drift-tube layers (26 planes for each x and y). Reconstructed track starts on one of the plane and ends on another plane.

A.1 Noise hit rejection

Averaged number of MRD hits is about 30 $\sim$ 40 per one spill. These hits include some fraction of noise hits caused by the electronics. They have a tendency of following;

- Some particular channels frequently make these fake hits.
- Many of them record TDC count of less than 5 count.

Rejection of these noise hit is performed as follows;

1. First, noisy tubes which had hits over 10% of spills in suitable time period are masked. These are about 50 channels (0.8%) through out the whole run (see Figure A.2). These bad channels are randomly distributed and no localization is found.

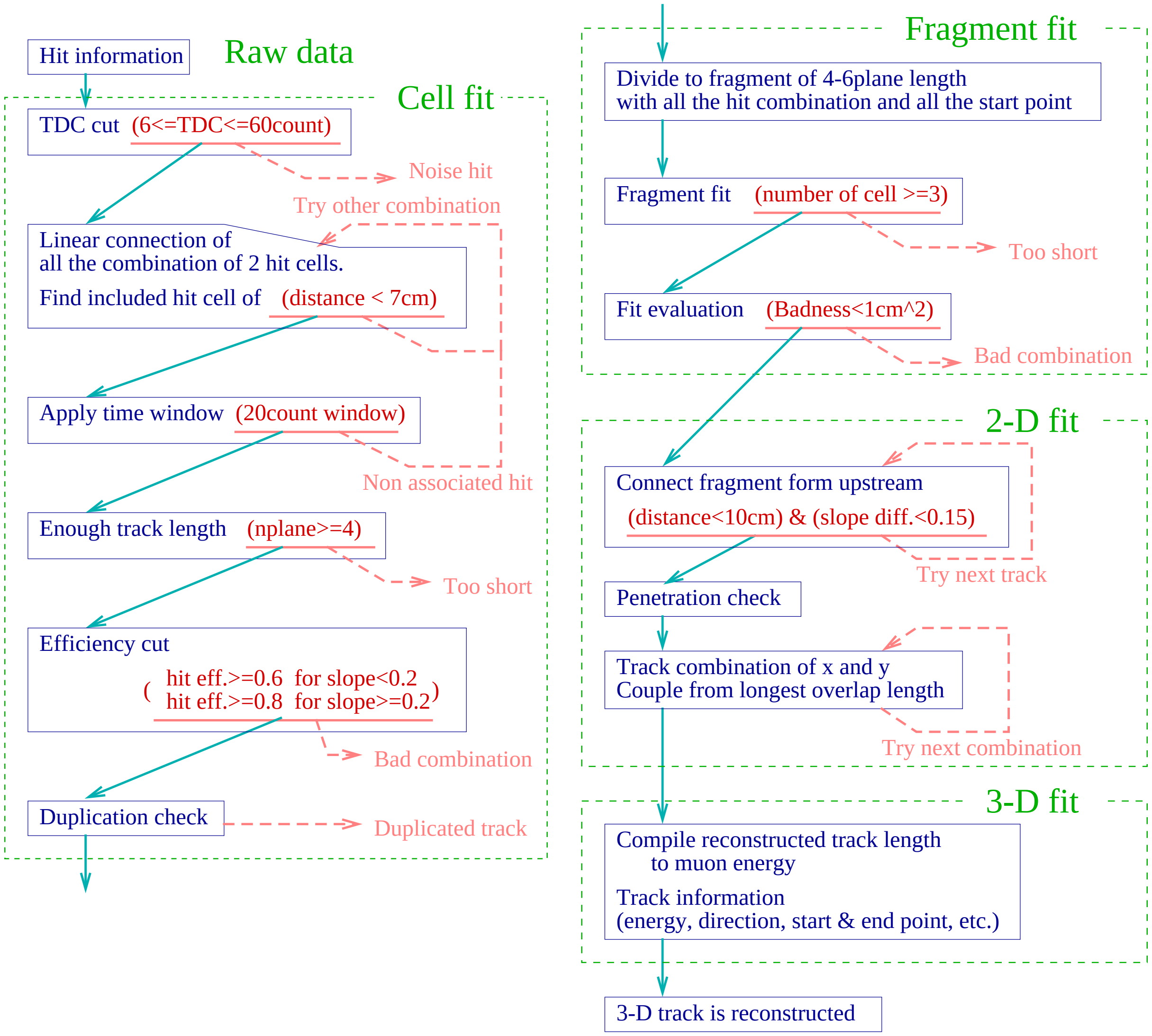

Figure A.1: Flow chart of the MRD tracker algorithm.

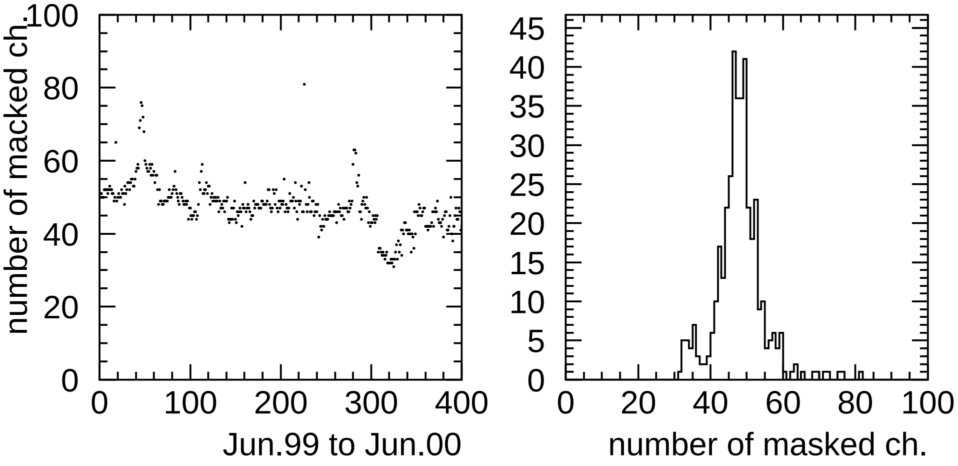

Figure A.2: Number of masked channels due to the high trigger rate from June 1999 to June 2000. The left figure is the history plot, where horizontal axis corresponds to the dataset number. The right figure is the accumulated distribution. The simulation adopts 57 masked channels, which is a little conservative estimation.

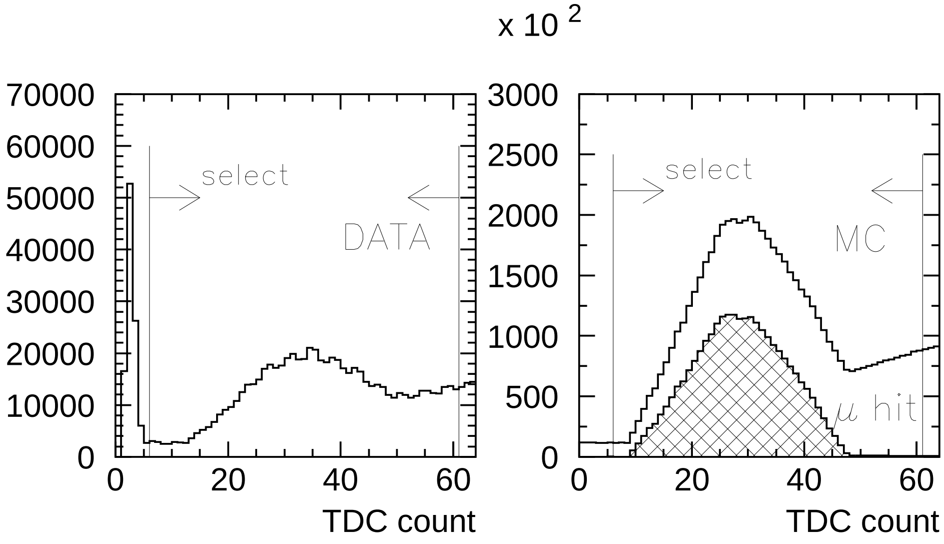

Figure A.3: TDC distribution of hit cells (1 TDC count = 50 ns). The left figure shows the observed data and the right figure is the neutMC simulation. Hatched area shows the hits originated by muons, in neutMC.

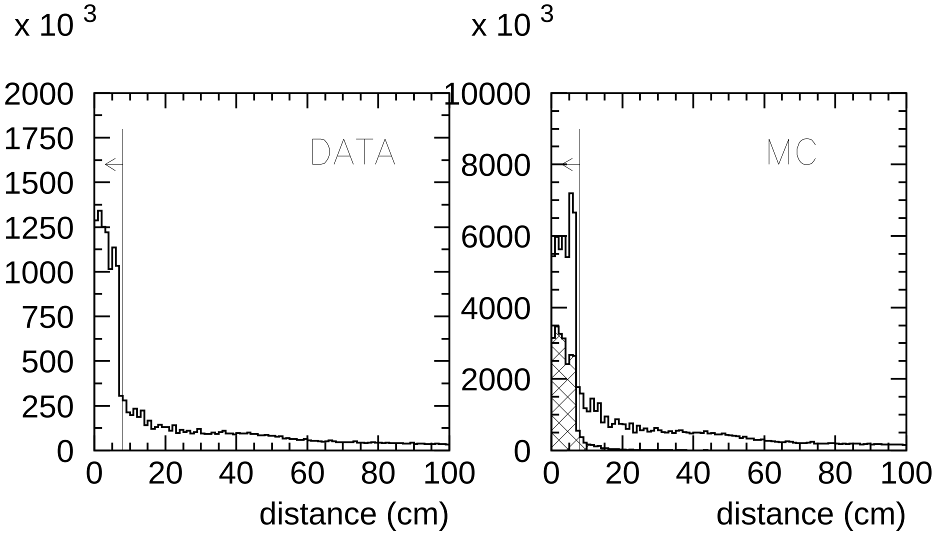

Figure A.4: Distance from the connected track to each hit wire position. True muon combinations are also shown by the hatched area.

2. Next, TDC cut of $6 \leq T \leq 60$ count is applied. Figure A.3 clearly shows the electrical noise rejection by this cut. The hits from neutrino-induced event distribute from 10 count to 50 count, smeared by the drift time. There are delayed background hits, which are mostly distributed at the top front side of the detector volume. They are considered as low energy neutron activities, called "sky-shine. In Figure A.3, the simulated distribution is also shown.

A.2 Cell fit

1. All hits are connected by Cell fit. It tries all the combinations of 2 hits of more than 4 planes apart from each other. It connects the two wire positions linearly and counts-up the "included" hit cells within 7 cm from the fitted line. Distributions of the distance are shown in Figure A.4.

2. Next, Cell fit searches 20 count time window where most associated hits are included there. 20 count (= 1μs) is the maximum drift time of the tube. With this cut, some accidental off timing hits are rejected.

3. The hit efficiency of each passing plane is calculated. The tracks are required the efficiency more than 60% (80%) for the opening angle $\tan\theta < 0.2$ ($\tan\theta > 0.2$).

track length	slope	
	< 0.2	≥ 0.2
4 plane	3 hit	4 hit
5 plane	3 hit	4 hit
6 plane	4 hit	5 hit
7 plane	5 hit	6 hit
8 plane	5 hit	7 hit
9 plane	6 hit	8 hit
10 plane	6 hit	8 hit

Table A.1: Required hit per each track length for the efficiency cut.

Table A.1 notes the required hits per each track length. 2-dimensional view of this cut criteria is shown in Figure A.5.

A.3 Fragment fit

1. For cell fit track, fragments with 4 to 6-plane length are picked-up. All the hits are assigned as the start point for each fragment. All the patterns are taken when some planes have more than one hit in one plane.

2. In each fragment, first 3 or 4 hit cells are fitted with linear line, considering drift distance from the wire. The particle arrival time (T_0) is searched for starting from $T_{max} - 20$ count to T_{min}, with 1 TDC count step, where T_{max} and T_{min} are the maximum and minimum TDC count of the hits in each fragments, respectively. Drift distance is calculated from the Formula 3.13. From this drift distance, 2 possibility is exist, upper or lower side of the wire. Then all the combination is considered. "*Badness*" is evaluated as following residual length;

$$\begin{aligned}
S_{XX} &= \Sigma(X_i - <X>)^2 \\
S_{YY} &= \Sigma(Y_i - <Y>)^2 \\
S_{XY} &= \Sigma(X_i - <X>) \cdot (Y_i - <Y>) \\
slope &= \frac{S_{XY}}{S_{XX}} \\
slice &= <Y> - slope \cdot <X> \\
badness &= \frac{S_{YY} - S_{XY} \cdot slope}{Ncell - 2} \qquad \text{(A.1)}
\end{aligned}$$

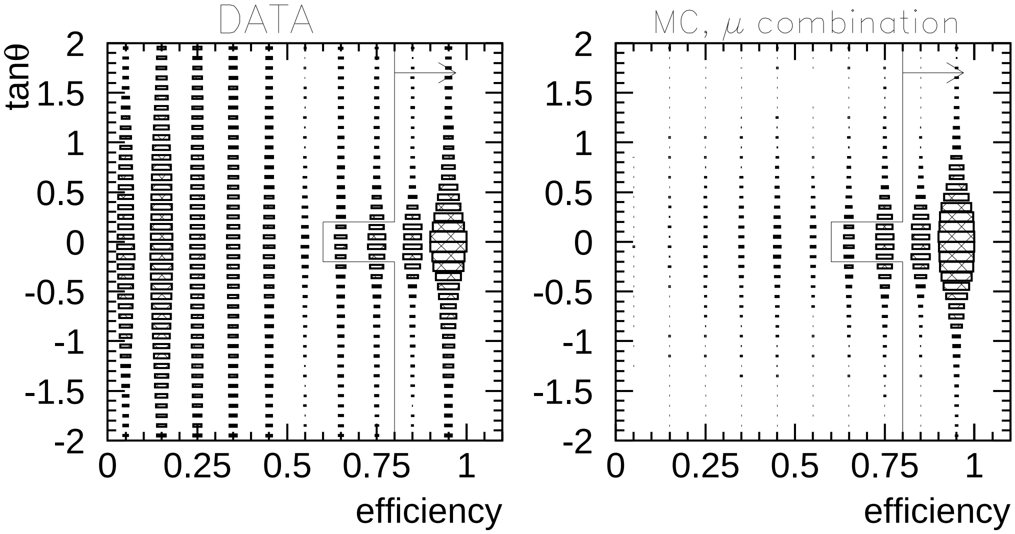

Figure A.5: Distributions of slope and efficiency of the tested tracks.

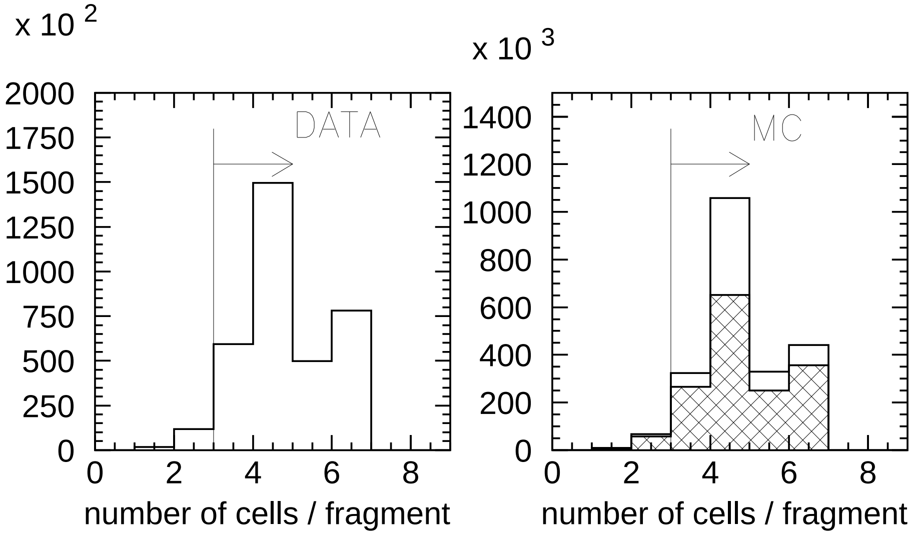

Figure A.6: Number of hit cells in each fragments. Shaded area corresponds to the muon combinations.

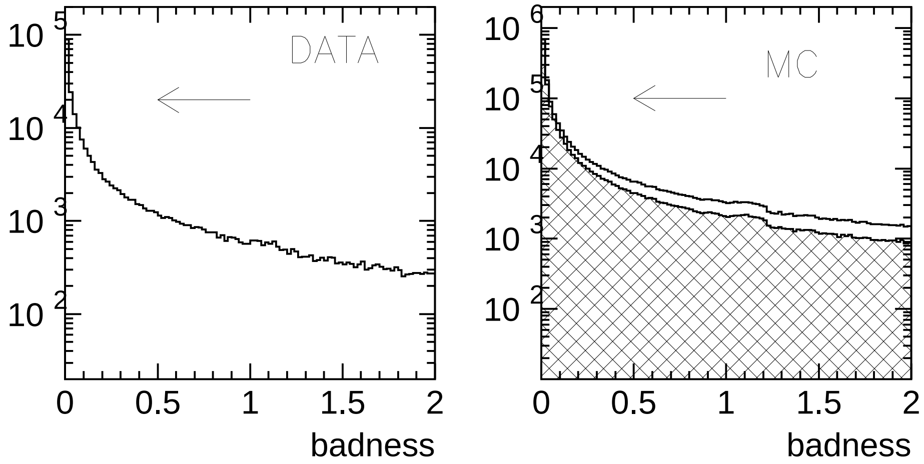

Figure A.7: Badness distribution. Hatched area corresponds to the muon combinations.

All the case of hit pattern, T_0, and drift side are tested and best combination is selected. *Badness* distribution is shown at Figure A.7. $badness < 1$ is required for an appropriate fit.

A.4 2-D fit

1. From many fitted fragments, most upstream fragment is assumed as the start fragment of the 2-D track, at first. Next fragments are searched for whose start plane is same or before end plane of the initial fragment. To connect next one, two parameters are considered. One is the closest distance between the start point of the next fragment and initial track (*rdist*), and the other is the opening angle between two tracks (θ_{ab}). The requirement is $rdist < 10$ cm and $\tan\theta_{ab} < 0.15$ (Figure A.8).
2. After all the sequential fragments are picked-up, next upstream fragment is considered among remained tracks.
3. T_0 is calculated as the average of fragments in each 2-D tracks.

A.5 3-D fit

1. 3-D fit process connects 2-D tracks in different view. From all the combination of both X-view and Y-view, the overlap length along the z-axis is considered. 3-D

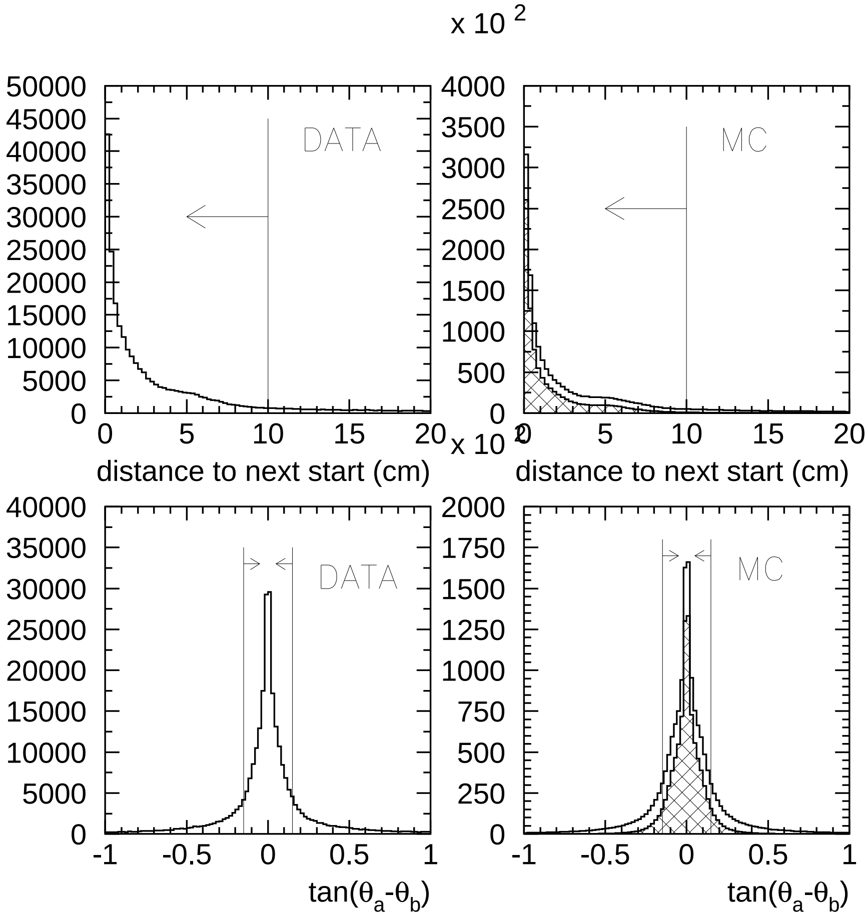

Figure A.8: Distributions of the distance between the first track and next start point (rdist), and angle of two tested tracks. Shaded area corresponds to the muon combinations.

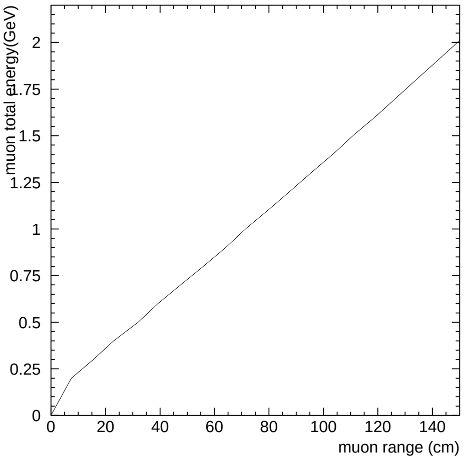

Figure A.9: Conversion function from muon range to muon total energy.

Conversion function from muon range to muon total energy.

tracks are picked up from the best combination that has a longest overlap length among remaining track.

2. Track slope in each view is defined from the linear line between most upstream hit point and most downstream one in both sides view independently.

3. The start and end-points are defined as most upstream and downstream z-position of X-view and Y-view. If 2-D track does not have hit at start or stop point, the positions are calculated by a extrapolation using the slope.

4. Assuming the track is made by muon, muon energy is reconstructed from the path length in the iron plates. In this path length calculation, event vertex and end point is assumed to be at the middle of the iron plate. A conversion function, which is shown in Figure A.9, is estimated by GEANT Monte Carlo simulation and good agreement with the numerical integration of the Bethe-Bloch equation [99].

5. T_0 is the average of that of two 2-D tracks in both view.

6. Some evaluation values are calculated for following event selection section; difference of the start point, difference of the end point, and the difference of fitted T_0 between two 2-D tracks.

Appendix B

Neutrino Profile of Vertex-Contained Events at MRD

For the cross check, another profile analysis is performed using the vertex-contained (VC) neutrino events.

B.1 Event Selection

Event sample is selected with following criteria. The selection is also shown in Figure 7.2.

1. **Consistency between X-view and Y-view,** described in Chapter 7.1.3.
2. **Longest track selection,** described in Chapter 7.1.3.
3. **Time window,** described in Chapter 7.1.3.

9. **SAMPLE-A-dash, for profile study.**
   The vertex point is required being in Fiducial-A, while the end point is not required being contained.

   This causes a little contamination of the cosmic ray backgrounds. But the rate is negligibly small (it is also suggested by the T_0 distribution in Figure 7.5).

This SAMPLE-A-dash includes the events that penetrate one or more iron plate ($N_{layer}^{iron} \geq 1$), instead of ($N_{layer}^{iron} \geq 2$) for SAMPLE-A. This lower threshold is necessary to keep selection efficiency around the edge region, because some muons with large angle penetrate to outside of MRD and leave hits only in two drift-tube-layers (this is $N_{layer}^{iron} = 1$). Thank to this lower threshold, SAMPLE-A-dash have better efficiency for low energy neutrinos than SAMPLE-A, as shown in Figure 7.6. Although the events with $N_{layer}^{iron} = 1$ contains about 22% of the hadron activity.

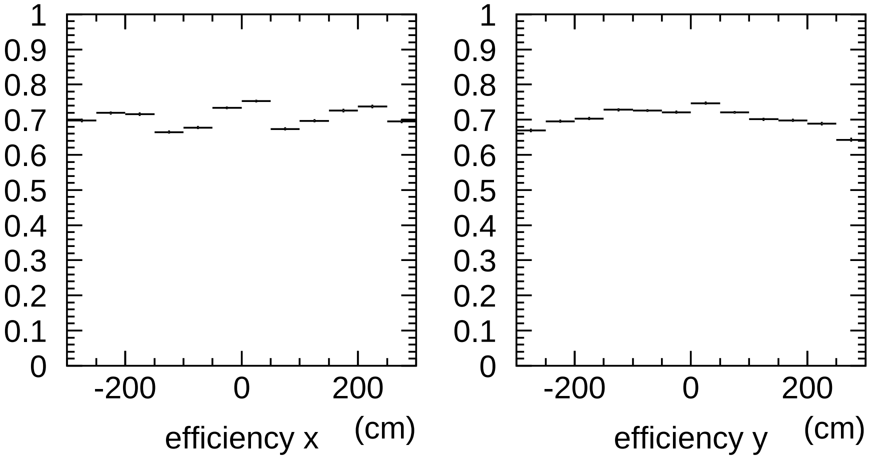

Figure B.1: Selection efficiency for SAMPLE-A-dash, as a function of reconstructed vertex point of x and y. This efficiency is estimated by neutMC of 250 kA case.

B.2 Profile of vertex-contained (VC) events

The vertex distribution of SAMPLE-A-dash is obtained for certain time periods. Since there are drift-tube gaps at y-tubes, the selection efficiency of there ($-150 < x < 50$ cm and $50 < x < 150$ cm) is 5 $\sim$ 10% lower than other area (shown in Figure B.1). This non-uniformity is compensated by applying the efficiency correction. The efficiency is almost uniform in each position except the gap area, and neutrinos with any energy range also gives the uniform efficiency. This uniform efficiency is an advantage of this analysis method, because the systematic bias of the efficiency correction makes little effect for profile determination.

Figure B.2 shows the vertex profile of this analysis for Nov.99 to Jun.00 run. They again prove the neutrino beam direction pointing to SK, and the profile width is well reproduced by neutMC.

Profile reconstruction test by neutMC with shifted beam axis

The profile reconstruction is tested as Chapter **??**. Simulated VC profile with shifted beam axis are reconstructed by the same procedure. The fitted results are summarized in Table 7.4. The results agree with the nominal input axis, less than 12 cm.

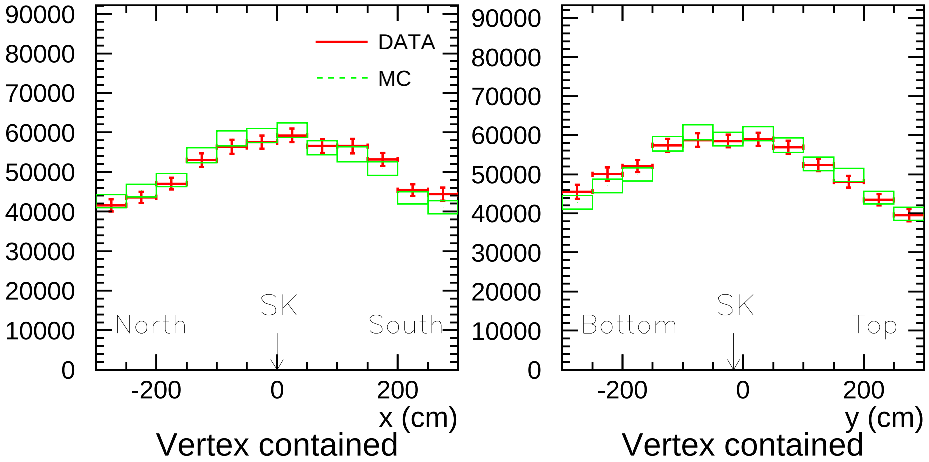

Figure B.2: Vertex profile of vertex-contained (VC) events in MRD for Nov.99 to Jun.00 run. DATA (cross) and neutMC (box) with same reconstruction are overlaid. Normalization of both figures is done by the area under the histograms. Error bars are due to data statistics and also MC statistics of the applied efficiency correction.

beam shift	method	center	x (cm)	center	y (cm)	width	x (cm)	width	y (cm)
Center	(nominal)	(0)		(−16)					
	VC	−1	±2	−13	±2	291	±4	287	±4
X +50cm	(nominal)	(+50)		(−16)					
	VC	+60	±6	−11	±5	285	±9	279	±9
Y +50cm	(nominal)	(0)		(+34)					
	VC	+5	±5	+46	±6	273	±8	286	±10
Y −50cm	(nominal)	(0)		(−66)					
	VC	+2	±5	−68	±7	280	±9	294	±10

Table B.1: Reconstruction test of VC profile, with neutMC with shifted beam axis.

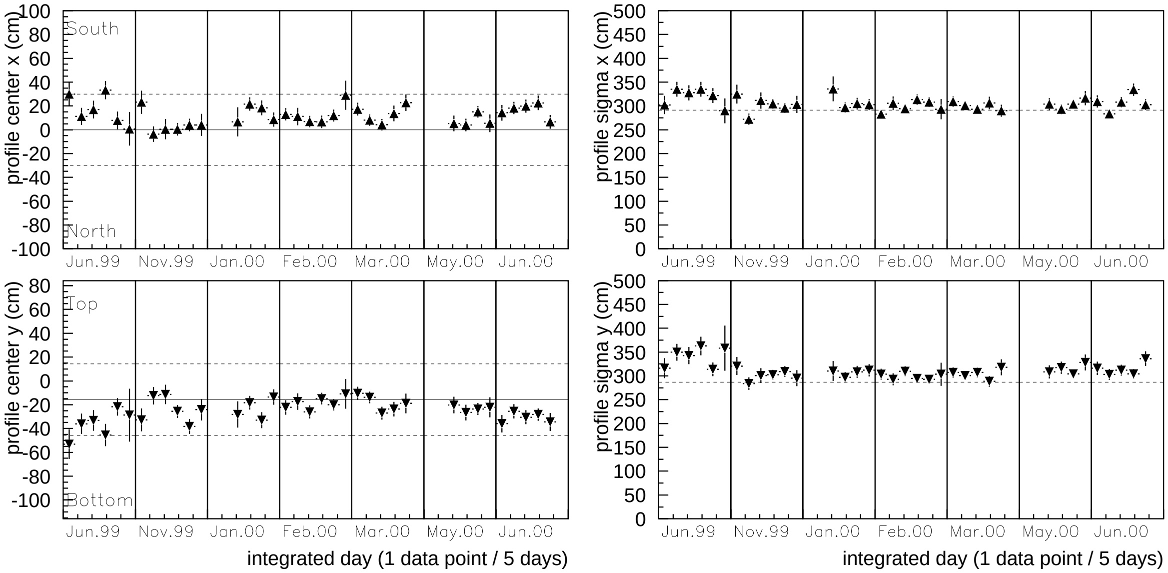

Figure B.3: Stability of the neutrino profile center (left figure) and width (Gaussian sigma, in right figure) from June 1999 to June 2000, obtained from VC analysis. Each definition of figures are same as Figure 7.16

B.3 Stability of the profile

Neutrino profiles from VC events are integrated every five days and fitted with Gaussian function to obtain center and width (r.m.s.). The results are shown in Figure B.3. They show the profile center is always pointed within 1 mrad, and the width agrees to that of neutMC.

These results can be directly compared with the results of FC-all analysis in Figure 7.16. Figure B.4 shows a correlation of the fitted center from two methods. They prove the consistency of the two profile analyses.

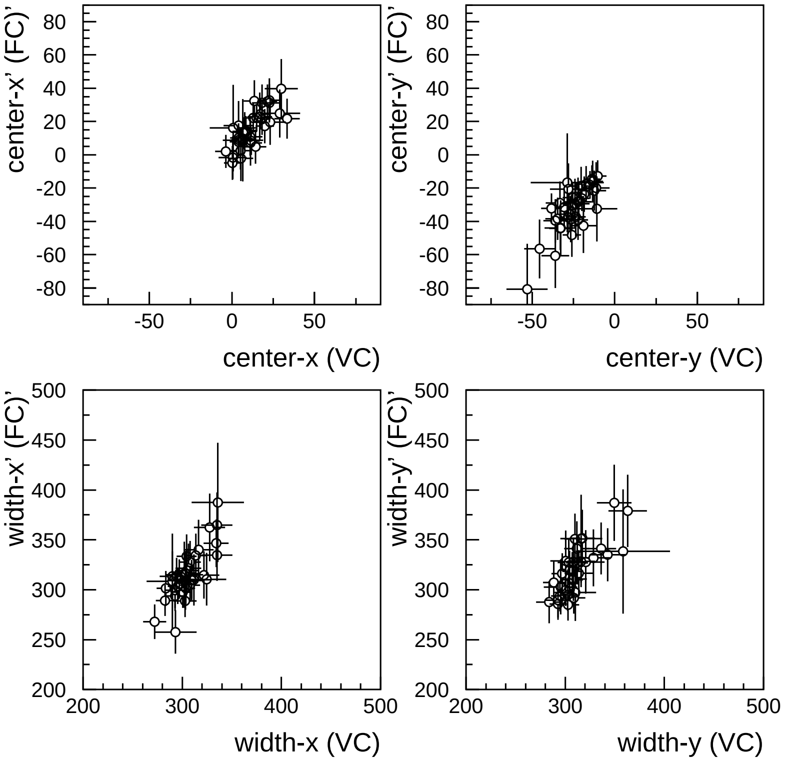

Figure B.4: Consistency of the neutrino profile center (top) and width (bottom), between FC-all analysis and VC analysis. One data points correspond to the result of each 5 days.

Appendix C

TDC fit

In 1kt and SK, the event vertex point is reconstructed using "TDC fit" routine. "TDC fit" routine reconstructs the vertex point using hit time (TDC) information of inner PMTs. This routine is originally developed and used in Kamiexperiment and Super-Kamiokande experiment [61].

TDC fit contains following three steps;

1. "Point fit", which searches a rough vertex from only the time information of the PMTs.

2. "Ring edge search", which searches the direction and opening angle of the Cherenkov cone.

3. "The fine vertex fit", which determines more precise vertex by taking account of the track length of the charged particle.

The steps 2 and 3 are iterated until the distance between the previous vertex and the latest one becomes less than 50 cm.

When particle emits Cherenkov photons from a certain point in the water tank, the observed TDC distribution corresponds the time of flight between the PMTs and the vertex. Therefore, the distribution of "residual" time, which is the time after time-of-flight of Cherenkov photons of each PMT is subtracted, shows a sharp peak smeared by time resolution. The time residual t_i of the i-th hit PMT is defined as;

$$t_i = t_i^0 - (n/c) \times |\vec{P_i} - \vec{O}| - < t > \tag{C.1}$$

where, n is the refractive index of water, c is the light velocity, t_i^0 is the hit time of the i-th PMT, $< t >$ is the average of t_i, $\vec{P_i}$ means the position vector of the i-th PMT, and $\vec{O}$ is the position vector of an assumed vertex position.

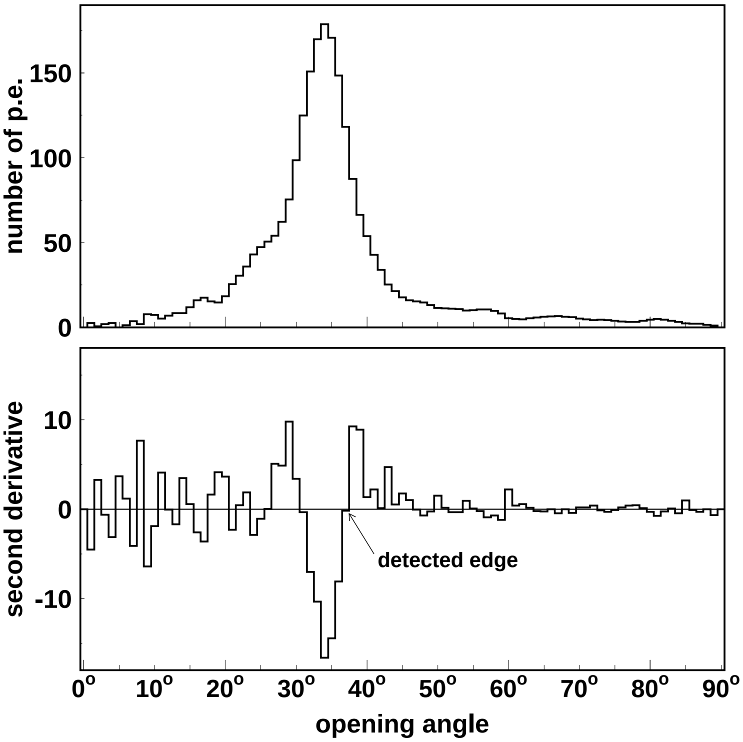

Figure C.1: Effective charge $CH(\theta)$ distribution (upper) and its second deviation (lower), as a function of opening angle θ.

In the realistic case, the time residual distribution has a certain width due to the particle running in the water, and has also a long tail caused by scattered light.

Considering this effect, "goodness function" G_p is defined as;

$$G_p = \frac{1}{N_{hit}} \sum_i \exp\left(-\frac{t_i^2}{2\sigma^2}\right) \tag{C.2}$$

where, N_{hit} is the number of hit PMTs in inner detector, and σ is the typical time resolution of 2.5 ns. The point fit searches the position where G_p is maximum. The resolution of this point fit is about 40 cm.

After the vertex $\vec{O}$ is determined, overall particle direction $\vec{d_p}$ is calculated from the weighted average of observed charge C_i as follows;

$$\vec{d_p} = \sum\nolimits_i \frac{\vec{P_i} - \vec{O}}{|\vec{P_i} - \vec{O}|} \times C_i \tag{C.3}$$

Next, the angular distribution of effective charge $CH(\theta)$ is calculated from the defined axis around $\vec{d_p}$, and the result is typically shown in Figure C.1. The effective charge means the observed charge with acceptance of PMT and water transparency correction. As shown in Figure C.1, Cherenkov ring edge is obtained at the nearest zero-crossing point of $\frac{d^2CH(\theta)}{d\theta^2}$ outer than the peak of $CH(\theta)$. Assumed direction $\vec{d}$, Q value is written in a following equation;

$$Q = \int_0^{\theta_{edge}} \frac{CH(\theta)}{\sin\theta_{edge}} d\theta \times \left(\left| \frac{dCH(\theta)}{d\theta} \right|_{\theta=\theta_{edge}} \right)^2 \times \exp\left(-\frac{(\theta_{edge} - \theta_C)^2}{2\sigma_\theta^2} \right) \tag{C.4}$$

where, θ_C is the Cherenkov angle expected from the total charge in the corn, and σ_θ is its resolution. Optimum direction $\vec{d}$ where Q maximizes is adopted to the next final vertex fit.

At the final fit process, two goodnesses G_I and G_O are calculated with following formula;

$$\begin{aligned} G_I &= \sum_{inside of ring edge} \frac{1}{\sigma_i^2} exp\left(-\frac{t_i^2}{2\sigma^2}\right) \\ G_O &= \sum_{out of ring} \frac{1}{\sigma_i^2} max\left[exp\left(-\frac{t_i^2}{2\sigma^2}\right), 0.8 \cdot exp\left(-\frac{t_i}{T_l}\right)\right] \end{aligned} \tag{C.5}$$

where, σ_i is the time resolution of the i-th PMT, which is a function of its charge. The choice in G_O means whether the observed photon hits directly or with scattering. T_l is the typical time delay of scattered photons. T_l of 20 ns is used in the calculation. The evaluation indicator is the sum of these two goodness values;

$$G_T = \frac{G_I + G_O}{\sum_i \frac{1}{\sigma_i^2}} \tag{C.6}$$

In the calculation of G_I, particle path length is considered from the total charge which are within the 70° cone. t_i is re-calculated with unfolded emission point along the track, instead of the unique point in initial "point fit".

These procedures are iterated several times, until both the vertex position and direction are determined at the maximum G_T.

Appendix D

Experimental Test of the Vertex Reconstruction at 1kt

In order to check the vertex reconstruction using TDC fit, experimental test is performed using cosmic ray [52]. A long light-tight pipe (Cosmic Ray Pipe) is installed in the water tank. Trigger scintillation counters are set at both side of the pipe. A cosmic ray muon that hits these counters generally makes one muon-like Cherenkov rings starting at the end of the pipe. Several data are taken with the pipe end at −2 m to +3 m from the center, as shown in Figure D.1.

Figure D.2 shows the results of the fitted vertex when the pipe end was set at z(height) = +1 m. Data samples are sorted to the fully-contained muon events (whose end point is contained in the tank), and the Partially-contained muon events (which are penetrated to out of the inner tank). The partially-contained events are identified when the maximum signals in each PMT exceed to 200 photo-electron. Typical results of the vertex reconstruction are shown in Figure D.2. The vertex reconstruction in horizontal direction is good, whereas the reconstruction along the particle direction (vertical direction) sometimes makes miss-reconstruction to the forward direction, in particular for the partially-contained events. This tendency is reproduced by the Monte Carlo simulation, although there is a small discrepancy compare to the data. Table D.1 summarizes the mean position of the reconstructed vertices along the particle direction for each data set.

The reason of this tendency is considered that; the TDC fit gives poor constraint for the vertex determination along the particle direction, because the TDC values of hit PMTs are close to each other. When the neutrino event sometimes makes multi-rings, the vertex reconstruction is better than the single-ring case.

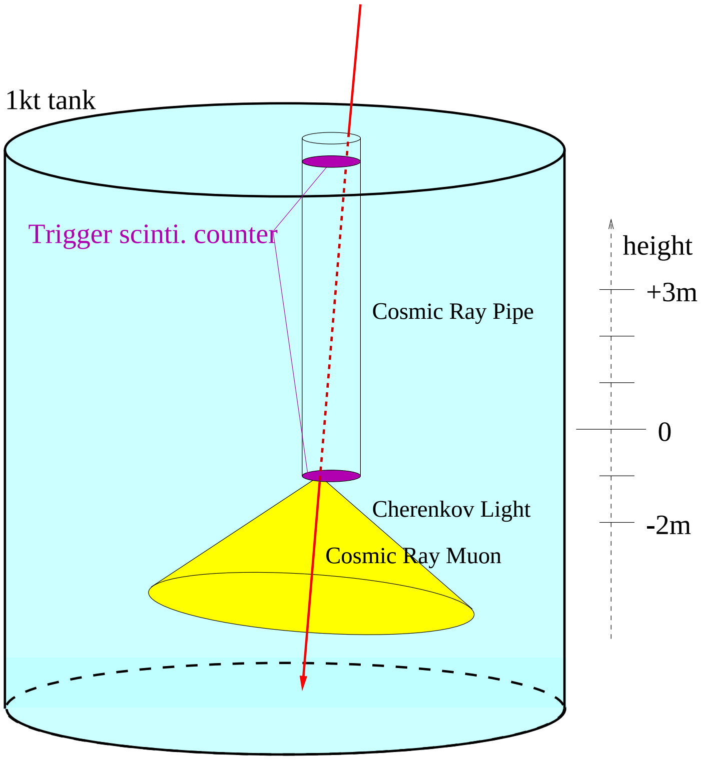

Figure D.1: Set-up of the Cosmic Ray Pipe measurement.

Pipe end position (Vertical)	DATA		MC	
	Fully	Partially	Fully	Partially
+3 m	+2.97 m	+2.31 m	+3.10 m	+2.46 m
+2 m	+2.02 m	+1.51 m	+2.17 m	+1.67 m
+1 m	+1.23 m	+0.72 m	+1.13 m	+0.84 m
0 m	+0.17 m	−0.33 m	+0.23 m	+0.07 m
−1 m	−0.94 m	−1.47 m	−0.82 m	−1.09 m
−2 m	−2.27 m	−2.19 m	−1.95 m	−2.14 m

Table D.1: Fitting results of the Cosmic Ray Pipe measurement, with pipe end position of +3 m (upper side) to −2 m (lower side). Cosmic ray muons go down to “minus” direction in this coordinate.

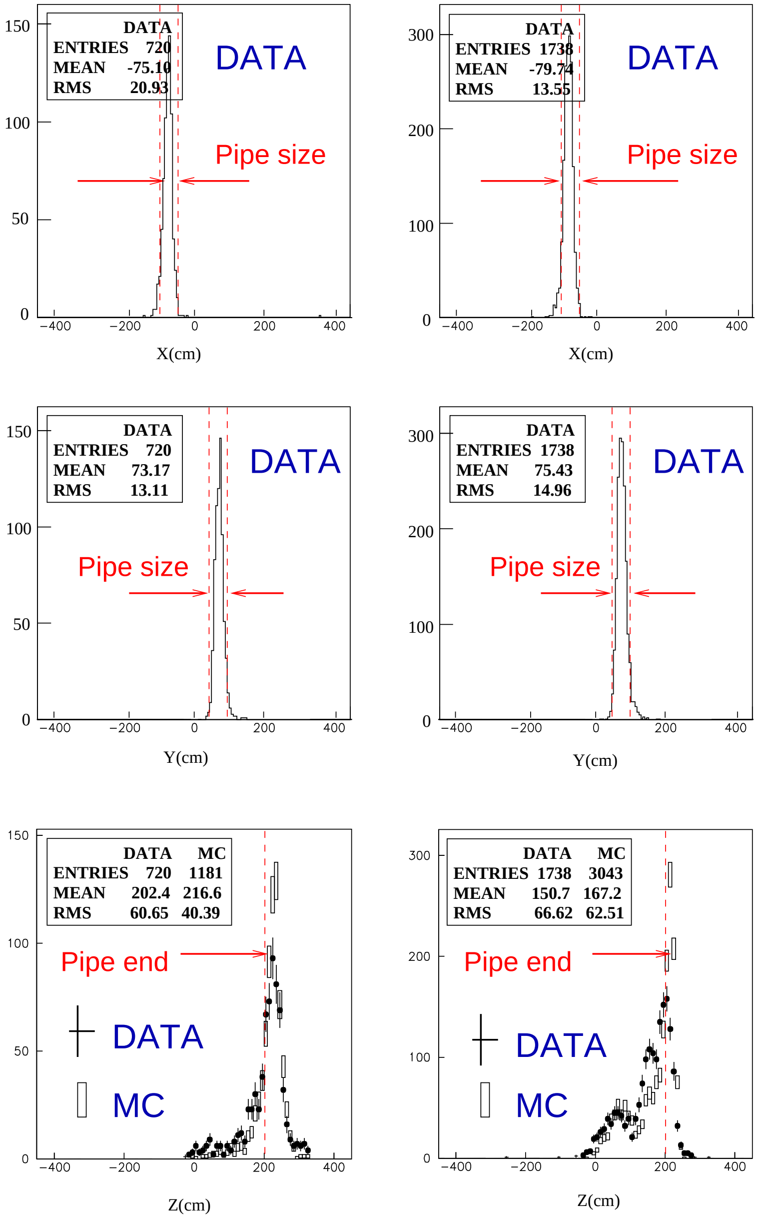

Figure D.2: Fitting results of the Cosmic Ray Pipe measurement at $z = +1$ m height from the center. Upper and middle 4 figures are distributions of the fitted vertex in the horizontal direction, while lower 2 figures are the vertex in the vertical direction ("z" in these figures). The left figure of each shows the events whose end-points are contained in the detector (fully-contained), and the right figure are the events that are penetrated out of the inner vessel (partially-contained). In the vertical direction, the fitted results of the Monte Carlo simulation are overlaid (box).

Appendix E

Analysis of June 1999 Run

In June 1999, the experiment was performed with different target diameter and different current of HORN magnets from other running period. Therefore, the produced pion and neutrino distributions are different. Then, data of Jun.99 run are independently analyzed, with corresponding Monte Carlo simulations. In particular, PIMON analysis and muon spectrum in MRD are affected by the different pion distributions and different neutrino energy spectrum. In this chapter, analysis results of Jun.99 run are presented.

E.1 PIMON analysis results in Jun.99 run.

The configurations of the HORN magnet and PIMON are summarized in Table 6.1. The obtained Cherenkov photon distributions are shown in Figure E.1, with simulated distributions by beamMC. They show the agreement between the observed distributions and the simulation based on Cho model, better than GCALOR/FLUKA model.

Figure E.1 shows the reconstructed neutrino energy spectrum and the flux ratio. The results again show agreement between the reconstructed results and the simulated ones, within the quoted systematic errors.

Table E.1 and Table E.2 shows the systematic error of these plots. These errors are explained in Chapter 6.1.6. In particular, these errors are different from that in Nov. run.

4. **Difference between the low and high beam intensity.**
   In June PIMON run, the profile was about 20 $\sim$ 30% (50%) narrower in the horizontal (vertical) profile comparing to the ones in normal run. Muon rate in SPD was about 30% larger. This is considered that the high energy muons are sensitive to the targeting efficiency, and beamMC quantitatively reproduced the increase. Systematic errors are assigned based on the comparison between these simulations with two profiles.

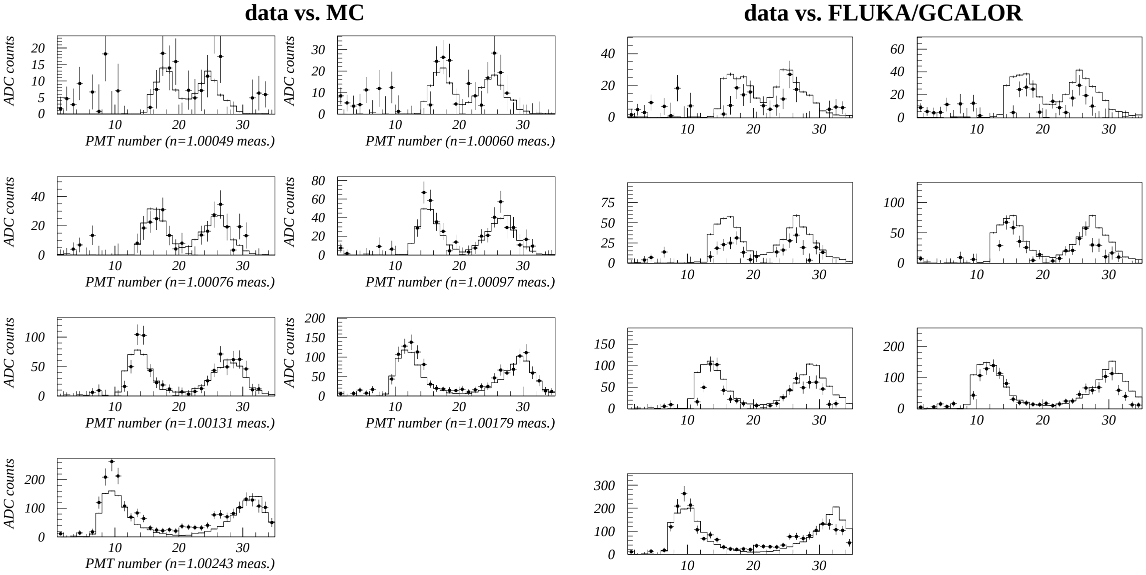

Figure E.1: Comparison of the Cherenkov photon distribution with measurement (dots) and two sets of beamMC (histograms), for Nov. 1999 run. The simulation in left figures is based on Cho model and the simulation in right figures is based on GCALOR/FLUKA model. Definition of these figures are same as Figure 6.3.

5. **Beam stability during the PIMON measurement.**
   The fluctuation of the proton beam center is 3.6 mm and 0.3 mm for x and y in V39-SPIC, 0.2 mm and 0.6 mm for x and y in TGT-SPIC, during the June run. Fluctuation of the rate of SPD was 4.6%, and the profile center is stable within ±8 cm. These fluctuations give the systematic error.

8. **Proton injection point to the target.**
   Muon profiles measured by SPD have less than 10 cm shift compared to the normal run, which confirms that the proton injection point is within 2 mm in Jun. The systematic error is estimated by the beamMC study in both case.

16. **PMT saturation correction.**
    Another systematic error, due to the non-linearity correction is assigned, only in June run (see 3.2.6).

Jun. 1999		Errors on spectrum at near			
	Energy bin (GeV)	1 − 1.5	1.5 − 2	2. − 2.5	> 2.5
1	Fitting error	±11.7%	±9.2%	±17.2%	+25.1%
16	PMT saturation correction	±0.5%	±1.2%	±1.4%	±30%
2	Mirror reflectivity	−1.4%	+4.2%	−3.5%	−8.7%
3	Refractive index uncertainty	—	—	—	—
4	Low and high beam intensity	−5.5%	±1.0%	+10.0%	+7.0%
5	Beam stability (PIMON run)	±1.9%	±4.3%	±5.0%	±12.7%
6	ϕ asymmetry of the HORN field	−2.9%	−0.9%	+32.6%	−19.0%
7	PIMON alignment	—	—	—	—
8	Proton injection point	−1.5%	+6.8%	−10.0%	+8.9%
9	MIRROR-OFF subtraction	—	—	—	—
10	Electro-magnetic subtraction	—	—	—	−74%
11	Fitting method	+6.8%	−7.7%	−15.3%	$^{+12\%}_{-21\%}$
12	Pion decay before PIMON	±0.9%	±1.9%	±2.8%	±1.3%
13	Radial distribution of pions	—	—	±2.3%	±20%
14	Kinematic bin of pions	+2.0%	−2.7%	−7.2%	−1.3%
		+13.9%	+13.2%	+39%	+49%
	Total	−13.6%	−13.3%	−27%	−88%

June 1999		Errors on spectrum at far			
	Energy bin (GeV)	1 − 1.5	1.5 − 2	2. − 2.5	> 2.5
1	Fitting error	±14.7%	±9.6%	±19.3%	+26.7%
16	PMT saturation correction	±0.8%	±1.2%	±2.0%	±20%
2	Mirror reflectivity	−1.6%	+3.1%	—	−9.0%
3	Refractive index uncertainty	—	—	—	—
4	Low and high beam intensity	−7.0%	−6.5%	+4.5%	+6.5%
5	Beam stability (PIMON run)	±3.2%	±3.7%	±5.0%	±12.8%
6	ϕ asymmetry of the HORN field	−2.4%	−7.5%	+38.8%	−10.7%
7	PIMON alignment	—	—	—	—
8	Proton injection point	−2.5%	+9.1%	−10.0%	+3.6%
9	MIRROR-OFF subtraction	—	—	—	—
10	Electro-magnetic subtraction	—	—	—	−60%
11	Fitting method	+11.0%	−10.2%	−12.3%	$^{+1.6\%}_{-32\%}$
12	Pion decay before PIMON	±2.3%	±5.7%	±6.3%	—
13	Radial distribution of pions	—	—	±1.4%	±21%
14	Kinematic bin of pions	+1.4%	−2.7%	−7.4%	−13.0%
		+18.8%	+15.2%	+44.4%	+42.3%
	Total	−17.2%	−18.8%	−27.1%	−77.5%

Table E.1: Systematic errors of neutrino spectrum at near and far detector in Jun. run.

Errors on flux ratio (June 1999, HORN current 200 kA)

	Energy bin (GeV)	$0-0.5$	$0.5-1$	$1-1.5$	$1.5-2$	$2.-2.5$	>2.5
1	Fitting error			$^{+3.2\%}_{-4.5\%}$	$^{+6.2\%}_{-4.9\%}$	$^{+2.0\%}_{-5.7\%}$	$^{+8.5\%}_{-5.8\%}$
16	PMT saturation correction			$\pm0.6\%$	$\pm0.5\%$	$\pm1.3\%$	$\pm4.2\%$
2	Mirror reflectivity			—	—	-3.5%	—
3	Refractive index uncertainty			—	—	—	—
4	Low and high beam intensity			-6.0%	-5.3%	-6.6%	$\pm0.5\%$
5	Beam stability (PIMON run)			$\pm1.0\%$	$\pm1.5\%$	$\pm3.4\%$	$\pm1.1\%$
6	ϕ asymmetry of the HORN field			$+0.5\%$	-6.7%	$+4.7\%$	$+9.4\%$
7	PIMON alignment			—	—	—	—
8	Proton injection point			-1.0%	$+2.1\%$	-0.6%	-4.9%
9	MIRROR-OFF subtraction			—	—	—	—
10	Electro-magnetic subtraction			—	—	—	$+72\%$
11	Fitting method			$+4.0\%$	$^{+1.4\%}_{-3.0\%}$	$^{+3.2\%}_{-4.6\%}$	-14.5%
12	Pion decay before PIMON			$\pm1.4\%$	$\pm3.8\%$	$\pm3.4\%$	$\pm1.6\%$
13	Radial distribution of pions			—	—	$\pm1.0\%$	$\pm7.2\%$
14	Kinematic bin of pions			-0.6%	—	—	-13.0%
15	Hadron model (MC)	$^{+5.1\%}_{-9.5\%}$	$^{+7.3\%}_{-2.5\%}$				
		$+5.1\%$	$+7.3\%$	$+5.5\%$	$+7.8\%$	$+8.7\%$	$+73.6\%$
	Total	-9.5%	-2.5%	-7.8%	-11.1%	-11.1%	-22.5%

Table E.2: Systematic errors of neutrino flux ratio (Φ_{far}/Φ_{near}) in Jun. run.

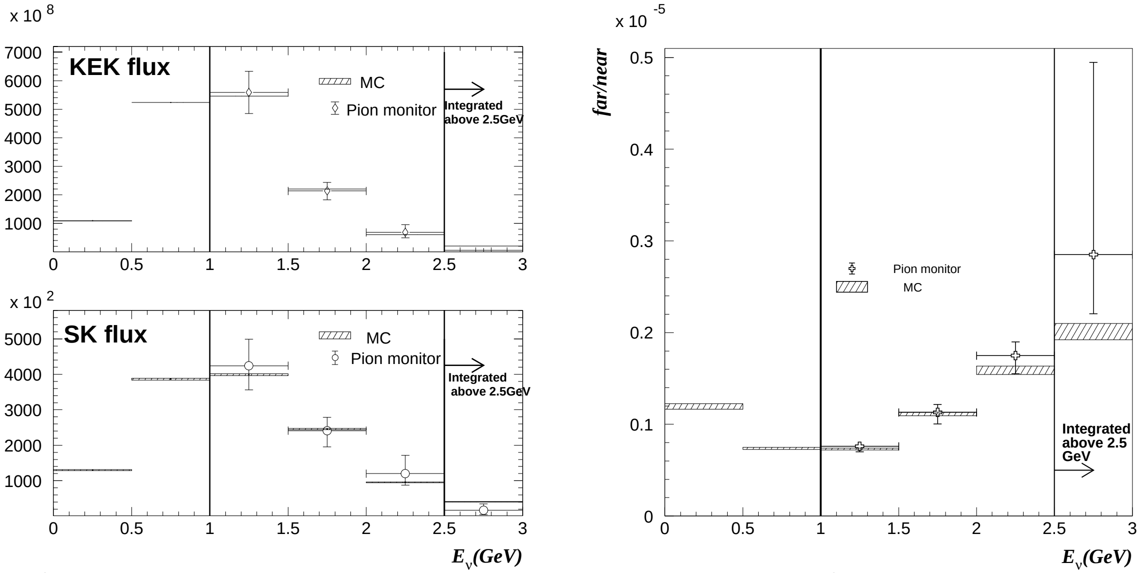

Left: Reconstructed neutrino energy spectrum at near and far site in Jun.99 run. Right: Reconstructed ratio of far and near as a function of energy. Notations are same as Figure 6.5.

E.2 Neutrino Profile at MRD

Figure E.2 shows the acceptance-corrected vertex profile of FC-Low-Energy and FC-High-Energy analysis (described in Chapter 7.3), in Jun.99 run. They prove that neutrino beam is pointed towards SK, and neutMC well reproduces the profile.

E.3 Muon Distributions at MRD

Figure E.3 shows the reconstructed muon energy spectrum and angular distribution of SAMPLE-C, for data of Jun.99 run and neutMC. The results can be reproduced by neutMC within the uncertainty of the hadron interaction inside the iron nuclei (nuclear effect), as discussed in chapter 4.2.7.

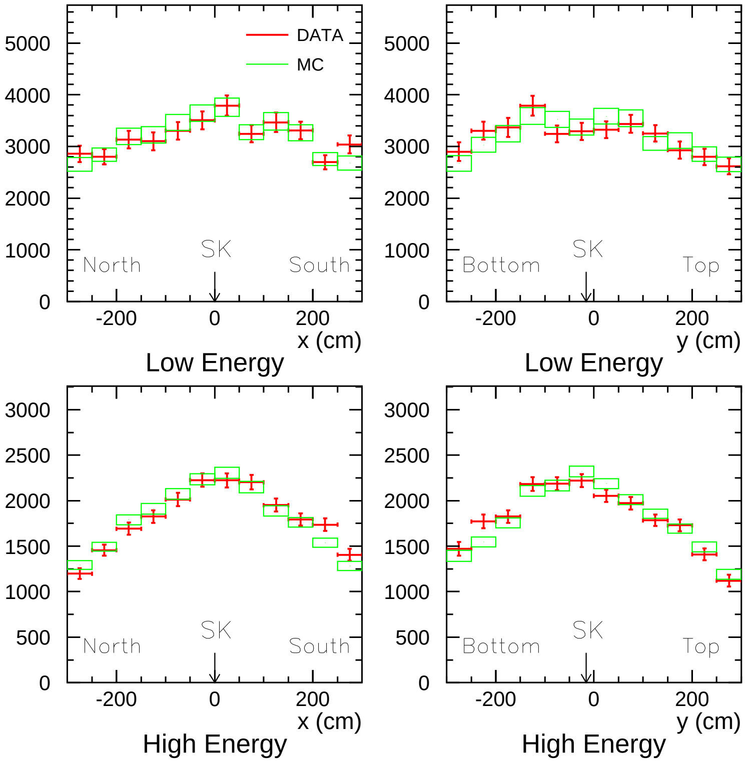

Figure E.2: Corrected vertex profile in June 1999 run (HORN current 200 kA). Definitions are same as Figure 7.15.

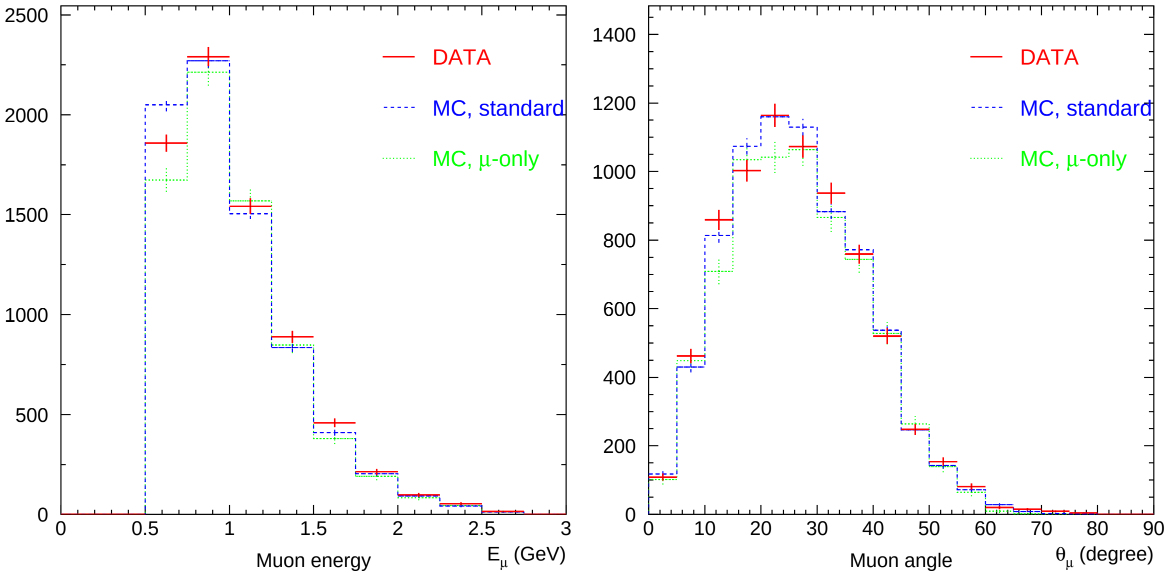

Figure E.3: Muon spectrum and polar angle distribution observed in MRD. ($I_{horn} = 200$kA, in Jun.99 run.) Definitions are same as Figure 7.17.

Appendix F

Comparison Between MRD and 1kt

F.1 Event Rate Comparison

In this thesis, two neutrino observations are presented, one is the iron interacted events using MRD, and the other is the water interacted events using 1kt detector. Comparison of them provides not only the cross check of the each detector measurement, but also the relative cross section of neutrino interaction on different nuclei. In this section comparison of the event rate is discussed.

Iron interacted events in MRD are summarized in Table 7.6. Water interacted events in 1kt are summarized in Table 8.2. Each event rate is normalized to its fiducial mass, which corresponds to the number of target nucleon.

Ratio of these two normalized event rates is given by;

$$R_{MRD/1kt} = \frac{r_{corr}^{MRD}/M_{MRD}}{r_{corr}^{1kt}/M_{1kt}} \tag{F.1}$$

where, r_{corr}^{MRD} and r_{corr}^{1kt} are the efficiency corrected event rates observed at MRD and 1kt, with P.O.T. normalization. M_{MRD} and M_{1kt} are their fiducial mass. This ratio $R_{MRD/1kt}$ means following physical explanation;

$$R_{MRD/1kt} = \frac{k \int \Phi_{MRD}(E_\nu) \cdot \sigma_{Fe}(E_\nu) dE_\nu}{k \int \Phi_{1kt}(E_\nu) \cdot \sigma_{H_2O}(E_\nu) dE_\nu} \tag{F.2}$$

where, Φ_{MRD} and Φ_{1kt} are the neutrino flux per unit P.O.T. per unit area, averaged over their fiducial area (MRD: 3 m radius, typically 306 m from the target, 1kt: 2 m radius, typically 290 m from the target), σ_{Fe} and σ_{H_2O} are the cross sections per one nucleon in iron or water nuclei, and k is a normalization factor corresponding to Avogadro constant N_A. This comparison is free from an absolute flux uncertainty and an absolute cross section uncertainty.

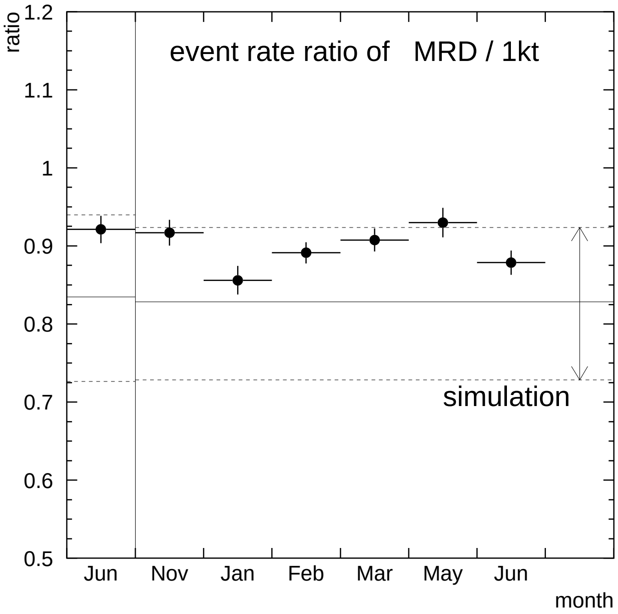

Figure F.1: Ratio of the observed event rate at MRD over the rate at 1kt, monthly plotted. Error bars are only the statistical errors of the observed event. Monte Carlo prediction is also overlaid (solid line: center value, dashed line: systematic error range).

Figure F.1 shows the $R_{MRD/1kt}$ in each month. Systematic errors quoted there are discussed in the next section.

Systematic errors from neutrino event detection and event rate correction are also considered as the error of the Monte Carlo prediction ratio. They are estimated as shown in Table F.1. Systematic errors of the event detection are already discussed in Section 7.5.3 and 8.2.3. Besides them, there are correlated errors some part of which are canceled between MRD and 1kt. They are estimated from the same discussion as Chapter 10.

F.2 Discussion about $R_{MRD/1kt}$

The result shows that the event rate ratio $R_{MRD/1kt}$ from the observation and from the simulation is roughly consistent within more than 10% level uncertainty. This is one of the demonstrations of the consistency check of MRD observation and 1kt observation. The systematic errors dominantly come from the uncertainty of the neutrino flux below 1GeV, and the lack of understanding of the neutrino interaction on iron nuclei.

They will be improved when further detailed analysis of neutrino interacted events in near

Item		for Jun.99	for Nov.99 to Jun.00
1	MRD measurement (Table 7.7)	$+5.1-1.9\%$	
1	1kt measurement (Table 8.3)	$\pm 5.3\%$	
2	P.O.T. normalization	$\pm 1.0\%$	$\pm 0.9\%$
3	Neutrino profile (direction)	-0.5%	-0.3%
4	Proton targeting stability	$+2.1-0.0\%$	
8	$\sigma_{Fe}/\sigma_{H_2O}$ including p and π interaction in nuclei	$+3.4-7.3\%$	
5(a)	NC/CC uncertainty	$+3.1-2.7\%$	
5(b)	in-elastic cross section	$+3.0-3.3\%$	
6(a)	Neutrino energy spectrum	$+8.3-8.1\%$	$\pm 6.5\%$
	Total	$+12.6\%$ -13.0%	$+11.5\%$ -12.1%

Table F.1: Systematic error estimation against the Monte Carlo prediction of $R_{MRD/1kt}$.

detector give more knowledge about both our neutrino beam and the neutrino interaction process. This can be achieved, in particular, by analyzing Fine Grain detector (FGD) measurements.

Appendix G

Various Distributions of the Observed Events in SK

Various distributions of the observed 28 events in SK are shown here. So far, statistics of observed events have not been enough. Thus, no physics results are discussed, yet.

Visible energy (E_{vis}) distribution

Figure G.1 shows the reconstructed visible energy distribution. The distribution of simulated events (no oscillation) is overlaid, which is normalized by the expected number of events derived from 1kt analysis. Visible energy has a correlation to the initial neutrino energy, although some fraction of energy may be lost by invisible particles, like neutrinos, neutrons, and protons, or may be pent to the produced muons and mesons.

Number of ring, particle identification

Standard ring-counting routine and the particle identification routine [61] are applied for the observed events. Following table summarizes the number of events in each category. Expected number of events without oscillation (N^{SK}_{exp}) are also shown.

	DATA	N^{SK}_{exp}
Fully-contained events (total)	28	37.8
1-ring, μ-like	14	20.9
1-ring, e-like	1	2.0
multi-ring	13	14.9

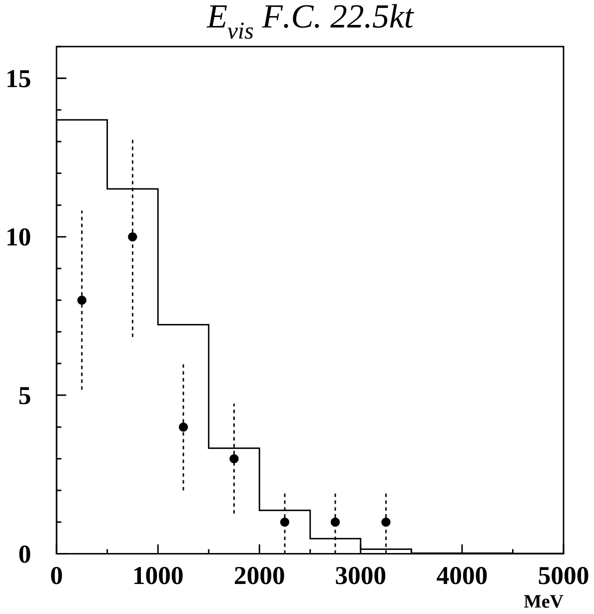

Figure G.1: Visible energy distribution for SK event. Observed events are shown by closed circles, and histogram shows the Monte Carlo expectation in null oscillation hypothesis, normalized by the expected number of events derived from 1kt measurement.

Momentum and angular distribution

Figure G.2-(A),(B) shows the momentum and the angular distribution for 1-ring μ-like events. The simulated (neutMC) distributions without oscillation are overlaid.

If the μ-like ring is really the muon, and it comes from Quasi-elastic scattering, neutrino energy E_ν can be calculated by following formula;

$$E_\nu = \frac{m_N \cdot E_\mu - m_\mu^2/2}{m_N - E_\mu + p_\mu \cos\theta_\mu} \tag{G.1}$$

where, $m_N(\sim 0.94$ GeV) and $m_\mu(\sim 0.106$ GeV) are nucleon and muon mass, E_μ, p_μ, θ_μ are the measured muon energy, momentum, and polar angle with respect to the neutrino beam direction. For the event selection criteria, the simulation (neutMC) says 53% of events come from CC quasi-elastic scattering, when the oscillation does not occurs. Therefore, if the oscillation occurs, entries in some particular energy bins are significantly decreased.

Figure G.2-(C) shows the reconstructed neutrino energy distribution for 1-ring μ-like events, by the Formula G.1. Current number of events is not enough to discuss the spectrum distortion.

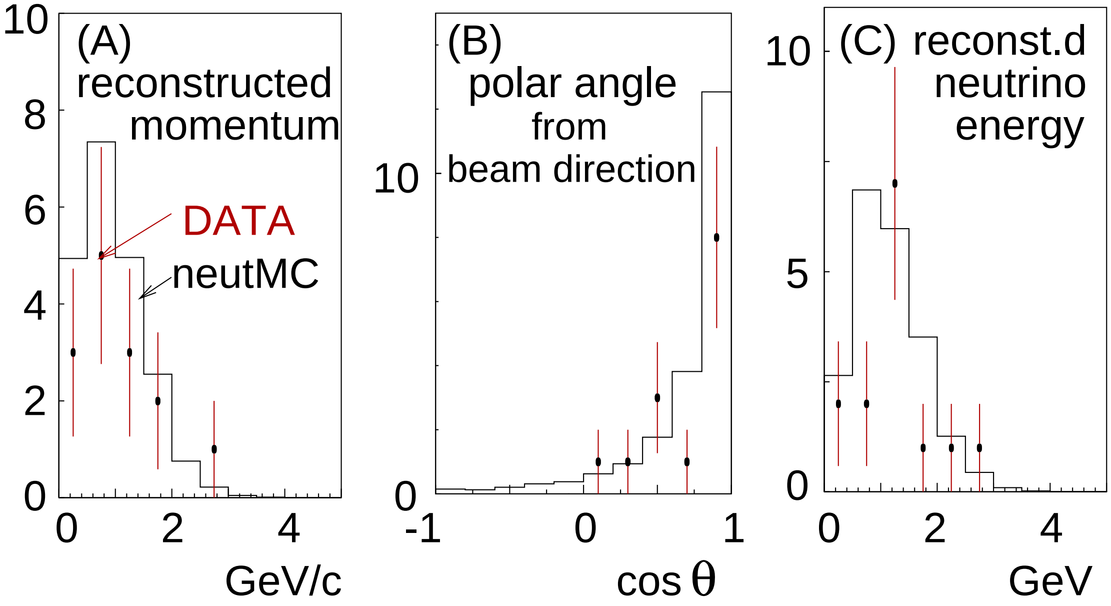

Figure G.2: (A) Reconstructed momentum distribution for 1-ring μ-like events in SK. (B) Reconstructed polar angle distribution with respect to the beam direction, for 1-ring μ-like events. (C) Reconstructed neutrino energy distribution, assuming the Quasi-elastic scattering, for 1-ring μ-like events. In each figure, simulated distributions without oscillation are overlaid (histogram).

List of Tables

List of Figures

Bibliography

[1] Particle Data Group, Eur. Phys. J. **C15**, 1-878 (2000), and http://pdg.lbl.gov/.

[2] Holzschuh, Rep. Prog. Phys. **55**, 1035 (1992).

[3] Ch. Weinheimer *et. al.*, Phys. Lett. **B460**, 219 (1999) ; V. M. Lobashev *et. al.*, Phys. Lett. **B460**, 227 (1999) ;

[4] Loredo *et. al.*, ANYAS **571**, 601 (1989) ; F. T. Avignone III and J. I. Collar, Phys. Rev. **D41**, 682 (1990) ; D. N. Spergel and J. N. Bahcall, Phys. Lett. **B200**, 366 (1988).

[5] K. Assamagan *et. al.*, Phys. Rev. **D53**, 6065 (1996).

[6] R. Barate *et. al.*, Eur. Phys. J. **C2**, 395 (1998).

[7] Z. Maki, M. Nakagawa and S. Sakata, Prog. Theor. Phys. **28**, 870 (1962).

[8] M. Kobayashi and T. Maskawa, Prog. Theor. Phys. **49**, 652 (1973).

[9] Y. Fukuda *et. al.*, Phys. Lett. **B433**, 9 (1998) ; Y. Fukuda *et. al.*, Phys. Lett. **B436**, 33 (1998).

[10] Y. Fukuda *et. al.*, Phys. Rev. Lett. **81**, 1562 (1998) ; S. Fukuda *et. al.*, Phys. Rev. Lett. **85**, 3999 (2000).

[11] K. S. Hirata *et. al.*, Phys. Lett. **B205**, 416 (1988) ; Phys. Lett. **B280**, 146 (1992).

[12] Y. Fukuda *et. al.*, Phys. Lett. **B335**, 237 (1994).

[13] R. Becker-Szendy *et. al.*, Phys. Rev. **D46**, 3720 (1992).

[14] R. Clark *et. al.*, Phys. Rev. Lett. **79**, 345 (1997).

[15] W. W. M. Allison *et. al.*, Phys. Lett. **B449**, 137 (1999).

[16] K. Daum *et. al.*, Z. Phys. **C66**, 417 (1995).

[17] M. Aglietta *et. al.*, Europhys. Lett. **8**, 611 (1989).

[18] Y. Fukuda *et. al.*, Phys. Rev. Lett. **82**, 2644 (1999) ; Y. Fukuda *et. al.*, Phys. Lett. **B467**, 185 (1999).

[19] B. C. Barish for MACRO Collaboration, Nucl. Phys. (Proc. Suppl.) **B91**, 141 (2001).

[20] B. T. Cleveland *et. al.*, Astrophys. J. **496**, 505 (1998).

[21] J. N. Abdurashitov *et. al.*, Phys. Rev.**C60**, 055801 (2000).

[22] W. Hampel *et. al.*, Phys. Lett. **B447**, 127 (1999).

[23] E. Bellotti, Nucl. Phys. (Proc. Suppl.) **B91**, 44 (2001).

[24] J. N. Bahcall, M. H. Pinsonneault, and S. Basu, astro-ph/0010346, submitted to Astrophys. J.

[25] Y. Fukuda *et. al.*, Phys. Rev. Lett. **77**, 1683 (1996).

[26] Y. Fukuda *et. al.*, Phys. Rev. Lett. **81**, 1158 (1998).

[27] S. Fukuda *et. al.*, hep-ex/0103033, submitted to Phys. Rev. Lett. ; Y. Fukuda *et. al.*, Phys. Rev. Lett. **82**, 1810 (1999) ; Phys. Rev. Lett. **82**, 2430 (1999).

[28] CHOOZ experiment: M. Apollonio *et. al.* Phys. Lett. **B466**, 415 (1999).

[29] Palo Verde experiment: F. Boehm *et al.*, Phys. Rev. **D62**, 072002 (2000) : Bugey experiment: B. Achkar *et al.*, Nucl. Phys. **B434**, 503 (1995) : Krasnoyarsk experiment: G. S. Vidyakin *et al.*, JETP Lett. **59**, 390 (1994) : Gösgen experiment: G. Zacek *et al.*, Phys. Rev. **D34**, 2621 (1986).

[30] L. Ludovici for CHORUS Collaboration, Nucl. Phys. (Proc. Suppl.) **B91**, 177 (2001).

[31] M. Mezzetto for NOMAD Collaboration, Nucl. Phys. (Proc. Suppl.) **B91**, 184 (2001).

[32] F. Dydak *et. al.*, Phys. Lett. **B134**, 281 (1984).

[33] F. Bergsma *et. al.*, Phys. Lett. **142**, 103 (1984).

[34] G. B. Mills for LSND Collaboration, Nucl. Phys. (Proc. Suppl.) **B91**, 198 (2001).

[35] G. B. Mills for KARMEN Collaboration, Nucl. Phys. (Proc. Suppl.) **B91**, 191 (2001).

[36] A. Piepke for KamLAND Collaboration, Nucl. Phys. (Proc. Suppl.) **B91**, 99 (2001).

[37] A. O. Bazarko for MiniBooNE Collaboration, Nucl. Phys. (Proc. Suppl.) **B91**, 210 (2001).

[38] K. Nishikawa *et. al.*, "Proposal for a Long Baseline Neutrino Oscillation experiment, using KEK-PS and Super-Kamiokande" KEK-PS proposal (E362) (1995) ; and the first results are presented in hep-ex/01030001, to be published in Phys. Lett. B.

[39] M. Yoshida, Ph.D thesis of Osaka University (2001), unpublished.

[40] H. Noumi *et. al.*, Nucl. Instrum. and Meth. **A398**, 399 (1997).

[41] H. Sato, Proc. Particle Accelerator Conference, (1999) ; K. Takayama, ICFA Beam Dynamics Newsletter **20**, (1999).

[42] K. H. Tanaka *et. al.*, KEK preprint 91-27.

[43] M. Ieiri *et. al.*, *prepared for 1st Asian Particle Accelerator Conference (APAC 98), Tsukuba, Japan*, page 579-581 (1998).

[44] Y. Yamanoi *et. al.*, KEK preprint 97-225 ; Y. Yamanoi *et. al.*, KEK preprint 99-178 ; Y. Suzuki *et. al.*, Proc. of Int. Conf. on Accelerator and Large experimental Physics Control system, 266 (1997).

[45] M. Kohama, Ph.D thesis of Kobe University (2000), unpublished.

[46] T. Maruyama, Ph.D thesis of Tohoku University (2000), unpublished.

[47] Private communication with T. Matsumoto (KEK-PS-E248 AIDA experiment group).

[48] T. Inagaki, Master thesis of University of Tokyo (1998), unpublished, in Japanese.

[49] HAMAMATSU PHOTONICS K.K. "PHOTOMULTIPLIER TUBE -principle to application-".

[50] H. Noumi *et. al.*, will be published.

[51] A. Suzuki *et. al.*, Nucl. Inst. and Meth. **A329**, 299 (1993).

[52] A. Shima, Master thesis of Kyoto University (2001), unpublished, in Japanese.

[53] Y. Kobayashi, Master thesis of University of Tokyo (1999), unpublished, in Japanese.

[54] H. Ikeda *et. al.*, Nucl. Inst. and Meth. **A320**, 310 (1992) ; T. Tanimori *et. al.*, IEEE Trans. Nucl. Sci. **36**, 497 (1989).

[55] S. Nakayama, Master thesis of University of Tokyo (1999), unpublished, in Japanese.

[56] Y. Asano *et. al.*, Nucl. Instr. and Meth. **A259**, 430 (1987).

[57] T. Ishii *et. al.*, "Muon Range Detector as a K2K Near Detector - Construction and Performance -" submitted to Nucl. Instr. and Meth. **A**.

[58] Y. Ikegami *et. al.*, IEEE Trans. on Nucl. Sci. **36**, 665 (1989).

[59] A. Suzuki *et. al.*, Nucl. Instr. and Meth. **A453**, 165 (2000).

[60] Y. Hayato *et. al.*, Phys. Rev. Lett. **83**, 1529 (1999) ; M. Shiozawa *et. al.*, Phys. Rev. Lett. **81**, 3319 (1998).

[61] M. Shiozawa, Ph.D thesis of University of Tokyo (1999), unpublished ; K. Ishihara, Ph.D thesis of University of Tokyo (1999), unpublished ; K. Okumura, Ph.D thesis of University of Tokyo (1999), unpublished ; and Y. Fukuda *et. al.*, "The SUPERKAMIOKANDE DETECTOR", in preparation.

[62] T. Tsushima, Master thesis of Tohoku University (1997), unpublished, in Japanese.

[63] H. G. Berns and R. J. Wilkes, IEEE Trans. Nucl. Sci. **47**, 340 (2000) ; S. Yamada, Master thesis of University of Tokyo (1999), unpublished, in Japanese.

[64] T. A. Gabriel, J. D. Amburgey, and B. L. Bishop, "Calor : A Monte Carlo Program Package For The Design And Analysis Of Calorimeter Systems" ORNL/TM-5619 ; T. A. Gabriel, Nucl. Instr. and Meth. **A349**, 106 (1994).

[65] A. Fassó *et. al.*, Proc. IV Int. Conf. on Calorimetry in High Energy Physics, 493 (1993).

[66] R. Brun *et. al.*, CERN DD/EE/84-1 (1987).

[67] Y. Cho *et. al.*, Phys. Rev. **D4**, 1967 (1971).

[68] J. R. Sanford and C. L. Wang, BNL-AGS internal report, BNL-11299 and BNL-11479 (1967) unpublished ; C. L. Wang, Phys. Rev. Lett. **25**, 1068 (1970).

[69] J. G. Asbury *et. al.*, Phys. Rev. **178**, 2086 (1969).

[70] G. J. Marmer *et. al.*, Phys. Rev. **179**, 1294 (1969) ; G. J. Marmer *et. al.*, Phys. Rev. **D3**, 1089 (1971).

[71] A. Yamamoto, ”Study On Low-Energy Intense Kaon Beam” KEK 81-13.

[72] M. Nakahata *et. al.*, J. Phys. Soc. Jpn. **55**, 3786 (1986).

[73] C. H. Llewellyn Smith, Phys. Rep. **3C**, 261 (1972).

[74] K. L. Miller *et. al.*, Phys. Rev. **D26**, 537 (1982).

[75] S. J. Barish *et. al.*, Phys. Rev. **D16**, 3103 (1977).

[76] N. J. Baker *et. al.*, Phys. Rev. **D23**, 2499 (1981).

[77] S. Bonetti *et. al.*, Nuovo Cimento **A38**, 260 (1977).

[78] S. V. Belikov *et. al.*, Z. Phys. **A320**, 625 (1985).

[79] K. Abe *et. al.*, Phys. Rev. Lett. **56**, 1107 (1986) ; C. H. Albright *et. al.*, Phys. Rev. **D14**, 1780 (1976).

[80] F. A. Brieva and A. Dellafiore, Nucl. Phys. **A292**, 445 (1977).

[81] D. Rein and L. M. Sehgal, Ann. of Phys. **133**, 79 (1981); D. Rein, Z. Phys. **C35**, 43 (1987).

[82] G. M. Radecky *et. al.*, Phys. Rev. **D25**, 1161 (1982).

[83] T. Kitagaki *et. al.*, Phys. Rev. **D34**, 2554 (1986).

[84] M. Pohl *et. al.*, Lett. al Nuovo Cimento **24**, 540 (1979).

[85] M. Glück, E. Reya, and A. Vogt, Z. Phys. **C67**, 433 (1995).

[86] J. Barish *et. al.*, Phys. Rev. **D17**, 1 (1978).

[87] H. Sarikko, *Proc. of the NEUTRINO'79*, 507 (1979)

[88] S. Barlag, *et. al.*, Z. Phys. **C11**, 283 (1982).

[89] T.Sjöstrand *et al.*, CERN-TH-7112-93 (1994).

[90] P. Musset and J. P. Vialle, Phys. Rep. **C39**, 1 (1978).

[91] J. E. Kim *et. al.*, Rev. Mod. Phys. **53**, 211 (1981).

[92] D. Rein and L. M. Sehgal, Nucl. Phys. **B223**, 29 (1983) ; P. Marage *et. al.*, Z. Phys. **C31**, 191 (1986).

[93] S. J. Barish *et. al.*, Phys. Rev. **D19**, 2521 (1979).

[94] N. J. Baker *et. al.*, Phys. Rev. **D25**, 617 (1982).

[95] S. Ciampolillo *et. al.*, Phys. Lett. **84B**, 281 (1979).

[96] L. L. Salcedo, E. Oset *et. al.*, Nucl. Phys. **A484**, 557 (1988).

[97] T. S. Kosmas and E. Oset, Phys. Rev. **C53**, 1409 (1996).

[98] M. Takatsuki, Master thesis of Kobe University (2001), unpublished, in Japanese.

[99] V. Tumakov, K2K-note DETECTOR/MUC/98-002.

Acknowledgement

I would like to express my great appreciation to my adviser, Prof. Koichiro Nishikawa. He guides me in fascinating “High Energy Physics” world, and always supports my reserch activities. I admire his smart viewpoint to the physics, and his lead of the K2K experiment. I wish to extend my appreciation to Prof. K.Nakamura, Prof. Y.Totsuka, Prof. Y.Suzuki, Prof. C.K.Jung, and Dr. M.Sakuda. Their management of K2K experiment enables me to accomplish my works.

My study depends on the hard work of many collaborators. Chapter 7 is supported by MRD group, Dr. T.Ishii, Dr. A.Sakai, Mr. K.Shiino, Mr. K.Tauchi, Dr. S.B.Lee, and Mr. J.H.Choi. Chapter 6 is supprted by Beam Monitor group, Dr. T.Hasegawa, Dr. T.Maruyama, Dr. J.Hill, Dr. W.Gajewski, Dr. M.Kohama, Mr. T.Kadowaki, Mr. E.Seo, and Mr. H.Yokoyama. Chapter 8 is supported by 1kt group, Dr. Y.Itow, Dr. M.Miura, Dr. S.Mine, Dr. T.Nakaya, Mr. C.Mauger, Mr. S.Nakayama, and Mr. A.Shima. Chapter 9 is supported by K2K-SK group, Dr. K.Kaneyuki and Mr. S.Yamada, as much as the Super-Kamiokande collaborators. I have great thank for the complete data-taking works performed by Dr. T.Kobayashi, Dr. Y.hayato, Dr. M.Yoshida, and Mr. H.G.Berns. Many times I have a support of FGD group, Dr. T.Ishida, Dr. Y.Oyama, Dr. A.C.Suzuki, Dr. T.Chikamatsu, Dr. H.Ishino, Dr. H.Park, Dr. S.Boyd, Dr. B.J.Kim, Dr. V.Tumakov, Mr. E.Sharkey, Mr. T.Iwashita, Mrs. E.J.Jeon, and Mrs. H.Yokoyama. I got an advice and discussion of the physics of neutrino interaction from Mr. J.Kameda. I would like to express my gratitude to all of these collaborators, giving me a lot of discussion of the analysis as much as the neutrino physics. I am deeply grateful to KEK-PS accelerator group and Beam-channel group, for their hard work on providing stable neutrino beam. I always appreciate to Mr. M.Taino and Beam-channel group members, for supporting the experiment and care about us. I am very happy to accomplish this experiment with all of the collaborators, including Mr. M.Nakamura, Mr. M.Etoh, Mr. S.Echigo, Mr. S.Kenmochi, Mr. T.Umeda, Mrs. E.M.Jeong, Mrs. H.K.Lee, Mr. M.Kitamura, Mr. T.Inada, Mr. G.Kume, Mr. M.Onchi, Mr. S.Kishi, and Mrs. M.Takatsuki.

I am grateful to our laboratory members in Kyoto University, especially, Prof. N.Sasao, Dr. H.Sakamoto, Dr. T.Nomura, Dr. T.Nakaya, Mr. M.Suehiro, Dr. H.R.Sakai, Dr. Y.Ushiroda, Mr. T.Akky.Fujiwara, Mr. S.Mukai, Mr. H.Yokoyama, Mr. I.Kato, Mr. A.Shima, Mr. H.Maesaka, Dr. A.K.Ichikawa, and Prof. K.Nishikawa, for a many physics (and beyond-physics?) discussion.

I thank KEK, ICRR, and the Japan Society for Promotion of Science, for financial support and promotion of this study.

Finally, I gratefully acknowledge my family and my best friends, for a lot of encouragement and support throughout my physicist life.